Floquet calculations of atomic photo-electron spectra in intense laser fields

Day, Henry Clive

Floquet Calculations of Atomic Photo-Electron Spectra in Intense Laser Fields

by

Henry Clive Day B.Sc (Dunelm)

A thesis submitted to the University of Durham in candidature for the degree of Doctor of Philosophy

May 1997

Abstract

We present the results of Floquet calculations of rates of photo-detachment from a short-range three-dimensional model atom in an intense high-frequency laser field. We find that beyond a certain intensity the atom becomes progressively more stable against ionisation and that at this intensity the ATI spectrum exhibits a plateau of the kind that has recently been reported in the literature [101]. We also discuss the angular distribution of the photoelectrons and examine the special case of a laser-induced degeneracy in the frequency-intensity plane.

In the Floquet method one represents the time-dependent Schrödinger equation by an infinite series of coupled time-independent equations, although in practice one must truncate these to a system of finite size. We study the consequences of this truncation by performing a series of calculations for the rate of (resonant) multiphoton detachment from a one-dimensional model atom in a laser field. We find that if the wavefunction is modified to take full account of the truncation then the number of equations which must be retained in order to obtain accurate results is significantly reduced.

In performing a Floquet calculation for a real atomic system it is generally assumed that the atom remains at all times in a single diabatic Floquet state, rather than in a superposition of such states. By constructing a suitable two-state model we investigate the validity of this approximation and discuss the usefulness of the Floquet method in modelling an actual experiment.

We present results for the multiphoton ionisation of H($1s$) by a monochromatic circularly polarised field and by a linearly polarised bichromatic field of commensurable frequencies. In the monochromatic case we draw qualitative comparisons with the predictions of Keldysh theory and use the concept of a propensity rule to explain why the angular distributions remain essentially perturbative at high intensities. In the bichromatic case we study the structure of the ATI spectrum and in particular the role played by a relative phase. The angular distributions are found to be strongly affected by the low-frequency field even when its intensity is too small to cause any appreciable ionisation of the system.

Acknowledgements

I would like to thank my supervisor, Dr Robert Potvliege, for accepting me as a research student in Durham and for always being there on the many occasions when I have needed help and guidance. I would also like to offer my sincere thanks to Dr Lydia Heck for her unstinting kindness and generosity in helping me with all my computational and technical problems throughout the last four years. Further, I would like to acknowledge the many fruitful discussions I have had with Dr Jim McCann, illuminating a few of the murkier corners of mathematics and physics. Other people whose time I gratefully acknowledge include Martin Plummer and Martin Dörr.

Many thanks go to my officemates Simon Gouldsworthy, Emine Mese, Andrew Fearnside, Peter Davies and Alex Ng for the friendship and support they have offered in the face of various adversities. I would also like to thank the friends who have made my life in Durham such a happy experience, Christian Caron, Maria Farsari and Peter G Davies. Rumour has it that the 'G' stands for *Gerber*. Most of all I would like to give my heartfelt thanks to my family who have unquestioningly given me their total love and support throughout my studies, both pre- and post-graduate.

Finally, I would like to acknowledge the financial support of the Engineering and Physical Sciences Research Council (EPSRC) during the major part of my studies. Additional thanks must go to the Atomic Theory Reseach Group here in Durham and to Professor Alfred Maquet of the *Laboratoire de Chimie Physique-Matière et Rayonnement, Université Pierre et Marie Curie* for the financial support that enabled me to attend conferences in Crete and Paris respectively.

Declaration

I declare that the work contained in this thesis has not previously been submitted for a degree, either at this university or at any other. All the work presented herein was conducted by the author, unless explicitly stated otherwise.

Henry C Day

May 1997

Contents

Chapter 1

Introduction

1.1 Multiphoton Processes

In this thesis we study several aspects of the interaction of a one-electron atom (or model atom) with an intense laser field. The interaction between an atomic system and a radiation field has been central to physicists' understanding of quantum theory since its inception and for most of this time a perturbative approach has been wholly adequate. But in the early 1960s the advent of the laser as a source of coherent light afforded us our first opportunity to study high-order absorption and emission processes and as the laser technology improved it became apparent that many-order perturbation theory is not always sufficient. This technology-driven discovery of photon-atom dynamics is an ongoing process and the development, in particular of high-frequency sources of intense light, is still far from its conclusion.

Multiphoton processes are those involving the simultaneous absorption of more than one quantum of radiation. For a bound state in a given atomic system it may be that the absorption of one photon (of a specific frequency) does not impart sufficient energy to ionise the atom. (Henceforth we abbreviate single-photon ionisation as SPI.) Instead the atom may simultaneously absorb many photons from the radiation-rich laser field, passing through a number of virtual (intermediate) states before reaching the continuum. These virtual states are not true eigenstates of the atom and their lifetime is limited

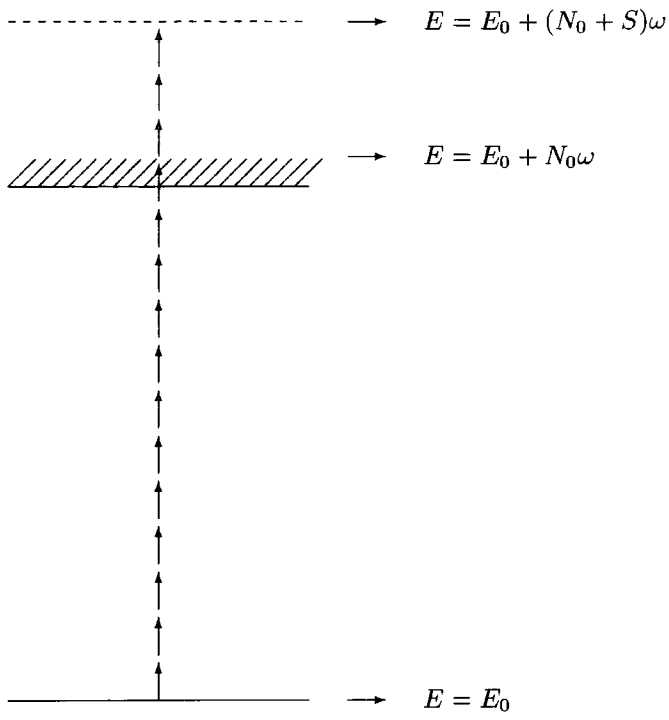

Figure 1.1: A schematic diagram illustrating the multiphoton ionisation of H($1s$)by radiation of wavelength 1064 nm. Fifteen photons are absorbed in total of which three are surplus to the N_0 that are necessary if the atom is to be ionised by the field.

to the order of one cycle of the incident laser field. An example of multiphoton ionisation (MPI) is the ionisation of Hydrogen atoms in their ground state by a YAG:Nd laser (whose characteristic wavelength is 1064 nm). In this example the minimum number of photons that must be absorbed in order that ionisation might occur is twelve. This process is illustrated in figure 1.1. Here the atom absorbs $N = N_0 + S = 15$ photons of which $N_0 = 12$ are sufficient for ionisation of the atom to be an open channel and $S = 3$ are surplus photons. If $S > 0$ (or equivalently, $N > N_0$) then the ionisation process is tautologically referred to as 'above-threshold ionisation' (ATI) or, more aptly, excess-photon ionisation. E denotes the energy of the atom during the ionisation process and E_0 denotes the initial energy of the atom (dressed by the field) before any photons have been absorbed.

When $N > N_0$ quanta are taken from the field one of two possibilities will occur. Firstly the atom may give up all of the energy it has gained by emit-

ting a single photon of energy $N\omega$ - a process known as harmonic generation. Very high harmonics have been generated in this way, for example, the 109^{th} harmonic of 806 nm radiation in Neon [91]. Processes such as this may in future be developed as a useful source of coherent x-ray radiation. Secondly the electron may leave the vicinity of the atom (or, more properly, the residual ion) carrying with it all of the surplus energy. Since this energy was originally acquired in integer multiples of the photon energy the outgoing electrons will conform to a discrete energy spectrum with peaks separated in energy by ω and labelled by $S = 0, 1, 2...$ This is known as an ATI spectrum. Harmonic spectra and ATI spectra share many common features but in this thesis we are concerned exclusively with the ATI spectra. Early experimental observations of MPI processes include the detection of two-photon ionisation of the I^- ion by Hall *et al* [66] in 1961 and the discovery of seven-photon ionisation of Xenon by Voronov and Delone [155] in 1965. However these first experiments were not sufficiently refined to yield well-resolved spectra of electron energies. Multiphoton continuum-continuum transitions were first observed by Weingartshofer *et al* who studied multiphoton absorption and emission processes in the context of laser-stimulated electron scattering [158].

One of the first experiments to demonstrate a clearly-resolved ATI spectrum was performed by Agostini *et al* [3] in 1979 using a gas of Xenon atoms and a Nd^{+++}-glass laser (1064nm). Using the fundamental beam to excite the atoms the lowest open ionisation channel requires 11-photon absorption and it was found that the dominant factor affecting the energy of the ejected electrons is the ponderomotive acceleration imparted to the electrons as they leave the focus of the laser beam. Therefore only a single broad maximum in the photo-electron spectrum was observed. But by using the second harmonic of this laser to ionise the atoms, rather than the fundamental beam, it was expected that the ponderomotive acceleration should be reduced by a factor of approximately 20. This allowed an additional peak due to the absorption of $N = N_0 + 1 = 7$ photons to be easily discerned in the electron energy spectrum. This second ATI peak had a magnitude of about one tenth that of the first above-threshold peak, in accordance with the relatively low

intensity of the electric field (8×10^{12} W/cm^2). Over the following decade the resolution of ATI experiments improved dramatically and two contrasting regimes were observed: on the one hand there are the long laser pulses in which the positions of the ATI peaks, while always separated by the photon energy ω, remain independent of intensity; and on the other hand there are the short pulses in which the energies at which the ATI peaks occur shift strongly with the intensity of the incident beam. The crucial parameter in delineating these two cases is the ratio $\beta = R_0/(v\tau)$ of the time taken by the electron to leave (in a radial direction) the focus of the laser to the laser pulse duration τ. Here, R_0 is the radius of the focal point and v is the electron velocity [83].

Let us briefly discuss the two limiting cases. With $\beta \ll 1$ we have a long laser pulse which allows ample time for electrons to leave the focal region while the pulse is still strong and, in doing so, acquire an additional translational energy. That is, the ponderomotive energy associated with the quiver motion of the electron in the field is entirely converted into kinetic energy when the electron is accelerated by the field-gradient (ponderomotive) force. Now, before ionisation, the energy levels of the atom in the field experience an intensity dependent Stark shift approximately equal to (negative) the ponderomotive energy and this energy must additionally be supplied (by photon absorption) for ionisation to occur. Thus, once the electron has left the focal region, these two effects cancel each other, leaving a series of ATI peaks whose position is independent of the laser intensity. With $\beta \gg 1$ we have the opposite extreme in which the laser pulse dies away while the electrons still lie in the focal region and in this instance the ponderomotive energy is not recovered by the electron and is instead returned to the field. Thus, depending on the value of β, some or all of the ponderomotive energy possessed by the electron in the laser-field may be removed by the field when the pulse finishes and if this occurs then the observed ATI peaks will be shifted to lower energy-values. The value of the ponderomotive energy depends strongly on intensity and so the shift in the energies at which the ATI peaks occur gives us an indication of the intensity-dependence of the ionisation process in these

shorter pulses.

At low intensities (dependent on the wavelength of the laser) we expect multiphoton ionisation to be accurately described by perturbation theory. We can define the perturbative regime in terms of the quiver-amplitude α_0 of the electron in the field, $\alpha_0 = \mathcal{E}_0/\omega^2$, by claiming that we expect perturbative behaviour for intensities and wavelengths such that $\alpha_0 < 2$. This figure is only approximate and is based on empirical evidence. For example, at $\lambda = 2128$ nm and $I = 10^{12}$ W/cm^2 we have $\alpha_0 = 11.7$ a.u., placing us in a highly non-perturbative regime whereas at the same intensity but with $\lambda = 266$ nm we obtain $\alpha_0 = 0.73$ a.u. which is well within the bounds of perturbation theory. In this perturbative limit it is predicted that the rate for ionisation by N-photon absorption should scale with the N^{th} power of the laser intensity, *viz.* $(dP_N/dt) \propto I^N$, where P_N is the ionisation probability. Thus $N+1$-photon absorption is always less probable than N-photon absorption, so, while perturbation theory predicts a long series of ATI peaks it also predicts that the first above-threshold peak must be the highest and that the others with $N > N_0$ must be monotonically decreasing in height. Note that this was indeed what Agostini had found in his first successful experimental investigation [3].

Perturbation theory has been used to derive analytic expressions for the total and partial rates of multiphoton ionisation for a one-electron atom in an electric field [86] and also for the angular distributions of the resulting photo-electrons. In the case of linear polarised light the *angular distributions* are strongly concentrated along the axis of polarisation (i.e. perpendicular to the propagation axis) while for circularly polarised light the electrons are distributed mostly into the polarisation plane (i.e. at right angles to the quantisation axis). Indeed, in the latter case one obtains a particularly simple expression for the angular distribution. This is because each photon absorbed alters both the orbital angular momentum and magnetic quantum numbers l and m by one unit and so, for an initial state which is spherically symmetric (such as the ground state of Hydrogen), the transition amplitude $T_N(\theta)$ is proportional to the spherical harmonic $Y_{N,N}(\theta,\phi)$ (where N is the

total number of photons absorbed). Thus the angular distribution of photo-electrons ejected from such a state is [86]

$$\frac{d\Gamma_N}{d\theta} = \mid T_N(\theta) \mid^2 \propto \sin^{2N}\theta \tag{1.1}$$

where Γ_N is the total rate on ionisation into channel N.

Both experimental and theoretical investigations of strong-field photo-electron spectra have seen dramatic developments over the last fifteen years. Muller *et al* [96] demonstrated in 1983 that the ATI peaks shift not only according to the Ponderomotive energy of the electron oscillating in the field but also with the quadratic (AC) Stark shift of the atomic energy levels. Because the binding energies of Rydberg states are small, the shifts in their eigen-energies induced by the field are essentially just the ponderomotive energy. However, the AC Stark shift for an atomic ground state in an intense laser field may be greater than the Ponderomotive shift and, except at the highest experimentally relevant frequencies, is always negative [24]. Thus, the Rydberg and continuum states will typically shift upward relative to the low-lying states, resulting in an increase in the ionisation potential of the atom [21]. As the intensity increases an ionisation channel that is initially open may close due to this light-induced deepening of the potential well and at still higher intensities there may be further channel closures. The (real) energy below which N-photon ionisation is not possible is referred to as the 'N-photon threshold'. Thus, returning to our example from figure 1.1 of the multiphoton ionisation of H($1s$), we find that at low intensities $N_0 = 12$ photons are sufficient to ionise the atom but at intensities $I > 4 \times 10^{12}$ W/cm^2 the $1s$ energy level is shifted below the 12-photon threshold, giving $N_0 = 13$. This channel-closing is demonstrated especially clearly by short-ranged potentials. Here the closure of an ATI channel is reflected in the total rate of ionisation which dips sharply as the intensity approaches an N-photon threshold and then increases once again on the other side. The same is not usually true of a long-ranged potential such as the Coulomb potential [119]. In the corresponding ATI spectrum the first peak is at first suppressed and then disappears entirely as one crosses the threshold. In experimental spectra the picture is not quite this simple because the intensity varies continuously during the pulse and so

even if a certain channel is closed at the peak intensity there may still be electrons ejected into that channel during the rise or fall of the pulse. There have been many experimental studies of this channel-closing phenomenon: Lompré *et al* [89] have observed the closing of up to three ATI channels in Helium at an intensity of 4.42×10^{13} W/cm^2 using 532 nm light; Xiong *et al* [162] have used the longer wavelength of the CO^2 laser (10.6 μm) to observe hundreds of missing peaks in the MPI of Xenon at an intensity of 10^{13} W/cm^2.

Recent experimental studies of photo-electron spectra have revealed several new and exciting phenomena including plateau regions in the envelope of ATI peak heights and side-lobes in the angular distributions of the ejected electrons. Paulus *et al* [100] measured the ATI spectra for rare gas atoms in strong laser fields at 630 nm. They found that (to varying degrees) all the atoms studied exhibited a plateau region in the ATI spectrum over which the height of the ATI peaks holds approximately constant. The onset of this plateau region is found to occur at electron energies of around 20 eV. One-dimensional and three-dimensional model calculations by these authors reveal that this effect is essentially a single-electron phenomenon and does not relate to core-excitation. A suggested mechanism is that the observed energy spectrum is actually a superposition of two parts. Firstly there is a photo-electron energy distribution arising from those electrons that are ionised 'directly' within a single optical cycle. One then adds to this a second spectrum arising from those photo-electrons that are initially produced with approximately zero kinetic energy and are then swept back towards the core by the electric field. In doing so these electrons may acquire additional energy by absorbing more photons and their energy distribution will be quite different from that of the electrons that are ionised in a single step. This process is also described in detail by Kulander *et al* [82]. Both Paulus *et al* [101] and Yang *et al* (including Kulander) [163] then continue by applying the same reasoning to the angular distributions of the photo-electrons. Yang *et al* measure the angular distribution of photo-electrons from Xenon and Krypton in a strong field of wavelength 1.05 μm. Both groups find that the

side-lobes (or scattering rings) occur only in ATI channels corresponding to the beginning of the plateau region. This is consistent with an explanation involving rescattering from the ionic core of the tunneling component of the continuum wavefunction.

1.1.1 Stabilisation Phenomena

There has been intense interest and speculation in recent years concerning the phenomenon known as strong-field (or adiabatic) stabilisation. This is the highly counter-intuitive effect whereby an atom (or ion) becomes more resistant to ionisation with increasing intensity of the incident laser field. There are many reasons why at atom might tend to stabilise in an intense field and until recently there has been some confusion concerning the region of applicability of each mechanism. One can broadly summarise these stabilisation phenomena under four headings: transient stabilisation, interference stabilisation, resonant stabilisation and adiabatic stabilisation. (See, for example, Muller in [98].) Each may apply only to certain atoms or ions, within a specific range of intensities and for a particular range of frequencies. Essentially one can trace these effects back to the fact that an electromagnetic field is an AC phenomenon and thus, on average, should tend not to displace or accelerate electrons with respect to the nucleus.

Transient stabilisation may occur in short laser pulses and is based on the concept of electronic wave-packets. The idea is that one state out of a manifold of (Rydberg) states, all lying within the bandwidth of the laser, is being ionised. If all of the states in the manifold couple to the same continuum then one can describe the original manifold in terms of a new basis set (consisting of linear combinations of the original manifold states) in which only one of these new states couples to the continuum. (The other basis states are all orthogonal to the ionising basis state and so have no coupling to the continuum). When the original manifold state is projected onto the new basis of states, only the component that is projected onto the single ionising state can be ionised directly. (This component is assumed to be small.) The remaining

population is trapped in the other basis states that are impervious to ionisation. These basis states are not true eigenstates of the Hamiltonian but are coupled to each other by it. That is, population may transfer from the non-ionising basis states to the ionising state by two-photon Λ-transitions via the continuum. Thus, all of the population will eventually be ionised (hence the nomenclature 'transient stabilisation') but this eventual ionisation will occur over an unusually long time-scale. This kind of stabilisation has been studied experimentally by Hoogenraad *et al* [71].

Interference stabilisation is in many respects very similar to transient stabilisation. Again one should picture a group of Rydberg states, all of which couple to the same continuum. (In this instance the states need not lie within the bandwidth of the laser.) One assumes that these states are populated by a quantum-mechanical Rydberg wavepacket (not necessarily localised in space) and the upshot is that there is destructive interference between the ionisation from each of the various states to the single continuum state. In other words, population that is ionised from one state will immediately be recaptured by Λ-transitions into one of the other states, trapping the population in this series of bound states. The most important distinction between this and the transient stabilisation is that here the interference remains destructive, leading to lifetimes for these wave-packets that may be very long indeed. This model of ionisation out of a Rydberg state was obtained by Fedorov and Movsesian [50] in 1988.

Resonance stabilisation is perhaps something of a misnomer. It involves the idea of a 'stabilisation window' which is actually nothing more than an anti-resonance. The idea is that Stark shift will alter the relative distances between various pairs of bound states and that within a specific intensity window a given pair of states may be shifted out of resonance, leading to a temporary decrease in the ionisation rate as the intensity increases. This does perhaps satisfy our definition of a stabilisation process but then so also does the simple mechanism of a channel closure. Resonance stabilisation phenomena have been investigated recently by Faisal and collaborators [46].

Adiabatic stabilisation is a phenomenon associated with super-intense fields and is not a dynamical process. Unlike all of the other mechanisms described above it involves only a single bound state of the atom (which may be a Rydberg state or a low-lying state) and is a steady-state property of the ionisation rate. In order to reach the adiabatic stabilisation regime one must (in practice) first increase the intensity through the range of values in which the ionisation rate is greatest. This has become known as 'death valley' and is a serious obstacle to the experimental study of this phenomenon. However, experiments can be (and have been) performed using atoms initially prepared in circular Rydberg states for which the maximal rate of ionisation is not too severe. De Boer *et al* [8] [9] have carried out experiments (following this prescription) demonstrating adiabatic stabilisation of the $5g$ state in Neon by a laser field at 620 nm with an intensity of a few 10^{13} W/cm^2. Strong-field stabilisation is in fact associated with high-frequency fields in which, as the intensity increases, the electron spends increasingly little time in the vicinity of the nucleus. Viewed from the rest-frame of a free electron oscillating in the field it is then clear that as the magnitude of the oscillations increases, the probability of ionisation - represented by the interaction of the electron with the nucleus - decreases.

1.2 Principles of Photon-Atom Interactions

In this section we give a brief overview of the physical concepts that are fundamental to a description of photon-atom interactions. This consists essentially of choosing to think in terms of the characteristic atomic scales of length and time. A number of good approximations then arise naturally by contrasting the physical dimensions of the field with those of an atomic system. Throughout this thesis we choose to express all quantities in *atomic units* (a.u.) in which $\hbar = e = m_e = 1$ where m_e is the mass of an electron. Therefore these constants do not appear in any of our equations. For the sake of simplicity we will limit the following discussion to the case of a monochromatic, linearly polarised, laser field interacting with a one-electron

atom. The scope of this thesis is of course much broader and the necessary generalisations will be introduced as and when necessary.

1.2.1 The Interaction Hamiltonian

The theory of MPI processes can be formulated in either a fully quantum-mechanical or a semi-classical formalism. In the semi-classical approach it is the radiation field that is treated classically: it is represented by an effective Hamiltonian consistent with Maxwell's equations. This semi-classical treatment (usually) leads to a Hamiltonian which is periodic in time due to the assumed, sinusoidal, time-dependence of the electromagnetic field. It has been demonstrated by Shirley and Stenholm [145] that the semi-classical and fully quantised theories are equivalent in the strong-field limit. Let us start from from the semi-classical standpoint and consider the Schrödinger equation for an atom in the absence of an external field,

$$H_A\Psi(\boldsymbol{r},t) = i\frac{\partial}{\partial t}\Psi(\boldsymbol{r},t) \tag{1.2}$$

where

$$H_A = \frac{\boldsymbol{p}^2}{2} + V(r) \tag{1.3}$$

and $\boldsymbol{p} = -i\boldsymbol{\nabla}$ is the canonical momentum. Adopting the so-called 'minimum-coupling' prescription one can introduce the radiation field simply by substituting the kinematical momentum for the canonical momentum, *viz.*

$$\boldsymbol{p} \rightarrow \boldsymbol{p} - \frac{1}{c}\boldsymbol{A}(\boldsymbol{r},t) \tag{1.4}$$

where $\boldsymbol{A}(\boldsymbol{r},t)$ is the vector potential of the field, and by simultaneously adding another term representing the scalar electromagnetic potential ϕ [45]. Thus the atom in the field may be represented by the Hamiltonian

$$H = \frac{1}{2}\left(\boldsymbol{p} - \frac{1}{c}\boldsymbol{A}(\boldsymbol{r},t)\right)^2 - \phi + V(r) \tag{1.5}$$

This prescription is justified (classically) because it correctly reproduces the equation of motion - the Lorentz equation - when substituted into the classical

canonical equations. Let us also recall the gauge invariance of the electromagnetic potentials $\{\boldsymbol{A}, \phi\}$. The electric field $\boldsymbol{\mathcal{E}}$ and the magnetic field $\boldsymbol{\mathcal{B}}$ are obtained (classically) by simple differentiations of the potentials, *viz.*

$$\boldsymbol{\mathcal{E}} = -\frac{1}{c}\frac{\partial \boldsymbol{A}}{\partial t} + \nabla\phi \tag{1.6}$$

and

$$\boldsymbol{\mathcal{B}} = \boldsymbol{\nabla} \wedge \boldsymbol{A} \tag{1.7}$$

But we can transform the electromagnetic potentials according to

$$\boldsymbol{A} \rightarrow \boldsymbol{A}' = \boldsymbol{A} + \boldsymbol{\nabla}\Lambda \tag{1.8}$$

and

$$\phi \rightarrow \phi' = \phi + \frac{1}{c}\frac{\partial \Lambda}{\partial t} \tag{1.9}$$

and one readily finds that under these transformations the corresponding fields transform as $\boldsymbol{\mathcal{E}} \rightarrow \boldsymbol{\mathcal{E}}' = \boldsymbol{\mathcal{E}}$ and $\boldsymbol{\mathcal{B}} \rightarrow \boldsymbol{\mathcal{B}}' = \boldsymbol{\mathcal{B}}$. This is an example of local gauge invariance (or a gauge transformation of the second kind). Thus, one may freely choose the gauge in which $\boldsymbol{\nabla} \cdot \boldsymbol{A} = 0$ and $\phi = 0$. This is known as the *radiation gauge* and is sometimes also referred to as the *Coulomb gauge* or the *transverse gauge.*

With this choice of gauge we can rewrite the semi-classical Hamiltonian of the atom in the radiation field (equation (1.5)) as

$$H = H_A + H_I(\boldsymbol{r}, t) \tag{1.10}$$

where

$$H_I(\boldsymbol{r}, t) = -\frac{1}{c}\boldsymbol{p} \cdot \boldsymbol{A}, (\boldsymbol{r}, t) + \frac{1}{2c^2}\boldsymbol{A}(\boldsymbol{r}, t) \cdot \boldsymbol{A}(\boldsymbol{r}, t) \tag{1.11}$$

and the parentheses indicate that one should take the usual anti-commuting combination. Electromagnetic waves are oscillations of the electromagnetic field and, as such, can be quantised by analogy to the one-dimensional harmonic oscillator. (This is known as *second quantisation* [45].) For a one-dimensional oscillator q it can readily be shown that the Hamiltonian

$$H = \frac{m}{2}\dot{q}^2 + \frac{m\omega^2}{2}q^2 \tag{1.12}$$

can [141], by means of the transformation

$$q = \frac{1}{\sqrt{2m\omega}}(a\mathrm{e}^{-i\omega t} + a^{\dagger}\mathrm{e}^{+i\omega t}), \qquad [a, a^{\dagger}] = 1 \tag{1.13}$$

be expressed in the form

$$H = \omega\left(a^{\dagger}a + \frac{1}{2}\right) \tag{1.14}$$

Recall that in the radiation gauge we have

$$\boldsymbol{\mathcal{E}} = -\frac{1}{c}\frac{\partial \boldsymbol{A}}{\partial t}, \qquad \boldsymbol{\mathcal{B}} = \boldsymbol{\nabla} \wedge \boldsymbol{A} \tag{1.15}$$

and that, in the absence of external currents, $\boldsymbol{A}$ satisfies the free wave equation. We can expand the radiation field in a Fourier series

$$\boldsymbol{A}(\boldsymbol{r}, t) = \sum_{\boldsymbol{k}} \boldsymbol{A}_{\boldsymbol{k}}(t)\, \mathrm{e}^{i\boldsymbol{k}\,\cdot\,\boldsymbol{r}} \tag{1.16}$$

in which the individual oscillation amplitudes $\boldsymbol{A}_{\boldsymbol{k}}(t)$ may be decomposed into sums of annihilation and creation operators, in the manner of equation (1.13). In order to do this we must also obtain the quantities that are analogous to m and ω. But it is known that the total energy of the radiation field is given by

$$H_{\mathrm{rad}} = \frac{1}{8\pi}\int d\boldsymbol{r}\,(\boldsymbol{\mathcal{E}}^2 + \boldsymbol{\mathcal{B}}^2) = \frac{L^3}{8\pi}\sum_{\boldsymbol{k}}\left(\frac{1}{c^2}\left|\frac{\partial \boldsymbol{A}_{\boldsymbol{k}}}{\partial t}\right|^2 + |\,\boldsymbol{k} \wedge \boldsymbol{A}_{\boldsymbol{k}}\,|^2\right) \tag{1.17}$$

where L is the dimension of the quantisation volume of the field. Comparing equations (1.12) and (1.17) one can readily identify $m \to 1/(4\pi c^2)$ and $\omega \to ck$.

Further, one may represent the vector field $\boldsymbol{A}_{\boldsymbol{k}}$ by two polarisation vectors $\hat{\boldsymbol{\epsilon}}_{\boldsymbol{k},\lambda}$ $(\lambda = 1, 2)$ which are orthogonal both to $\boldsymbol{k}$ and to each other [53]. Thus we obtain

$$\boldsymbol{A}(\boldsymbol{r}, t) = \sum_{\boldsymbol{k},\lambda}\left(\frac{2\pi c}{kL^3}\right)^{1/2}[a_{\boldsymbol{k},\lambda}\hat{\boldsymbol{\epsilon}}_{\boldsymbol{k},\lambda}\exp(i\boldsymbol{k}\,\cdot\,\boldsymbol{r} - i\omega_{\boldsymbol{k}}t) + a^{\dagger}_{\boldsymbol{k},\lambda}\hat{\boldsymbol{\epsilon}}^{*}_{\boldsymbol{k},\lambda}\exp(-i\boldsymbol{k}\,\cdot\,\boldsymbol{r} + i\omega_{\boldsymbol{k}}t)] \tag{1.18}$$

where $\omega_{\boldsymbol{k}} = ck$. The values of $\boldsymbol{k}$ are fixed by assuming periodic boundary conditions on the boundaries of the volume L^3. Continuing the analogy to the oscillator, we require

$$[a_{\boldsymbol{k},\lambda}, a^{\dagger}_{\boldsymbol{k},\lambda}] = \delta_{\boldsymbol{k},\boldsymbol{k}'}\delta_{\lambda,\lambda'}, \qquad [a_{\boldsymbol{k},\lambda}, a_{\boldsymbol{k},\lambda}] = [a^{\dagger}_{\boldsymbol{k},\lambda}, a^{\dagger}_{\boldsymbol{k},\lambda}] = 0 \tag{1.19}$$

In this scheme, $a_{\boldsymbol{k},\lambda}$ annihilates (and $a^{\dagger}_{\boldsymbol{k},\lambda}$ creates) a quantum of wave number $\boldsymbol{k}$ and polarisation λ. Substituting equation (1.18) into (1.17) one obtains the Hamiltonian of the free radiation field,

$$H_{\text{rad}} = \sum_{\boldsymbol{k},\lambda} \omega_{\boldsymbol{k}} \left(a^{\dagger}_{\boldsymbol{k},\lambda} a_{\boldsymbol{k},\lambda} + \frac{1}{2} \right) \tag{1.20}$$

Let us introduce the operator $\hat{N}_{\boldsymbol{k},\lambda} = a^{\dagger}_{\boldsymbol{k},\lambda} a_{\boldsymbol{k},\lambda}$. This has eigenstates of the form

$$\mid n_{\boldsymbol{k},\lambda}\rangle = \frac{1}{\sqrt{n_{\boldsymbol{k},\lambda}!}} (a^{\dagger}_{\boldsymbol{k},\lambda})^{n_{\boldsymbol{k},\lambda}} \mid 0\rangle \tag{1.21}$$

corresponding to eigenvalues $n_{\boldsymbol{k},\lambda} = 0, 1, 2, ...$ The state populated by zero photons (vacuum state) is written as $\mid 0\rangle$. One can express the eigenstates of the non-interacting radiation field H_{rad} as products of the states $\mid n_{\boldsymbol{k},\lambda}\rangle$ [45], *viz.*

$$\mid ..., n_{\boldsymbol{k},\lambda}, ...\rangle = \prod_{\boldsymbol{k}_i} \prod_{\lambda_i} \mid n_{\boldsymbol{k}_i,\lambda_i}\rangle \tag{1.22}$$

These states possess energies

$$E = \sum_{\boldsymbol{k}} \sum_{\lambda} \omega_{\boldsymbol{k}} \left(n_{\boldsymbol{k},\lambda} + \frac{1}{2} \right) \tag{1.23}$$

The operator $a_{\boldsymbol{k},\lambda}$ reduces the occupation number $n_{\boldsymbol{k},\lambda}$ of the mode $\{\boldsymbol{k}, \lambda\}$ by one unit whilst leaving all the other occupation numbers unchanged,

$$a_{\boldsymbol{k},\lambda} \mid ..., n_{\boldsymbol{k},\lambda}, ...\rangle = \sqrt{n_{\boldsymbol{k},\lambda}} \mid ..., n_{\boldsymbol{k},\lambda}, ...\rangle \tag{1.24}$$

Consequently the energy is lowered by an amount $\omega_{\boldsymbol{k}}$ and the operator $a_{\boldsymbol{k},\lambda}$ is referred to as an annihilation operator. Specifically, it destroys a photon in the mode $\{\boldsymbol{k}, \lambda\}$, i.e. with momentum vector $\boldsymbol{k}$, polarisation vector $\hat{\boldsymbol{\epsilon}}_{\boldsymbol{k},\lambda}$ and

energy $\omega_{\boldsymbol{k}}$. Conversely, $a^{\dagger}_{\boldsymbol{k},\lambda}$ is the creation operator of photons with these quantum numbers,

$$a^{\dagger}_{\boldsymbol{k},\lambda} \mid ..., n_{\boldsymbol{k},\lambda}, ...\rangle = \sqrt{n_{\boldsymbol{k},\lambda}+1} \mid ..., n_{\boldsymbol{k},\lambda}+1, ...\rangle \tag{1.25}$$

Thus the total Hamiltonian for an atom coupled to the quantised radiation field may be written as

$$H = H_A + H_I + H_{\text{rad}} \tag{1.26}$$

where the terms on the right-hand side are given (respectively) by equations (1.3), (1.11) and (1.20). In the interaction Hamiltonian H_I the term in $\boldsymbol{A}$ gives rise to processes in which a single photon is annihilated or created. The term in $\boldsymbol{A}^2$ represents the creation or destruction of two photons, or alternatively, the simultaneous annihilation and creation of a photon.

1.2.2 Semi-Classical Theory

In an electromagnetic field the intensity I and the electric field amplitude $\mathcal{E}$ of the radiation are related to the photon density by

$$I = \frac{c}{8\pi} \mid \mathcal{E} \mid^2 = \langle n \rangle \frac{c\omega}{L^3} \tag{1.27}$$

where $\langle n \rangle$ is the average occupation number [12]. From this it is clear that in an intense field the average number of photons $\langle n \rangle$ contained in the field will be very great indeed compared to the number of photons exchanged with the atom. Thus, in an intense field one finds that stimulated processes dominate spontaneous processes by an enormous factor. A classical field is unable to account for the phenomenon of spontaneous emission but when this process is relatively insignificant one may justifiably treat the electromagnetic field as a classical field. In this semi-classical approach the electron follows a classical orbit with a smoothly varying velocity, whereas in the fully quantal treatment the energy changes of the electron are determined only by the number of photons absorbed or emitted [13].

Having decided that it is reasonable to approximate the radiation field by a semi-classical field we can rewrite the vector potential (1.18) as

$$\boldsymbol{A}(\boldsymbol{r},t) = \sum_{\boldsymbol{k},\lambda} \hat{\boldsymbol{\epsilon}}_{\boldsymbol{k},\lambda}[q_{\boldsymbol{k},\lambda}(t)\exp(i\boldsymbol{k}\cdot\boldsymbol{r}) + q^*_{\boldsymbol{k},\lambda}(t)\exp(-i\boldsymbol{k}\cdot\boldsymbol{r})] \tag{1.28}$$

where $q_{\boldsymbol{k},\lambda}(t)$ are coefficients replacing the creation and annihilation operators, $\boldsymbol{k}$ is a propagation vector, and λ has the same meaning as previously. Let us recall the classical wave equation for the vector potential in free space,

$$\left(\nabla^2 - \frac{1}{c^2}\frac{\partial^2}{\partial t^2}\right)\boldsymbol{A}(\boldsymbol{r},t) = 0 \tag{1.29}$$

By substituting (1.28) into (1.29) and projecting onto a plane wave from the left one obtains the equations governing the coefficients $q_{\boldsymbol{k},\lambda}(t)$ and $q^*_{\boldsymbol{k},\lambda}(t)$ [45],

$$\begin{aligned} \frac{\partial^2}{\partial t^2}q_{\boldsymbol{k},\lambda}(t) + c^2k^2q_{\boldsymbol{k},\lambda}(t) &= 0 \\ \frac{\partial^2}{\partial t^2}q^*_{\boldsymbol{k},\lambda}(t) + c^2k^2q^*_{\boldsymbol{k},\lambda}(t) &= 0 \end{aligned} \tag{1.30}$$

These equations can be satisfied by all complex $q_{\boldsymbol{k},\lambda}(t)$ which are solutions of the first-order equations

$$\frac{\partial}{\partial t}q_{\boldsymbol{k},\lambda}(t) = -i\omega_{\boldsymbol{k}}q_{\boldsymbol{k},\lambda}(t) \tag{1.31}$$

where $\omega_{\boldsymbol{k}} = ck$ is the well-known dispersion relation for electromagnetic waves in free space.

For a monochromatic laser field of constant amplitude, the vector potential (1.28) simplifies to

$$\boldsymbol{A}(\boldsymbol{r},t) = \boldsymbol{\epsilon}A_0\cos(\boldsymbol{k}\cdot\boldsymbol{r} - \omega t + \delta) \tag{1.32}$$

where $\boldsymbol{\epsilon} \equiv \boldsymbol{\epsilon}_{\boldsymbol{k},\lambda}$ is the polarisation vector, $A_0 \equiv q_{\boldsymbol{k}}(0)$ is the fixed amplitude, $|\,\boldsymbol{k}\,| \equiv \omega/c$ is the wave-number and δ is an arbitrary phase-shift of the field. In terms of this vector potential, the semi-classical Hamiltonian for an atom in the laser field may be written, in general, as

$$H = H_A + \frac{1}{2c}[2i\boldsymbol{A}(\boldsymbol{r},t)\cdot\nabla + i\nabla\cdot\boldsymbol{A}(\boldsymbol{r},t)] + \frac{1}{2c^2}\boldsymbol{A}(\boldsymbol{r},t)\cdot\boldsymbol{A}(\boldsymbol{r},t) - \phi \tag{1.33}$$

and, more simply, in the radiation gauge as

$$H = H_A + \frac{1}{c} i\boldsymbol{A}(\boldsymbol{r},t)\cdot\boldsymbol{\nabla} + \frac{1}{2c^2}\boldsymbol{A}(\boldsymbol{r},t)\cdot\boldsymbol{A}(\boldsymbol{r},t) \tag{1.34}$$

where H_A is the reference Hamiltonian given by

$$H_A = -\frac{1}{2}\nabla^2 + V(r) \tag{1.35}$$

and we have used the fact that $\boldsymbol{\nabla}\cdot\boldsymbol{A} = 0$ in this gauge.

1.2.3 The Dipole Approximation

A further simplification is made possible by considering the form of the plane wave $\exp(i\boldsymbol{k}\cdot\boldsymbol{r})$ in equation (1.28). It is known that in free space a monochromatic electromagnetic field can be derived from two scalar functions, say u and v, known as Debye potentials. These functions must satisfy the scalar Helmholtz equation

$$(\nabla^2 + k^2)\begin{Bmatrix} u \\ v \end{Bmatrix} = 0 \tag{1.36}$$

and they can be expanded on a basis of spherical harmonics, *viz.*

$$v = \sum_{l=0}^{\infty}\sum_{m=-l}^{l} a_{lm}\zeta_l^m, \qquad u = \sum_{l=0}^{\infty}\sum_{m=-l}^{l} b_{lm}\zeta_l^m \tag{1.37}$$

where the functions ζ_l^m are given by

$$\zeta_l^m(r,\theta,\phi) = \begin{Bmatrix} h_l(kr) \\ j_l(kr) \end{Bmatrix} Y_l^m(\theta,\phi) \tag{1.38}$$

and the spherical harmonics defined by [11]

$$Y_l^m(\theta,\phi) = (-1)^m \left[\frac{(2l+1)}{4\pi}\frac{(l-m)!}{(l+m)!}\right]^{1/2} \sin^m\theta \frac{d^m}{d(\cos\theta)^m} P_l(\cos\theta) e^{im\phi} \tag{1.39}$$

The radial functions h_l and j_l are the spherical Hankel and Bessel functions respectively [2]. One uses the spherical Bessel functions when the radiation field is regular at the origin ($r = 0$). The Hankel functions are used to describe fields behaving as outgoing waves at asymptotically large distances ($r \sim \infty$).

In terms of the Debye potentials u and v one can express the electric field vector as [147]

$$\boldsymbol{\mathcal{E}} = [\boldsymbol{\nabla} \wedge \boldsymbol{\nabla} \wedge (\boldsymbol{r}v)] + [i\omega \boldsymbol{\nabla} \wedge (\boldsymbol{r}u)] \tag{1.40}$$

where the first term represents electric multipoles and the second term re-spresents magnetic multipoles. Using this expansion our plane wave can be written in the form [13]

$$\exp[i\boldsymbol{k} \cdot \boldsymbol{r}] = 4\pi \sum_{l=0}^{\infty} \sum_{m=-l}^{l} i^l j_l(kr) Y_l^m(\theta, \phi) Y_l^{m*}(\theta', \phi') \tag{1.41}$$

where the unprimed angles are co-ordinates of the position vector and the primed angles are co-ordinates of the momentum vector. This expression is known as a *multipole expansion.* (An interesting discussion of multipole expansions is given by Cohen-Tannoudji *et al* in their treatise on quantum mechanics [24].)

It is known that the function $\mid j_l(kr) \mid$ is negligible for arguments $kr \ll 2l\pi$ [2]. Thus, in a spherical region of radius R, only the spherical harmonics of order $l \leq R/\lambda$ can contribute to the electromagnetic field. (Here, $\lambda = 2\pi c/\omega$ is the wavelength corresponding to the laser frequency ω.) In this region of radius R one can therefore express the field as a sum of multipoles (harmonics) of order $l \leq R/\lambda$. If R represents the physical dimensions of an atom (say, a few Angstroms) then the electromagnetic field can be adequately represented by a number of multipoles approximately equal to R/λ. But a typical laser wavelength is $\lambda = 2,000 \rightarrow 20,000$ Å and so the radiation field can be accurately represented by retaining only the zeroth order in the multipole expansion, *viz.*

$$\exp[i\boldsymbol{k} \cdot \boldsymbol{r}] = j_0(kr) \approx \frac{1}{kr} \sin(kr) \tag{1.42}$$

Thus, for small arguments kr one can readily approximate $\exp[i\boldsymbol{k} \cdot \boldsymbol{r}] = 1$ which is evidently equivalent to just retaining the first term in the Taylor series for this function. This is known as the dipole approximation. Note that the magnetic component of the electromagnetic field is now implicitly neglected since

$$\boldsymbol{\nabla} \wedge \boldsymbol{A}(t) = 0 \tag{1.43}$$

1.2.4 Gauge Transformations of the Second Kind

In the dipole approximation, the vector potential for a monochromatic laser field of constant amplitude becomes

$$\boldsymbol{A}(t) = A_0 \cos(\omega t + \delta)\hat{\boldsymbol{\epsilon}}_{\boldsymbol{z}} \tag{1.44}$$

for linear polarisation, or more generally,

$$\boldsymbol{A}(t) = A_0[\sin(\xi/2)\cos(\omega t + \delta)\hat{\boldsymbol{\epsilon}}_{\boldsymbol{x}} - i\cos(\xi/2)\sin(\omega t + \delta)\hat{\boldsymbol{\epsilon}}_{\boldsymbol{y}}] \tag{1.45}$$

for an elliptically polarised beam propagating in the z direction. The ellipticity parameter ξ takes the value $\pm\pi/2$ for a circularly polarised beam and zero for a linearly polarised beam (which in this case would be polarised along the y axis). In order to consider an actual laser pulse one should replace the constant amplitude A_0 with a temporal envelope $A_0(t)$.

The semi-classical Hamiltonian (1.34) for an atom in the field may now be written as

$$H = H_A + \frac{1}{c} i\boldsymbol{A}(t)\cdot\boldsymbol{\nabla} + \frac{1}{2c^2}A^2(t) \tag{1.46}$$

In this form the Hamiltonian is already in what is referred to as the *velocity gauge*. That is, the interaction is expressed in terms of the operator $\boldsymbol{\nabla}$ which is associated with the momentum or velocity of the particle. The term which is quadratic in the field contains no spatial dependence and can easily be removed by making a local gauge transformation (also known as a gauge transformation of the second kind [55]); see Gavrila in [57]

$$\Psi(\boldsymbol{r}, t) \rightarrow \Psi'(\boldsymbol{r}, t) = \exp\left[\frac{i}{2c^2}\int^t A^2(t')dt'\right]\Psi(\boldsymbol{r}, t) \tag{1.47}$$

This new wavefunction is found to satisfy the Schrödinger equation

$$i\frac{\partial}{\partial t}\Psi'(\boldsymbol{r}, t) = \left[-\frac{1}{2}\nabla^2 + V(r) + \frac{1}{c}i\boldsymbol{A}(t)\cdot\boldsymbol{\nabla}\right]\Psi'(\boldsymbol{r}, t) \tag{1.48}$$

and from this we identify the Hamiltonian as

$$H = H_A + \frac{1}{c} i\boldsymbol{A}(t)\cdot\boldsymbol{\nabla} \tag{1.49}$$

The velocity gauge is not always the most appropriate framework in which to represent the atom-field interaction. We define an alternative gauge transformation (of the second kind) by

$$\Psi(\boldsymbol{r},t) \rightarrow \Psi''(\boldsymbol{r},t) = \exp\left[-\frac{1}{c} i\boldsymbol{r}\cdot\boldsymbol{A}(t)\right]\Psi(\boldsymbol{r},t) \tag{1.50}$$

and substitute this ansatz into the Schrödinger equation whose Hamiltonian is the semi-classical Hamiltonian (1.34). Using the relation

$$\boldsymbol{\mathcal{E}}(t) = -\frac{1}{c}\frac{\partial}{\partial t}\boldsymbol{A}(t) \tag{1.51}$$

we obtain the Schrödinger equation satisfied by the wavefunction $\Psi''(\boldsymbol{r},t)$, namely [45]

$$i\frac{\partial}{\partial t}\Psi''(\boldsymbol{r},t) = \left[-\frac{1}{2}\nabla^2 + V(r) - \boldsymbol{r}\cdot\boldsymbol{\mathcal{E}}(t)\right]\Psi''(\boldsymbol{r},t) \tag{1.52}$$

In this form we see that the full Hamiltonian is

$$H = H_A - \boldsymbol{r}\cdot\boldsymbol{\mathcal{E}}(t) \tag{1.53}$$

and that the atom-field interaction is now written in terms of position rather than momentum. Hence the nomenclature *length gauge* for the Hamiltonian expressed in this form.

In the absence of any approximations (beyond the dipole approximation) the velocity and length forms of the atom-plus-field Hamiltonian are of course entirely equivalent but when further approximations are introduced the equivalence is no longer exact. (See, for example, the description of the Floquet method in section 1.3.2.) In practice one should always attempt to verify explicitly that calculated results are gauge-independent to the required degree of accuracy. The choice of gauge depends on the nature of the application and for ionisation processes the velocity gauge is often the more appropriate. This is because the magnitude of the interaction Hamiltonian in the

length gauge increases with r and so when the ionising electron travels beyond the spatial confines of the atom the interaction term becomes large and may cause instabilities in the calculation. Throughout this thesis we adopt the velocity gauge in the simplified form given in equation (1.49). (In some other types of calculation the wavefunctions may be known most accurately at large distances, making the length gauge the method of preference.)

1.2.5 The Kramers-Henneberger Frame

For an atom in an ultra-intense laser field the motion of the electron will be approximately that of a free electron in the field (i.e. oscillations of large amplitude along the polarisation axis) and the electron will interact with the nucleus only very briefly at the mid-point of its oscillations (This interaction time is clearly very short because it coincides with the moment at which the electron experiences its maximal velocity.) A classical (free) electron driven by the field $\boldsymbol{A}(t)$ has a 'quiver' motion whose radius is given by the vector $\boldsymbol{\alpha}(t)$ (see Gavrila in [57]), *viz.*

$$\boldsymbol{\alpha}(t) = -\frac{1}{c}\int^{t} \boldsymbol{A}(t')dt' \tag{1.54}$$

which, for the linearly polarised beam of equation (1.44), can be written as

$$\boldsymbol{\alpha}(t) = \boldsymbol{\alpha_0}\cos\omega t, \qquad \boldsymbol{\alpha_0} = -\frac{1}{\omega c}\boldsymbol{A_0} \tag{1.55}$$

Thus, the amplitude of this quiver motion is given by $\alpha_0 = A_0/(c\omega)$. The Kramers-Henneberger transformation consists of performing a spatial translation into the (non-inertial) rest-frame of a free electron in the electric field, i.e. $\boldsymbol{r} \rightarrow \boldsymbol{r} - \boldsymbol{\alpha}(t)$ [77] [69].

This co-ordinate translation can be effected by transforming the wavefunction according to

$$\Psi(\boldsymbol{r}, t) \rightarrow \Psi^{(\mathrm{KH})}(\boldsymbol{r}, t) = \exp[\boldsymbol{\alpha}\cdot\boldsymbol{\nabla}]\Psi(\boldsymbol{r}, t) \tag{1.56}$$

In this so-called *Kramers-Henneberger frame* (KH frame) the external field is entirely incorporated into the KH potential

$$V^{(\mathrm{KH})}(\boldsymbol{r}, t) = V(\boldsymbol{r} - \boldsymbol{\alpha}(t)) \tag{1.57}$$

where V is simply the atomic potential of equation (1.35). Thus the Schrödinger equation satisfied by $\Psi^{(\mathrm{KH})}$ is

$$i\frac{\partial}{\partial t}\Psi^{(\mathrm{KH})}(\boldsymbol{r},t) = \left[-\frac{1}{2}\nabla^2 + V^{(\mathrm{KH})}(\boldsymbol{r},t)\right]\Psi^{(\mathrm{KH})}(\boldsymbol{r},t) \tag{1.58}$$

Given that $\boldsymbol{\alpha}(t))$ is periodic in time one can express the KH potential as a Fourier series, *viz.*

$$V(\boldsymbol{r}-\boldsymbol{\alpha}(t)) = \sum_{n=-\infty}^{\infty} \mathrm{e}^{-in\omega t}V_n(\boldsymbol{\alpha_0};r) \tag{1.59}$$

where the Fourier coefficients

$$V_n(\boldsymbol{\alpha_0};r) = \frac{1}{2\pi}\int_0^{2\pi/\omega} \mathrm{e}^{in\omega t}V(\boldsymbol{r}-\boldsymbol{\alpha}(t))dt \tag{1.60}$$

are independent of time. Therefore, one can recast the Schrödinger equation as

$$i\frac{\partial}{\partial t}\Psi^{(\mathrm{KH})}(\boldsymbol{r},t) = \left[-\frac{1}{2}\nabla^2 + V_0(\boldsymbol{\alpha_0};r) + \sum_{n\neq 0}\mathrm{e}^{in\omega t}V_n(\boldsymbol{\alpha_0};r)\right]\Psi^{(\mathrm{KH})}(\boldsymbol{r},t) \tag{1.61}$$

The general solution of this equation is discussed in detail by Gavrila in [57] but we are interested primarily in the conditions under which the time-dependent terms $V_n(\boldsymbol{\alpha_0};r)$, $n\neq 0$ can be neglected.

It was shown by Gavrila and Kaminski [56] that this is the case when the frequency of the incident field is infinitely large. One is then left with only the time-independent potential $V_0(\boldsymbol{\alpha_0};r)$. Since the laser field is completely included in the space-translated potential it is obvious that the so-called KH-eigenstates satisfying this approximate equation (i.e. retaining only the zeroth mode) experience no ionisation. Let us use $E^{(\mathrm{KH})}$ to denote the (real) eigen-energies of these KH eigenstates. One can then put a few of the (lowest order) time-dependent terms $V_n(\boldsymbol{\alpha_0};r)$, $n\neq 0$ back into the Hamiltonian and treat them as perturbations to the zeroth order term. By this method one may calculate the ionisation rates from these KH states. At large but finite frequencies such that $\omega \gg \mid E^{(\mathrm{KH})} \mid$ and $\omega\alpha_0^2 \gg 1$ calculations have been performed by Pont and Gavrila [110] which show that under these conditions the KH eigen-energies are very close to the bound-state energies of

the exact Hamiltonian. Further, the ionisation rates obtained by including the time-dependent perturbations are found to be in good agreement with other theoretical predictions [21]. The KH frame is the natural frame of reference in which to discuss the adiabatic stabilisation phenomenon described in section 1.1.1. Gavrila and co-workers [109] observed that, under the high-frequency and high-intensity conditions described above, the atoms can stabilise in their KH eigenstates. In other words, the terms $V_n(\boldsymbol{\alpha}_0; r)$ with $n \neq 0$ in equation (1.61) are of decreasing importance as the intensity of the laser-field increases.

1.3 Theoretical Treatments

1.3.1 Time-Dependent Theories

The most straightforward approach to obtaining the eigen-energies and eigenfunctions of an atom or ion in an intense laser field is to directly integrate the time-dependent Schrödinger equation. In this approach the spatial variables are discretised and the wavefunction is represented on a grid of points extending sufficiently far that the wavefunction has virtually zero amplitude at the boundaries over the entire duration of the laser pulse. In order to accomplish this one must proceed with time-steps that are very small on the time-scale of the shortest relevant physical period, namely the optical period. At a typical wavelength of 532 nm the optical period is given by $\tau = 2\pi/\omega \approx 1.8$ fs and a typical laser pulse might last for, say 1 ps, and so contains approximately 600 optical cycles. One may very well need to take as many as 300 time-steps per cycle in order to keep numerical inaccuracies within reasonable bounds [108]. The great disadvantage of direct time-integration as a method of solving the Schrödinger equation for realistic physical problems is that real atoms are three-dimensional and so the huge number of time-steps is combined with an equally unwieldy number of spatial grid-points. The upshot of all this is that at present the computational load is too great (in the generic case) for calculations to be viable. By 'generic' we mean a system which does not

possess any special symmetries under which the dimensionality or number of equations in the system can be reduced. (An example of such a system is an atom irradiated by an elliptically polarised field.)

There are however simplifications that can be introduced to reduce the size of the problem. Firstly, one may choose to consider a problem in which the light is linearly polarised. In the dipole approximation the system is then axially symmetric about the polarisation axis, thus reducing the number of dimensions to two. Calculations of this type have been performed by Kulander *et al* [81] to study, for example, the effect of bound-state resonances on harmonic spectra. An alternative approach is to expand the wavefunction on a basis of spherical harmonics, resulting in a series of coupled equations relating the coefficients of the various angular momentum states. Working in the length gauge and again choosing a linearly polarised field, the coupled equations relating the coefficients of these harmonics only contain coupling terms between the coefficients of states whose angular momentum differs by one unit. This reduces the computational burden considerably and several authors, e.g. LaGattuta [85] and Krause *et al* [78], have utilised this method to perform numerical three-dimensional calculations. Even when adopting this approach, only short-pulse simulations (e.g. 20 optical cycles) are feasible.

The most convenient simplification to make is to replace the three-dimensional problem by an analogous one-dimensional model which one hopes will capture all of the relevant physics. In reality this is a huge position to take, for example: the Coulomb potential must be replaced by some model potential; the transverse structure of the electric field must be neglected; and the magnetic field is also neglected [21]. The most commonly used one-dimensional potential is the so-called soft-Coulomb or 'Rochester' potential

$$V(x) = -\frac{1}{(1+x^2)^{1/2}} \tag{1.62}$$

Thanks to the Coulomb tail that this model-potential possesses the one-dimensional model can exhibit some characteristics of real atoms such as Rydberg series of excited states and bound-free coupling matrix elements

that extrapolate continuously across the continuum limit. The most important aspect of these one-dimensional models is that, because of the ease of computation, they can readily be used to test other calculational approaches. For example: Javanainen *et al* [72] [73] have compared ATI spectra obtained from Keldysh calculations with those obtained from numerical simulations; and Pindzola and Dörr [106] have compared the results of Floquet calculations with *ab initio* numerical results. Other model potentials include the one-dimensional square-well potential [48] [154] and the more general stepwise-constant potential [136].

A second class of time-dependent methods may be summarised as 'Volkov final state theories'. In these one can picture the ionising electron making a transition between two well-defined states: the initial bound Coulomb wavefunction and the final free-electron Volkov solution. The Volkov state is an exact solution of the Schrödinger equation for a 'free' electron in a plane-wave electric field. Within the dipole approximation the Volkov wavefunction may be written as

$$\Psi_V(\boldsymbol{r},t) = \exp\left(i[\boldsymbol{p}-\boldsymbol{A}(t)]\cdot\boldsymbol{r} - i\int_0^t \frac{1}{2}[\boldsymbol{p}-\boldsymbol{A}(t')]^2 dt'\right) \tag{1.63}$$

where $\boldsymbol{p}$ is the electronic momentum. The main assumption in this method is that the initial state of the atom in the laser-field is accurately represented by a field-free eigenstate of the atom, neglecting the laser-induced Stark shifting of the energy levels. A second assumption is that the electron does not interact with the residual ion as it leaves the region of the atomic potential. This Volkov final state model was first used by Keldysh [74] in a study of tunneling ionisation. The same idea has been used extensively in calculations by Faisal [44] and Reiss [133]. Collectively, these Volkov final state methods are referred to as Keldysh-Faisal-Reiss (KFR) models [21]. It is found that the predictions of KFR theory are in surprisingly good agreement with experimental data [15] and with other theoretical results [31] over a wide range of intensities.

1.3.2 Floquet Theory

Floquet theory is distinct from the theories discussed in section 1.3.1 in that it represents the time-dependent Schrödinger equation as an infinite series of coupled *time-independent* equations. In order to do this one must assume a monochromatic laser field (or a linear combination of several such fields) and a constant electric field-strength for each field. We discuss this method in greater detail than was afforded to the other approaches because all of the calculations presented in this thesis are based on the Floquet formalism. Let us start from the Schrödinger equation for a one-electron atom in a laser field

$$H(t) \mid \Psi(t)\rangle = i\frac{\partial}{\partial t} \mid \Psi(t)\rangle \tag{1.64}$$

where the Hamiltonian $H(t) \equiv H_A + H_I(t)$ comprises a field-free term H_A and another term $H_I(t)$ representing the interaction of the atom with the field. This interaction Hamiltonian may be written as the sum of two time-dependent potentials, *viz.*

$$H_I(t) = V_+ \mathrm{e}^{-i\omega t} + V_- \mathrm{e}^{+i\omega t} \tag{1.65}$$

In physical terms, the time-independent operators $V_\pm$ correspond to the absorption or emission of a quantum of radiation.

The Floquet theorem states that if an operator (e.g. the total energy operator) is periodic in time, such that $H(t+\tau) = H(t)$, then its eigenfunctions (i.e. wavefunctions) can be written in the form

$$\mid \Psi(t)\rangle = \mathrm{e}^{-iEt} \mid \Phi(t)\rangle \tag{1.66}$$

and further, that the Floquet vector $\mid \Phi(t)\rangle$ is also periodic in time with the same period τ as the external field. This vector can therefore be expanded in a Fourier series

$$\mid \Phi(t)\rangle = \sum_{n=-\infty}^{\infty} \mathrm{e}^{-in\omega t} \mid \psi_n\rangle \tag{1.67}$$

such that the *harmonic components* $\mid \psi_n\rangle$ are independent of time. Substituting this Floquet-Fourier ansatz, (1.66) and (1.67), into the time-dependent

Schrödinger equation one readily obtains an infinite set of coupled algebraic equations for the harmonic components

$$[H_A - E - n\omega] \mid \psi_n\rangle + V_+ \mid \psi_{n-1}\rangle + V_- \mid \psi_{n+1}\rangle = 0 \qquad (1.68)$$

Here, the *quasi-energy* E is a complex number representing both the energy of the atom dressed by the field and its rate of decay due to ionisation. It is usual to express this as

$$E = E_0 + \Delta - i\frac{\Gamma}{2} \qquad (1.69)$$

where E_0 is the field-free atomic eigen-energy, Δ is the (real) Stark shift induced by the field, and Γ is the 'width' of the dressed state (and represents the cycle-averaged ionisation rate). This interpretation of the imaginary component of E arises naturally by considering the total probability density obtained from the Floquet wavefunction (i.e. equation (1.66)).

Using the ansatz described above many studies have been performed on atomic Hydrogen irradiated by an intense laser field. One of the first applications of the Floquet theorem to atomic systems was made by Shirley [144] in 1965. Much early work was also performed by Zel'dovich and is summarised in his review paper [164]. A much more powerful application of this method was devised by Maquet *et al* [92] in which the harmonic components are expanded on a basis of (real) L^2 functions and the resulting matrix equation is solved by inverse iteration [129]. A variation on this method in which the harmonic components are instead expanded on a basis of complex Sturmian functions was developed by Shakeshaft and co-workers [142] [116] [117] [119] in the late 1980s. In particular, MPI of Hydrogen in low-frequency laser fields has been extensively studied [143] [111] [113], as have MPI processes in high-frequency fields [38] [124]. Generalisations to the monochromatic Sturmian-Floquet theory include the MPI of Hydrogen in two-colour laser fields of commensurable frequencies [121] [123] and of incommensurable frequencies [33]. Rates of high harmonic generation have also been calculated using the Sturmian-Floquet method [119] [94]. One of the most interesting applications of this method is the simulation of an experiment carried out

by Rottke *et al* [134] in Bielefeld in 1990. In this experiment very accurate photo-electron spectra were obtained for the ionisation of Hydrogen by a linearly polarised beam (of around 600 nm) at intensities up to 10^{14} W/cm^2. The Floquet calculations correctly predict the positions of the ATI peaks and reveal very good agreement with the fine structure of the first ATI peak. In order to make this comparison it is necessary to perform Floquet calculations at many fixed intensities and then to interpolate and integrate these results over the spatial and temporal extent of the laser pulse such that the true variation in intensity is reproduced.

Another powerful application of the Floquet idea is the recent R-matrix-Floquet theory developed principally by Burke, Joachain and Francken [17] [18]. This is based on the earier R-matrix theory of Burke *et al* [5] [16] (and on the pioneering work of Wigner in nuclear physics [160]) in which configuration space is divided into an internal ($r < a$) and an external ($r > a$) region where the boundary ($r = a$) is positioned to enclose the atomic core. In each region one can, by means of unitary transformations, choose the most suitable form for the interaction Hamiltonian. This allows one to use Hermitian Floquet theory (in the length gauge) in the internal region and standard methods for the description of electron-atom interactions (in the velocity gauge) in the external region. The theory has been further developed [34] [36] [37] to include a second boundary (at $r = a'$) beyond which one makes a further transformation to the acceleration frame. The region $a < r < a'$ is then referred to as the 'propagation' region and the most distant region is denoted the 'asymptotic' region. The R-matrix-Floquet method is especially valuable because it permits accurate calculations for multiphoton processes in complex atoms, taking full account of the electron-electron correlations. Many results have been obtained for the MPI of the Noble gases (e.g. [130] [84] [88]) and most recently for the two-colour multiphoton processes. This versatile method also encompasses harmonic generation processes [58] and is being further developed to describe scattering phenomena.

1.4 Overview of Calculations

In this thesis we study the multiphoton ionisation of Hydrogen - and of a variety of one-electron model atoms - by intense laser fields, including both the high-frequency and low-frequency extremes. Whilst in every chapter we are concerned with the structure of the ATI spectrum and with the angular distribution of the photo-electrons, the physical mechanisms (and their interpretations) that are involved differ from application to application. In chapter two we present a methodical study of photo-detachment from a three-dimensional, spherically symmetric, square-well potential by an intense high-frequency laser field. The bound-state structure of this model-atom is described initially in the absence of an external field and then with the inclusion of a high-frequency field. Wavelengths of 1064 nm, 600 nm and 256 nm are considered and in each case we examine both the weak-field and strong-field limits. At 256 nm we observe strong-field suppression of photo-detachment for intensities above 4.9×10^{14} W/cm^2 and we detect a plateau in the ATI spectrum at this same intensity. The photo-electron energy in this plateau region matches that found by other authors. Further, we illustrate a laser-induced degeneracy between the ground state and a resonance pole corresponding to a p-state shifted in the energy plane by -ω. This degeneracy arises in the parameter-space defined by the frequency and intensity of the incident field.

In chapter three we consider the possibility of explicitly correcting the asymptotic momenta in a Floquet calculation to allow for the truncation of the Floquet system to a finite number of equations. To address this question we perform calculations for a one-dimensional square-well potential both with and without shifting the channel-momenta from their analytic (non-truncated) values to the self-consistent values for the truncated system. We find that, provided one retains sufficiently many equations to represent adequately all the physical couplings, the results obtained from both approaches are identical. However, this critical number of equations is much smaller when using the self-consistent momenta and the total calculation is correspondingly

faster as a result.

In chapter four we consider the validity of the single diabatic Floquet state approximation when applied to resonant multiphoton ionisation processes in atomic Hydrogen. Following the work of Potvliege and Shakeshaft [116] we derive a coupled-states formalism in which the dynamics are studied in the context of a model consisting of two dressed states of the atom in the laser field. We present separate arguments based respectively on Landau-Zener theory and on the analytic structure of the quasi-energy in the complex plane, which show that when the intensity profile passes rapidly through the multiphoton resonance there is a strong probability of transition between the two levels of the atom. We then present numerical results showing that in the case of an avoided crossing (at 204 nm) this prediction is readily satisfied, whereas for a true crossing (both at 608 nm and at 300 nm) the picture is more complicated and there are some indications (arising from a RWA calculation) that greater transfer may actually occur when the intensity profile varies slowly and smoothly. A surprising conclusion from these calculations is that the inclusion of a resonant coupling between the ground and excited states tends not to increase the total ionisation yield over a complete laser pulse. Comparisons are drawn between our results and those calculated by B Piraux using the method of direct integration of the (exact) time-dependent Schrödinger equation [108]. For each laser pulse studied (some of which incorporate a plateau at constant intensity) agreement between these methods is excellent.

In chapters five to seven we present the results of Sturmian-Floquet calculations for the ionisation of atomic Hydrogen by, firstly, a monochromatic circularly polarised laser field at 608 nm and, secondly, a bichromatic field comprising a fundamental beam at 1064 nm together with its fifteenth harmonic. Chapter five serves as an introduction to these calculations and includes an exposition of the Sturmian-Floquet method, a description of the Sturmian-Floquet code used for the present calculations, and an explanation of the method by which we convert the partial rates of MPI into photoelectron spectra for a laser pulse of finite duration. Chapter six then gathers

together the results that we have obtained for the monochromatic circularly polarised beam. Partial rates and the corresponding angular distributions have been obtained over many ATI channels and over a representative range of laser intensities, the lowest of which is 2×10^{13} W/cm^2 and the highest of which is 6.2×10^{14} W/cm^2. The partial rates are found to be consistent with the low-frequency formulae of Nikishov and Ritus [99] and the angular distributions are found to depart very little from perturbative predictions, even at the very highest field-strengths. This counter-intuitive behaviour is discussed in terms of the propensity rules for atomic photo-absorption and photo-emission processes. A heuristic derivation of the relevant propensity rules is included as an appendix.

In chapter seven we present the results of our two-colour Sturmian-Floquet calculation and compare our results, in the case of the partial rates of ionisation, with those of Véniard *et al* [151], and, in the case of the angular distributions, with the results of Cionga [98]. However, we are able to perform accurate calculations at higher intensities then were possible using Cionga's radiative dressing approach (see section 5.1). All of the results presented in this chapter are, in principle, currently accessible to experiment. We perform calculations at a fixed intensity of the harmonic beam (10^9 W/cm^2) together with various intensities of the fundamental ranging from 5×10^{11} W/cm^2 to 2×10^{13} W/cm^2. The role of the relative phase of the two beams is investigated and it is found that this phase is important only at the highest intensity considered. Our partial rates of ionisation follow the same pattern as those of Véniard *et al* (at a shorter wavelength) and our angular distributions (at low intensities) are qualitatively similar to those of Cionga. In particular we observe that, even at very low intensities of the fundamental, the angular distribution into the channel corresponding to the absorption of a single harmonic photon (or equivalently, to fifteen low-frequency photons) is very different from the $\cos^2\theta$ function that one would expect for a one-photon absorption process (and that one does indeed obtain when applying the harmonic field alone).

Chapter 2

The Spherically Symmetric Square Well

2.1 Introduction

One of the most valuable methodologies available to us in physics has always been the ability to construct simplified models of a complex phenomenon in order to investigate in isolation certain aspects of the system. Square-well models are frequently used to simulate a variety of potential wells in quantum mechanics. In these models the potential takes a constant value (negative for an attractive potential) inside the well and is zero elsewhere. The one-dimensional square-well model has found many applications in atomic theory over the last two decades, but the three-dimensional (spherically symmetric) square-well model has seldom been the subject of extensive calculations. Rather, it is an important text-book model in scattering theory [12]. The reason for this lack of research interest is self-evident: a three-dimensional model potential may not be significantly more amenable to analysis than the physical potential under investigation. However, there are two problems in representing a physical system by a one-dimensional model. Firstly there will be some aspects of the system (e.g. angular distributions) which cannot be included in a one-dimensional model, and secondly there may be qualitative differences in behaviour between one-dimensional and three-dimensional systems. Recently these one-dimensional square-well models have been re-

peatedly used in the study of Hydrogen atoms in super-intense fields, usually within the context of the Kramers-Henneberger (KH) frame and the associated approximation (see e.g. [154] [49]). The interest in one-dimensional model potentials can be ascribed primarily to the fact that their piecewise-constant nature allows them to be solved by different methods than other one-dimensional potentials and often this treatment will be (at least nearly) wholly analytic. It is frequently assumed that results obtained through the investigation of (various) one-dimensional model potentials should possess qualitative similarities to the actual properties of atomic Hydrogen despite the absence of any totally convincing theoretical justification to underpin this belief [72] [73] [136] [153]. The three-dimensional square-well model is a big step closer to reality than the one-dimensional models, and results obtained from this model (subject to the same parameters as in the one-dimensional case) are an important check on the validity, indeed generality of the one-dimensional models. Our aim here then, has been to study (using the three-dimensional model) the Hydrogen atom subjected to a super-intense laser field under a variety of parameter regimes suitable for exhibiting behaviours characteristic of multiphoton processes. We begin our study with an understanding of the well in the absence of an external field, and then proceed to introduce an incident laser field represented - in the dipole approximation - by an electric field vector. Phenomena which have been investigated include quasi-energy trajectories, partial rates of multiphoton ionisation (ATI spectra), angular distributions of the photo-electrons, and laser-induced degenerate states (LIDS). Atomic units are used throughout, except where specifically indicated otherwise.

2.2 The Atom in the Absence of an External Field

2.2.1 Theoretical Description

Let us start from the Schrödinger equation for an atom in the absence of an external field (see equations (1.2) and (1.3) in section 1.2.1),

$$\left[-\frac{1}{2}\nabla^2 + V(r)\right]\psi_{Elm}(\boldsymbol{r}) = E\psi_{Elm}(\boldsymbol{r}) \tag{2.1}$$

where E is the total energy of state $\mid \psi_{Elm}\rangle$. The three-dimensional spherically symmetric square well potential of depth $V_0 < 0$ and range a is given by

$$V(r) = \begin{cases} V_0 & r < a \\ 0 & r > a \end{cases} \tag{2.2}$$

where V_0 is defined to be negative. For a central potential such as this one can solve Schrödinger's equation by separating variables, *viz.*

$$\psi_{Elm}(\boldsymbol{r}) = R_{El}(r)Y_{lm}(\theta, \phi) \tag{2.3}$$

and due to the spherical symmetry one is then only interested in the radial function $R_{El}(r)$. This function satisfies the following equations,

$$\left[-\frac{1}{2}\left(\frac{d^2}{dr^2} + \frac{2}{r}\frac{d}{dr}\right) + \frac{l(l+1)}{2r^2}\right] R_{El}(r) = (E - V_0)R_{El}(r) \quad (r < a) \tag{2.4}$$

and

$$\left[-\frac{1}{2}\left(\frac{d^2}{dr^2} + \frac{2}{r}\frac{d}{dr}\right) + \frac{l(l+1)}{2r^2}\right] R_{El}(r) = ER_{El}(r) \qquad (r > a) \tag{2.5}$$

corresponding to the two regions $r < a$ and $r > a$. Following Bransden and Joachain [12] let us consider each region separately:

(i) $r < a$.

The solution here is a spherical Bessel function,

$$R_{El}(r) = Aj_l(Kr) \tag{2.6}$$

where A is some normalisation constant and $K^2 = 2(E - V_0)$. Although all the spherical Bessel functions satisfy the same differential equations j_l is the only allowable Bessel function here because R_l must be finite everywhere, including at the origin.

(ii) $r > a$.

Here one should define $k^2 = -2E$ and by replacing k with $\tilde{k} = ik$, $R_{El}(\tilde{k}r)$ will satisfy essentially the same spherical Bessel equation as previously. Since here $r > a > 0$ one need not be restricted to the spherical Bessel function which is regular at the origin, and the proper linear combination of functions is instead determined by the asymptotic behaviour of the solutions. In fact the only choice which does not increase exponentially at large r is $h_l^{(1)} = j_l + in_l$, hence

$$R_{El}(r) = Bh_l^{(1)}(\tilde{k}r) \tag{2.7}$$

The eigen-energies are obtained by matching the internal and external solutions at the boundary $r = a$. A concise way of representing the continuity of both the radial function and its derivative is to match instead the logarithmic derivative $(1/R_{El})(dR_{El}/dr)$, thereby eliminating normalisation constants and any other common terms. The matching condition (for given l) is a transcendental equation. For simplicity we restrict ourselves to the cases $l = 0$ and $l = 1$. Using the change of variables $\rho = Ka$ and $\eta = ka$ one obtains the matching equations,

$$\rho \cot \rho = -\eta \,, \qquad (l = 0) \tag{2.8}$$

and

$$\frac{\cot \rho}{\rho} - \frac{1}{\rho^2} = \frac{1}{\eta} + \frac{1}{\eta^2} \,, \qquad (l = 1) \tag{2.9}$$

where

$$\rho^2 + \eta^2 = \gamma^2 \equiv -2V_0 a^2 \tag{2.10}$$

which can be solved either numerically or graphically [12]. Clearly if γ is sufficiently small then there will be no bound states at all and as γ increases

there will first appear an s-state and then a p-state and so on. The eigen-energies $E(\eta)$ are given by

$$E = -\frac{k^2}{2} = -\frac{1}{2a^2}\eta^2 = \frac{V_0}{\gamma^2}\eta^2 \tag{2.11}$$

2.2.2 Results

Computing these eigen-energies serves two purposes: firstly to examine the dependence of the number of bound states on the well-parameters V_0 and a; and secondly as a source of data to be used in comparison with the calculation with an external electric field, in the limit that the field intensity approaches zero. The transcendental equation given by (2.8) or (2.9) with (2.10) can be solved numerically by any implementation of the Newton-Raphson algorithm (e.g. [129]), starting from an initial guess for η and converging towards a solution of the equations until some pre-defined tolerance condition is satisfied. Note that by equation (2.10) the ρ dependence is eliminated and the problem becomes one-dimensional. Considering collectively all the values of angular momentum it is not immediately obvious how many bound states there are to be found, but taking each angular momentum in isolation it is easy to see from the graphical representation of the equations (see fig. 2.1) that the number of bound states depends solely on γ - the 'well-parameter' - and that as γ increases from zero the number of bound states of a given angular momentum also increases from zero, rising by one for each unit-of-π increase in γ. From equation (2.10) one would therefore expect the number of bound states to increase separately with both a and V_0; indeed it is intuitively obvious that a well which is either wider or deeper will support more bound states. This behaviour is illustrated in figures 2.2 and 2.3. Now from figure 2.1 we note that along a given solution ρ is roughly constant whereas η varies rapidly, so let us express the eigen-energies in terms of ρ only as

$$E = V_0 + \left(\frac{\rho^2}{2}\right)\frac{1}{a^2} \tag{2.12}$$

then one can deduce the relations

$$E \propto V_0 + \text{ constant} \tag{2.13}$$

and

$$(E - V_0) \propto \frac{\text{constant}}{a^2} \tag{2.14}$$

corresponding to figures 2.2 and 2.3 respectively. This explains how a single eigen-energy varies as the well is distorted.

One finds that for $0 \leq \gamma \leq \pi/2$ there are no s-states (or indeed any bound states at all) and that beyond $\gamma = \pi/2$ there occurs an additional s-state for each further π added to γ. Similarly, the well supports no p-states for $\gamma < \pi$ while for every π beyond this one further p-state is allowed. In the work which follows we have, for simplicity, chosen to work with a well supporting only one bound state (necessarily an s-state) in the zero-field limit. That is, we have chosen $\pi/2 < \gamma < \pi$ and in particular, $V_0 = -4$ eV and $a = 2$ Å (corresponding to $\gamma = 2.05$). The bound state of this well has an eigen-energy of -0.477 eV. This single-state potential could for example be used as a model for H^-, or indeed for negative ions in general.

2.3 The Atom in the Presence of an External Field

2.3.1 Theoretical Description

Consider the spherically symmetric square-well potential in the presence of an electromagnetic (laser) field. The square-well which we have chosen to work with has dimensions $V_0 = -4$ eV and $a = 2$ Å (see above). In addition we consider laser fields of various wavelengths, initially 1064 nm (the YAG:Nd wavelength) and later as short as 256 nm. Since a photon at 1064 nm has a corresponding energy of just over 1.1 eV the potential well will (at least at low intensities) be susceptible to single photon detachment, although as the intensity of the incident radiation increases multiphoton processes will

soon become dominant. The magnetic field is of many orders of magnitude weaker than the electric one and (in the dipole approximation) is neglected. Our method is to find the most general possible solutions of the system, both inside and outside the well, which are linear combinations of Volkov states (as explained below). Both real and virtual transitions may occur, though in the process of photo-detachment the electron must carry energy only from real photons since virtual processes must take place over a (very short) finite time interval, in accordance with Heisenberg's indeterminacy principle. The ejected electrons may leave in any direction from the atom.

Let the Hamiltonian of the system be

$$H(t) = H_A + H_I(t) \tag{2.15}$$

where H_A is the field-free Hamiltonian of section 2.2,

$$H_A = -\frac{1}{2}\nabla^2 + V(r) \tag{2.16}$$

and $H_I(t)$ is the potential due to the laser field

$$H_I(t) = -\frac{1}{c}\boldsymbol{A}(t)\cdot\boldsymbol{p} \tag{2.17}$$

where we are working in the velocity gauge. Assuming linear polarisation the vector potential $\boldsymbol{A}(t)$ is given by

$$\boldsymbol{A}(t) = \boldsymbol{A}_0 \cos\omega t \tag{2.18}$$

The 'free particle' solutions of the time-dependent Schrödinger equation

$$\left[i\frac{d}{dt} - H(t)\right]\psi(t) = 0 \tag{2.19}$$

are known to be Volkov waves

$$\psi(\boldsymbol{r},t) = N_c \exp(-iEt)\exp[-i\boldsymbol{\alpha}(t)\cdot\boldsymbol{k}]\exp(i\boldsymbol{k}\cdot\boldsymbol{r}) \tag{2.20}$$

where

$$\boldsymbol{\alpha}(t) = -\frac{1}{c}\int^t dt'\boldsymbol{A}(t') = -\frac{1}{\omega c}\boldsymbol{A}_0 \sin\omega t \tag{2.21}$$

and $E = k^2/2$. N_c is a normalisation constant.

By expanding in Floquet harmonics the Volkov wave can now be written as

$$\psi(\boldsymbol{r},t) = \mathrm{e}^{-iEt}\sum_N \mathrm{e}^{-iN\omega t}\psi_N \tag{2.22}$$

with harmonic components

$$\psi_N(\boldsymbol{r}) = N_c J_N\left(-\frac{1}{\omega c}\boldsymbol{A_0}\cdot\boldsymbol{k}\right)\mathrm{e}^{i\boldsymbol{k}\cdot\boldsymbol{r}} \tag{2.23}$$

where N represents the total number of photons absorbed or emitted. Without using any explicit form for the ψ_N it can easily be shown by substituting (2.22) into (2.19) that the ψ_N satisfy the coupled channel equations

$$(E + N\omega - H_A)\psi_N(\boldsymbol{r}) = V_+\psi_{N-1}(\boldsymbol{r}) + V_-\psi_{N+1}(\boldsymbol{r}) \tag{2.24}$$

where we have replaced

$$H_I(t) \equiv V_+\mathrm{e}^{-i\omega t} + V_-\mathrm{e}^{i\omega t} \tag{2.25}$$

whose two parts correspond to the absorption or emission of a single photon, and $V_- = V_+^\dagger$ with

$$V_+ = -\frac{1}{2c}\boldsymbol{A_0}\cdot\boldsymbol{p} \tag{2.26}$$

The harmonic components ψ_N can be further expanded in partial waves,

$$\psi_N(\boldsymbol{r}) = 4\pi N_c\sum_{l,m} i^l Y^*_{lm}(\hat{\boldsymbol{k}})J_N\left(-\frac{1}{\omega c}\boldsymbol{A_0}\cdot\boldsymbol{k}\right)Y_{lm}(\hat{\boldsymbol{r}}\,)j_l(kr) \tag{2.27}$$

But the other spherical Bessel functions obey the same differential equations and recurrence relations as j_l which implies that j_l can be generalised to some linear combination of functions, *viz.* $(Aj_l + Bn_l)$ or $(Ch_l^{(1)} + Dh_l^{(2)})$. Hence

$$\psi(\boldsymbol{r},t) = \mathrm{e}^{-iEt}\sum_N \mathrm{e}^{-iN\omega t}4\pi N_c\sum_{l,m} i^l Y^*_{lm}(\hat{\boldsymbol{k}})J_N\left(-\frac{1}{\omega c}\boldsymbol{A_0}\cdot\boldsymbol{k}\right)Y_{lm}(\hat{\boldsymbol{r}})b_l(kr) \tag{2.28}$$

where b_l stands for any spherical Bessel function. (Of course the choice for b_l will depend on the required boundary conditions.) Other solutions can now be found by remembering to include virtual transitions as well as real ones. One can effect this by replacing N by $N - M$ (any integer M) where M

differs from N in that it represents only the real photons and then defining a 'channel wavevector' k_M *viz.*

$$\frac{k_M^2}{2} = E + M\omega \tag{2.29}$$

(effectively redefining E) such that the exponential at the front, e^{-iEt}, absorbs the new factor of $\mathrm{e}^{iM\omega t}$. So the wavefunction may now be written as

$$\psi^{(M)}(\boldsymbol{r}, t) = \mathrm{e}^{-iEt} \sum_N \mathrm{e}^{-iN\omega t} \psi_{N-M}(\boldsymbol{r}) \tag{2.30}$$

where

$$\psi_{N-M}(\boldsymbol{r}) = 4\pi N_c \sum_{l,m} i^l Y_{lm}^*(\hat{\boldsymbol{k}}_{\boldsymbol{M}}) J_{N-M}\left(-\frac{1}{\omega c}\boldsymbol{A_0}\cdot\boldsymbol{k_M}\right) Y_{lm}(\hat{\boldsymbol{r}}) b_l(k_M r) \tag{2.31}$$

Let us now consider the two regions $r < a$ and $r > a$:

(a) Internal region:
Clearly the most general solution will be a linear superposition of the $\psi^{(M)}(\boldsymbol{r}, t)$,

$$\psi_{\mathrm{int}} = \mathrm{e}^{-iEt} \sum_N \mathrm{e}^{-iN\omega t} \int d\hat{\boldsymbol{k}} \sum_M \psi_{N-M}(\boldsymbol{K_M}, \boldsymbol{r}) f_M(\hat{\boldsymbol{k}}) \tag{2.32}$$

where $\boldsymbol{K_M}$ are the interior channel wavevectors defined by

$$K_M^2 = 2(E' + M\omega), \qquad \boldsymbol{K_M} = K_M \hat{\boldsymbol{k}} \tag{2.33}$$

with $E' = E - V_0$, and f_M are unknown functions whose usefulness will become apparent. The final step is to expand two parts of the wavefunction in spherical harmonics:

$$f_M(\hat{\boldsymbol{k}}) = \sum_{\rho,\eta} f_{M\rho\eta} Y_{\rho\eta}(\hat{\boldsymbol{k}}) \tag{2.34}$$

and

$$4\pi i^l Y_{lm}^*(\hat{\boldsymbol{K}}_{\boldsymbol{M}}) J_{N-M}\left(-\frac{1}{\omega c}\boldsymbol{A_0}\cdot\boldsymbol{K_M}\right) = \sum_{\lambda,\mu} J(N-M, K_M, l, m)_{\lambda\mu} Y_{\lambda\mu}^*(\hat{\boldsymbol{k}}) \tag{2.35}$$

where $J_{\lambda\mu}$ is just a matrix element with respect to this basis of spherical harmonics.

Substituting these into (2.32) one can use the orthonormality of the spherical harmonics and perform the integration to get

$$\psi_{\text{int}} = \mathrm{e}^{-iEt} \sum_N \mathrm{e}^{-iN\omega t} \sum_M \sum_{l,m} \sum_{\lambda,\mu} f_{M\lambda\mu} J(N-M, K_M, l, m)_{\lambda\mu} Y_{lm}(\boldsymbol{r}) j_l(K_M r) \tag{2.36}$$

where j_l has now been chosen because we require the solution to be regular at the origin. The underlying symmetry of the problem requires that the azimuthal quantum number be conserved. This means that by choosing the initial state to have $l = 0$ (and therefore $m = \mu = 0$) and the axis of quantisation of angular momentum to lie along the direction of polarisation, m and μ will remain zero throughout and so one can drop these summations. Hence

$$\psi_{\text{int}} = \mathrm{e}^{-iEt} \sum_N \mathrm{e}^{-iN\omega t} \sum_{M,l,\lambda} f_{M\lambda} J(N-M, K_M, l)_\lambda Y_{l0}(\boldsymbol{r}) j_l(K_M r). \tag{2.37}$$

(b) External region:

The situation here is identical to the interior except that one retains $k_M(E)$ instead of going to $K_M(E')$ since here $E' = E - V = E$. Therefore the exterior wavefunction is

$$\psi_{\text{ext}} = \mathrm{e}^{-iEt} \sum_N \mathrm{e}^{-iN\omega t} \sum_{M,l,\lambda} g_{M\lambda} J(N-M, k_M, l)_\lambda Y_{l0}(\boldsymbol{r}) h_l^{(1)}(k_M r) \tag{2.38}$$

where $h_l^{(1)}$ has been chosen for the same reasons as in section 2.2.

The quasi-energy E and the unknown coefficients $f_{M\lambda}$ and $g_{M\lambda}$ are determined by matching the interior and exterior wavefunctions at the boundary $r = a$. For each value of N and l one requires that

$$\sum_{M,\lambda} J(N-M, K_M, l)_\lambda j_l(K_M a) f_{M\lambda} = \sum_{M,\lambda} J(N-M, k_M, l)_\lambda h_l^{(1)}(k_M a) g_{M\lambda} \tag{2.39}$$

and

$$\sum_{M,\lambda} J(N-M, K_M, l)_\lambda \left.\frac{d}{dr} j_l(K_M r)\right|_{r=a} f_{M\lambda} = \sum_{M,\lambda} J(N-M, k_M, l)_\lambda \left.\frac{d}{dr} h_l^{(1)}(k_M r)\right|_{r=a} g_{M\lambda} \tag{2.40}$$

Moving the right hand sides here over to the left this system of linear equations can be represented by the matrix equation

$$\tilde{\boldsymbol{M}} \begin{pmatrix} \boldsymbol{f} \\ \boldsymbol{g} \end{pmatrix} = 0 \tag{2.41}$$

where $\boldsymbol{f}$ and $\boldsymbol{g}$ are column vectors whose components are the $f_{M\lambda}$ and $g_{M\lambda}$ respectively (in some order). Since the rows of $\boldsymbol{f}$ and $\boldsymbol{g}$ are labelled by M and λ these must also be the labels for the columns of $\tilde{\boldsymbol{M}}$, leaving l and N to label the rows of $\tilde{\boldsymbol{M}}$. Note that the ranges of N and M are the same, as are the ranges of l and λ, making $\tilde{\boldsymbol{M}}$ a square matrix.

2.3.2 Computational Considerations

Equation (2.41) will have non-trivial solutions if and only if $det.(\tilde{\boldsymbol{M}}) = 0$. This corresponds to $\tilde{\boldsymbol{M}}$ having a zero eigenvalue, so the problem is to find a quasi-energy E such that $\tilde{\boldsymbol{M}}$ - all of whose elements $M_{Nl,M\lambda}$ depend on E - has a zero eigenvalue.

Given that $det.(\tilde{\boldsymbol{M}}) = 0$ if and only if at least one eigenvalue $\lambda_M = 0$ one can start from a good guess for E and then home in on the exact quasi-energy by minimising the modulus of the eigenvalue (λ_M) closest to zero - which is to be calculated at each step. Given that every element of $\tilde{\boldsymbol{M}}$ is a function of the quasi-energy this can be very time-consuming indeed. Of course all four indices of $\tilde{\boldsymbol{M}}$ have infinite ranges but these can each be truncated at some certain values beyond which it is assumed that the couplings have no further physical significance. (This subject will be investigated fully in chapter three and, pre-empting our conclusions there, we find that the truncation of the Floquet system *is* empirically justified.) That is, one can take some positive integers α and β such that $-\alpha \leq M, N \leq +\alpha$ and $0 \leq l, \lambda \leq \beta$ will include all the relevant couplings. Note that α is the same for M and N, and β is the same for l and λ. This ensures that $\tilde{\boldsymbol{M}}$ is still a square matrix. The required values of α and β cannot be predetermined; the optimal values must be determined empirically for a given wavelength and intensity of the incident radiation. It is crucial to keep α and β as small as possible because

the computational load increases as the square of each of them and can easily become unmanageable. Specifically, the number of matrix elements $M_{Nl,M\lambda}$ to be evaluated at each step of the minimisation is

$$T = [2(\beta + 1)(2\alpha + 1)]^2 \tag{2.42}$$

which for typical values $\alpha = 15$ and $\beta = 8$ gives $T > 3 \times 10^5$.

In fact fully three quarters of the coefficients $f_{M\lambda}$ and $g_{M\lambda}$ can be neglected as they are required by parity to be zero. In particular (when starting from a state of even parity such as the dressed ground state) $\psi_N(\boldsymbol{r})$ must have the same parity as the photon number N and so the only coefficients $f_{M\lambda}$ and $g_{M\lambda}$ which need to be considered are those for which M and λ have the same parity. The numerical problem consists of iteratively performing the following three tasks until convergence with respect to E is obtained:

(a) Calculate the necessary matrix elements $M_{Nl,M\lambda}$;

(b) Compute the smallest eigenvalue λ_M of $\tilde{\boldsymbol{M}}$;

(c) Minimise λ_M as a function of the quasi-energy.

Let us now discuss briefly the salient theoretical aspects of these calculations. One can see from equations (2.39) and (2.40) that each matrix element $M_{Nl,M\lambda}$ is the product of a matrix element $J_\lambda(N, M, l)$ with some kind of spherical Bessel function $b_l(M)$ or its derivative. Calculating the spherical Bessel function of a complex argument can easy be accomplished using Miller's algorithm (i.e. downwards recursion)

$$b_{l-1}(z) = -b_{l+1}(z) + \frac{(2l+1)}{z}\, b_l(z) \tag{2.43}$$

and the derivatives can be computed using the recurrence relation

$$\frac{db_l(z)}{dz} = b_{l-1}(z) - \frac{(l+1)}{z}\, b_l(z) \tag{2.44}$$

where in both cases the zeroth order function is known. The matrix elements J_λ are defined implicitly in equation (2.35) which readily yields the explicit expression

$$J(N - M, K_M, l, m)_{\lambda\mu} = 4\pi i^l \int d\Omega\, Y^*_{lm}(\theta, \phi) J_{N-M}(a_M \cos\theta) Y_{\lambda\mu}(\theta, \phi) \tag{2.45}$$

where a_M is a complex coefficient which depends on K_M. After a little manipulation (and dropping the azimuthal index once more) one can write

$$J(N-M,K_M,l)_\lambda = 4\pi i^l \sqrt{\left[(2l+1)(2\lambda+1)\right]} \int_0^1 dx\; P_l(x) P_\lambda(x) J_{N-M}(a_M x) \tag{2.46}$$

where P_l are the Legendre polynomials. This integral can readily be performed either analytically or numerically.

There are many packages available for finding the eigenvalues of a general matrix but most of these can be regarded as inefficient because here we require only the one eigenvalue λ_M out of typically more than a hundred eigenvalues. Therefore the method of choice is that of 'inverse iteration' [129] in which one repeatedly solves the linear equations

$$(\tilde{\boldsymbol{M}} - \lambda'_M)\phi^{\lambda_M}(i+1) = \phi^{\lambda_M}(i) \tag{2.47}$$

beginning with some random initial vector $\phi^{\lambda_M}(0)$, where λ'_M is an approximation to the true eigenvalue λ_M and ϕ^{λ_M} is the corresponding eigenvector. Writing the solution to (2.47) in the eigenstate basis

$$\mid \phi^{\lambda_M}(i+1)\rangle \; = \sum_j \frac{\mid (\lambda_M)_j\rangle \, \langle (\lambda_M)_j \mid}{(\lambda_M)_j - \lambda'_M} \mid \phi^{\lambda_M}(i)\rangle \tag{2.48}$$

it can be seen that if λ'_M is a good approximation to λ_M then the projection in (2.48) will amplify the $\mid \lambda_M\rangle$ component of vector $\mid \phi^{\lambda_M}(i)\rangle$ at the expense of the others. When convergence is reached the eigenvalue λ_M is given by

$$\mid \phi^{\lambda_M}(i+1)\rangle \; = \frac{1}{(\lambda_M - \lambda'_M)} \mid \phi^{\lambda_M}(i)\rangle \tag{2.49}$$

Since in my case we are minimising towards a zero eigenvalue we take $\lambda'_M = 0$ so that

$$\lambda_M = \frac{\phi^{\lambda_M}(i)}{\phi^{\lambda_M}(i+1)} \tag{2.50}$$

The minimisation process utilises a function, say, $F(E,\alpha,\beta)$ which receives the quasi-energy E together with the parameters α and β and returns the modulus of the (complex) smallest eigenvalue λ_M. Regarding the complex

number E as a pair of two real numbers we then have to minimise a real function of two real variables. Many N-dimensional minimisation routines are available but these often require knowledge of the function's derivatives. The method of choice which has proved to be robust (although slow in terms of the number of function evaluations performed) is the 'Amoeba' routine [129]. This is a downhill simplex method where in two dimensions the simplex is a triangle. The method is to calculate the function value at the vertices of the simplex and then perform a series of steps such as reflection, contraction, expansion or some combination of these. An appropriate series of steps will converge to a minimum of the function. The number of steps required for convergence depends strongly on the accuracy of the initial guess for the quasi-energy but for the present application one can say that, typically, more than one hundred steps are needed.

Before moving on present the results of these calculations there are two further theoretical points which should be discussed. Firstly one can note from expressions (2.29) and (2.33) for $\boldsymbol{k_M}$ and $\boldsymbol{K_M}$ respectively that there is an indeterminacy of sign in these definitions. That is, if a wavevector sweeps through π radians in the complex plane the corresponding quasi-energy will move through 2π radians. We choose the branch cut to be along the negative real axis. We lift the degeneracy by requiring that the wavevectors must be physically meaningful, that is, by imposing either 'ingoing' or 'outgoing' asymptotic behaviour. In the zero-field limit the correct choice is self-evident.

Secondly there are additional solutions to the problem which are not of the Volkov type. These correspond to one of the internal wavevectors $\boldsymbol{K_M}$ becoming zero, in which case the Schrödinger equation for a channel wavefunction Φ_M,

$$\frac{-1}{2}\nabla^2\Phi_M = (E - V_0 + M\omega)\Phi_M \tag{2.51}$$

becomes just the Laplace equation

$$\nabla^2\Phi_M = 0 \tag{2.52}$$

Separating variables, *viz.*

$$\Phi_M(r,\theta,\phi) = R_E(r)Y_{lm}(\theta,\phi) \tag{2.53}$$

the radial function $R_E(r)$ then satisfies just a homogeneous Euler equation

$$\left[r^2\frac{d^2}{dr^2} + 2r\frac{d}{dr} - \delta\right] R_E(r) = 0 \tag{2.54}$$

where $\delta \in \mathcal{R}$ is the constant of separation. By substituting $r = \mathrm{e}^x$ this becomes

$$\left[\frac{d^2}{dx^2} + \frac{d}{dx} - \delta\right] R_E(x) = 0 \tag{2.55}$$

whose classes of solution lie outside the general solution previously obtained. The effect of these spurious solutions in our calculations can be severe, and will be described in section 2.4.

2.4 Results

2.4.1 Introductory Discussion

As outlined in section 2.3 the main method of solution employed to solve our coupled equations is the minimisation of the modulus of the smallest (complex) eigenvalue λ_M of the corresponding matrix $\tilde{\boldsymbol{M}}$ as a function of the complex quasi-energy E. It is therefore inherent in the method that when seeking to calculate various physical quantities (e.g. the quasi-energy, the partial rates of ionisation and the differential rates of ionisation it is always the quasi-energy which is best converged with respect to the number of harmonic components and partial waves taken into account in the calculation. Compared to the one-dimensional square-well model subject to laser-radiation of the same wavelength and intensity the three-dimensional model requires relatively fewer harmonic blocks (i.e. above threshold couplings) to give a well-converged quasi-energy, but the presence of angular momentum in the three-dimensional case increases the size of the calculation enormously; (see equation (2.42)). Indeed at high intensities the problem of

producing angular distributions which are well-converged with respect to α and β is intractable, so high must these parameters become. The calculations have been performed mainly on one from a cluster of IBM RISK 6000 processors and the bulk of the CPU time is spent repeatedly diagonalising the matrix $\tilde{\boldsymbol{M}}$.

There is another more serious problem of physical rather than computational origin: this is the qualitative behaviour of the bound-state structure of the well as the incident intensity becomes large. The difference between the one-dimensional and three-dimensional models is striking in this respect. Let us first consider these two cases separately.

The Dressed Potential Well in One Dimension

Here it is well known that beyond some critical intensity the well exhibits a dichotomy along the polarisation axis of the electric field and that this splitting of the potential becomes more complete as the intensity becomes still higher. That is, the zero-field potential is symmetrically stretched along the beam axis and acquires two minima with equal and opposite displacements from the origin. The shallowest point of the potential is in fact the mid-point, i.e. $x = 0$. The probability density of the electron thus becomes clumped at two points spaced symmetrically at a distance of α_0 to either side of the origin (i.e. the nucleus), where α_0 is the amplitude of oscillations of a free electron in the electric field, given by

$$\alpha_0 = \frac{\mathcal{E}_0}{\omega^2} \propto \frac{\sqrt{I}}{\omega^2} \tag{2.56}$$

where $\mathcal{E}_0$ is the amplitude of the electric field,

$$\boldsymbol{\mathcal{E}}(t) = \boldsymbol{\mathcal{E}_0} \cos(\omega t), \qquad \mathcal{E}_0 = \mid \boldsymbol{\mathcal{E}_0} \mid \tag{2.57}$$

Whilst at high intensities the effect of $\alpha_0(I)$ is to elongate the potential well (along the field-axis), the depth of the potential $V(I)$ decreases (in magnitude), most of all in the neighbourhood of the nucleus; (see figure 2.4). This can most readily be described in the Kramers-Henneberger (KH)

frame (see section 1.2.5 and also the review by Gavrila in [57]), the non-inertial rest frame of an electron oscillating in the field, i.e. $x \longrightarrow x - \alpha(t)$ where $\alpha(t) = \alpha_0 \cos(\omega t)$. Expanding the potential in a Fourier series one has

$$V(x - \alpha(t)) = \sum_{n=-\infty}^{\infty} V_n(x, \alpha_0) \mathrm{e}^{in\omega} \tag{2.58}$$

with

$$V_n(x, \alpha_0) = \frac{1}{2\pi} \int_{-\pi}^{\pi} V(x - \alpha_0 \cos(\omega t)) \mathrm{e}^{-in\omega t} d(\omega t) \tag{2.59}$$

The high-frequency approximation (sometimes referred to as the Kramers-Henneberger *approximation* [154]) consists of neglecting all the non-zero modes in this sum and holds exactly in the limit of infinitely high intensity and frequency [56] [57]. Hence we obtain

$$V(x - \alpha(t)) \approx V_{t.a.}(x; \alpha_0) = \frac{1}{2\pi} \int_{-\pi}^{\pi} V(x - \alpha_0 \cos(\omega t)) d(\omega t) \tag{2.60}$$

where $V_{t.a.}$ is the time-averaged (or Kramers-Henneberger) potential. The physical justification for this is that under very high frequencies the electron will only perceive the 'smeared-out' charge of the nucleus while oscillating with amplitude α_0 due to the applied field. Considering the shallowest part of the potential (i.e. at $x = 0$) for some $\alpha_0 > a$ we see that

$$V_{t.a.}(0; \alpha_0) = \frac{1}{2\pi} \int_{-\pi}^{\pi} d\theta \, V(\alpha_0 \cos\theta) = V_0 \left[1 - \frac{2}{\pi} \arccos\left(\frac{a}{\alpha_0} \right) \right] \equiv V_0'(\alpha_0) \tag{2.61}$$

where we have used the fact that the square-well potential takes the value zero whenever its argument has an absolute value greater than the half-width a, and takes the value V_0 otherwise. Remembering that the potential is deepest at the two nodes $x = \pm\alpha_0$ one can also define a new (half-)width for the well,

$$a'(\alpha_0) = \alpha_0 \tag{2.62}$$

such that the square-well of width a' and depth V_0' is at all points both narrower and shallower than the actual dressed potential. This square-well has a number of bound states governed by

$$\gamma^2(a', V_0') = 2V_0' a'^2 = \left(\frac{2aV_0}{\pi} \right) \alpha_0 \tag{2.63}$$

and so as the intensity becomes large the number of bound states supported increases indefinitely. Thus, by comparison, the dressed *one-dimensional* square-well potential also supports an ever-increasing number of bound states.

The Dressed Potential Well in Three Dimensions

We can now contrast the above with the case of the dressed three-dimensional square-well potential. Naively one might expect qualitatively similar behaviour to the one-dimensional case, i.e. the appearance of an unlimited number of light-induced states at sufficiently high intensities, but whilst the well undergoes an analogous lengthening along the field axis (let us denote this the z-axis) there is no corresponding increase in range in the perpendicular (radial) plane. The problem is of course cylindrically symmetric. Unfortunately it is not at all trivial to determine how the number of bound states varies with increasing intensity. The KH transformation in this case is given by $\boldsymbol{r} \longrightarrow \boldsymbol{r} - \boldsymbol{\alpha}(t)$ with $\boldsymbol{\alpha}(t) = \boldsymbol{\alpha_0}\cos(\omega t)$ and $\boldsymbol{\alpha_0} = \boldsymbol{\mathcal{E}_0}/\omega^2$, and the corresponding potential takes the form

$$V_{t.a.}(\boldsymbol{r} - \boldsymbol{\alpha}(t)) = \frac{1}{2\pi}\int_{-\pi}^{\pi} V(\boldsymbol{r} - \boldsymbol{\alpha_0}\cos(\omega t))d(\omega t) \tag{2.64}$$

Following the same arguments as in the one-dimensional case we find that this potential can be written as

$$V_{t.a.}(\boldsymbol{r}, \boldsymbol{\alpha_0}) = \frac{V_0}{\pi}\begin{cases} \arccos(-\beta - z) & -1-\beta \leq z < -1+\beta \\ [\arccos(-\beta - z) - \arccos(\beta - z)] & -1+\beta \leq z \leq 1-\beta \\ -\arccos(\beta - z) & 1-\beta < z \leq 1+\beta \\ 0 & \text{otherwise} \end{cases} \tag{2.65}$$

where we have defined $\beta = (a'^2 - \rho^2)^{1/2}$ with $a' \equiv a/\alpha_0$. (Here ρ is the radial coordinate in a system of cylindrical polar coordinates $\boldsymbol{r} = (\rho, z)$ in which both variables have been scaled by $1/\alpha_0$.) One must take care to select for each of the three segments the appropriate branch of the arccos function such that the potential is continuous across the boundaries. This dressed potential is illustrated for the sample value of $\alpha_0 = 10$ a.u. in figure 2.5. Segments

of the dressed potential with either ρ or z held constant (and with various values of α_0) are displayed in figures 2.6 and 2.7 respectively. In the region $-1+\beta \leq z \leq 1-\beta$ the expression simplifies to

$$V_{t.a.}(\boldsymbol{r}, \boldsymbol{\alpha_0}) = \frac{V_0}{\pi} \arccos[z^2 - \beta^2 + (\gamma^2 - \delta^2)^{1/2}] \tag{2.66}$$

where $\gamma = 1-z^2-\beta^2$ and $\delta = 2z\beta$. Further, if z is small, one can approximate

$$V_{t.a.}(\boldsymbol{r}, \boldsymbol{\alpha_0}) \approx \frac{V_0}{\pi} \arccos\left[1 - 2\beta^2 + \frac{1}{2}(z^2 - \beta^2)^2\right] \tag{2.67}$$

which holds whenever $z^2 < 1 + \sqrt{2} - \beta^2$. A comparison of this function with the exact time-averaged potential (see figure 2.8) reveals that with increasing α_0 the agreement is very good indeed.

Unfortunately any useful 'comparison potential' (e.g a cylinder either enclosing or enclosed by $V_{t.a.}$; c.f. the rectangle in one dimension) is non-separable in the (scaled) ρ and z coordinates and the corresponding Schrödinger equation is amenable only to a massive numerical calculation. Let us give one simple example of a comparison: the spherical potential whose depth is at all points greater than or equal to that of the dressed potential and whose radius equals the half-length along the z-axis of the dressed potential, thereby enclosing it completely. We want to consider the limit of α_0 becoming large, and in this regime the deepest points in the dressed potential, $\boldsymbol{r} = \pm\alpha_0\hat{\boldsymbol{z}}$, correspond to a depth

$$V_{\max} \approx \frac{V_0}{\pi}\left(\frac{2a}{\alpha_0}\right)^{1/2}\left(1 + \frac{1}{12}\frac{a}{\alpha_0}\right) \tag{2.68}$$

retaining only the two leading orders in a/α_0. Thus we see that this maximum depth scales with α_0 as

$$V_{\max}(\alpha_0) \propto \frac{1}{\sqrt{\alpha_0}} \tag{2.69}$$

whilst the radius, given by $a_{\max} = \alpha_0 + a$, increases linearly in α_0. Recalling that the number of bound states supported by the potential well is governed by the parameter $\gamma^2 = -2V_{\max}a_{\max}^2$ it is clear that $\gamma \propto \alpha_0^{3/4}$. But, the potential well under consideration is at all points deeper than the actual potential we are interested in, so to have proved that the number of bound states it supports proliferates with increasing α_0 is not informative.

It may instead be possible to separate the Schrödinger equation for some kind of ellipsoid of constant potential in confocal elliptic co-ordinates and this would in principle allow the possibility of a meaningful comparison with the true Kramers-Henneberger potential $V_{t.a.}$. However, we leave this question open as a subject for future work. Let us also note that (except at the extremities of its oscillations) the electronic motion is very rapid along the field axis and (relatively) much slower in the radial direction and so it may be reasonable to talk in terms of an *adiabatic separability* [98] of the motion in these two perpendicular directions. This embodies the idea that when motion in a system is very rapid in one specific direction and much slower in the perpendicular plane then one can consider these two motions as being effectively decoupled and in our case one would then expect the number of bound states to proliferate, just as for the one-dimensional model. This is due to the fact that in one dimension there is always a minimum of one bound state irrespective of how small γ may become. But the results we have obtained (see section 2.4.2) do not support this conclusion and instead demonstrate that in three dimensions beyond a certain critical intensity the dressed potential is unable to support any bound states at all.

2.4.2 Quasi-Energy Trajectories

General Features

Recall from section 2.3 that the square-well which we are working with has dimensions $V_0 = -4$ eV and $a = 2$ Å and supports (in the field-free limit) just one bound state with energy $E_0 = -0.477$ eV. All of the frequencies which we have considered satisfy $\omega > \mid E_0 \mid$ and so at low intensities single-photon ionisation is the dominant process. So how might we expect the quasi-energy to vary at low intensities? Recall (from section 1.3.2) that in the Floquet picture the quasi-energy (as a function of intensity and frequency) is given by

$$E = E_0 + \Delta - i\frac{\Gamma}{2} \tag{2.70}$$

where Δ is the total Stark shift

$$\Delta = \Delta_{AC} - E_P \tag{2.71}$$

Here, E_P is the ponderomotive energy

$$E_P = \frac{\mathcal{E}_0^2}{4\omega^2} \tag{2.72}$$

and Δ_{AC} is the quadratic Stark shift for an oscillating (alternating current) field [53]. The relative importance of E_P and Δ_{AC} in (2.71) depends crucially upon the frequency ω. In the long-wavelength regime, say, $\lambda > 1$ μm the ponderomotive term dominates and the total energy shift is negative. Indeed, in the limit of $\lambda \to \infty$ we have a static field in which the Stark shift is known explicitly to be negative. At the opposite extreme, with $\omega \gg \mid E_0 \mid$, we find that the total energy shift is positive even at the very lowest intensities. Physically we can understand this high-frequency behaviour in terms of the high-frequency approximation for the atom-plus-field potential in which the electron is oscillating. We know from section 2.4.1 that at high frequencies and intensities the potential well exhibits a dichotomy (along the field axis) with an increasingly shallow 'neck' at the origin thus it is clear that in this limit the energy levels are going to be pushed upwards. In between these two extremes we have the intriguing case of a wavelength for which we do initially (i.e. at low intensity) have a negative energy shift but then at high (but still easily accessible) intensities this shift reverses and we enter a regime which can be described within the high-frequency framework.

The Low-Frequency Regime

Our own calculations start at the relatively long wavelength of 1064 nm (corresponding to a photon energy $\omega = 1.16$ eV $\approx 2 \mid E_0 \mid$). Recall (from section 1.1) that $\mathcal{E}_0^2 \propto I$ and that $\Gamma \propto I^N$ where N is the order of the ionisation process then we see from (2.71) and (2.72) that both Δ and Γ should vary linearly with the intensity for as long as one remains in the perturbative regime. Figure 2.9 shows the quasi-energy trajectory at this constant wavelength as the intensity increases from zero upwards into the

multiphoton regime. The three curves shown reach a maximum intensity of $I = 10^{12}$ W/cm^2. It is always necessary to test empirically the convergence of the result with respect to the number of harmonic blocks $(2\alpha + 1)$ and angular momenta $(\beta + 1)$. As the intensity increases further the shift is still more negative, suggesting that the high-frequency picture is not valid in this instance. At an intensity of $I \approx 5 \times 10^{12}$ W/cm^2 we reach the one-photon cut, i.e. at intensities higher than this the energy level has been pushed downwards to such an extent that one-photon ionisation is no longer an open channel. Notice that as we approach this critical point $\Re\mathrm{e}(E) = -\omega$ the total rate of ionisation decreases sharply (see figures 2.10 and 2.11).

If one were to follow this same pole across the cut (onto the next Riemann sheet) it would become a 'shadow pole', a solution with unphysical boundary conditions. Recall equation (2.33) defining the internal channel wavevectors. For each channel the square-root function has two branches, representing different physical states. For a decaying (bound) state the imaginary component of the quasi-energy must be negative, and the wavefunction must behave as an outgoing wave in the open channels whilst asymptotically vanishing in the closed channels. (Here, *open* refers to channels with $M\omega > \mid \Re\mathrm{e}.(E') \mid$ whereas *closed* refers to the case $M\omega \leq \mid \Re\mathrm{e}.(E') \mid$ where $E' = E - V_0$.) Therefore the wavevectors should satisfy $-\pi/4 < \arg(K_M) \leq 0$ in the open channels and $\pi/2 < \arg(K_M) \leq 3\pi/4$ in the closed channels. States satisfying both of these inequalities are known as *physical states* whereas those which do not are called *shadow states* [117] [48]. Thus, with an untruncated Floquet-Fourier expansion of the wavefunction the Schrödinger equation has infinitely many solutions for *each* energy level, only one of which is truly physical. In order to study the physical pole on that second sheet it is necessary to start at zero intensity from a shadow pole which has the correct boundary conditions (determined by the signs assigned to the channel wavevectors) to become physical once one has crossed the one-photon cut. Typically the physical pole becoming a shadow pole and the shadow pole becoming physical will cross the relevant cut with slightly different widths, hence the need to return to zero intensity in order to follow the quasi-energy trajectory onto

each new sheet.

The Quasi-Energy Surface

By examining the surface $\lambda_M(E)$ we are able to judge the importance of the 'spurious' solutions alluded to in section 2.3. From equation (2.33) we see that these are located at positions

$$E = V_0 - M\omega \tag{2.73}$$

in the complex energy-plane, i.e. lying on the real axis and separated by intervals of the photon energy ω. We find that the depth of the minimum of λ_M with respect to E which we identify with the 'true' quasi-energy (relative to the background) depends mostly on the coupling parameters α and β and that in a calculation taking into account many couplings the minimum becomes difficult to discern. Typically the 'false' minimum is much broader than the true one (though not as deep) and in this sense is a strong attractor in the minimisation process. The small step-size in intensity which must be taken to overcome this problem results in a very significant increase in computational time. Figures 2.12, 2.13, 2.14 and 2.15 show the surface $\lambda_M(E)$ at low intensity ($I = 5 \times 10^{10}$ W/cm^2) at $\lambda = 1064$ nm for differing parameter values α and β. The position of the quasi-energy is marked by a bold arrow in each case and is $(-0.48167628, -0.00509161)$ eV (independent of α and β).

Even at this low intensity we find that the actual quasi-energy is not visible at all on the larger scale section of the energy plane and that the broad, spurious attractor is the main feature of the surface. Thus a guess for the quasi-energy which is correct to within a few percent of its true value is totally inadequate for minimisation purposes. The results in figures 2.12 and 2.13 show that the quasi-energy is located at its expected position and can be found by a minimisation procedure provided one starts with an excellent 'guess'. In these figures the parameter values are $\alpha = \beta = 3$, i.e. 4 angular momenta and 7 Floquet blocks. In contrast, figures 2.14 and 2.15 have $\alpha = 4$

and $\beta = 5$, i.e. 6 angular momenta and 9 Floquet blocks, and here - even on the very fine scale of figure 2.15 - we see no evidence of the quasi-energy which our numerical results tell us is there. At such a low incident intensity these parameter values are unnecessarily high but at high intensities of, say, a few 10^{12} W/cm^2 we must include very many couplings for convergence to a constant quasi-energy and the problem of needing an accurate guess becomes very severe. We would like to point out that the points in the energy plane at which the function is evaluated have *not* been deliberately chosen to include the exact minimum of the function and therefore the actual minimum value (as revealed numerically by the searching process) is several orders of magnitude deeper than indicated and in all cases is smaller than 10^{-12}. At high intensities this difficulty becomes even more severe. Let us take as an example a calculation of the quasi-energy of the well of depth $V_0 = -8$ eV and width $a = 2$ Å at a wavelength of $\lambda = 800$ nm for which the intensity of $I = 5 \times 10^{12}$ W/cm^2 is very high indeed. The smallest calculation to yield a converged quasi-energy at this frequency and intensity is that with parameters $\alpha = \beta = 6$ (i.e. 7 angular momenta and 13 Floquet blocks). The quasi-energy surface is shown in figure 2.16 and one immediately observes the sharpness of the minimum in this surface. This unwelcome aspect of our calculations is a general feature of those calculations in which many couplings are included and is unrelated to this particular intensity and frequency.

The High-Frequency Regime: A Discussion

What form do these quasi-energy trajectories take at higher frequencies $\hbar\omega \gg \mid E_0 \mid$? Here it is observed that whilst at very low intensities the Stark shift is negative it soon reverses, becoming positive and at high intensities shifting the eigen-energy monotonically towards the continuum. Meanwhile the total rate of ionisation steadily increases up to some critical intensity (typically a few 10^{14} W/cm^2 but depending on the wavelength) and then falls off quite sharply. This may well be the onset of the *adiabatic stabilisation* much argued over in the literature (see for example Grochmalicki *et al* [65], Geltman [61] and Muller in [98]), however a certain caution should

be exercised before making such claims. By stabilisation we mean a decrease in the cycle-averaged decay-rate of the atom as the field-strength increases, but it should be stressed that the ionisation rate in the stabilisation regime may still be very high. There are many distinct mechanisms by which stabilisation might occur and each will typically manifest in a different regime of intensity and frequency but most of these mechanisms rely on the manifold of (dressed) atomic states, i.e. either interference between the different levels or population trapping in high-lying Rydberg states. These are collectively known as *dynamic stabilisation* processes (see the discussion in chapter one). In contrast we have adiabatic stabilisation which is a quasi-static property of the ionisation rate and can therefore occur for a single isolated energy level. Given that we are working within the (time-independent) Floquet picture and that our three-dimensional square-well potential has only one bound state we must, by default, restrict our study to adiabatic stabilisation. The essence of this process is that at high field-strengths the electron is driven by the field, undergoing oscillations of an amplitude much greater than the extent of the field-free wavepacket. Viewed from the (accelerating) rest-frame of a (classical) free electron in the field the force from the external field is almost exactly balanced by the inertial forces [56] and the cancellation would be exact in the absence of a nuclear potential. Thus any non-periodic effects such as ionisation must be a result of interactions with the potential of the atomic nucleus. Of course, in the rest-frame of the electron the nucleus is rapidly oscillating and one may therefore include this interaction in time-averaged form. The greater the amplitude of the electron's quiver motion (in the lab-frame) the less time it spends in the neighbourhood of the nucleus and hence the smaller the cycle-averaged probability of ionisation. Thus, as the laser intensity increases from zero the total rate of ionisation is expected to rise up to some certain maximum level and thereafter to decrease sharply as described. This will not occur at all frequencies because the assumption of the electron's quiver motion being that of a free particle in the field (and the external forces therefore being negated by inertial factors) is only valid at high frequencies. By this we mean a high photon energy relative to the (field-free) ionisation potential of the atom.

It has been found by Faisal *et al* [46] that the total rate of ionisation from certain states of the Hydrogen atom in a laser field decreases and exhibits a minimum over quite a wide intensity range beyond which the rate increases once more. This is found only at longer wavelengths $\omega < \mid E_0 \mid$ and so is perhaps not comparable to any of the cases we have studied. Nonetheless, it is worth remarking on such a novel feature, which has been termed a 'stabilisation window'. At zero-field the wavelengths which Faisal *et al* choose are not close to resonance with any higher-lying states but at the intensities at which they observe this phenomenon ($10^{12} - 10^{14}$ W/cm^2) we would expect to see many resonant enhancements of the ionisation rate due to Stark shifting of this state into and out of resonance with the manifold of Rydberg states. Naturally, in between these resonances the ionisation rate will exhibit troughs and it is the contention of these authors that the troughs are magnified by a destructive interference mechanism as the intensity scans over a range of resonances. Thus, given that it is essentially an interference effect which is described, we find the nomenclature of *adiabatic stabilisation window* to be most misleading and would prefer to call these minima anti-resonances. In our calculation described below we were unable to pursue the quasi-energy of our three-dimensional square-well to ultra-high intensities and so the question of whether the adiabatic stabilisation which we observe is only a transitory phenomenon remains, in principle, unanswered. However, since our potential well possesses only one known bound state (even at these high intensities) we can at least rule out any interference mechanism resulting in a temporary decrease in the photo-detachment yield.

The High-Frequency Regime: Results

Let us return to our model well with $V_0 = -4$ eV and $a = 2$ Å and start by examining its quasi-energy trajectory when a moderately high-frequency laser field is acting. As an example of an intermediate wavelength we choose $\lambda =$ 600 nm, corresponding to $\omega \approx 4 \mid E_0 \mid$. The results of this calculation are displayed in figure 2.17 for intensities ranging from zero up to $I = 3.5 \times 10^{12}$ W/cm^2. Included in this calculation are five angular momenta and nine

harmonic components and the results presented are absolutely converged with respect to both of these parameters. Here the Stark shift is negative at low intensities and increases in magnitude linearly with the intensity. But at $I = 1.71 \times 10^{12}$ W/cm^2 this situation reverses and the quasi-energy trajectory moves towards the negative imaginary axis, with a real part which soon becomes greater than the zero-field binding energy. This behaviour matches our earlier predictions. At the maximum intensity shown in this figure the real component of the energy has shifted to $\Re\mathrm{e}(E) = -0.475$ eV while the total rate of photo-detachment increases monotonically up to its final value of $\Gamma \approx 0.0093$ a.u.. In fact the movement of quasi-energy trajectories in the complex energy-plane is complicated by the presence of a one-photon resonance with a quasi-bound resonant state lying in the continuum. (In a multi-electron atom this would be termed an autoionising state.) We will describe this feature in detail in section 2.4.5. The pattern of behaviour of a quasi-energy shifting first negatively and then positively can also be seen in figure 2.33 for the curve at 746 nm. We see that with $\lambda = 748$ nm we are in a topologically distinct region and in contrast to the previous case the Stark shift is negative at all intensities.

Let us now study the high frequency regime using a deeper three-dimensional square-well with parameters $V_0 = -8$ eV and $a = 2$ Å and with $\lambda = 256$ nm. This has a solitary bound-state at $E = -3.17$ eV and the photon-energy is $E_\gamma = 4.85$ eV. The quasi-energy trajectory for intensities ranging from zero up to $I = 1.9 \times 10^{13}$ W/cm^2 is shown in figure 2.18. In this calculation we include only three angular momentum channels and seven harmonic components (with Floquet indices $-3 \rightarrow +3$) the results presented are totally converged with respect to both of these parameters. We see that even with $I > 10^{13}$ W/cm^2 we are well within the perturbative regime and very few angular momenta or Floquet numbers need be taken into account. Contrast this with the situation at 1064 nm (see fig. 2.9) in which significant deviations from perturbative behaviour are visible at intensities of a few 10^{11} W/cm^2. At 256 nm we observe that the total rate of photo-detachment reaches a peak at an intensity of 4.9×10^{14} W/cm^2 and has fallen to approximately

one half of that peak value by the time one reaches 10^{15} W/cm^2 (see figures 2.19 and 2.20). In the quasi-energy plane these two points correspond to $(-1.20, -0.801)$ eV and $(-0.497, -0.409)$ eV respectively. Figure 2.20 presents the total rate of photo-detachment as one approaches its maximum value and figure 2.21 shows the decline in this rate at yet higher intensities. In both cases we present the results of several calculations including differing numbers of couplings to illustrate the degree of convergence. The kink at approximately $I = 2.7 \times 10^{14}$ W/cm^2 in the curve corresponding to the inclusion of six angular momenta and fifteen Floquet blocks in figure 2.20 is simply spurious and we see from the other curve in this figure that when further couplings are added this feature vanishes. We find that above $I = 7 \times 10^{14}$ W/cm^2 the convergence is far from perfect, even when including very many couplings. All the curves do however follow a very consistent trend, leading us to have confidence in the qualitative accuracy of our results over this range of intensities. At intensities of around 10^{15} W/cm^2 the very high number of couplings needed to obtain a converged quasi-energy makes it increasingly difficult to distinguish the minimum of λ_M from the background noise. (Recall figure 2.16). Taking very small steps in intensity does allow one to proceed, the result being that the quasi-energy crosses the negative imaginary axis of the complex energy plane, entering the lower-right-hand quadrant at an intensity approaching 2×10^{15} W/cm ^{2}. In this region the real part of the quasi-energy is positive, meaning that the energy level lies in the continuum. We interpret this as meaning that the dressed potential is no longer able to support a bound state at this frequency and intensity. The three-dimensional dressed-potential clearly does not possess the spherical symmetry of the field-free problem and so a direct calculation of the eigen-energies of the dressed potential is not at all trivial and has not been performed. Following this unphysical state further into the right-hand half-plane reveals that it does not turn back to resume a physical character.

Adiabatic Stabilisation

It was first speculated as long ago as the 1970s that atoms in super-intense high-frequency fields might stabilise with increasing intensity but it is only very recently that extensive numerical studies have been performed to test this prediction and that experimental verification has become possible. The first numerical study of the stabilisation regime (within the time-independent Kramers-Henneberger frame) was carried out by Gavrila and co-workers in the mid 1980s [57] [109] and predicted that a maximum in the ionisation rate should occur at high (but in some cases accessible) intensities - a region which is currently referred to as 'death valley' - beyond which the ionisation rate becomes sharply suppressed. For atomic ground states the intensities required to enter the stabilisation regime are extremely high (due to the condition that the frequency should be larger than the binding energy of the atom, whilst keeping a large value of the oscillation amplitude α_0) and this makes experimental verification quite problematic. However, for many Rydberg states the requirements are less stringent and some experimental investigations have successfully demonstrated the onset of stabilisation [8] [9]. The most recent and most accurate work on this phenomenon take the Floquet approach, either in the context of the new R-Matrix-Floquet theory (see, for example, Joachain in [87] and Dörr *et al* [36]) or in that of the very versatile Sturmian-Floquet method [124] [98]. These new methods are highly satisfactory in that they do not make any high-frequency approximation and indeed a detailed comparison with the results from fully time-dependent calculations (e.g. [73] [106]) reveals excellent quantitative agreement. All of these studies predict a strong suppression of ionisation in the high-frequency, super-intense regime. The difficulty in testing these predictions experimentally is that in order to reach the stabilisation regime in a given pulse of laser light one must first pass through the death valley in which the ionisation yield is very high, leaving few (if any) of the initial atoms intact to be stabilised. As described in section 1.1.1, this problem can be largely avoided by using atoms which are prepared initially in a circular Rydberg state and which therefore suffer less from ionisation than does the ground-state. Ex-

periments have been performed along these lines for the $5g$ Rydberg state in Neon (with a pump wavelength of 286 nm to excite the atom into the initial Rydberg state and a probe wavelength of 620 nm) and reveal a decreasing ionisation yield with increasing field-strength [8] [9].

S Geltman, however, maintains that all the numerical simulations of stabilisation processes thus far are flawed in various ways and indeed that the phenomenon of non-dynamic stabilisation does not exist [60] [59] [61]. He believes that the Floquet calculations are compromised by the tacit assumption that the 'total rate of ionisation' is a meaningful quantity in the super-intense regime. While the Floquet approach is of course only valid for states with a lifetime much greater than the optical period the stabilisation under discussion is expected to occur at intensities well below this upper bound and so we do not see this as an obstacle. The calculations utilising the Kramers-Henneberger frame are rightly questioned concerning the possible side-effects of the time-averaging procedure (see equation (2.60)) at finite frequencies of the incident radiation. Geltman performs calculations of his own for an ultra-intense electric field abruptly applied to, firstly, a Dirac δ-function potential and secondly, a Hydrogen atom. These calculations approximate the electronic wavefunction as a spreading Volkov wavepacket. For reasons outlined below we do not regard the delta-potential as a suitable model atom with which to test stabilisation phenomena and the approximations made in the Hydrogenic calculation, while plausible, are in our view more severe than those made by other authors (e.g. [124]).

A short-range potential is (in a mathematical rather than physical sense) commonly understood to mean one who's long-range amplitude falls off faster than $1/r$, thus the Coulomb potential is not short-range in contrast to any kind of square-well potential. The qualitative behaviour of particles in a short-range potential is quite different to that of particles in a long-range potential, most notably because a short-range potential can only support a limited number of bound states whereas a long-range potential must possess a manifold of infinitely many energy levels. However severe an effect the short-range nature of our potential may have on dynamical stabilisation

processes we see no reason to be surprised at the presence of adiabatic stabilisation. Krainov and Preobrazhenskii [76] have studied the delta-function potential (i.e. a zero-range potential) in the context of adiabatic stabilisation by a circularly polarised ultra-strong laser field and find no decrease whatsoever in the total rate of ionisation as a function of field-strength and go further, claiming that the same should hold for all atoms. This potential is chosen because the calculations may be performed analytically. We note however that the zero-range potential does not even approximately model any real atom and instead is sometimes used to model interaction potentials which lack a Coulomb tail, for example, the interaction between an electron and a negative ion. However, negative ions behave differently from atoms in many respects and it is perfectly possible that in strong fields the ionisation potential may increase rather than decrease. Moreover, in the photo-detachment of negative ions it is likely that autoionising states will be populated and that this will further facilitate the stripping of electrons from the ion. Singly negatively charged ions are notoriously difficult to describe accurately (due to the loosely bound outer electron) and we are not aware of any theoretical calculations having been performed or experimental data obtained for the photo-detachment rates of negative ions in the high-frequency and high-intensity regime. However, H^- has been studied extensively at both perturbative and non-perturbative intensities within the R-Matrix-Floquet approach [37] [19] and this work may well be extended to still higher intensities in the near future. The lack of stabilisation exhibited by the delta-potential in the study by Krainov and Preobrazhenskii may also stem from their use of circularly rather than linearly polarised radiation. Experimental evidence for stabilisation phenomena comes only in the context of linearly polarised beams. (Of course, a zero-range potential, possessing only a single bound state, would not exhibit any kind of dynamic stabilisation either although with the appearance of light-induced states this may become possible in principle.) Our own results clearly show that adiabatic stabilisation is not restricted to long-range potentials and that it can occur in systems possessing only one bound state.

2.4.3 Partial Rates of Multiphoton Ionisation

Theoretical Considerations

Partial rates are a way of partitioning the total rate of electron ejection from the well according to the necessarily discrete energies which the electrons possess; i.e. each electron must emerge with the Stark-shifted ground state energy plus ω for each of some M real photons absorbed, *viz.*

$$E_e = E_0 + \Delta + M\omega \tag{2.74}$$

Only the M real photons are included (rather than the total number N absorbed) because virtual processes should not be physically observable. This emission energy E_e defines a cycle-averaged velocity v_M,

$$\frac{1}{2} v_M^2 = E_e \tag{2.75}$$

The differential rate for M-photon absorption and ejection into a solid angle Ω is

$$R_M(\theta) \equiv \frac{d\Gamma_M}{d\Omega} = v_M \mid F_M(\theta) \mid^2 \tag{2.76}$$

where Γ_M are the partial rates and $F_M(\theta)$ is the M-photon absorption amplitude, (i.e. M real photons.) The cylindrical symmetry of the problem removes any azimuthal dependence, leaving F_M a function of (θ) only. It will be shown (see section 2.4.4) that the $F_M(\theta)$ are related to the 'external' coefficients $g_{M\lambda}$ of equation (2.38) by

$$F_M(\theta) = \frac{4\pi}{ik_M} \sum_\lambda Y_{\lambda 0}(\theta) g_{M\lambda} \tag{2.77}$$

The $g_{M\lambda}$ are calculated during the inverse iteration procedure and so can simply be utilised here to calculate the partial rates. Given that the $g_{M\lambda}$ are determined only up to an overall normalisation the expression we obtain for the partial rates is

$$\Gamma_M \propto \frac{v_M}{\mid k_M \mid^2} \int d\theta \left[\sin\theta \left| \sum_\lambda g_{M\lambda} (2\lambda + 1)^{1/2} P_\lambda(\cos\theta) \right|^2 \right] \tag{2.78}$$

and these Γ_M are also known as the branching ratios, i.e. the physically important quantity is the set of ratios between the Γ_M as M increases.

Experimentally, the peaks in the above-threshold-ionisation (ATI) spectrum are separated by the photon energy ω, but the position of any given peak depends also on the length of the pulse. For short pulses equation (2.74) above is found to hold, whilst for long pulses the positions of the ATI peaks are accurately predicted by the formula

$$E_e = E_0 + M\omega \tag{2.79}$$

i.e. neglecting the effect of the Stark shift Δ to the ground state energy E_0. The qualitative difference is that for a short pulse the field-strength will diminish whilst the electron is still within the field, whereas for a long pulse the electron leaves the focal region whilst the intensity is still high. This affects the energy spectrum of the ejected electrons because the electron in the field possesses, in addition to the energy of equation (2.74), a ponderomotive energy E_P (see equation (2.72)) whose physical origin is the time-averaged energy associated with the classical oscillations of an electron in the laser field [21]. In the short-pulse limit this additional energy is returned to the field as it dies away, leaving the electron with an energy predicted by (2.74). However, in the long-pulse regime the edge of the beam acts as a *ponderomotive potential* down which the electron is accelerated as it leaves the focal region, converting the ponderomotive energy into kinetic energy. Since the Stark shift is dominated by the ponderomotive term (see equation (2.71)) this increase in the outgoing electron's energy approximately cancels out the decrease in that final energy due to the increase in the ionisation threshold and so the net result is that the measured electron energies are given by equation (2.79). Specifically the mechanism is as follows [21]: write the electron's velocity in two parts v_t and v_o representing translational and oscillatory motion respectively, then the average kinetic energy of the electron in the beam can be written as

$$E_{KE} = \frac{1}{2}\langle v_t \rangle^2 + \frac{1}{2}\langle v_o \rangle^2 \tag{2.80}$$

Now the second term - which represents the ponderomotive energy of the

electron - can be viewed as defining the ponderomotive potential down which the electron slides as it moves out of the laser beam. The ponderomotive energy of the electron is then transferred to its translational energy, leading to the result above.

Results of our Calculations

In the Floquet picture the pulse is (supposedly) of infinite duration and so we might naively expect equation (2.79) above to hold. But, Floquet calculations assume a homogeneous laser field, i.e. no transverse intensity dependence, and so there can be no ponderomotive potential and one returns to equation (2.74) to obtain the energy spectrum of the ejected electrons. Let us now return to the case study at the end of section 2.4.2, namely the well of depth $V_0 = -8$ eV and width $a = 2$ Å, with $\lambda = 256$ nm. Figures 2.22 to 2.24 show the partial rates of multiphoton ionisation from this well at three characteristic intensities: (i) a relatively low intensity, $I = 1.3 \times 10^{14}$ W/cm^2 (fig. 2.22); (ii) the intensity corresponding to the maximum total rate of ionisation, namely, $I = 4.9 \times 10^{14}$ W/cm^2 (fig. 2.23); (iii) a significantly higher intensity, $I = 8.0 \times 10^{14}$ W/cm^2 (fig. 2.24) at which the total rate is considerably lower. The quasi-energies E are $(-2.438, -0.4055)$ eV, $(-1.222, -0.8045)$ eV and $(-0.628, -0.555)$ eV respectively. In each case the partial rates are determined only up to an overall normalisation factor which, in this case, we fix such that the sum of the partial rates (taken over all of the open channels $M \geq 1$ included in the computation) equals the total rate of ionisation defined by $\Gamma = -2\Im\mathrm{m}(E)$. Note that at all intensities the zeroth ATI channel $S = 0$ is in fact just $M = 1$, i.e. there are no channel closings at this wavelength. Also, at each intensity we check the convergence of the partial rates with respect to the numbers of partial waves and Floquet blocks included in the computation. Computational difficulties place an upper bound on the values which these parameters can take, and this problem becomes increasingly severe at high intensities, in opposition to the physical demand that more couplings rather than fewer are needed as the intensity increases. From figure 2.22 we see that at this relatively low

intensity the branching ratios between adjacent ATI peaks are approximately equal, resulting in a steady exponential decline in the height of the peaks as the above-threshold photon index S increases. We find that the calculation taking 10 angular momenta and 37 Floquet blocks is completely converged with respect to the angular momenta up to channel $S = 8$ (inclusive) and is completely converged with respect to the Floquet components up to channel $M = 15$. Given that the highest channel included in the calculation is $M = 18$ this is a surprisingly good result.

We now look to see whether the results are qualitatively different at the higher intensities. At $I = 4.9 \times 10^{14}$ W/cm^2 we see that although the results are not fully converged beyond the fourth above-threshold channel there is a clear plateau in the ATI spectrum between (approximately) peaks $S = 4$ and $S = 11$. We note that the onset of this plateau corresponds to a photo-electron energy of $4\omega \approx 19.4$ eV. It had until recently been assumed that ATI spectra in the non-perturbative regime follow the same simple pattern of an exponentially diminishing series of peaks, separated by integer multiples of the photon energy. (That is, apart from the substructures which are due to bound states shifting onto and out of resonance.) However it has recently been discoved both experimentally and numerically that, at least in the rare gases, the series of ATI peaks undergoes a change of gradient (or as a special case, a plateau) over the mid-section of the spectrum before decreasing exponentially again as expected [8] [9] [100] [101]. Indeed the experimental and numerical results to date show this effect playing a role at intensities of a few 10^{14} W/cm^2 and for photo-electrons with energies greater than approximately 20 eV. This figure is in strikingly good agreement with our own results. Clearly this phenomenon cannot be attributed to channel-closing due to threshold shifts because the ponderomotive shift in this instance is only about 2 eV [163] [82]. Numerical simulations by other authors, e.g. [100] [65] [63] [64] have concentrated on one-dimensional models which are known to 'exaggerate' physical effects and the result of our three-dimensional calculation adds weight to these results. The fact that these simple models are able to reproduce this phenomenon at all clearly indicates

that it is a single-electron process rather than one involving excitation of the atomic core. A tentative physical explanation might involve a rescattering process: the electron is driven by the field and will sometimes escape directly and other times rescatter off the atomic nucleus and in doing so absorb more photons [82]. Thus the observed photo-electron spectrum may be a superposition of the spectra from the directly ionised and the rescattered electrons.

Why should this process be involved at $I = 4.9 \times 10^{14}$ W/cm^2 but not at $I = 1.3 \times 10^{14}$ W/cm^2? Well, there is a clear physical difference between these two cases which can be described in terms of a parameter Ξ introduced by Dörr *et al* [38]

$$\Xi \equiv \left(\frac{\omega}{2E_P}\right)^{1/2} = \frac{(2\omega^3)^{1/2}}{\mathcal{E}} \tag{2.81}$$

where $\mathcal{E}$ is the electric field-strength. This differs from the Keldysh parameter γ_K [74] (see also section 3.3.2) only in that the ionisation potential E_I of the latter is replaced here by the laser frequency ω. In a high-frequency context, such as the present discussion, this means that $\Xi > \gamma_K$. This new parameter is relevant to high-frequency fields whereas the Keldysh parameter is useful primarily in a low-frequency context. The Keldysh parameter can be interpreted as the ratio of the characteristic atomic orbital speed $\sqrt{2E_I}$ to the excursion speed $\omega\alpha_0$ of a free electron [38]. The parameter Ξ can therefore be analogously interpreted as the ratio of the speed $\sqrt{2\omega}$ of an ejected electron which has absorbed one photon from the field to the excursion speed of a free electron. In defining the characteristic speed of the ejected electron we assume that $E_I + \Delta + \omega \approx \omega$ (where Δ is the Stark shift of the initial state). Thus we have a perturbative regime $\Xi \gg 1$, a multiphoton regime $\Xi \gtrsim 1$ and a stabilisation regime $\Xi < 1$.

A multiphoton description of the photo-detachment process in terms of the parameter Ξ is only meaningful if the incident intensity is lower than the *critical intensity* I_{cr} above which the field suppresses the potential barrier to such an extent that the electrons can simply flow out over the top of the barrier. For the ground state of atomic Hydrogen it is known that $I_{cr} \approx$

10^{15} W/cm^2 but it may be significantly lower in the case of our spherically symmetric square-well model because the ionisation potential $E_I \approx 0.12$ a.u. is much smaller than that of H($1s$) [143]. At the lower of our two field-intensities (1.3×10^{14} W/cm^2) we have $\Xi = 1.74$ which allows an essentially perturbative description of the detachment process whereas at the higher intensity (4.9×10^{14} W/cm^2) we find that $\Xi = 0.898$ and this is consistent with our heuristic argument that $\Xi \approx 1$ close to the maximum in the ionisation rate.

And what of the still higher intensity $I = 8.0 \times 10^{14}$ W/cm^2? Here we are unable to fully converge our results even in the first above-threshold channel ($M = 1$). However all of our calculated results at this intensity display the same behaviour, namely, an initial fall in the heights of the ATI peaks (channels 0 to 3) followed by a sharp *increase* in the peak height up to around the ninth ATI channel at which the peak height is approximately one order of magnitude greater than that of channel $S = 0$. Thus the trend which we saw between the partial rates at 1.3×10^{14} W/cm^2 and 4.9×10^{14} W/cm^2 continues with the 'plateau' feature now becoming a slope of positive gradient. At this intensity the high-frequency parameter is $\Xi = 0.703$ placing us clearly within the intensity region beyond that in which the maximum rate of photo-detachment occurs. However it is also possible that in this instance we have $I \geq I_{cr}$, making a multiphoton picture of detachment dynamics redundant. One distinctive feature is that whereas at $I = 4.9 \times 10^{14}$ W/cm^2 we have total convergence with respect to the number of harmonic components up to the channel with ATI index $S = 14$, at $I = 8.0 \times 10^{14}$ W/cm^2 we find that even with fifteen above-threshold photons we cannot even converge the first channel. This is a further indication that we have entered a new dynamical regime in which multiphoton processes play little role, namely, over-the-barrier (OTB) ionisation in which the electrons can flow out directly over the top of the potential barrier as described above. We can confirm this by looking at the strength of the electric dipole interaction at this frequency and intensity. From section 1.2.4 we recall that the dipole moment $\boldsymbol{d} = e\boldsymbol{r}$ gives rise to an instantaneous Stark Hamiltonian (representing

the interaction energy) of

$$H_S = -e\boldsymbol{\mathcal{E}}(t)\cdot\boldsymbol{r} = -\mathcal{E}z \tag{2.82}$$

such that $\mid H_S \mid \leq \mathcal{E}_0\alpha_0$ where we have used the fact that α_0 is the excursion amplitude of the oscillating electron. Now, at 8.0×10^{14} W/cm^2 we have $\mathcal{E}_0 = \sqrt{8\pi I/c} \approx 0.15$ and with $\lambda = 256$ nm this gives $\alpha_0 = \mathcal{E}_0/\omega^2 \approx 5$ a.u.. Hence the peak interaction energy is $\mid H_S \mid = 0.75$ a.u.. Comparing this with the depth of the potential well, $V_0'(\alpha_0) > V_0 = -0.3$ a.u. we see that there is certainly scope for OTB photo-detachment at this intensity.

Finally we come to a comparison between the branching ratios at the three intensities already considered, shown collectively in figure 2.25. This makes clear the two types of behaviour discovered so far. Namely, the steady exponential decline in the ATI peak heights at low intensities and the initial decline followed by a plateau region (between channels $S = 5$ and $S = 11$) at higher intensities for which the value of the Keldysh parameter is less than unity. In all cases the results we have obtained are inaccurate beyond, roughly, the $S = 10$ channel due to an insufficient number of angular momenta being available in the calculation.

2.4.4 Angular Distributions of the Photo-Electrons

Derivation of an Expression for the Differential Rates

The angular distribution of ejected electrons contributing to a given partial rate Γ_M has already been introduced in all but name. It is the function $R_M(\theta)$ of equation (2.76), i.e.

$$R_M(\theta) = v_M \mid F_M(\theta) \mid^2 \tag{2.83}$$

and we can now show how the M-photon absorption amplitude $F_M(\theta)$ is obtained. This is achieved by considering the asymptotic behaviour of the channel wavefunctions $\psi_N(\boldsymbol{r})$. Recall (see equation (2.32)) that the most general solution in the external region takes the form

$$\psi_{\text{ext}}(\boldsymbol{r}, t) = \mathrm{e}^{-iEt} \sum_N \mathrm{e}^{-iN\omega t}\psi_N(\boldsymbol{r}) \tag{2.84}$$

where

$$\psi_N(\boldsymbol{r}) = \sum_M \int d\hat{\boldsymbol{k}} \psi_{(N-M)}(\boldsymbol{r}) g_M(\hat{\boldsymbol{k}}) \tag{2.85}$$

and

$$\psi_{(N-M)}(\boldsymbol{r}) = 4\pi N_c \sum_{l,m} i^l Y^*_{lm}(\hat{\boldsymbol{k}}_{\boldsymbol{M}}) J_{N-M}(-\boldsymbol{\alpha_0} \cdot \boldsymbol{k_M}) Y_{lm}(\hat{\boldsymbol{r}}) h_l^{(1)}(k_M r) \tag{2.86}$$

Here I have used that $\boldsymbol{\alpha_0} = (1/\omega c)\boldsymbol{A_0}$. We note from this that the radial behaviour of the channel wavefunctions $\psi_N(\boldsymbol{r})$ is given by that of the spherical Hankel function $h_l^{(1)}(k_M r)$.

Now for asymptotically large arguments $\mid z \mid \sim \infty$ and for fixed index l we know that

$$H_l^{(1)}(z) \sim \left(\frac{2}{\pi z}\right)^{1/2} \exp\left[i\left(z - \frac{\pi l}{2} - \frac{\pi}{4}\right)\right] \tag{2.87}$$

and that the spherical function is defined as

$$h_l^{(1)}(z) = \left(\frac{\pi}{2z}\right)^{1/2} H_{l'}^{(1)}(z) \qquad \text{where} \qquad l' = \frac{1}{2}(2l+1) \tag{2.88}$$

These combine to give the asymptotic expression

$$h_l^{(1)}(z) \sim \frac{1}{i^l} \frac{\mathrm{e}^{iz}}{iz} \tag{2.89}$$

and thus for $r \sim \infty$ we have

$$\psi_N(\boldsymbol{r}) \sim \sum_M \int d\hat{\boldsymbol{k}} 4\pi \left[\sum_{lm} Y^*_{lm}(\hat{\boldsymbol{k}}) Y_{lm}(\hat{\boldsymbol{r}})\right] J_{N-M}(-\boldsymbol{\alpha_0} \cdot \boldsymbol{k_M}) \frac{\mathrm{e}^{ik_M r}}{ik_M r} g_M(\hat{\boldsymbol{k}}) \tag{2.90}$$

which reduces to

$$\psi_N(\boldsymbol{r}) \sim \sum_M \left(\frac{4\pi}{ik_M}\right) J_{N-M}(-\boldsymbol{\alpha_0} \cdot \hat{\boldsymbol{r}} k_M) g_M(\hat{\boldsymbol{r}}) \frac{\mathrm{e}^{ik_M r}}{r} \tag{2.91}$$

using the orthogonality of the spherical harmonics.

Let us introduce the function $F_{MN}(\hat{\boldsymbol{r}})$ to represent the amplitude that the electron has absorbed M real photons when it absorbs a total of N photons. Then the harmonic components $\psi_N(\boldsymbol{r})$, representing the electron after it has

absorbed a total of N photons, both real and virtual, should satisfy the asymptotic boundary condition

$$\psi_N(\boldsymbol{r}) \sim \sum_M F_{MN}(\hat{\boldsymbol{r}}) \frac{\mathrm{e}^{ik_M r}}{r} \tag{2.92}$$

i.e. a purely outgoing wave behaviour. From this one can readily identify

$$F_{MN}(\hat{\boldsymbol{r}}) = \left(\frac{4\pi}{ik_M}\right) J_{N-M}(-\boldsymbol{\alpha_0} \cdot \hat{\boldsymbol{r}} k_M) g_M(\hat{\boldsymbol{r}}) \tag{2.93}$$

Now the net amplitude $F_M(\hat{\boldsymbol{r}})$ for absorbing M real photons is a coherent sum over all possible virtual absorptions, and in the zero-field limit one would have

$$F_{MN}(\hat{\boldsymbol{r}}) = F_M(\hat{\boldsymbol{r}}) \delta_{MN} \tag{2.94}$$

whilst at finite field-strengths $F_{MN}(\hat{\boldsymbol{r}})$ and $F_M(\hat{\boldsymbol{r}})$ are related by

$$F_{MN}(\hat{\boldsymbol{r}}) = \mathrm{e}^{i(N-M)\chi_M} J_{N-M}(-\boldsymbol{\alpha_0} \cdot \boldsymbol{k_M}) F_M(\hat{\boldsymbol{r}}) \tag{2.95}$$

where χ_M is a phase-factor which can be assumed to be small. Neglecting χ_M we can sum to obtain

$$\sum_N F_{MN}(\hat{\boldsymbol{r}}) = F_M(\hat{\boldsymbol{r}}) \sum_N J_{N-M}(-\boldsymbol{\alpha_0} \cdot \boldsymbol{k_M}) \tag{2.96}$$

but by identity

$$\sum_{l=-\infty}^{+\infty} J_l(z) = 1 \tag{2.97}$$

and thus we can write

$$F_M(\hat{\boldsymbol{r}}) = \left(\frac{4\pi}{ik_M}\right) g_M(\hat{\boldsymbol{r}}) \sum_N J_{N-M}(-\boldsymbol{\alpha_0} \cdot \hat{\boldsymbol{r}} k_M) \tag{2.98}$$

Reusing the identity this further reduces to

$$F_M(\hat{\boldsymbol{r}}) = \left(\frac{4\pi}{ik_M}\right) g_M(\hat{\boldsymbol{r}}) \tag{2.99}$$

Recall equation (2.34) giving an expansion for $g_M(\hat{\boldsymbol{r}})$ in terms of the spherical harmonics, then by remembering the cylindrical symmetry of the problem we have

$$g_M(\hat{\boldsymbol{r}}) = \sum_\lambda g_{\lambda M} Y_{\lambda 0}(\hat{\boldsymbol{r}}) \tag{2.100}$$

Hence the angular distribution of ejected electrons contributing to the partial rate Γ_M is

$$R_M(\theta) = \left(\frac{4\pi v_M}{\mid ik_M \mid^2}\right) \left| \sum_\lambda g_{\lambda M}(2\lambda+1)^{1/2} P_\lambda(\cos\theta) \right|^2 \tag{2.101}$$

and given that the $g_{\lambda M}$ are unnormalised we can write

$$R_M(\theta) \propto \left| \sum_\lambda g_{\lambda M}(2\lambda+1)^{1/2} P_\lambda(\cos\theta) \right|^2 \tag{2.102}$$

With knowledge of the matching coefficients $g_{\lambda M}$ the angular distributions are therefore trivial to evaluate, and we choose to normalise them such that the area under each equals unity.

Interpretation of the Photo-Electron Distributions

Due to the propensity rule (see the appendix to chapter six) that preferentially selects increasingly higher angular momentum states as additional photons are absorbed it is expected that the angular distributions of the ejected electrons will become more strongly peaked along the polarisation axis as the above-threshold photon index S increases [163]. At high intensities, ionisation is dominated by the tunneling of electrons into the continuum at times close to the peak of the electric field. When the electron leaves the atom it is accelerated along the polarisation axis by the laser field. It is predicted that the faster electrons will be emitted before or after the peak field strength is reached and are more likely to emerge close to the axis of polarisation. Therefore the angular distributions should become more elongated along this axis as S increases. However, recent experiments have shown this simple picture to be incomplete by discovering side-lobes (i.e. maxima) at between 30 and 45 degrees to the polarisation axis in the angular distributions of high-energy (i.e. high S) photo-electrons [163] [101]. These experiments were performed using Krypton and Xenon, and angular distributions have been measured for ATI peaks up to the 30^{th} order at various laser intensities above 10^{13} W/cm^2. Given the azimuthal symmetry of the system these side-lobes manifest physically as rings in the full angular distributions. The

energies are (empirically) seen to vary with the intensity-dependent ponderomotive energy $E_P = \mathcal{E}_0^2/(4\omega^2)$ (see equation (2.72)) and are approximately equal to $9E_P$. Thus, explanations involving doubly excited states or excitation of the atomic core must be discounted because these processes do not generate photo-electrons of sufficiently high energies.

This leaves single-electron processes but with the caveat that the atomic core must play some role because the experimental results from, say, Krypton and Xenon are markedly different [163]. The same authors have performed theoretical investigations which clarify the nature of the processes involved. Firstly, calculations were carried out using Keldysh theory (or the KRF model) in which the ionisation process is represented as a one-step transition from an initial Coulomb wavefunction to a final Volkov (dressed) wavefunction where any interaction between the final dressed-state and the ion core is neglected [133] [163]. The upshot here was that although side-lobes were predicted in the angular distributions of certain orders of the ATI spectrum the results bore little resemblance to the experimental data. A more powerful method which incorporates the physics of the interaction of the electron with both the laser field and the ion is the Single Active Electron (SAE) approximation. This method has previously been shown to provide accurate ionisation rates and ATI spectra for rare gases in the strong-field regime [138]. Applying it here then, Yang *et al* [163] have obtained qualitative behaviour in excellent agreement with experiment. In particular, the side-lobes in the angular distributions appear at the correct energy (i.e. close to $9E_P$) and have the same angle (approximately 45 degrees) to the polarisation axis as was found experimentally. Thus, one can conclude that these 'rings' in the full angular distributions should result from single-electron processes. It is proposed that in fact the same mechanism is jointly responsible both for the plateau in the ATI spectra at certain intensities and for the appearance of these rings. Namely, that the electron which is driven by the field is (in some cases) re-scattered off the atomic core, thereby gaining additional energy. At the field-strengths used both in experiment and in previous numerical simulations one is on the borderline between the multiphoton and

tunneling regimes but the fact that the scattering rings are still present at rather higher intensities suggests that in fact this re-scattering is related to the tunneling component of the wavefunction. Further, it has been noted that because the re-scattering of the electron off the atomic core depends sensitively on the short-range part of the Coulombic potential it is not surprising that the shape and strength of the scattering rings depend strongly on the atomic species.

Results of our Calculations

We now present the results of our own calculations. It is instructive to study here the same three cases for which we calculated the partial rates of photo-detachment because the latter are none other than the integral over angle of the former. Thus the parameters being used are: a well of depth $V_0 = -8$ eV and width $a = 2$Å at a wavelength of $\lambda = 256$ nm. The first intensity to be considered is $I = 1.3 \times 10^{14}$ W/cm^2 which, in the context of the short wavelength, is relatively low. In all of the following figures the differential rate into each ATI channel has been normalised such that the rate into that channel becomes unity when integrated over angles. Let us also reiterate that the axis of quantisation is taken along the polarisation axis of the field and so the angle of ejection θ of the outgoing electrons is measured from this polarisation axis rather than with respect to the propagation axis of the field. For clarity the angular distributions are displayed in two figures, with above-threshold channels 0 to 5 in figure 2.26 and channels 6 to 10 in figure 2.27. It is immediately evident that in all channels the rate of photo-electron ejection is greatest along the axis of polarisation of the laser. Further, this becomes increasingly true with increasing channel-index S, i.e. the partial rate into channel $S = 0$ is the most evenly distributed and that for channel $S = 9$ is the most peaked along the polarisation axis. Channel ten is the one anomaly but then we see from figure 2.22 that the calculation is not quite fully converged from this channel upwards so we do not provide any physical interpretation for this.

The picture at $I = 4.9 \times 10^{14}$ W/cm^2 is similar, with the distributions in all (converged) channels strongly peaked along the polarisation axis. Angular distributions of the partial rates in channels 1 to 4 are shown in figure 2.28. Once again, it is in channel $S = 0$ that the rate decreases most slowly with respect to θ, followed by $S = 1$ and then $S = 2$. The rate for channel $S = 3$ is probably not wholly converged (with respect to the number of angular momenta). At this intensity the Keldysh parameter takes the value $\gamma_K = 0.727$ and so (with a laser frequency which is only marginally larger than the ionisation potential) we might expect a significant tunneling contribution to the wavefunction. Experimental and numerical results by other authors lead us to look for side-lobes in the angular distributions for the ATI channels with index $S \approx (\Re\mathrm{e}(E) + 9E_P)/E_\gamma$ where E is the quasi-energy of the bound-state and E_γ is the photon-energy. With $\lambda = 256$ nm we obtain a ponderomotive energy $E_P = 1.4474I$ (where the intensity is expressed in atomic units) and so in this case we find that $S \approx 5.3$. Unfortunately our angular distributions are not converged with respect to the angular momenta in channels $S = 4$ upwards so we are unable to confirm this prediction. It may be significant though that $S = 4$ corresponds to the *onset* of the plateau region (see figure 2.23). Following previous authors [101] we suggest that it is only here in a narrow energy-window that the multiphoton component of the wavefunction (giving rise to the early part of the ATI spectrum) and the tunneling component of the wavefunction (giving rise to the plateau region) are of comparable size. Thus we have the possibility of interference between the two components generating the side-lobes which have been observed.

Finally we come to the highest intensity under investigation, namely $I = 8.0 \times 10^{14}$ W/cm^2. Our angular distributions for ATI channels 0 to 3 are shown in figure 2.29 and unsurprisingly we see that the rate for channel $S = 0$ is the most broadly distributed, with the distributions from the higher channels being successively more strongly peaked along the axis of polarisation. Let us see in which channels we might hope to observe side-lobes in the distributions. At this intensity we have $S \approx (\Re\mathrm{e}(E) + 9E_P)/E_\gamma = 9.0$ which lies well beyond those channels for which our angular distributions are even

approximately correct. Thus we learn nothing new from this highest intensity. Whilst our partial rates of photo-detachment clearly indicate which ATI channels we might expect to exhibit well-converged angular distributions we have also checked this explicitly at each of the intensities considered. At the lowest intensity $I = 1.3 \times 10^{14}$ W/cm^2 we find that the angular distributions are completely converged with respect to both the number of angular momenta and the number of Floquet blocks over at least the first eight ATI channels. At $I = 4.9 \times 10^{14}$ W/cm^2 we find that while the convergence is good in the lowest channels the angular distribution into channel $S = 3$ is a few percent away from convergence with respect to the number of angular momenta and of course the agreement becomes worse in the high channels. And at $I = 8.0 \times 10^{14}$ W/cm^2, we again observe that while the convergence with respect to the Floquet numbers is excellent over several ATI channels, a comparison between calculations including nine and ten angular momenta reveals that the results are not well converged with respect to this parameter. In summary these checks on convergence confirm our expectations from the partial rates in figures 2.22 to 2.24. We would also like to compare the angular distributions at the three characteristic intensities in a given channel and, for the sake of accuracy, we choose channels $S = 0, 1$ and 2. The results are displayed in figures 2.30 to 2.32 respectively. The trend that we observe from these figures is that in channel $S = 0$ the distribution is broadest at low intensity and becomes more strongly aligned with the polarisation axis at the higher intensities whereas with increasing channel index this picture reverses and the low intensity distribution is more strongly concentrated along the axis of polarisation than those at the higher intensities. (In drawing this conclusion we place little emphasis on the results from the highest intensity because of the numerical inaccuracies already discussed.) This pattern is in accordance with our expectation that the distributions into the higher-order channels develop sizeable lobes well separated from the polarisation axis at sufficiently high intensities and so there would be a shift in the probability distributions away from the polarisation axis in these cases. As discussed above, one would not expect any similar change of behaviour in the very lowest channels.

2.4.5 Laser-Induced Degeneracies

The concept of laser-induced degenerate states (LIDS) shares some aspects of the geometrical phase which, following the pioneering work by Berry, has found applications in all branches of physics. In atomic theory, recent examples of adiabatic degeneracies are described in [51] [121] [88] and the generality of this phenomenon (in quantum systems) is explained in [161]. The requirement is for a parameter space in which (at least) two parameters are varied in such a way that one traces out an adiabatic path around a degenerate point. A complete circuit around a degeneracy leads back to the initial state but with the addition of a dynamical and a geometrical (Berry) phase factor. These two parameters may, for example, be the real and imaginary parts of a complex field-strength (for a monochromatic field), the two frequencies of a bichromatic field, one intensity plus the relative phase from a bichromatic field, or the frequency and intensity of a monochromatic field. It is this last case which we have studied in the context of the spherically symmetric square-well model. Potvliege and Smith [121] have examined the degeneracy in the complex energy plane arising from variation of the intensity of the fundamental beam and the relative phase between the beams in a system whose incident field comprises the fundamental beam at 355 nm and its third harmonic. Here the degeneracy is between the $1s$ and $2p$ bound states and so, in contrast to the case below, in the limit of zero intensity both states lie on the negative real axis but topologically the paths traced out in the complex plane are identical.

Taking a well of given width a and depth V_0 one can construct a closed loop in the complex energy plane, encircling the degenerate point, from eight line-segments, alternately varying the intensity and the wavelength of the incident field. The degeneracy in this case is between the state linked adiabatically to the (only) field-free bound state and that linked to a resonance pole corresponding to a p-state (shifted in the energy plane by -ω). Given that the ground state has s-symmetry this is a one-photon resonance. The case we choose to study is defined by the parameters $a = 2$ Å and $V_0 = -4$ eV, corre-

sponding to a solitary bound state at an energy $E_b = -0.4767$ eV (see section 2.3). The resonance pole for this case is found at $E_a = (1.17285, -2.23850)$ eV in the complex energy plane and the degeneracy occurs at approximately the point ($\lambda = 747$ nm, $I = 4.5 \times 10^{13}$ W/cm^2), (see figure 2.33). The width of the resonance, $\Gamma = 4.48$ eV, is huge compared to any realistically measurable decay rate and the important question here is whether the well can be modified to simulate a physically interesting system. In this context there has been recent interest in the resonance series of Argon and Neon.

Application to Argon

Other authors [88] [84] have performed R-Matrix-Floquet calculations for Argon and Neon, taking fully into account the electron-electron correlation effects of these many-electron systems. For example, the one-photon resonance between the ground state of Argon and the $n = 4$ autoionising state from the resonance series Ar($2p^6 3s 3p^6 np\,^1P^0$) has been considered. Calculations of the intensity-dependent quasi-energies at field-strengths up to 5×10^{13} W/cm^2 have been carried out and reveal two degenerate points in the complex energy-plane. The phenomenon of LIDS is a topological property of the system and is therefore robust to changes in the experimental parameters.

To conclude this section we would like to try to customise our square-well potential such that the quasi-energies of its bound state and its 'autoionising' state match those of the corresponding states in Argon, as described above. In the field-free limit the two degenerate states in Argon are given by $E_b = -15.733$ eV and $E_a = (11.139, -0.0324)$ eV, and the idea is to adapt the defining parameters a and V_0 of our model well so as to reproduce (simultaneously) both of these states. The feasibility of this can be tested by initially choosing a pair (a, V_0) to give the correct value for E_b and then deforming both a and V_0 continuously with the constraint that the value of E_b should remain invariant. This leads to a trajectory for E_a in the lower-right-hand quadrant of the energy plane which, it can readily be seen (from figure 2.34), passes nowhere near the value given above. Indeed

it is a general feature of this trajectory that a real energy $\Re e.(E_a)$ which is not negligibly small always results in a similarly large imaginary component. We consider well-depths V_0 in the range $(-120, -30)$ eV and half-widths a in the range $(0.04, 0.10)$ nm. The data (arbitrarily) selected in figure 2.34 correspond to $(a, V_0) = (7.70\text{Å}, -46.6\text{eV})$, $(a, V_0) = (5.38\text{Å}, -71.5\text{eV})$ and $(a, V_0) = (3.94\text{Å}, -109.7\text{eV})$ respectively, in order of increasing $\Re e(E_a)$. Thus the spherically symmetric square-well model seems ill-suited to modelling realistic (or experimentally accessible) autoionising phenomena and we do not find this very surprising, given that no features of a complex atom are explicitly incorporated into the model.

2.5 Conclusions

The principal aim of this chapter has been to conduct a systematic study of the properties of a short-ranged three-dimensional potential well in a high-frequency, high-intensity laser field. Specifically we have investigated the possibility of adiabatic stabilisation occurring in a spherically symmetric square-well model atom. Our first step towards this goal was to set up the model atom in the absence of an external field. The structure of the bound-state spectrum of this model atom was described in terms of a 'well-parameter' γ and it was found that the number of bound states supported by this potential increases with both the width (a) and the depth (V_0) of the well. Adding an external electric field, a study has been made of the quasi-energy trajectory for a model atom that supports just one bound state in the field-free limit. The Stark shift of this solitary bound state in weak fields was found to depend strongly on the frequency of the incident radiation, with low-frequency fields inducing negative Stark shifts and high-frequency fields leading to positive Stark shifts. This picture is complicated by the presence in the complex energy-plane of a laser-induced degeneracy between the dressed state linked adiabatically to the field-free ground state and that originating from a resonance pole corresponding to a p-state (and shifted in the energy plane by -ω). In the high-frequency, high-intensity limit it was

found that the total rate of photo-detachment from the well reaches a maximum at an intensity of a few 10^{14} W/cm^2 and that beyond this point the rate is a monotonically decreasing function of intensity. Given the lack of Rydberg states in this model we interpret this decrease in the total rate as evidence of adiabatic stabilisation - a phenomenon not previously associated with short-ranged potentials. [76]. At an intensity higher than 10^{15} W/cm^2 it is observed that the quasi-energy moves into the continuum and that therefore the potential well no longer supports any bound states. This is believed to be a peculiarity of the spherically-symmetric square-well model.

The partial rates of ionisation and the differential (angle-resolved) rates have also been computed at intensities corresponding to different dynamical regimes. At the lowest intensity (1.3×10^{14} W/cm^2) it is found partial rates of ionisation are basically perturbative, i.e. the peak height undergoes an almost 'straight' exponential decline with increasing order of the ATI peaks. At the intensity corresponding to the maximum rate of photo-detachment (4.9×10^{14} W/cm^2) it is found that the partial rates exhibit a plateau region covering approximately seven ATI channels ($S = 4 \rightarrow 10$) and that the onset of this plateau region coincides with photo-electron energies of around 20 eV in close agreement with the findings of other authors [101]. Following previous authors (e.g. Kulander *et al* [82]) we interpret this as evidence of a superposition of electrons that ionise directly and those that rescatter off the ionic core. At very high intensity (8.0×10^{14} W/cm^2) we find it nearly impossible to obtain well-converged partial rates but we are able to discern from our results a common trend in which, rather than merely displaying a plateau, ATI peaks actually *increase* in magnitude (by a factor of about 100) over a region encompassing approximately seven ATI channels ($S = 4 \rightarrow 10$) before declining sharply again. At all three of the intensities mentioned above we find that the photo-electrons are preferentially distributed close the axis of polarisation and that this becomes increasingly true as the order of the ATI process increases. We are unable to obtain converged angular distributions into the higher ATI channels ($S > 3$) at all but the lowest intensity and so we are unable to confirm the presence of side-lobes in the angular

distributions which other authors associate with photo-electron spectra such as those we have obtained [163].

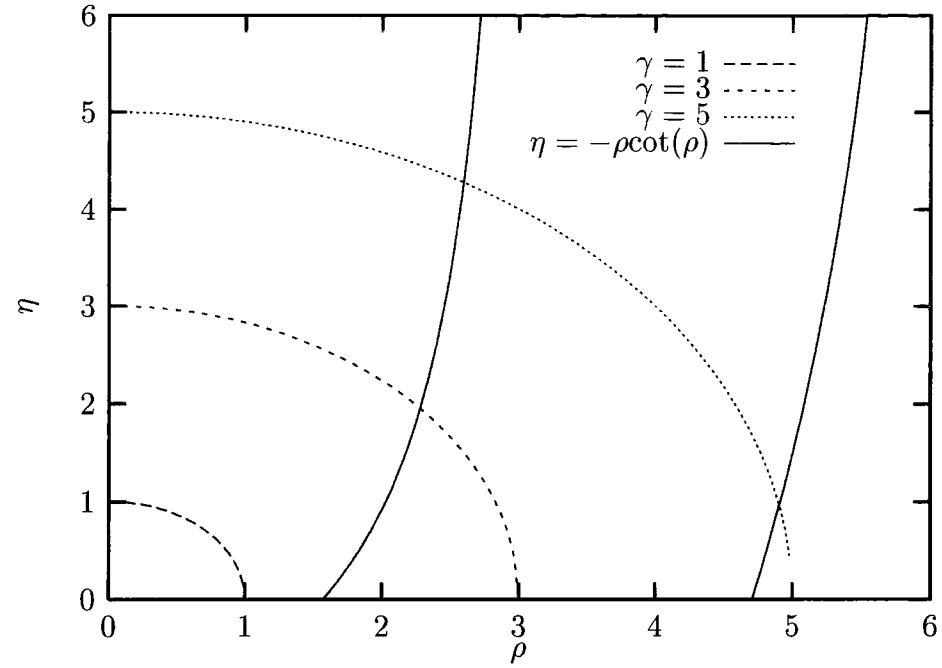

Figure 2.1: Graphical solutions of the transcendental equation for the s-wave.

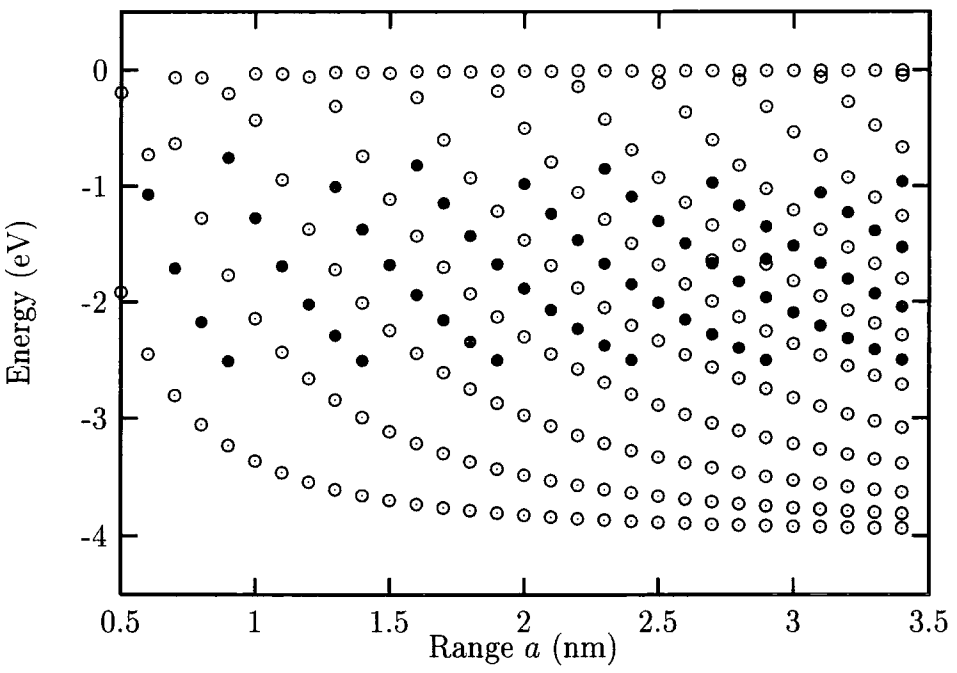

Figure 2.2: Eigen-energies of the 3D square-well in the absence of an external field. Symbols are: (●) s-states; (○) p-states. The higher angular momentum states have not been plotted.

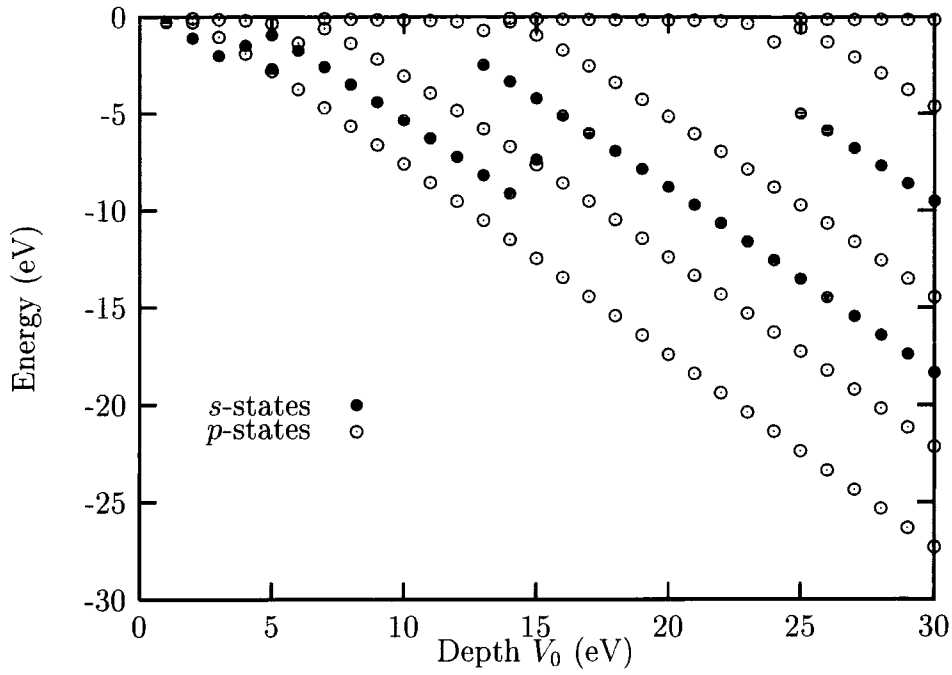

Figure 2.3: Eigen-energies of the 3D square-well in the absence of an external field. The higher angular momentum states have not been plotted.

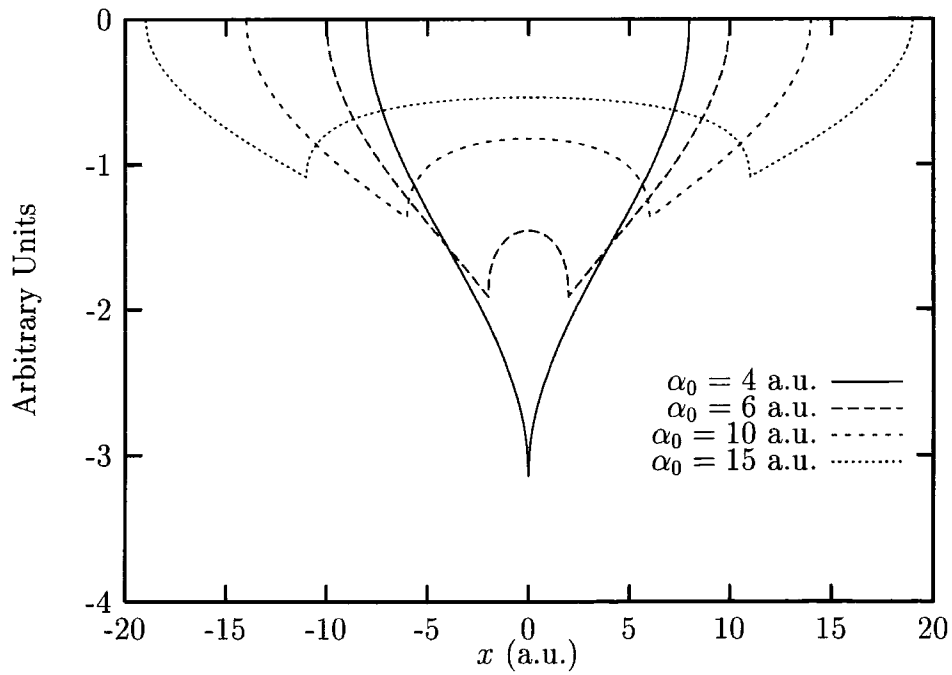

Figure 2.4: The dressed 1D square-well potential.

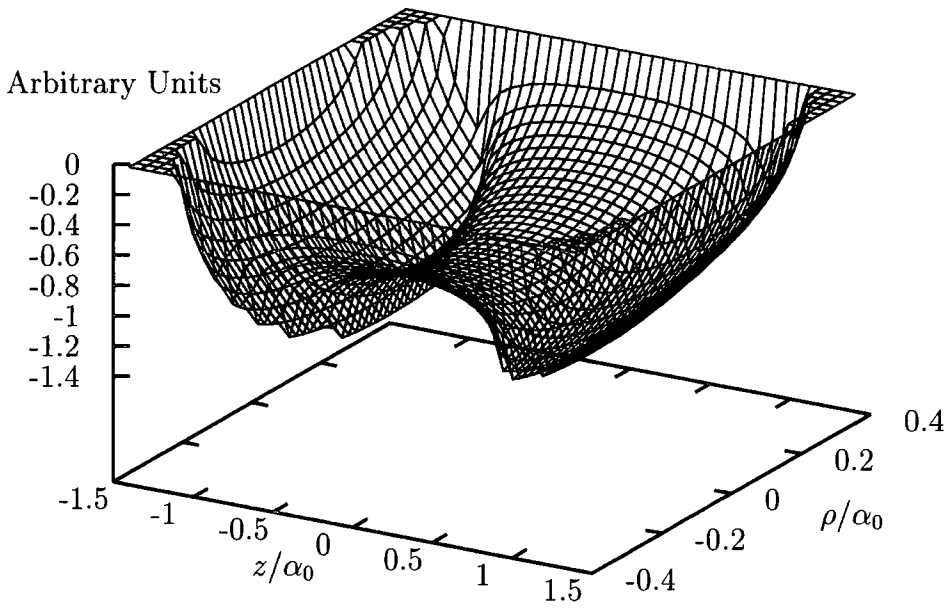

Figure 2.5: Dressed 3D square-well potential with $\alpha_0 = 8$ a.u..

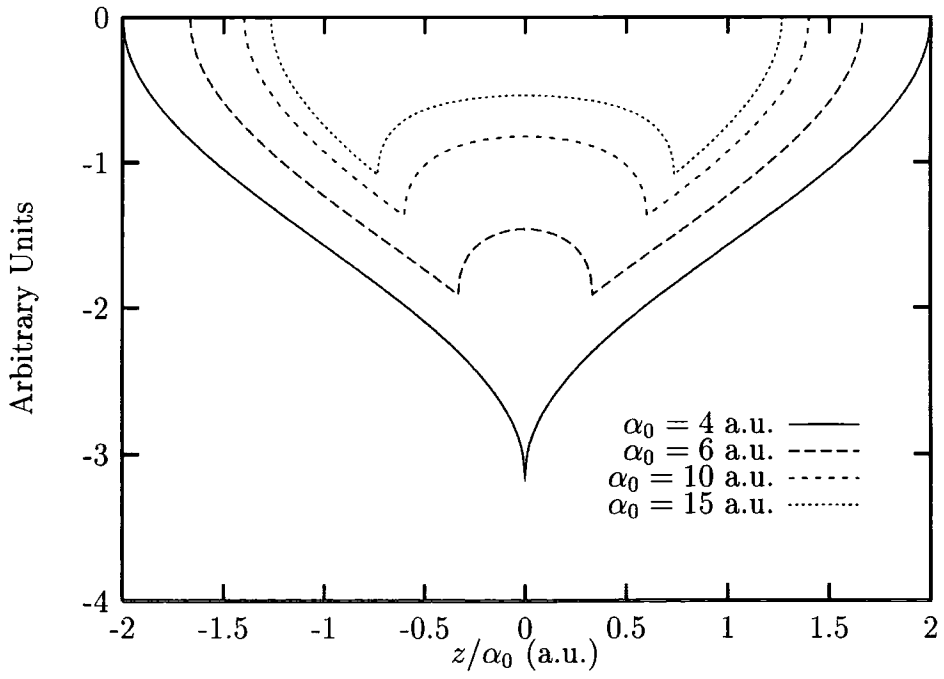

Figure 2.6: The dressed 3D square-well potential with $\rho = 0$.

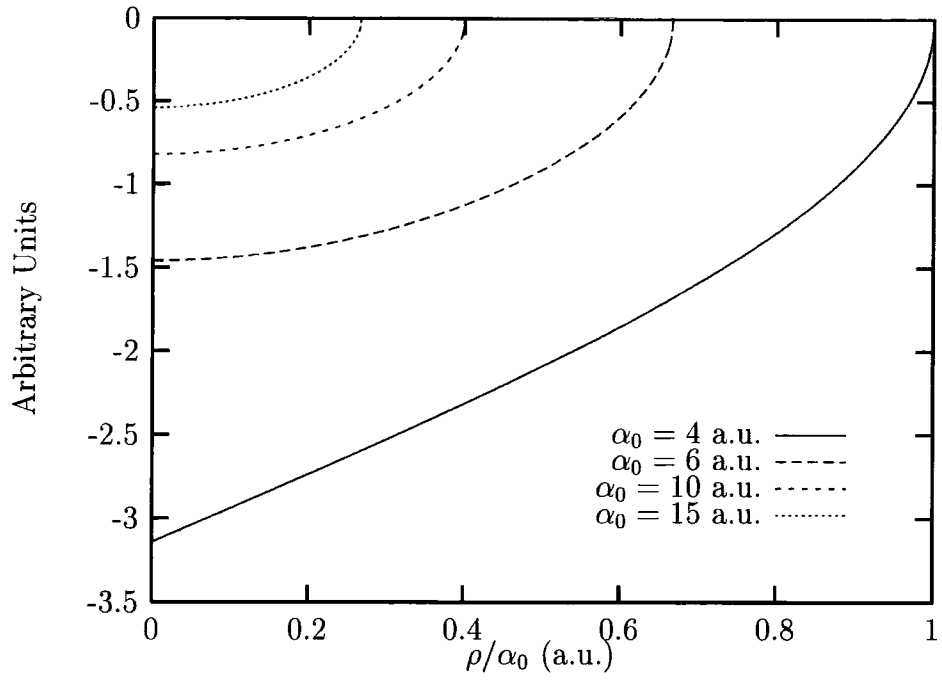

Figure 2.7: The dressed 3D square-well potential with $z = 0$.

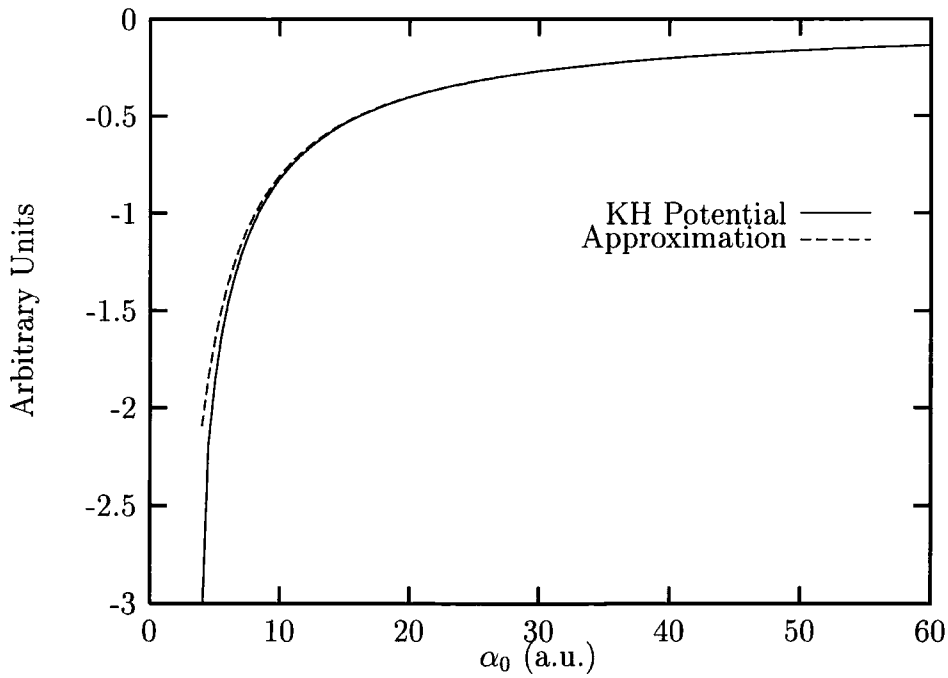

Figure 2.8: Approximation to the time-averaged potential evaluated at $(\rho, z) = (0, 0)$.

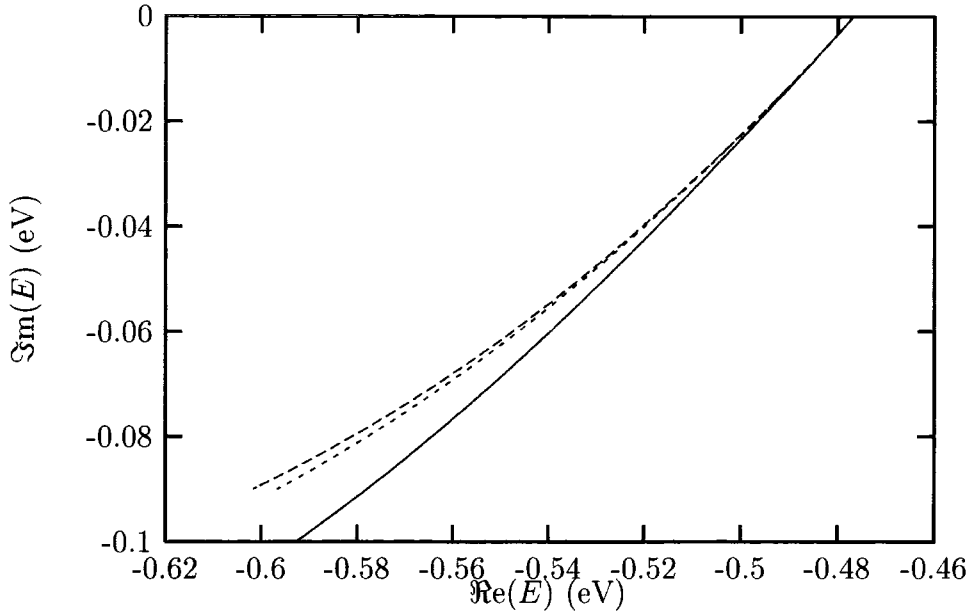

Figure 2.9: Quasi-energy of the 3D square-well with $\lambda = 1064$ nm and at low field strengths. Parameters are: (– – – –) 2 angular momenta and 3 Floquet blocks; (- - - - - -) 3 angular momenta and 3 Floquet blocks; (———) 3 angular momenta and 5 Floquet blocks.

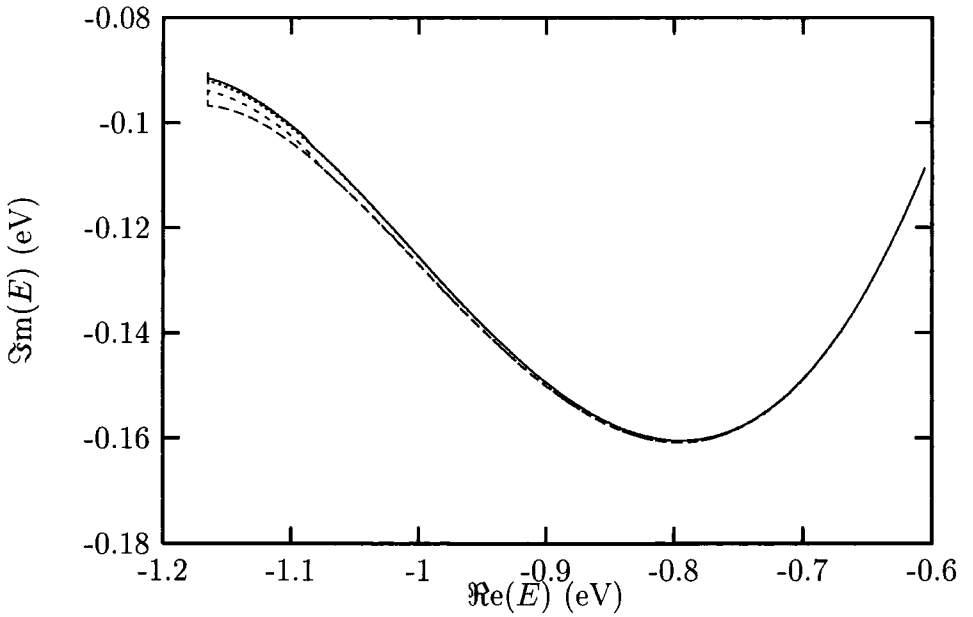

Figure 2.10: Quasi-energy of the 3D square-well with $\lambda = 1064$ nm and for intensities above 10^{12} W/cm^2. Parameters are: (– – – –) 4 angular momenta and 9 Floquet blocks; (- - - - - -) 4 angular momenta and 11 Floquet blocks; (· · · · · · · · ·) 5 angular momenta and 11 Floquet blocks; (———) 6 angular momenta and 11 Floquet blocks.

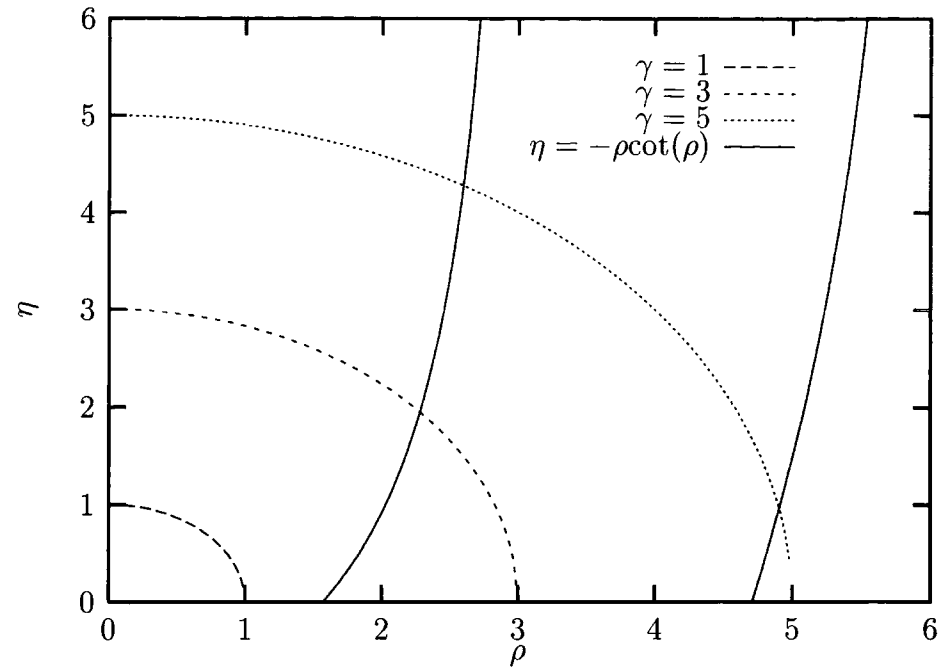

Figure 2.1: Graphical solutions of the transcendental equation for the s-wave.

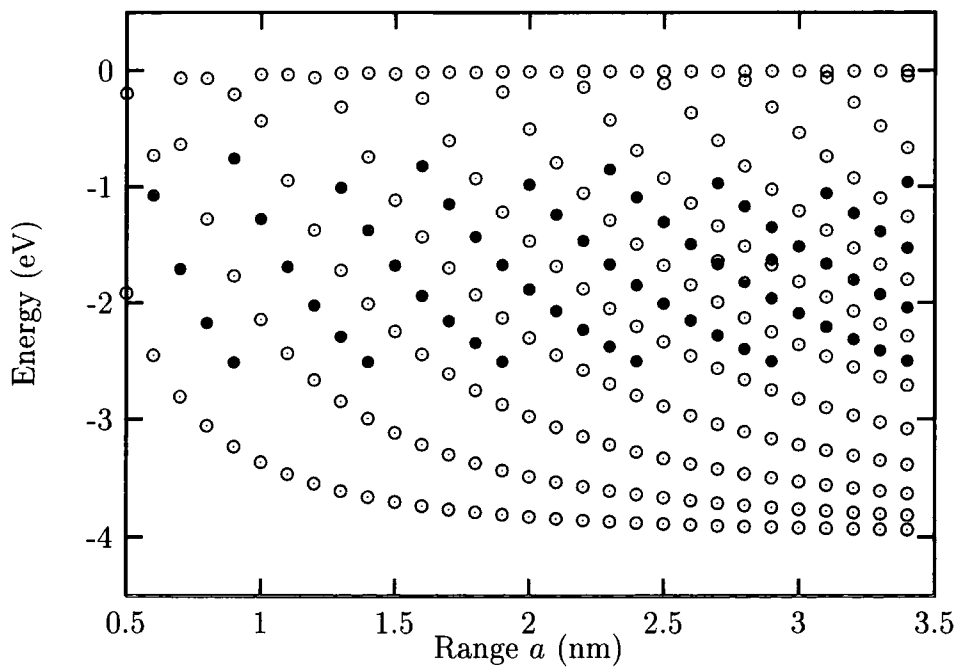

Figure 2.2: Eigen-energies of the 3D square-well in the absence of an external field. Symbols are: (●) s-states; (○) p-states. The higher angular momentum states have not been plotted.

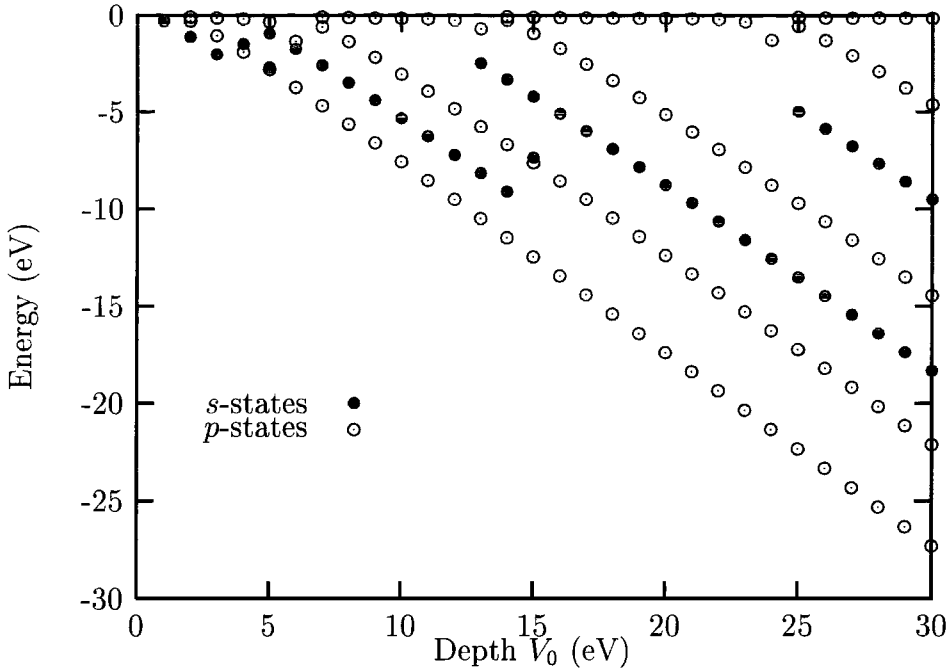

Figure 2.3: Eigen-energies of the 3D square-well in the absence of an external field. The higher angular momentum states have not been plotted.

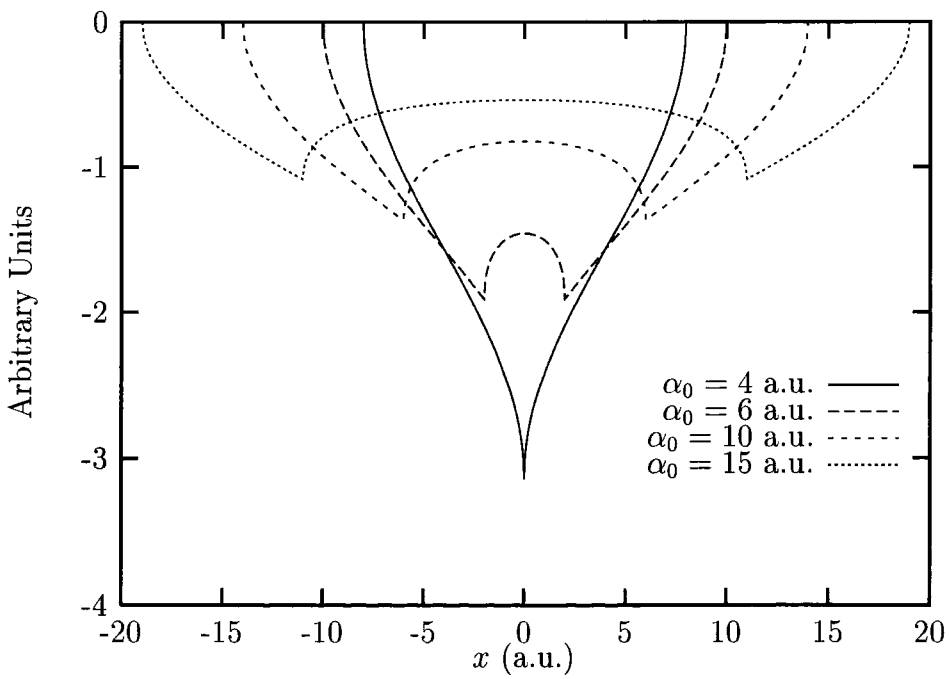

Figure 2.4: The dressed 1D square-well potential.

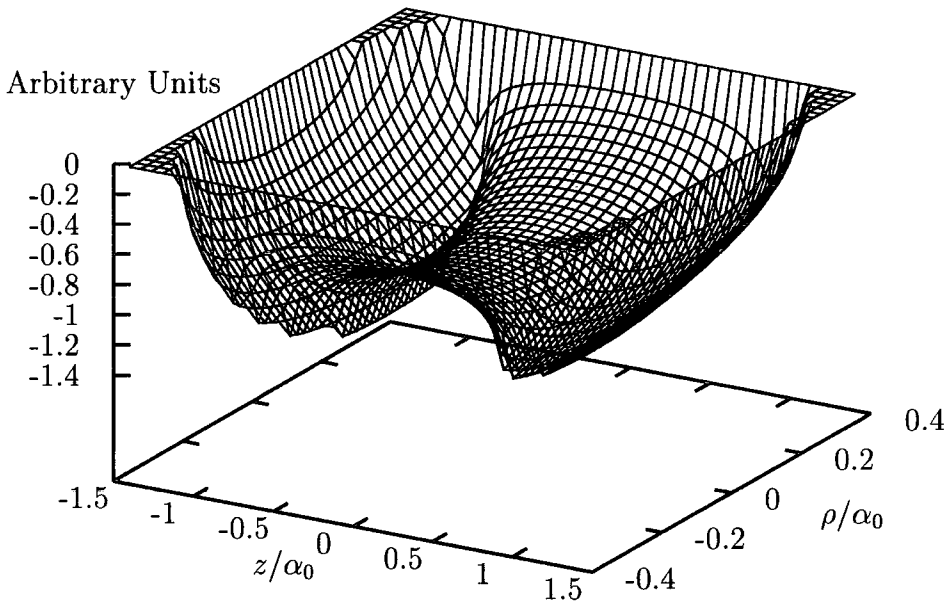

Figure 2.5: Dressed 3D square-well potential with $\alpha_0 = 8$ a.u..

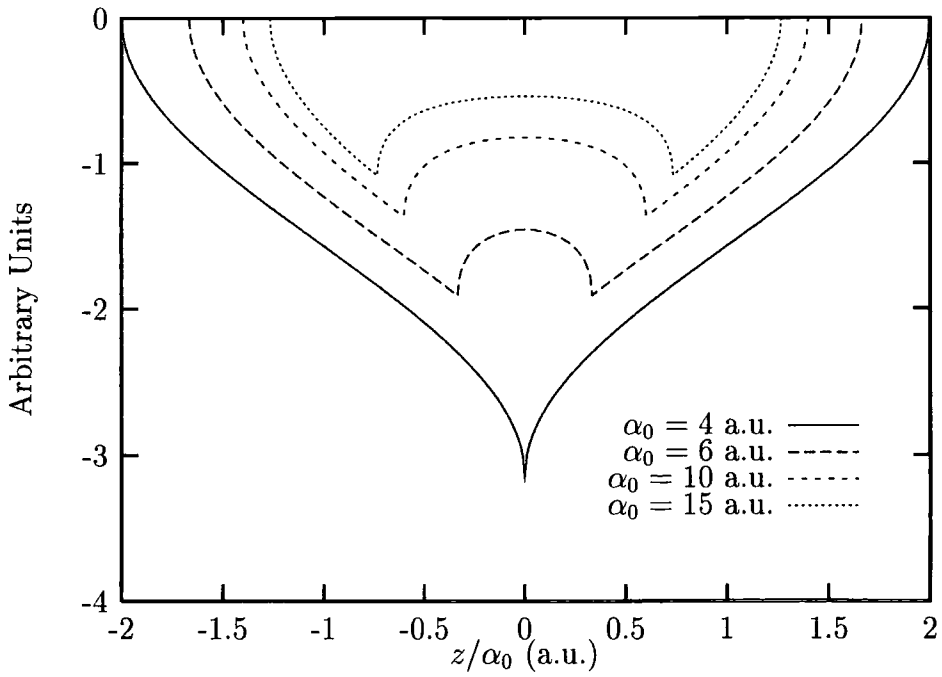

Figure 2.6: The dressed 3D square-well potential with $\rho = 0$.

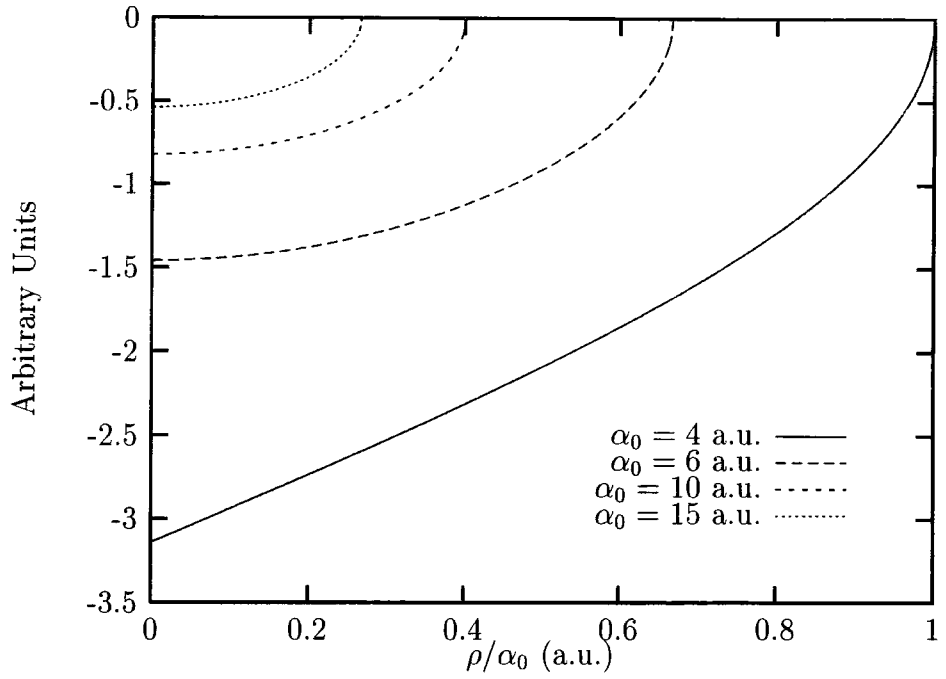

Figure 2.7: The dressed 3D square-well potential with $z = 0$.

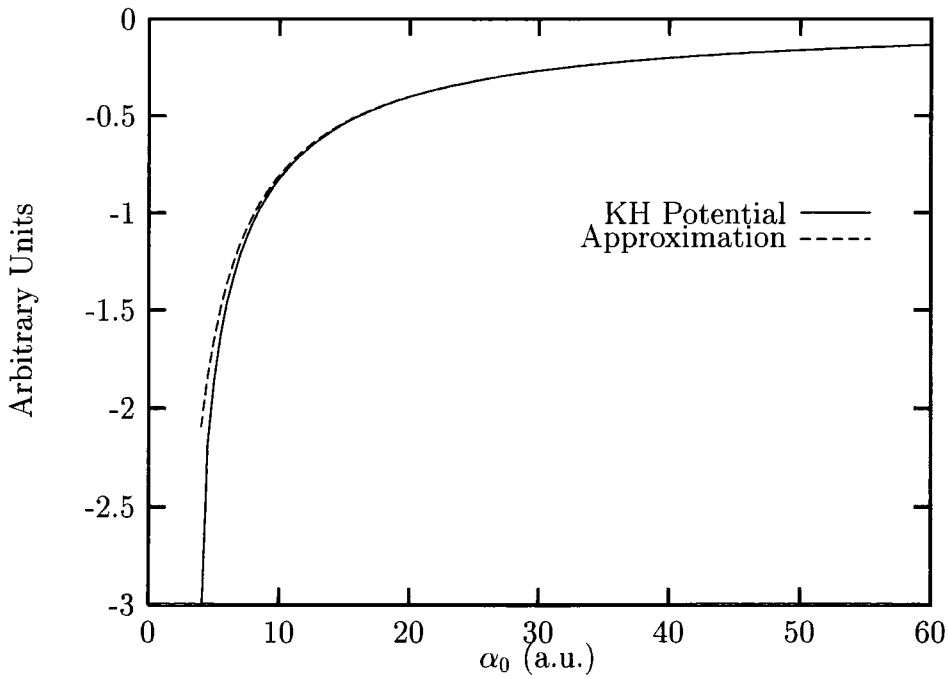

Figure 2.8: Approximation to the time-averaged potential evaluated at $(\rho, z) = (0, 0)$.

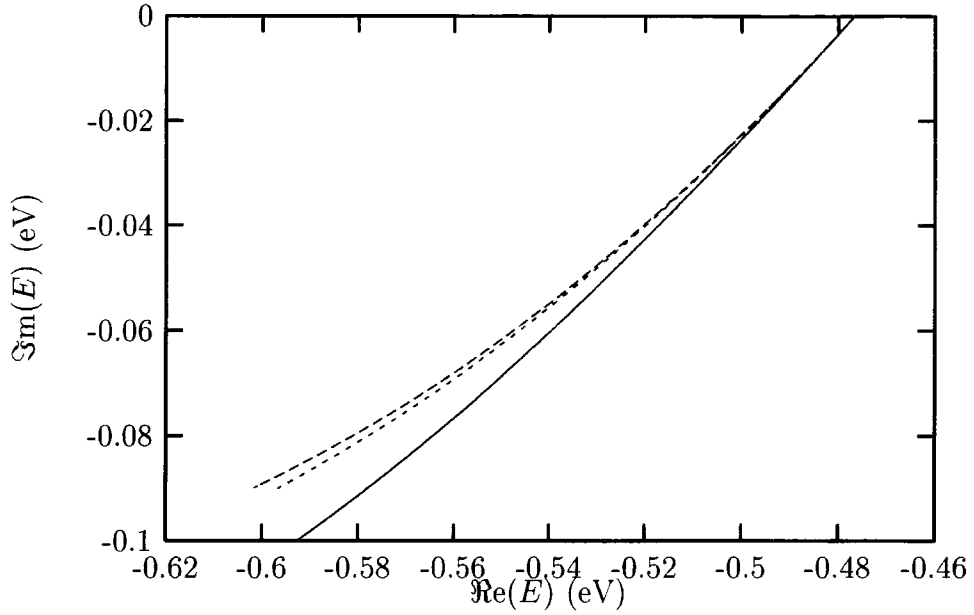

Figure 2.9: Quasi-energy of the 3D square-well with $\lambda = 1064$ nm and at low field strengths. Parameters are: (- - - -) 2 angular momenta and 3 Floquet blocks; (- - - - - -) 3 angular momenta and 3 Floquet blocks; (———) 3 angular momenta and 5 Floquet blocks.

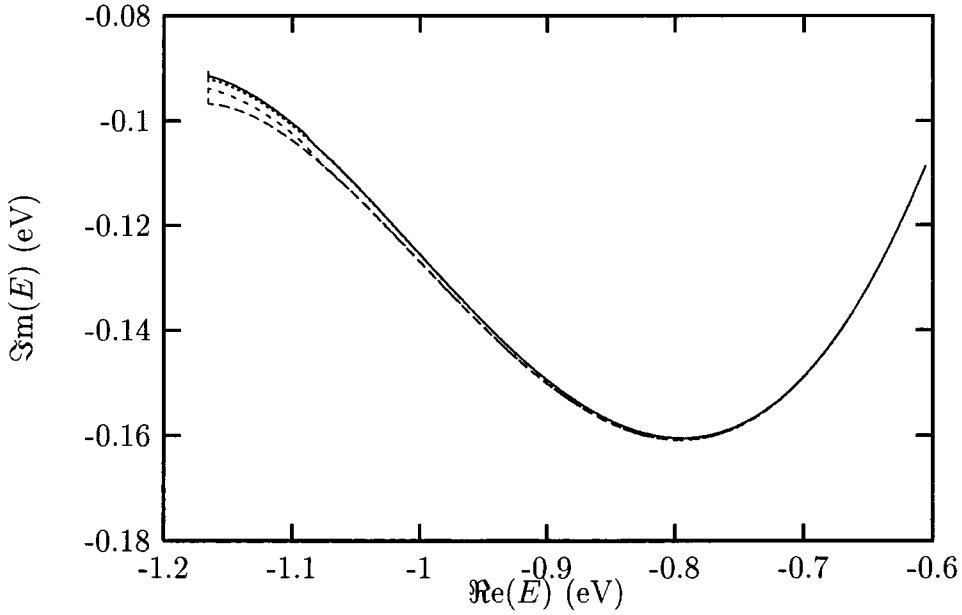

Figure 2.10: Quasi-energy of the 3D square-well with $\lambda = 1064$ nm and for intensities above 10^{12} W/cm^2. Parameters are: (- - - -) 4 angular momenta and 9 Floquet blocks; (- - - - - -) 4 angular momenta and 11 Floquet blocks; (· · · · · · · · ·) 5 angular momenta and 11 Floquet blocks; (———) 6 angular momenta and 11 Floquet blocks.

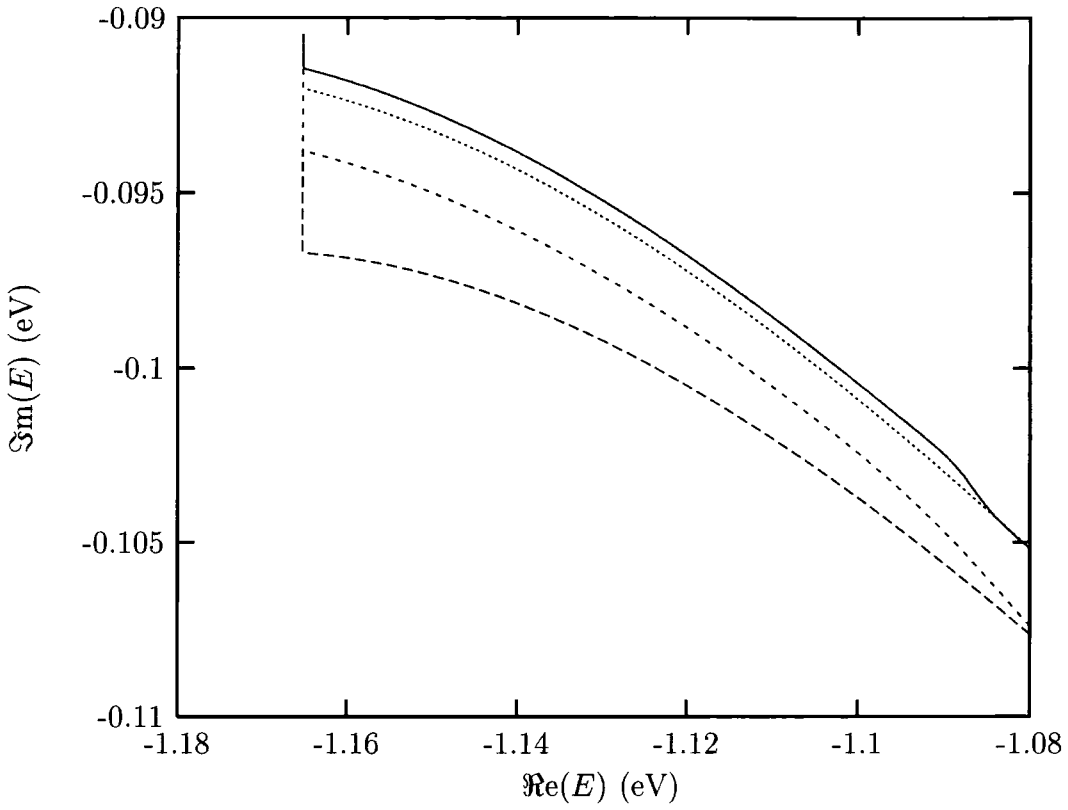

Figure 2.11: Quasi-energy of the 3D square-well with $\lambda = 1064$ nm as it approaches the one-photon cut. Parameters are: (– – – –) 4 angular momenta and 9 Floquet blocks; (- - - - - -) 4 angular momenta and 11 Floquet blocks; (·····) 5 angular momenta and 11 Floquet blocks; (———) 6 angular momenta and 11 Floquet blocks.

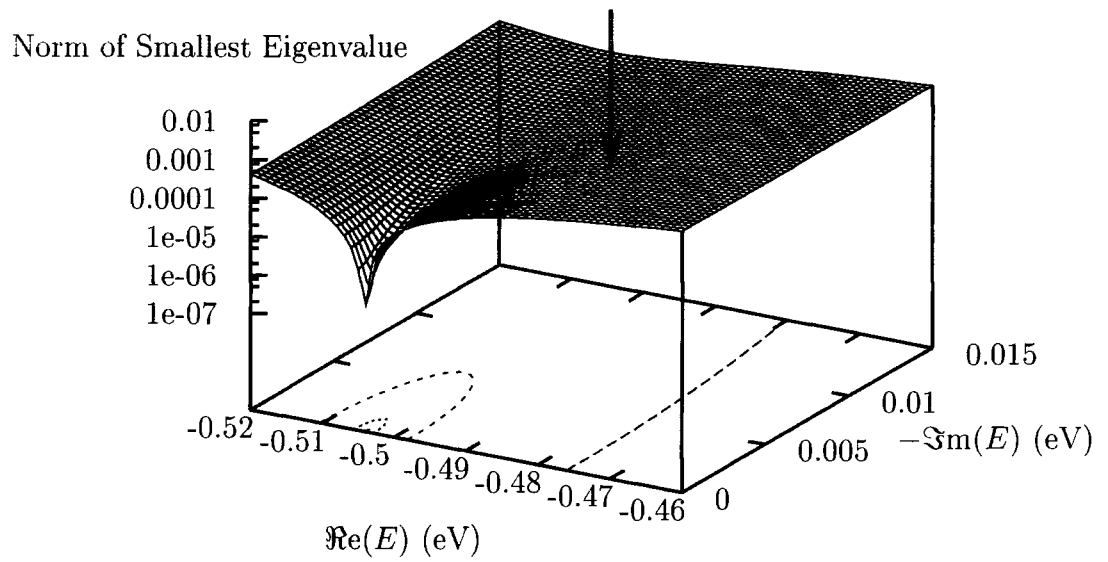

Figure 2.12: Quasi-energy surface at $I = 5 \times 10^{10}$ W/cm^2 with 4 angular momenta and 7 Floquet blocks. The bold arrow marks the actual position of the quasi-energy.

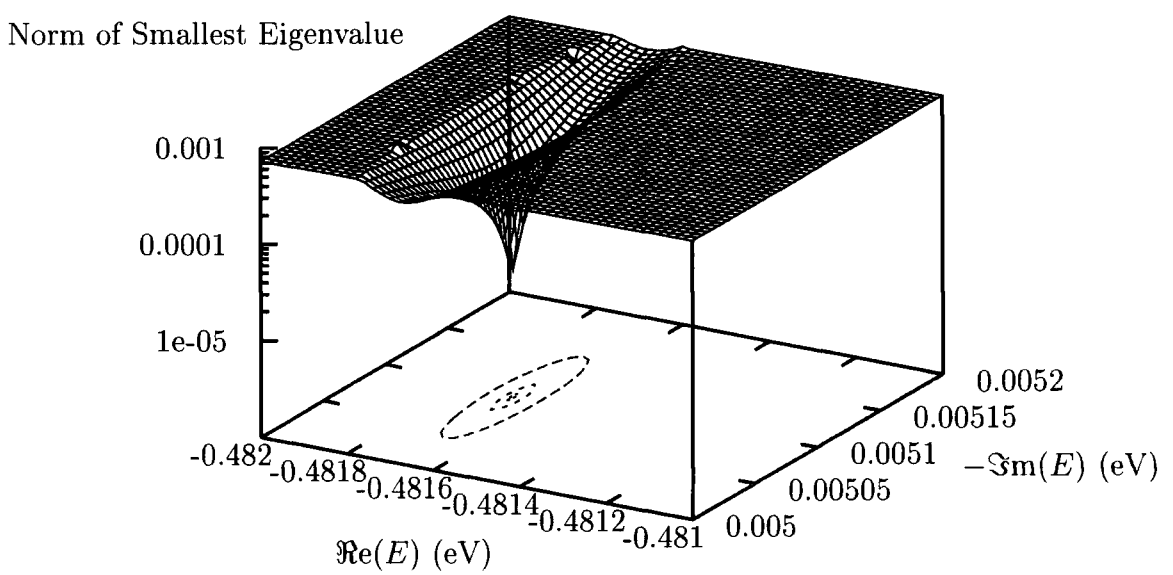

Figure 2.13: Quasi-energy surface at $I = 5 \times 10^{10}$ W/cm^2 with 4 angular momenta and 7 Floquet blocks.

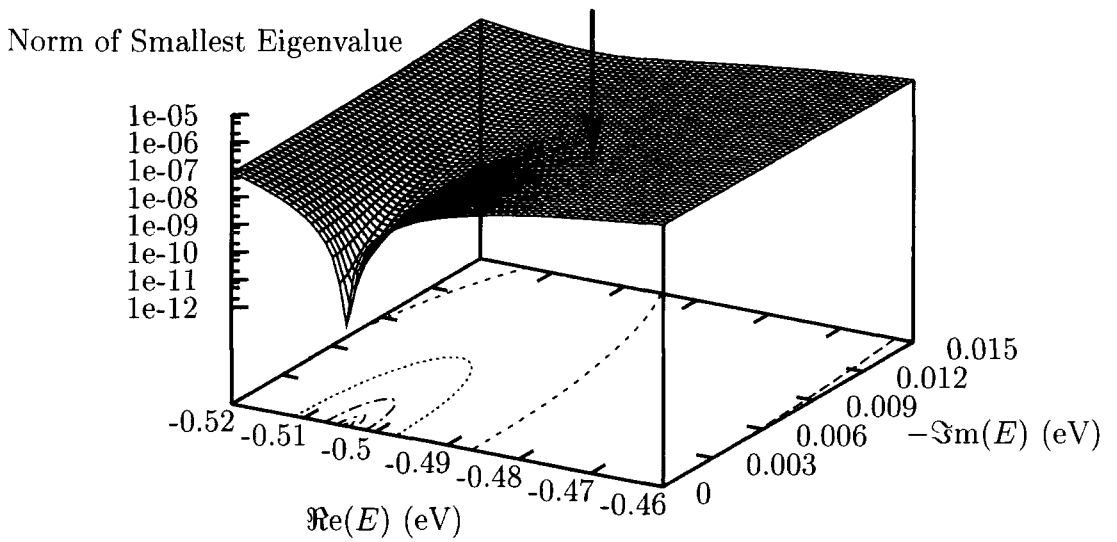

Figure 2.14: Quasi-energy surface at $I = 5 \times 10^{10}$ W/cm^2 with 6 angular momenta and 9 Floquet blocks. The bold arrow marks the actual position of the quasi-energy.

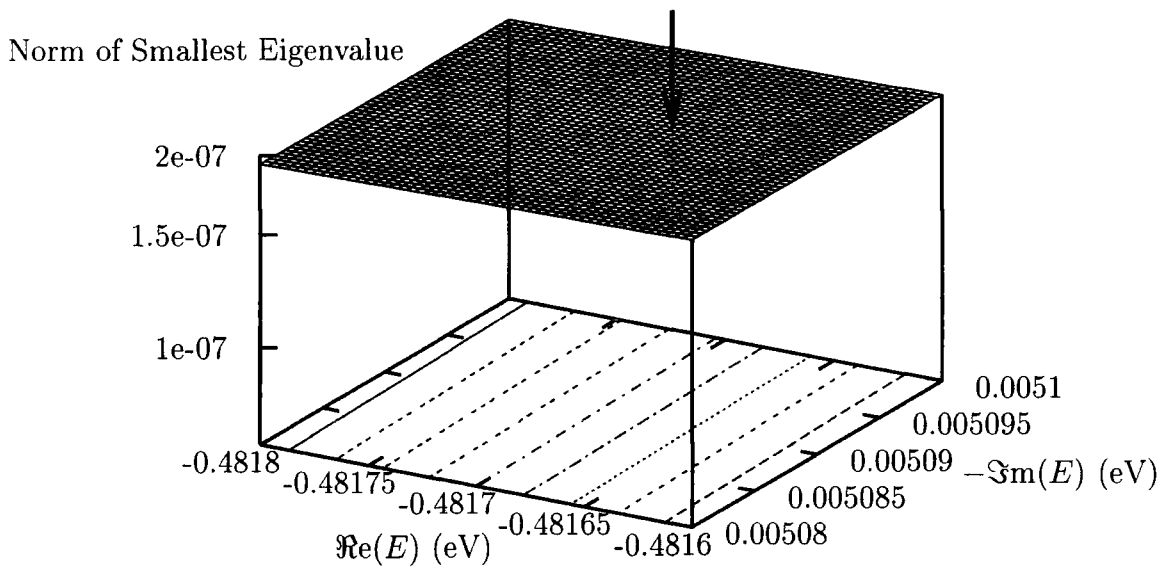

Figure 2.15: Quasi-energy surface at $I = 5 \times 10^{10}$ W/cm^2 with 6 angular momenta and 9 Floquet blocks. The bold arrow marks the actual position of the quasi-energy.

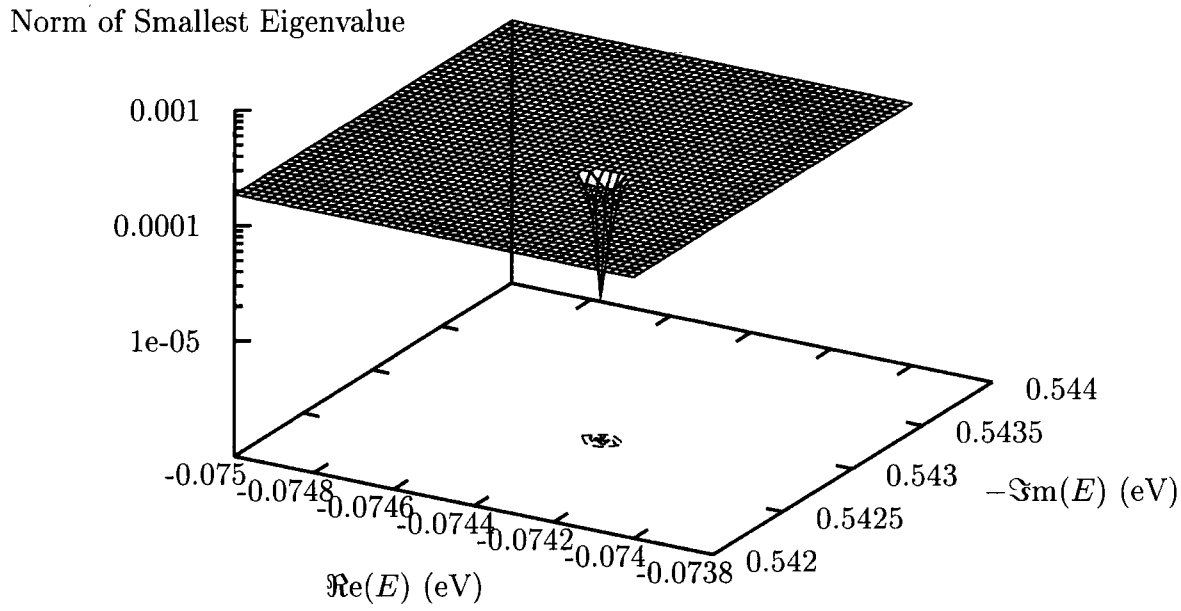

Figure 2.16: Quasi-energy surface at $I = 5 \times 10^{12}$ W/cm^2 with $\lambda = 800$ nm and with 7 angular momenta and 13 Floquet blocks.

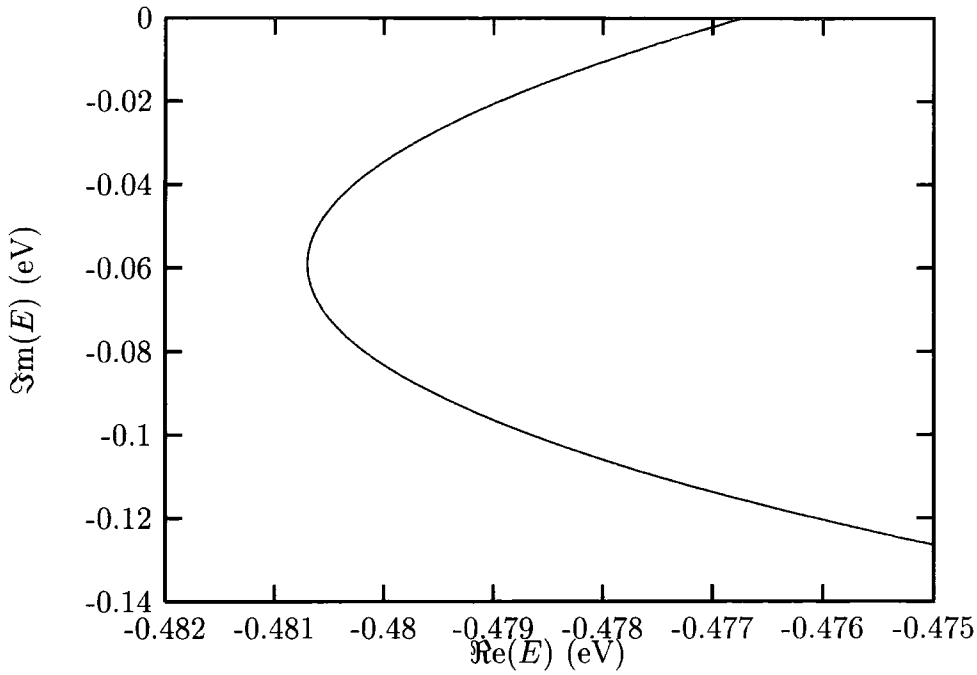

Figure 2.17: Quasi-energy of the 3D square-well at $\lambda = 600$ nm. The intensity of the linearly polarised radiation ranges from zero up to 3.5×10^{12} W/cm^2.

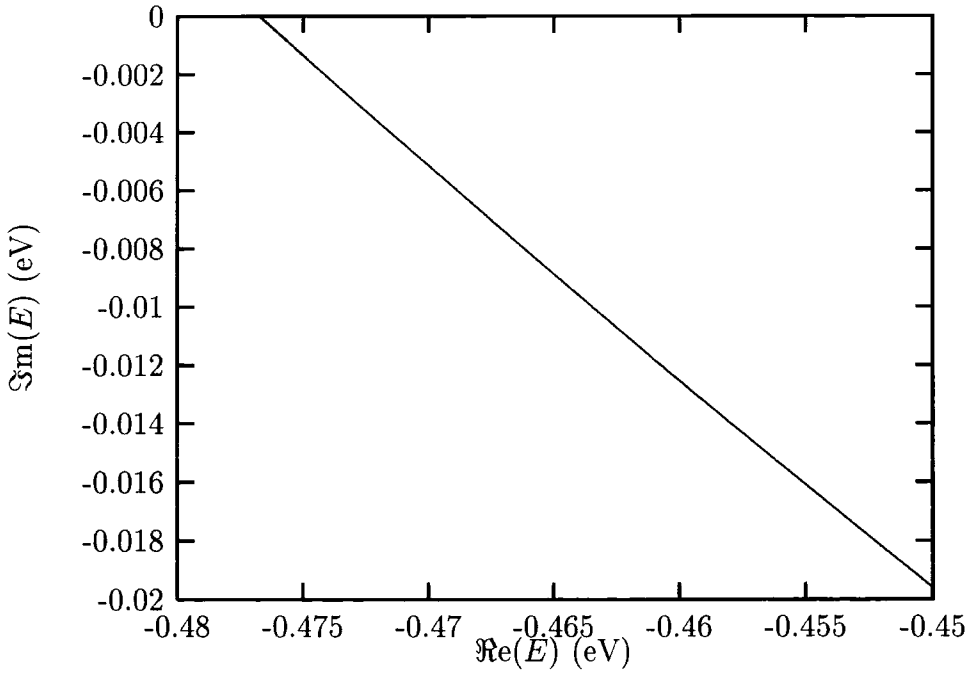

Figure 2.18: Quasi-energy of the 3D square-well at $\lambda = 256$ nm. The intensity of the linearly polarised radiation ranges from zero up to 1.9×10^{13} W/cm^2.

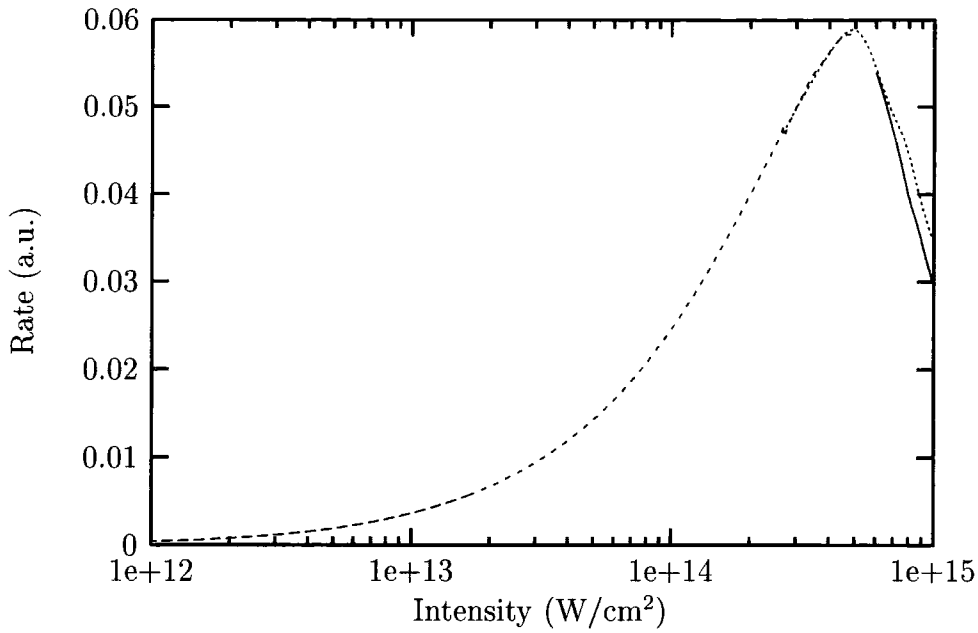

Figure 2.19: Rate of photodetatchment from the 3D square-well at $\lambda = 256$ nm. Parameters are: (- - - -) 5 angular momenta and 11 Floquet blocks; (- - - - - -) 6 angular momenta and 15 Floquet blocks; (·····) 7 angular momenta and 17 Floquet blocks; (———) 9 angular momenta and 17 Floquet blocks.

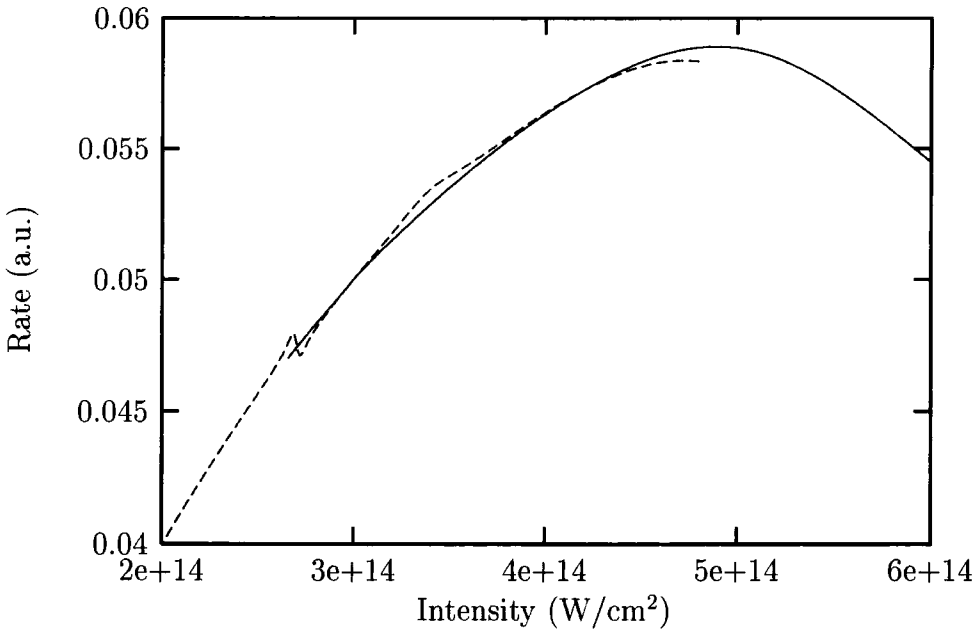

Figure 2.20: Rate of photodetatchment from the 3D square-well at $\lambda = 256$ nm. Parameters are: (- - - -) 6 angular momenta and 15 Floquet blocks; (———) 7 angular momenta and 17 Floquet blocks.

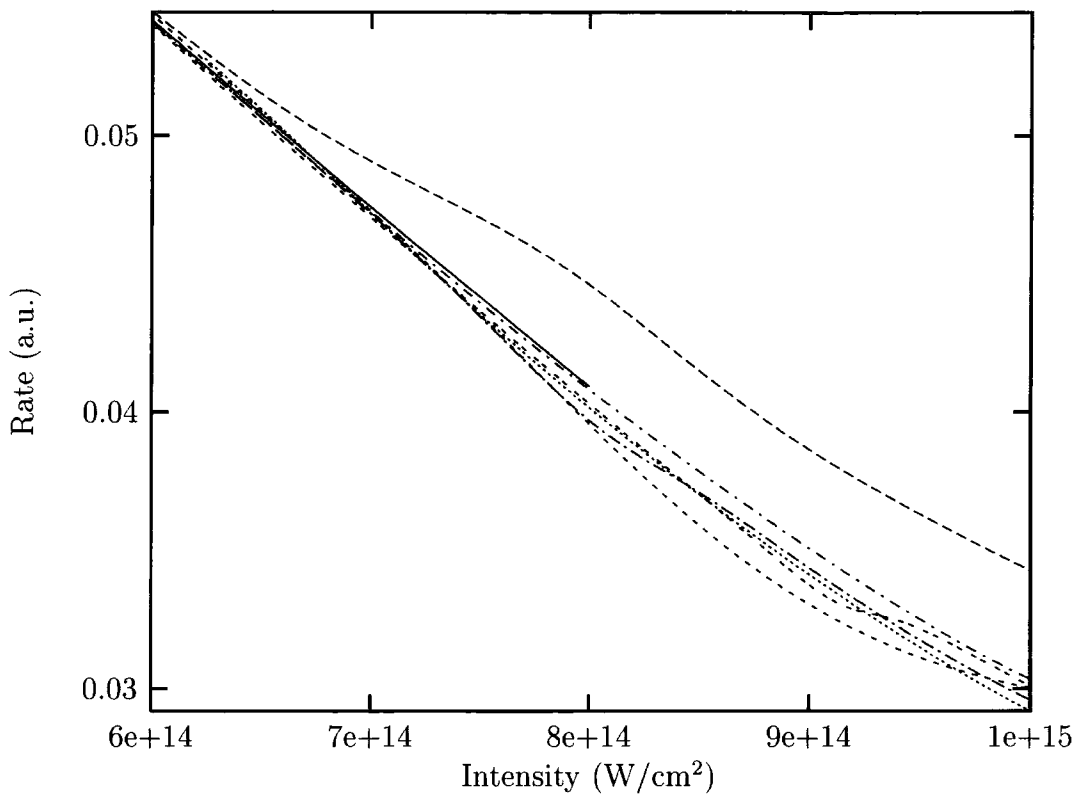

Figure 2.21: Rate of photodetatchment from the 3D square-well at $\lambda = 256$ nm. Parameters are: (– – – –) 7 angular momenta and 17 Floquet blocks; (- - - - - -) 8 angular momenta and 17 Floquet blocks; (· · · · · · · · ·) 8 angular momenta and 19 Floquet blocks; (— - — - —) 9 angular momenta and 17 Floquet blocks; (– – – – – –) 9 angular momenta and 19 Floquet blocks; (- - - - - - - -) 9 angular momenta and 21 Floquet blocks; (————) 10 angular momenta and 19 Floquet blocks.

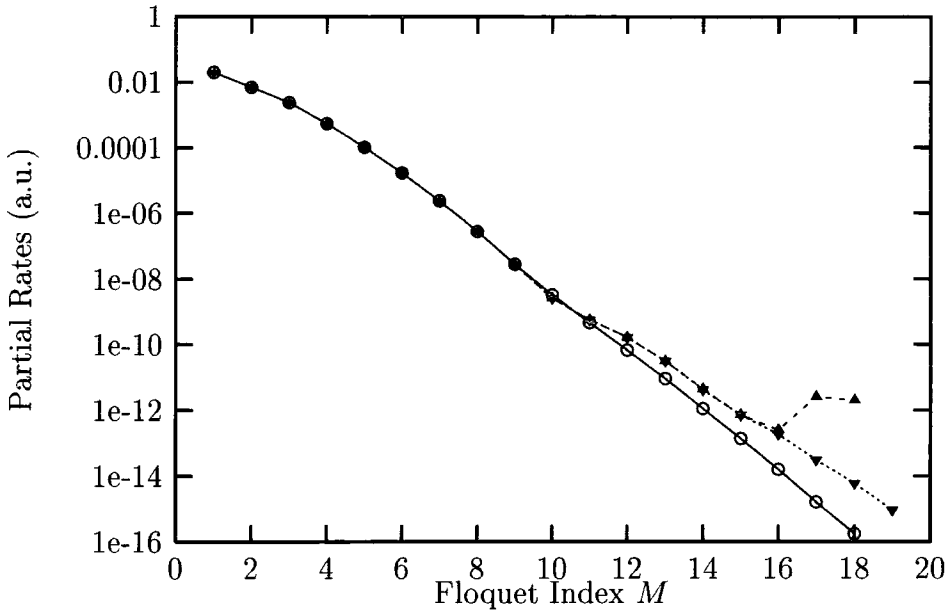

Figure 2.22: Partial rates (integrated over all angles) at $I = 1.3 \times 10^{14}$ W/cm^2. Parameters are: (—○—) 10 angular momenta and 37 Floquet blocks; (- - ▲ - - -) 11 angular momenta and 37 Floquet blocks; (· · · ▼ · · · ·) 11 angular momenta and 39 Floquet blocks.

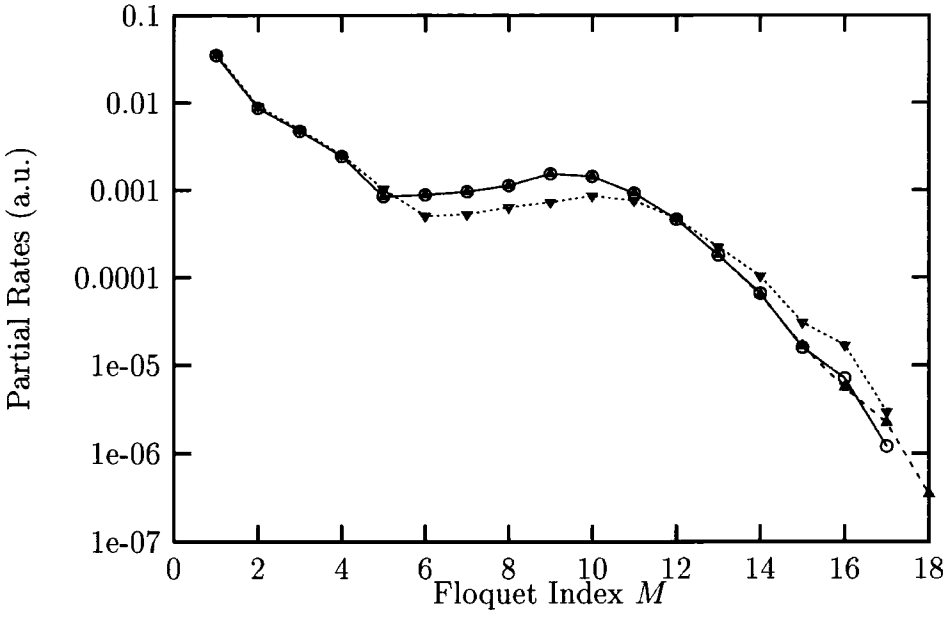

Figure 2.23: Partial rates (integrated over all angles) at $I = 4.9 \times 10^{14}$ W/cm^2. Parameters are: (—○—) 9 angular momenta and 35 Floquet blocks; (- - ▲ - - -) 9 angular momenta and 37 Floquet blocks; (· · · ▼ · · · ·) 10 angular momenta and 35 Floquet blocks.

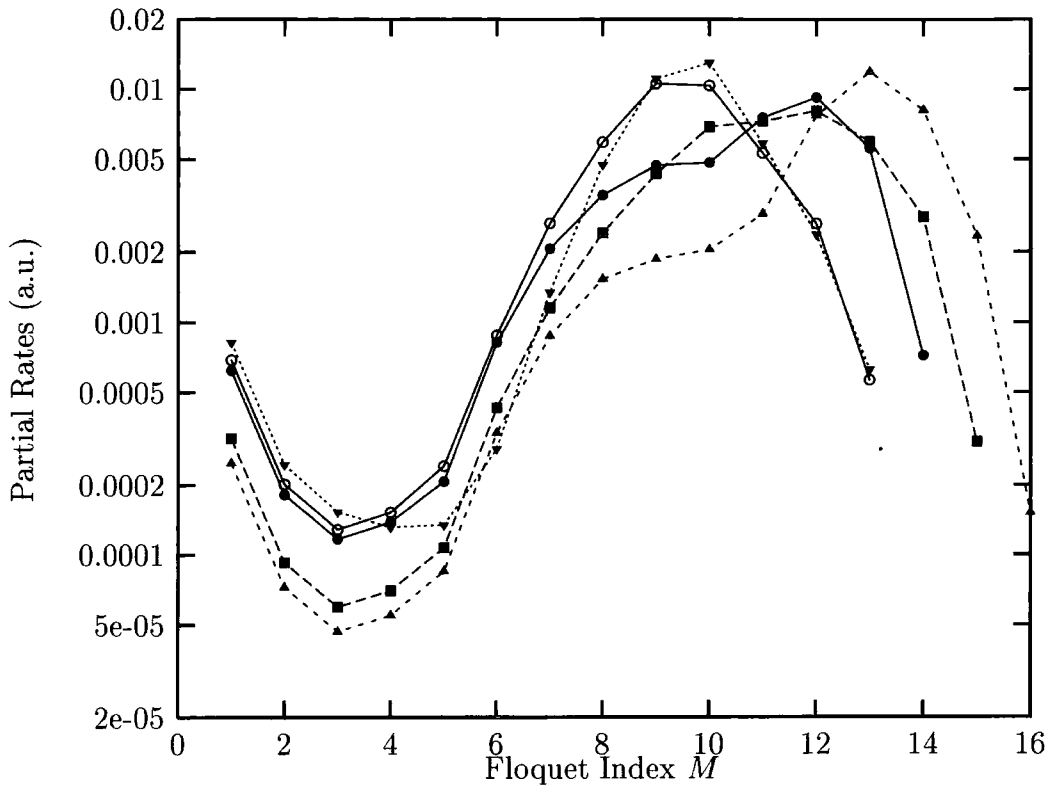

Figure 2.24: Partial rates (integrated over all angles) at $I = 8.0 \times 10^{14}$ W/cm^2. Parameters are: (—○—) 9 angular momenta and 27 Floquet blocks; (—●—) 9 angular momenta and 29 Floquet blocks; (- - ■ - -) 9 angular momenta and 31 Floquet blocks; (- - ▲ - - -) angular momenta and 31 Floquet blocks; (· · · ▼ · · · ·) 10 angular momenta and 27 Floquet blocks.

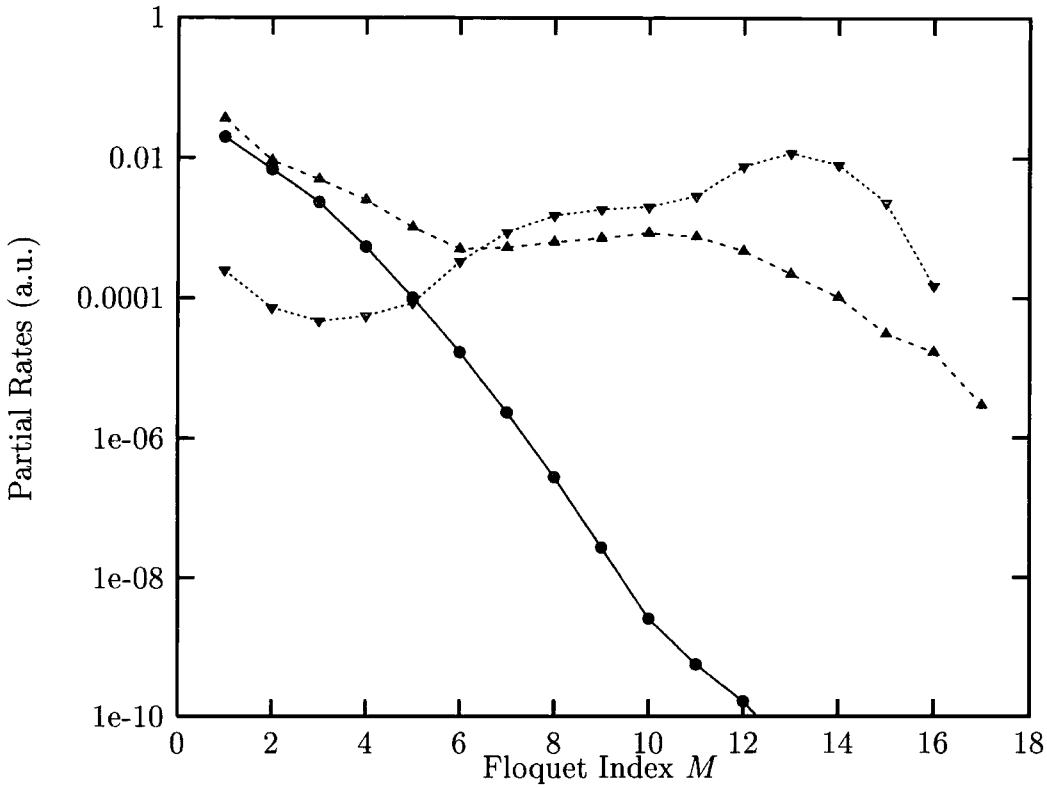

Figure 2.25: Partial rates at varying intensities: (—●—) 1.3×10^{14} W/cm^2; (- - ▲ - - -) 4.9×10^{14} W/cm^2; (· · · ▼ · · ·) 8.0×10^{14} W/cm^2.

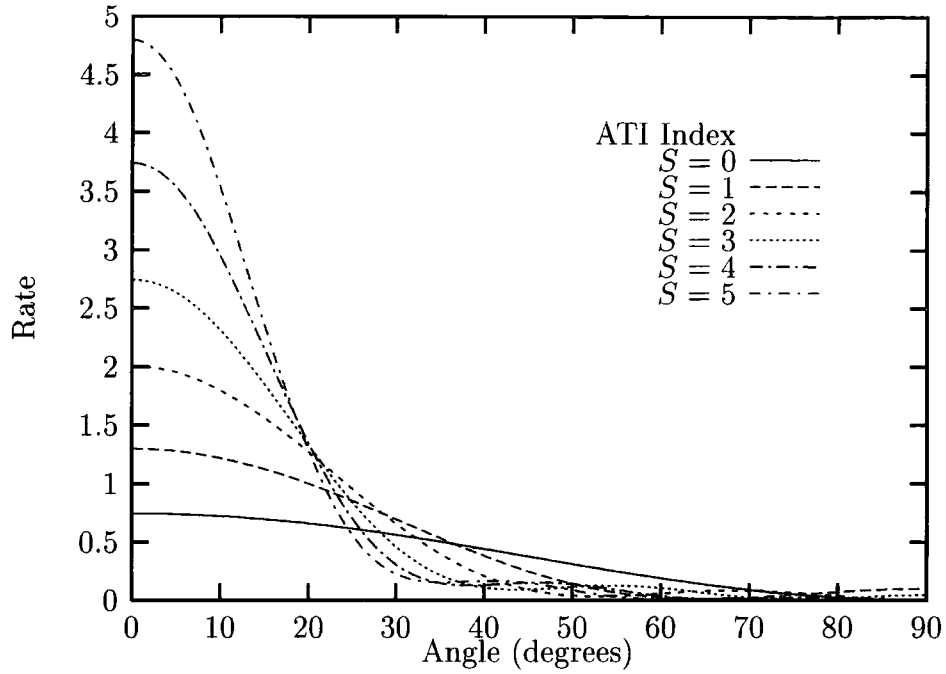

Figure 2.26: Angular distributions at $I = 1.3 \times 10^{14}$ W/cm^2 and $\lambda = 256$ nm. ATI channels $S = 0 \rightarrow 5$ only.

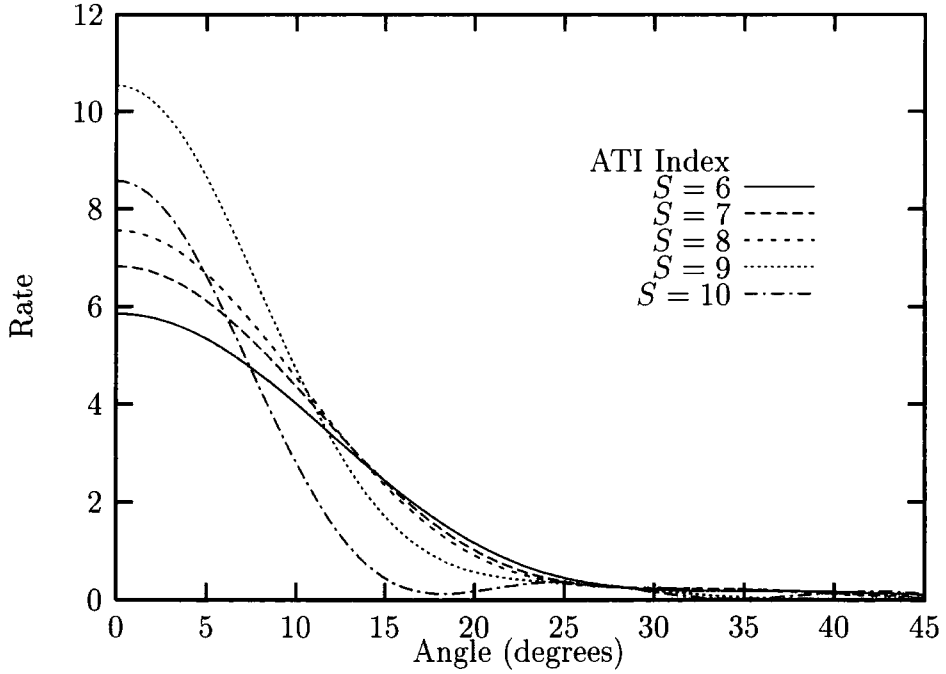

Figure 2.27: Angular distributions at $I = 1.3 \times 10^{14}$ W/cm^2 and $\lambda = 256$ nm. ATI channels $S = 6 \rightarrow 10$ only.

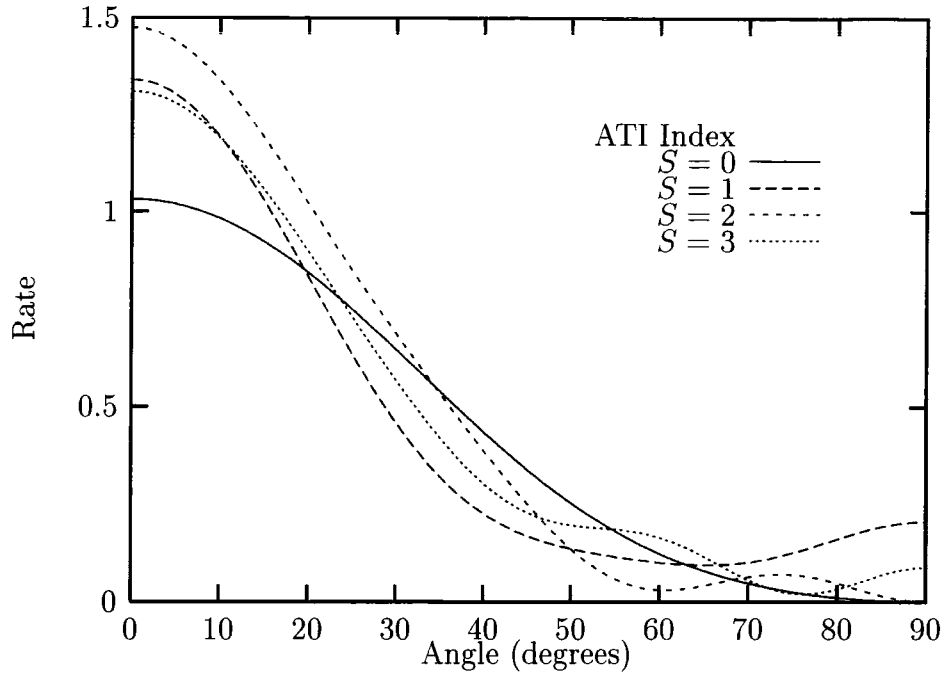

Figure 2.28: Angular distributions at $I = 4.9 \times 10^{14}$ W/cm^2 and $\lambda = 256$ nm. ATI channels $S = 0 \rightarrow 3$ only.

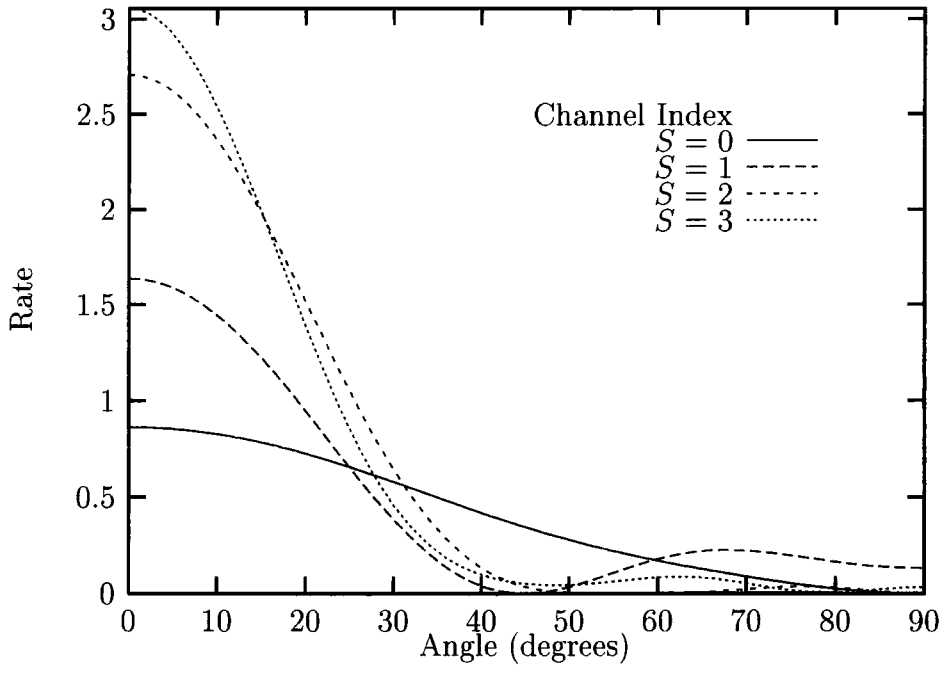

Figure 2.29: Angular distributions at $I = 8.0 \times 10^{14}$ W/cm^2 and $\lambda = 256$ nm. ATI channels $S = 0 \rightarrow 3$ only.

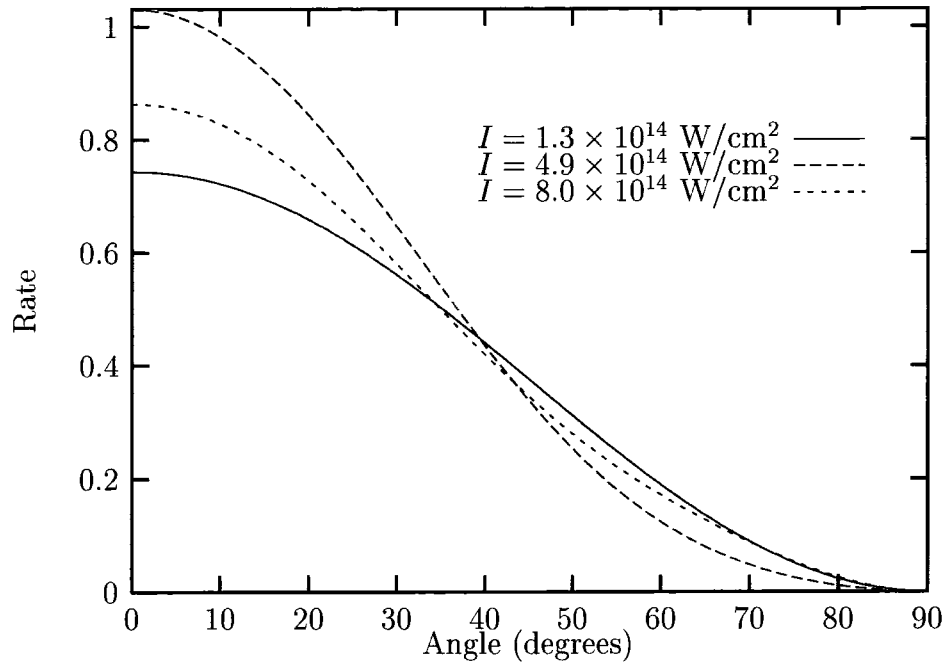

Figure 2.30: Angular distributions for channel $S = 0$ at varying intensities with $\lambda = 256$ nm.

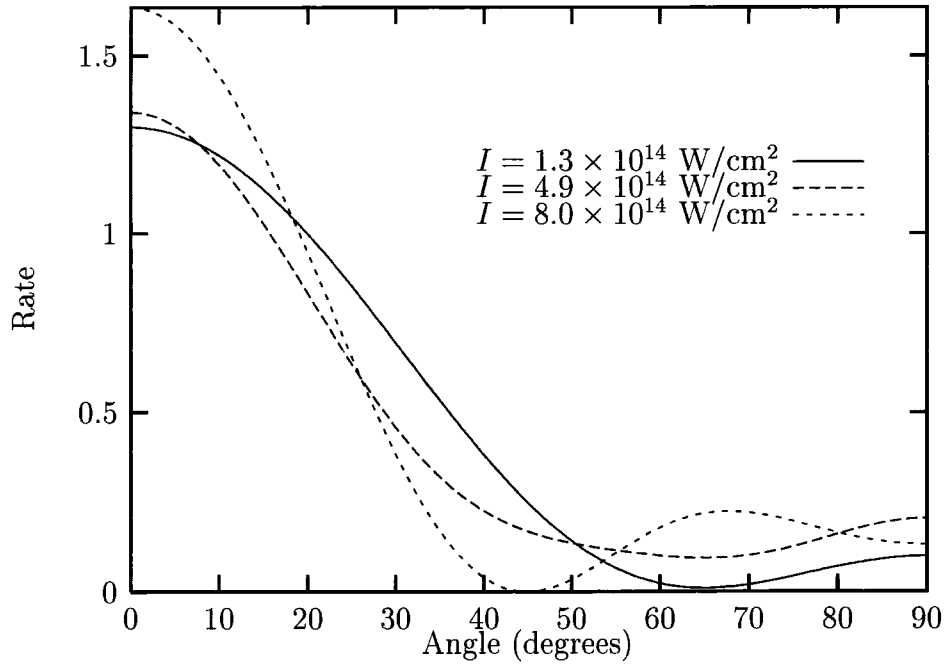

Figure 2.31: Angular distributions for channel $S = 1$ at varying intensities with $\lambda = 256$ nm.

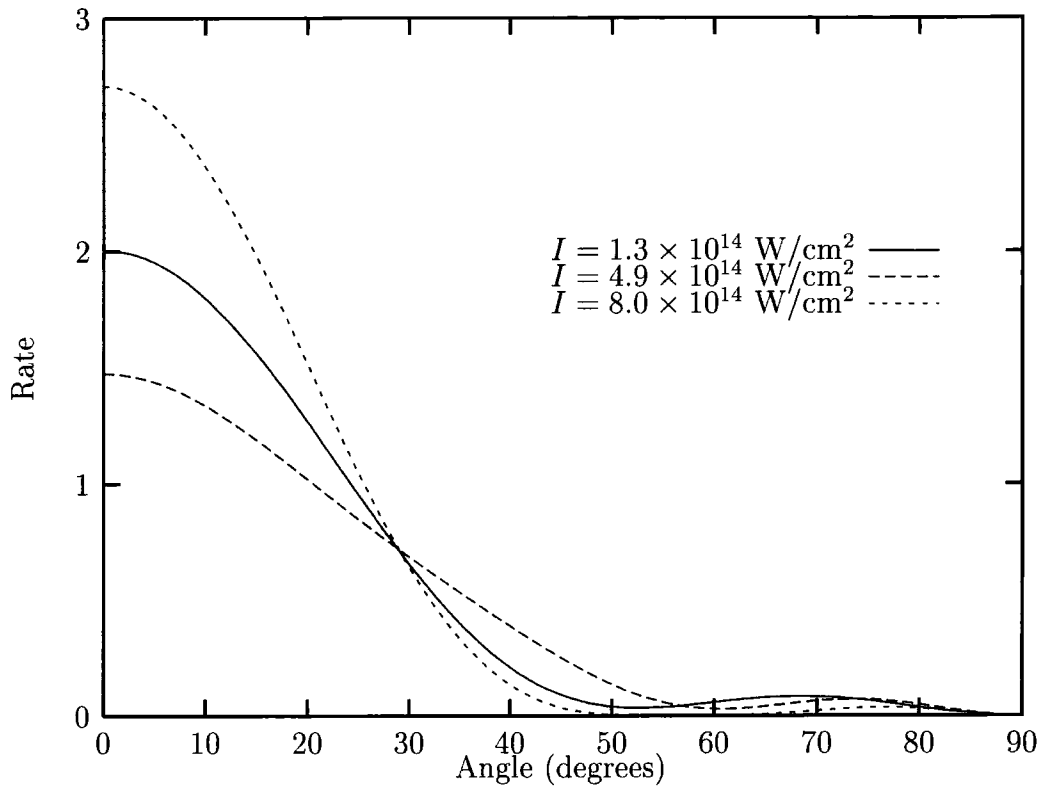

Figure 2.32: Angular distributions for channel $S = 2$ at varying intensities with $\lambda = 256$ nm.

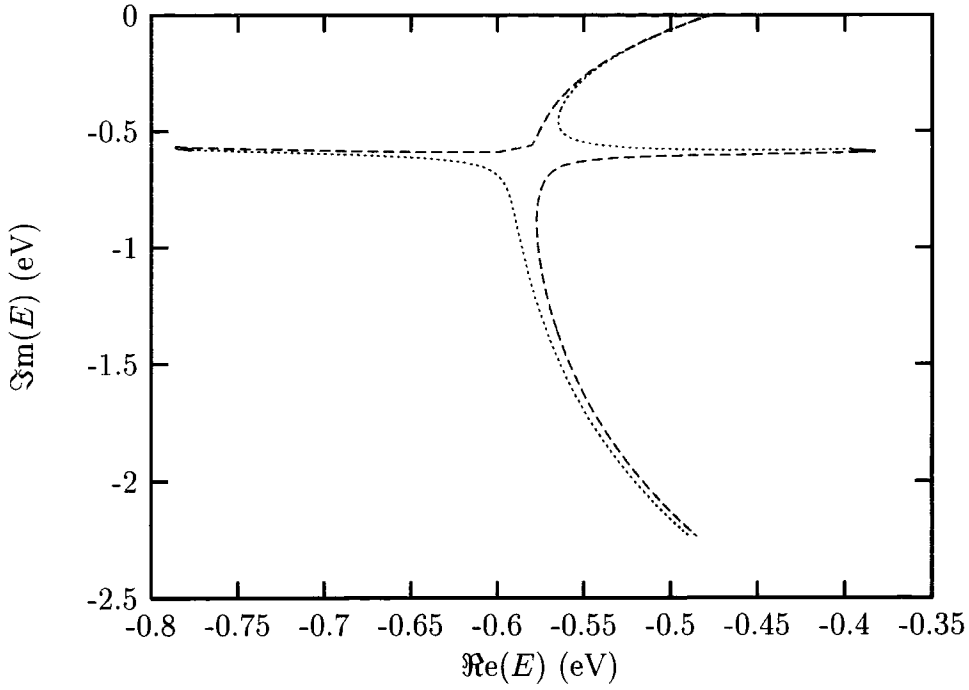

Figure 2.33: Quasi-energy trajectories encircling a degenerate point in the complex energy-plane. Parameters are: (- - - -) $\lambda = 748$ nm; (——) $I = 4.5 \times 10^{12}$ W/cm^2; (· · · · · · · · ·) $\lambda = 746$ nm.

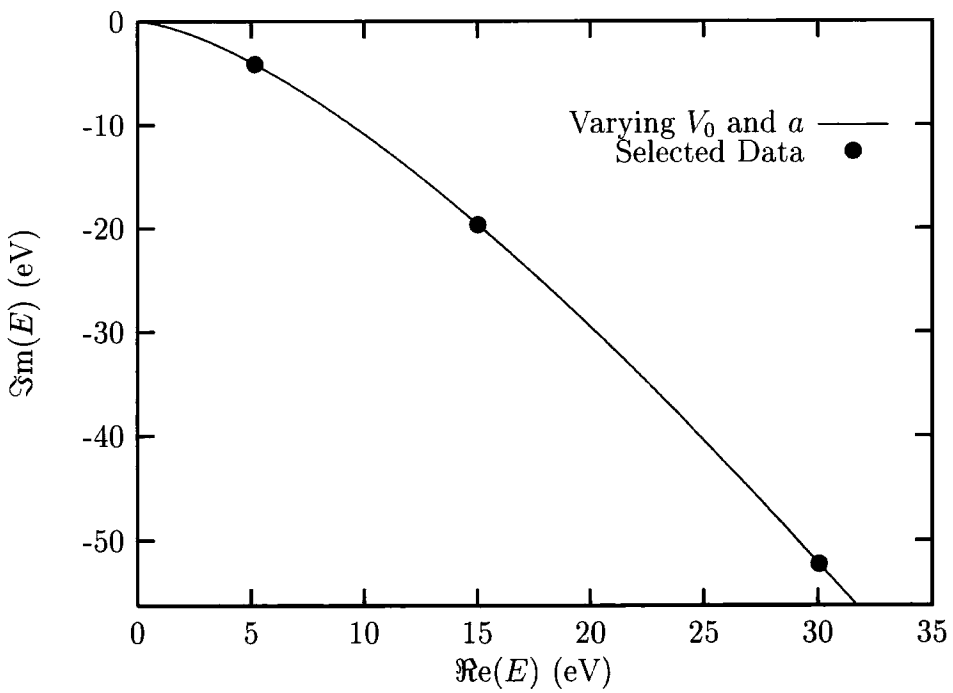

Figure 2.34: The set of allowed autoionising quasi-energies for a fixed bound-state energy of -15.73 eV while varying simultaneously the width and depth of the potential well.

Chapter 3

Asymptotic Momenta in Truncated Floquet Calculations

3.1 Introduction

Let us start by recalling the generic Floquet-Fourier expansion (in one spatial dimension) of section 1.3.2

$$\Psi(x,t) = \mathrm{e}^{-iEt} \sum_{N=-\infty}^{\infty} \mathrm{e}^{-iN\omega t}\, \psi_N(x) \tag{3.1}$$

where $\psi_N(x)$ are the time-independent harmonic components and the index N represents the total number of photons absorbed. In the velocity gauge, and provided that no further approximation is made, the harmonic components reduce to a superposition of ingoing or outgoing waves with wavenumbers $k_M = [2(E + M\omega)]^{1/2}$ at asymptotically large distance, with ω being the frequency of the incident photons. As described in section 2.3 one must in practice choose to truncate the series in equation (3.1) to a finite number of terms whose number is to be empirically determined. This truncation, however, results in intensity-dependent, M-dependent shifts in the asymptotic wavenumbers [34]. It has been assumed in most previous Floquet calculations (e.g. those described in chapter two and some R-Matrix-Floquet calculations, [17], [18] and [88]) that these shifts can be safely neglected provided enough harmonic components are retained in the Fourier series.

The validity of this assumption is questionable, and if it does hold one is

still left with the question of whether in practice these calculations could gain from allowing for the shifts in the wavenumbers. We have performed a representative series of computations for photo-detachment from the one-dimensional square well by a monochromatic field, both with and without taking the shifts into account. This case has the advantages of being sufficiently simple for rapid computations to be made and of being amenable to a (nearly entirely) analytic treatment. Other authors have recently considered the same question in the context of R-Matrix-Floquet theory and have found that one may incur considerable 'edge effects' by failing to allow for the truncation throughout the calculation [34].

3.2 The One-Dimensional Square-Well Model

Let us consider the one-dimensional square-well given by $V(x) = 0$ for $\mid x \mid > a$, $V(x) = V_0$ for $\mid x \mid \leq a$. In the velocity gauge the Schrödinger equation is

$$i\frac{\partial}{\partial t}\psi(x,t) = \left[-\frac{1}{2}\frac{\partial^2}{\partial x^2} + \frac{iA_0}{2c}\cos\omega t\,\frac{\partial}{\partial x} - V_0\right]\psi(x,t) \tag{3.2}$$

and by inserting the Floquet-Fourier ansatz (3.1) this time-dependent equation can be rewritten as an infinite system of coupled time-independent equations

$$\left[E + N\omega - \left(-\frac{1}{2}\frac{d^2}{dx^2} + V(x)\right)\right]\psi_N = V_+\,\psi_{N-1} + V_-\,\psi_{N+1} \tag{3.3}$$

where

$$V_+ = V_-^\dagger = -\frac{A_0}{2c}\,i\frac{d}{dx} \tag{3.4}$$

(c.f. equations (2.24) to (2.26)). Given that the potential $V(x)$ is constant (apart from at $x = \pm a$) equation (3.3) can be solved in terms of plane waves:

$$\psi_N(x) = \sum_M A_M\,u_{NM}\,\mathrm{e}^{-iq_M x} \qquad x < -a \tag{3.5}$$

$$\psi_N(x) = \sum_M B_M\,U_{NM}\,(\mathrm{e}^{-iQ_M x} + (-1)^N\mathrm{e}^{iQ_M x}) \qquad \mid x \mid < a \tag{3.6}$$

$$\psi_N(x) = \sum_M (-1)^N A_M \, u_{NM} \, \mathrm{e}^{iq_M x} \qquad x > a \tag{3.7}$$

Here the coefficients A_M and B_M are fixed by the condition that the ψ_N's must be continuous and have continuous derivatives at $x = \pm a$. Note that the form of the solution in the internal region has been chosen to have a definite parity. Namely, for even N we have $\psi_N(x) \sim 2\cos(Q_M x)$ and for odd N this becomes $\psi_N(x) \sim 2i\sin(Q_M x)$. The q_M's and Q_M's are the channel momenta in the external and internal regions respectively, and the u_{nm}'s and U_{nm}'s are functions of these momenta. These satisfy the quadratic eigenvalue problems

$$\left[E + N\omega - \frac{q_M^2}{2}\right] u_{NM} = -\frac{\alpha_0 \omega}{2} q_M \, (u_{N-1,M} + u_{N+1,M}) \tag{3.8}$$

$$\left[E + N\omega - \frac{Q_M^2}{2} - V_0\right] U_{NM} = -\frac{\alpha_0 \omega}{2} Q_M \, (U_{N-1,M} + U_{N+1,M}). \tag{3.9}$$

where $\alpha_0 = A_0/c\omega$ is the excursion amplitude of a free electron in the field. This representation offers good numerical efficiency because all of the 'eigenvalues' q_M and the corresponding 'eigenvectors' u_{NM} are obtained by solving this eigenvalue problem just once. (And similarly for the Q_M's and U_{NM}'s.) Observing that the index M has a constant value in each of the equations above we drop this index and rearrange to obtain

$$q^2 u_N - q\frac{A_0}{c}(u_{N+1} + u_{N-1}) - 2(E + N\omega)u_N = 0 \tag{3.10}$$

$$Q^2 U_N - Q\frac{A_0}{c}(U_{N+1} + U_{N-1}) - 2(E + N\omega - V_0)U_N = 0 \tag{3.11}$$

which are explicitly quadratic in the eigenvalues q and Q. Letting N run over its entire (truncated) range we then have matrix equations

$$(\boldsymbol{A}q^2 + \boldsymbol{B}q + \boldsymbol{C})\cdot\boldsymbol{u} = 0 \tag{3.12}$$

$$(\tilde{\boldsymbol{A}}Q^2 + \tilde{\boldsymbol{B}}Q + \tilde{\boldsymbol{C}})\cdot\boldsymbol{U} = 0 \tag{3.13}$$

where we identify

$$\boldsymbol{A} = \tilde{\boldsymbol{A}} = \boldsymbol{I} \tag{3.14}$$

$$\boldsymbol{B} = \tilde{\boldsymbol{B}} = -\frac{A_0}{c}\begin{pmatrix} 0 & 1 & 0 & \cdots & \cdots & 0 \\ 1 & 0 & 1 & & & \vdots \\ 0 & 1 & \ddots & \ddots & & \vdots \\ \vdots & & \ddots & \ddots & \ddots & 0 \\ \vdots & & & \ddots & \ddots & 1 \\ 0 & \cdots & \cdots & 0 & 1 & 0 \end{pmatrix} \tag{3.15}$$

$$\boldsymbol{C} = -2\begin{pmatrix} \ddots & & & \\ & E+(N-1)\omega & & 0 \\ & & E+N\omega & \\ & 0 & & E+(N+1)\omega \\ & & & & \ddots \end{pmatrix} \tag{3.16}$$

and

$$\tilde{\boldsymbol{C}} = -2\begin{pmatrix} \ddots & & & \\ & E+(N-1)\omega - V_0 & & 0 \\ & & E+N\omega - V_0 & \\ & 0 & & E+(N+1)\omega - V_0 \\ & & & & \ddots \end{pmatrix} \tag{3.17}$$

where $\boldsymbol{I}$ is the identity matrix.

A generalised eigenvalue problem in the form of a polynomial can always be solved by transforming it into a linear eigensystem. Specifically, a system of degree μ and size $n \times n$ reduces to a linear system of size $(\mu n) \times (\mu n)$. For a quadratic problem $(\boldsymbol{a}\lambda^2 + \boldsymbol{b}\lambda + \boldsymbol{c})\cdot\boldsymbol{x} = 0$ the expanded eigensystem is

$$\begin{pmatrix} 0 & \boldsymbol{I} \\ -\boldsymbol{a}^{-1}\cdot\boldsymbol{c} & -\boldsymbol{a}^{-1}\cdot\boldsymbol{b} \end{pmatrix}\begin{pmatrix} \boldsymbol{x} \\ \boldsymbol{y} \end{pmatrix} = \lambda\begin{pmatrix} \boldsymbol{x} \\ \boldsymbol{y} \end{pmatrix} \tag{3.18}$$

giving in our case

$$\begin{pmatrix} 0 & \boldsymbol{I} \\ -\boldsymbol{C} & -\boldsymbol{B} \end{pmatrix}\begin{pmatrix} \boldsymbol{u} \\ \boldsymbol{v} \end{pmatrix} = q\begin{pmatrix} \boldsymbol{u} \\ \boldsymbol{v} \end{pmatrix} \tag{3.19}$$

and

$$\begin{pmatrix} 0 & \boldsymbol{I} \\ -\tilde{\boldsymbol{C}} & -\tilde{\boldsymbol{B}} \end{pmatrix} \begin{pmatrix} \boldsymbol{U} \\ \boldsymbol{V} \end{pmatrix} = Q \begin{pmatrix} \boldsymbol{U} \\ \boldsymbol{V} \end{pmatrix} \tag{3.20}$$

where $\boldsymbol{v}$ and $\boldsymbol{V}$ are extensions of the eigenvectors $\boldsymbol{u}$ and $\boldsymbol{U}$ respectively. The quasi-energy E (together with the coefficients A_M and B_M) is fixed by matching the internal and external solutions at the boundary $x = \pm a$. When performing this matching one notes that the equality must hold for all values of x and t and that therefore the matching applies directly to each term $\{N, M\}$ in the expansions. In practice the resulting matching equations are solved by a trial and error method which iteratively homes in on the exact solution, provided that a sufficiently good initial guess is used (see section 2.3). Here the matrix of matching equations is:

$$\begin{pmatrix} & \vdots & & \vdots & \\ \cdots & U_{NM}\mathcal{L}_+(Q_M) & \cdots & -u_{NM}\mathrm{e}^{iq_M a} & \cdots \\ & \vdots & & \vdots & \\ \cdots & U_{NM}iQ_M\mathcal{L}_-(Q_M)) & \cdots & -u_{NM}iq_M\mathrm{e}^{iq_M a} & \cdots \\ & \vdots & & \vdots & \end{pmatrix} \begin{pmatrix} \vdots \\ A_M \\ \vdots \\ B_M \\ \vdots \end{pmatrix} = 0 \tag{3.21}$$

where the lower half of this matrix represents the matching of derivatives. The combinations $\mathcal{L}_\pm(Q_M)$ are given by

$$\mathcal{L}_\pm(Q_M) = \mathrm{e}^{-iQ_M a} \pm (-1)^N \mathrm{e}^{iQ_M a} \tag{3.22}$$

as in equation (3.6). The procedure at each iterative step is (i) to guess a quasi-energy E, (ii) to compute the channel momenta q_M and Q_M and the functions u_{NM} and U_{NM}, (iii) to construct the 'matching matrix' using these quantities, and finally (iv) to compute the smallest eigenvalue of this matrix; (the eigenvectors are not required). When this smallest eigenvalue is sufficiently small (i.e. several orders of magnitude smaller than its background value) then we can say that the determinant of the matching matrix is approximately zero and thus equation (3.21) must have non-trivial solutions. The parameter E for which this is the case is then the true quasi-energy.

Without truncation in the photon numbers N and M the 'generalised' channel momenta q_M and Q_M reduce to the physical momenta k_M and K_M, *viz.*

$$E = -\frac{1}{2}k_M^2 - M\omega\,, \qquad E - V_0 = -\frac{1}{2}K_M^2 - M\omega \tag{3.23}$$

and the equations for u_{NM} and U_{NM} become

$$(N-M)u_{NM} = -\frac{\alpha_0 q_M}{2}(u_{N-1,M} + u_{N+1,M}) \tag{3.24}$$

$$(N-M)U_{NM} = -\frac{\alpha_0 Q_M}{2}(U_{N-1,M} + U_{N+1,M}) \tag{3.25}$$

Thus the u_{NM}'s and U_{NM}'s are Bessel functions of index $(N-M)$,

$$u_{NM} = J_{N-M}(-\alpha_0 q_M), \qquad U_{NM} = J_{N-M}(-\alpha_0 Q_M) \tag{3.26}$$

That is, the Floquet wavefunction is a superposition of Volkov waves. If on the other hand the range of N and M is truncated, equations (3.8) and (3.9) must be solved numerically and the q_M's, Q_M's, u_{NM}'s and U_{NM}'s, may differ greatly from those given by equations (3.23) and (3.26), especially for those indices which lie close to the truncation value. The approach followed in most Floquet calculations (e.g. [116], [119] and [135]) is to solve the coupled-channel system of equations for the quasi-energy whilst ignoring the modifications to the channel momenta and corresponding eigenfunctions induced by the truncation. A rigorous approach, however, requires that one allows for the shift in the channel momenta by simultaneously solving (in for example the case of a square-well) the matching equations *and* equations (3.8) and (3.9) above. (See also refs. [34] and [36].)

3.3 A Resonant Process

For our study we have chosen to examine a resonant process (at moderate values of both frequency and intensity) and our results here corroborate those of other authors [49] who have studied the two limiting cases of short wavelength with very high intensity and long wavelength with relatively high

intensity using the same model potential well. Two main issues were addressed: Do both methods converge (with respect to the number of Floquet blocks) to the same results, and if so, which converges the faster? (The two methods referred to here are the calculations with and without making explicit allowance for truncation in the harmonic expansion.) To answer these questions we have compared the quasi-energies, channel-momenta and partial rates of photo-detachment obtained by the two methods. We have consistently found that the two methods do indeed converge to the same values, but that the number of above-threshold photons required for the quasi-energies to converge is about twice as large using the analytic momenta as it is with the numerically-evaluated shifted momenta. This difference in performance is less marked in calculations of the partial rates of photo-detachment but there is still a time advantage conferred by using the shifted momenta. The calculations themselves are described in detail below.

3.3.1 Introduction

A multiphoton resonance occurs between a pair of discrete energy levels separated by an integral multiple of the photon-energy, ω. A resonance is an interesting case to study because the total and partial rates of ionisation may be most sensitive here to changes in the channel momenta, and because it need not occur at a prohibitively high intensity. A low-order resonance is also to be preferred since one may then study several orders of above-threshold-ionisation without reaching prohibitively high photon numbers. We choose a one-dimensional square-well of depth $V_0 = -12$ eV and with parameter $\gamma \equiv (-2V_0a^2)^{1/2} = 3\pi/4$, giving us exactly two field-free bound states at energies $E_0 = -9.4323$ eV and $E_1 = -2.7438$ eV. At zero field this energy gap corresponds to a three-photon resonance at a wavelength of $\lambda = 556$ nm. What we require though is a three-photon resonance at a physically interesting intensity, say $I > 10^{12}$ W/cm^2. Therefore our calculation takes $\lambda = 550$ nm, leading to a broad resonant enhancement in the rate of ionisation from the ground state at an intensity $I \approx 4.8 \times 10^{13}$ W/cm^2. At this wavelength

the minimum number of photons required for ionisation to occur is $N_0 = 5$. In fact there are two problems to overcome in choosing the dimensions of the two-level well. Firstly, if the excited state lies near the continuum then its width is so great as to make the resonance too broad to be discerned, and secondly, if the excited state is chosen to lie deeper in the well then the ground state must also lie correspondingly deeper and its width becomes effectively zero relative to the real part of the quasi-energy. This latter case is problematic because if the real and imaginary components of the quasi-energy differ by a factor greater than the machine accuracy, i.e. roughly fourteen orders of magnitude, then it becomes impossible to compute. Thus the parameters which we have selected represent a compromise between these two extremes.

3.3.2 Total Rates of Multiphoton Detachment

Let us first examine the behaviour of the ground state with increasing intensity, using only the analytic momenta. The (converged) total rate of photo-detachment is marked with a solid curve in figures 3.1 and 3.2. We find that the photo-detachment rate increases steadily with intensity up to $I \approx 4 \times 10^{13}$ W/cm^2, holds roughly constant between there and $I \approx 5 \times 10^{13}$ W/cm^2, and thereafter increases very rapidly. The shoulder occurring at around $I = 4.5 \times 10^{13}$ W/cm^2 is of course the broad resonant enhancement in the rate that we have aimed for. The real part of the quasi-energy meanwhile shifts downwards, linearly in the intensity, crossing the five-photon cut at $I = 5.7 \times 10^{13}$ W/cm^2. We identify the very sharp increase in the rate at $I \approx 6 \times 10^{13}$ W/cm^2 with the transition from the multiphoton regime to the tunneling regime. The demarcation between these two regimes can be quantified in terms of the Keldysh parameter, γ_K [74], given by

$$\gamma_K \equiv \frac{\omega}{\mathcal{E}}(2E_I)^{1/2} \tag{3.27}$$

where E_I is the field-free binding energy of the atom and $\mathcal{E}$ is the peak field-strength of the electric field. In fact this is none other than the ratio of the characteristic time taken by the electron to tunnel through the barrier [90] to

the period of one cycle of the field $\boldsymbol{\mathcal{E}}(t)$. The barrier is created from the sum of the nuclear attraction and the instantaneous, classical electric field of the laser. This changes direction twice during each cycle and each time it reaches its maximum value the Coulomb barrier is suppressed sufficiently that some electrons may tunnel out, to be driven in the instantaneous direction of the field. This type of behaviour is characterised by $\gamma_K \ll 1$, whereas with $\gamma_K \gg 1$ the field has only a negligible effect on the Coulomb barrier and one is firmly in the multiphoton regime.

Given that the field-strength is related to the intensity via $\mathcal{E}^2 = 8\pi I/c$ and taking the values $\omega = 0.08284$ a.u. and $E_I = 0.3466$ a.u. one obtains for γ_K the relation

$$\gamma_K = \frac{5.38}{\sqrt{I(\mathrm{TW})}} \tag{3.28}$$

Thus at $I = 1 \times 10^{13}$ W/cm^2 we have the value $\gamma_K = 1.70$ whereas at $I = 6 \times 10^{13}$ W/cm^2 this becomes $\gamma_K = 0.69$, supporting our suggestion that tunneling becomes the dominant ionisation process as one reaches the latter intensity. There will be a critical, still higher field-strength or intensity at which the Coulomb barrier is - during part of the laser cycle - suppressed to such an extent that the electrons may simply flow out over the top of the barrier. (We use the term 'Coulomb barrier' loosely here to mean the analogous potential barrier in our model well. This is, of course, not a $1/r$ potential.) This is known as over-the-barrier (OTB) ionisation and will occur at field-strengths beyond the critical field-strength

$$\mathcal{E}_c = \frac{1}{a} \mid \Re\mathrm{e}(E) \mid \tag{3.29}$$

corresponding to the critical intensity

$$I_c = \frac{c}{8\pi}\mathcal{E}_c^2 \tag{3.30}$$

where a is the half-width of the square-well. (See also the discussion in section 2.4.3.) Now for non-zero intensities we have $\Re\mathrm{e}(E) \approx -10$ eV, leading to a critical intensity $I_c \approx 7 \times 10^{14}$ W/cm^2. This intensity is far beyond those which we are considering in the context of resonant ionisation and so OTB

ionisation can be assumed to play no role in our calculations. The calculations of reference [49] do reach this regime (at a very much longer wavelength) but the point is made that at such high intensities the total rate of ionisation is of the same order as the photon energy and that the electron therefore detaches from the well typically within one cycle of the field. Under these conditions the concept of a cycle-averaged rate becomes meaningless and the Floquet method is no longer applicable.

Figure 3.1 illustrates the convergence of the photo-detachment rate (calculated using the standard, analytic momenta) towards a steady result as the number of harmonic components retained in the truncated Floquet system is increased. For simplicity these calculations take a number of Floquet blocks which is symmetric about the index $N = 0$, i.e. we have symmetric ranges for N and M. Thus the number of harmonic blocks in a given calculation is $N_b = 2(N_0 + S) + 1$ where S is the number of above-threshold photons. Figure 3.1 shows the variation in the imaginary part of the intensity-dependent quasi-energy as the number of above-threshold photons is increased from zero to eleven; i.e. the smallest calculation presented in this figure includes 11 Floquet blocks whereas the largest includes 33 Floquet blocks. The rate of photo-detachment is found to be wildly wrong in the smaller calculations and only reaches convergence with eight or nine above-threshold photons. Given that $N_0 = 5$ we have that if $S = 9$ then $N_b = 29$ which - compared with a 'typical' Floquet calculation - is very large indeed for such a moderate intensity, but this is characteristic of one-dimensional models. Figure 3.2 displays the equivalent results in a calculation utilising the 'shifted' momenta and there are two clear conclusions one can draw. Firstly we see that with sufficiently many Floquet-blocks this calculation yields a result identical to that with the analytic momenta. Secondly, the number of above-threshold photons, S, required for convergence is only four compared to the eight or nine previously. So, we confirm what many have always assumed: namely that the analytic momenta give accurate results provided one includes sufficiently many channels. This caveat is important because at high intensities, as the number of channels to be included becomes very large (i.e. $N_b > 40$), the min-

imum in the quasi-energy surface by which one locates the true quasi-energy becomes indiscernible relative to the background, and the method fails. We find that using the shifted momenta facilitates a significant decrease in CPU time and, for those cases in which the standard calculation is too big to solve, is the only method of determining the quasi-energy.

3.3.3 Asymptotic Momenta

Figure 3.3 shows a few of the channel-momenta, both shifted and unshifted, for quasi-energies which are in all cases converged with respect to the number of channels ($N_b = 27$). In other words, at all intensities shown in this figure the value of E taken in equations (3.8) and (3.9) is the self-consistent quasi-energy solution. At zero-field all of the momenta in these open channels lie on the positive real axis and as the intensity increases up to a maximum of around 6×10^{13} W/cm^2 the momenta move downward into the fourth quadrant of the complex k-plane. For the inner channels, i.e. $\mid N \mid < N_0$, the agreement between the shifted and unshifted momenta is good, even to high intensities, but for the other channels, $\mid N \mid > N_0$, the momenta diverge to an increasing extent as the intensity increases. In the channels $\mid N \mid \gg N_0$ the momenta are very different even at low intensities. Note that the highest above-threshold channel included in this calculation is $N = 13$ (i.e. $S = 8$) and that the momenta from these outermost channels are not displayed in figure 3.3. At zero field-strength all of the momenta in the closed channels lie on the positive, purely imaginary values. When plotted in the complex k-plane, the momenta in some of these closed channels display a curious behaviour. Namely, a pair of the momenta will move along the positive imaginary axis in opposite directions and (at some critical intensity) undergoing an 'avoided crossing' after which they each branch out away from the imaginary axis with equal imaginary parts and equal but opposite real parts [49] [27]. The intensity at which this near-collision occurs is different for each pair of momenta and may be very small (e.g. less than 10^{13} W/cm^2 at this wavelength of 550 nm). When the square-moduli of the channel-

Table 3.1: A comparison of internal momenta in selected channels at an intensity of 5×10^{13} W/cm^2 firstly ignoring and secondly allowing for truncation of the system. Both sets of momenta are in a.u..

Floquet index	Analytic momentum	Shifted momentum	% Difference
0	(.26748, -.91506E-04)	(.26748, -.91825E-04)	(.00, .35)
+1	(.48707, -.50253E-04)	(.48707, -.50428E-04)	(.00, .35)
+2	(.63476, -.38560E-04)	(.63476, -.38694E-04)	(.00, .35)
+3	(.75406, -.32459E-04)	(.75406, -.32573E-04)	(.00, .35)
+4	(.85691, -.28564E-04)	(.85691, -.28663E-04)	(.00, .35)
+5	(.94867, -.25801E-04)	(.94871, -.25904E-04)	(.00, .40)
+6	(1.0323, -.23710E-04)	(1.0331, -.23967E-04)	(.07, 1.1)
+7	(1.1097, -.22057E-04)	(1.1156, -.22919E-04)	(.53, 3.9)
+8	(1.1820, -.20708E-04)	(1.2045, -.22382E-04)	(1.9, 8.1)
+9	(1.2501, -.19580E-04)	(1.3044, -.21712E-04)	(4.3, 10.9)
+10	(1.3147, -.18617E-04)	(1.4160, -.20764E-04)	(7.7, 11.5)
+11	(1.3763, -.17785E-04)	(1.5401, -.19617E-04)	(11.9, 10.3)
+12	(1.4352, -.17054E-04)	(1.6803, -.18332E-04)	(17.1, 7.5)
+13	(1.4918, -.16407E-04)	(1.8490, -.16891E-04)	(23.9, 2.9)

momenta are plotted (as in reference [27]) these pairs of momenta seem to coalesce into a single curve as the intensity increases due to their possessing the same norm. However this reduction in the total number of independent momenta does not appear to have a detrimental effect on the accuracy of the computation.

Let us also consider just one single representative intensity, say, $I = 2 \times 10^{13}$ W/cm^2 with $N_b = 27$. Once again, with this many channels both methods give identical quasi-energies but, as shown in figure 3.4, the momenta in the outer channels are quite different. In this figure each channel-momentum is marked with a symbol and the outermost channels are represented by those lying furthest to the right. A comparison at higher intensity may be made in tabular form. Let us choose $I = 5 \times 10^{13}$ W/cm^2 with $N_b = 27$. For selected channels the 'internal' momenta are displayed in table 3.1 and the 'external' momenta in table 3.2. All momenta are expressed in atomic units. In fact, for the shifted momenta at some arbitrary intensity there is no obvious connection between each momentum and a Floquet number n

Table 3.2: A comparison of external momenta in selected channels at an intensity of 5×10^{13} W/cm^2 firstly ignoring and secondly allowing for truncation of the system. Both sets of momenta are in a.u..

Floquet index	Analytic momentum	Shifted momentum	% Difference
0	(-.27189E-04, .90024)	(-.27283E-04, .90024)	(.35, .00)
+1	(-.30483E-04, .80296)	(-.30589E-04, .80294)	(.35, .00)
+2	(-.35363E-04, .69214)	(-.35486E-04, .69214)	(.35, .00)
+3	(-.43723E-04, .55980)	(-.43876E-04, .55980)	(.35, .00)
+4	(-.63690E-04, .38431)	(-.63912E-04, .38437)	(.35, .00)
+5	(.13415, -.18246E-03)	(.13415, -.18310E-03)	(.00, .35)
+6	(.42858, -.57110E-04)	(.42858, -.57309E-04)	(.00, .35)
+7	(.59107, -.41410E-04)	(.59109, -.41567E-04)	(.00, .38)
+8	(.71767, -.34105E-04)	(.71878, -.34642E-04)	(.15, 1.6)
+9	(.82507, -.29666E-04)	(.83796, -.31946E-04)	(1.6, 7.7)
+10	(.92001, -.26604E-04)	(.97150, -.30353E-04)	(5.6, 14.1)
+11	(1.0060, -.24329E-04)	(1.1255, -.27934E-04)	(11.9, 14.8)
+12	(1.0853, -.22553E-04)	(1.3002, -.25013E-04)	(19.8, 10.9)
+13	(1.1591, -.21117E-04)	(1.5064, -.21919E-04)	(30.0, 3.8)

but each momentum is linked adiabatically to a field-free momentum which will coincide with one of the analytic momenta and so we could label the high-intensity momenta in this sense. However, the physical interpretation of the q_M's and Q_M's as channel-momenta has no computational significance and provided that each eigenfunction f_{NM} or F_{NM} is linked with the correct momentum we can order them in any way we please. This corresponds simply to transposing rows in the matrix of matching equations, leaving the eigenvalues of the matching matrix unchanged. We find that, in accordance with the results presented in figure 3.3, the differences between the shifted and unshifted momenta are negligible in the channels $\mid N \mid < N_0$ and that they diverge as one approaches the truncation value of N. The maximal difference between the two cases is of the order of 30% for both the internal and external momenta.

M Dörr and co-workers [34] obtain very similar results for the channel momenta in atomic Hydrogen in a linearly polarised monochromatic laser field. Namely, the analytic momenta are a very good approximation to the shifted

momenta for the truncated system in the channels whose photon number lies in the middle of the truncated range, whereas for the channels at either extremity the error reaches approximately 30%, in close agreement with our own results. These comparative calculations form part of the on-going development of the new R-Matrix-Floquet code. By performing a perturbative analysis of the shifted momenta in the truncated system (for suitably weak fields) M Dörr *et al* demonstrate that, within this perturbative regime, only in the two outermost Floquet blocks is there any shift away from the analytic formulae and that this shift is of the order of $\mathcal{E}_0^2$.

3.3.4 Partial Rates of Multiphoton Detachment

A comparison involving the partial rates of photo-detachment can also be drawn between the two calculations. For the one-dimensional square-well it can be shown that these partial rates, Γ_M, are given by

$$\Gamma_M \propto v_M \mid A_M \mid^2 \tag{3.31}$$

where v_M is the cycle-averaged velocity of the ejected electron as described in section 2.4.3 and A_M is the 'external' coefficient from equations (3.5) and (3.7) [49]. This vector of coefficients A_M is the eigenvector of the matching matrix corresponding to the minimised smallest eigenvalue, typically of the order of 10^{-12}. However for an eigenvalue as small as this the matrix is, by definition, near singular and so numerical difficulties arise when computing the eigenvectors. We can circumvent this problem by shifting the eigenvector by an arbitrary constant, i.e. if the eigenvalue problem is of the form

$$\boldsymbol{M} \cdot \boldsymbol{x} = \lambda \boldsymbol{x} \tag{3.32}$$

one can write

$$(\boldsymbol{M} + \mu \boldsymbol{I}) \cdot \boldsymbol{x} = \boldsymbol{M} \cdot \boldsymbol{x} + \mu \boldsymbol{x} = (\lambda + \mu)\boldsymbol{x} \tag{3.33}$$

such that

$$\boldsymbol{M'} \cdot \boldsymbol{x} = \lambda' \boldsymbol{x} \tag{3.34}$$

where $\boldsymbol{M'} = \boldsymbol{M} + \mu\boldsymbol{I}$ and $\lambda' = \lambda + \mu$. Thus the new eigenvalue problem shares the same eigenvectors as the original problem but has eigenvalues shifted by a quantity μ which we choose to be unity. Let us examine the partial rates of photo-detachment at the near-resonant intensity of $I = 4 \times 10^{13}$ W/cm^2. Figure 3.5 shows that with sufficiently many Floquet blocks both the calculation using the analytic momenta and that with the shifted momenta converge to give the same partial rates. The number of Floquet-blocks required to give convergence in, say, the first ten above-threshold channels is in both cases much larger than that which is necessary for the quasi-energy to be fully converged. This is a characteristic feature of Floquet calculations. We find that with a given number of channels, in this case $N_b = 49$, the calculation using the shifted momenta is better converged with respect to this number than the calculation using analytic momenta, although the difference in performance is less marked than when looking at the quasi-energies. Specifically, we find that the shifted-momenta calculation is reasonably well converged in the first fifteen above-threshold channels whereas the other calculation is only converged in the first twelve such channels. However it is important that in the channels over which the partial rates have not converged to the values they would attain in a sufficiently large computation the results calculated using the shifted momenta remain close to the converged values in contrast to those calculated using the analytic momenta which are hugely in error.

3.4 Conclusions

In this chapter we have studied the effect of including in a Floquet calculation the correct self-consistent channel-momenta for the truncated system rather than those analytic momenta that are relevant to the non-truncated problem. We find that in both cases, provided that sufficiently many channels are included in the calculation, we obtain the same results for the quasi-energy and for the partial rates of photo-detachment. However the number of Floquet components that must be included in the calculation (in order to provide us with well-converged results) is much larger when relying on the

analytic momenta. This equates to a very sizeable increase in computer-time when compared to the calculation using shifted momenta. The themselves are found to differ by between one and thirty percent in the channels whose Floquet index is $\mid N \mid > N_0$. It is observed that some of the shifted momenta (in the closed channels) form pairs with equal imaginary parts and with equal and opposite real parts as the intensity increases. The norms of these momenta are then of course identical but this does not appear to have a detrimental effect on the accuracy of the computation [27].

It is conceivable that in some systems the gain in speed obtained by reducing the number of equations in the Floquet system may be offset by the burden of calculating the shifted momenta. This is the case to some extent in the one-dimensional calculation which we have performed but we find that in total our shifted momentum calculations are the more rapid and that when one takes longer wavelengths ($\lambda > 1$ μm) together with moderately high intensities the codes lacking the shifted momenta simply flounder due to the extreme number of Floquet channels which one must attempt to include. It is also possible that in some three-dimensional problems, explicit evaluation of the shifted momenta (repeated for each and every iteration) may be unduly time-consuming. However, it has been suggested by M Dörr [39] that in practice it may well be sufficient to compute the shifted momenta once in every five or ten iterations and in this way the computational burden could be significantly reduced. It is clear that for calculations using the recent R-Matrix-Floquet code the shifting of the channel-momenta is of considerable interest and practical importance.

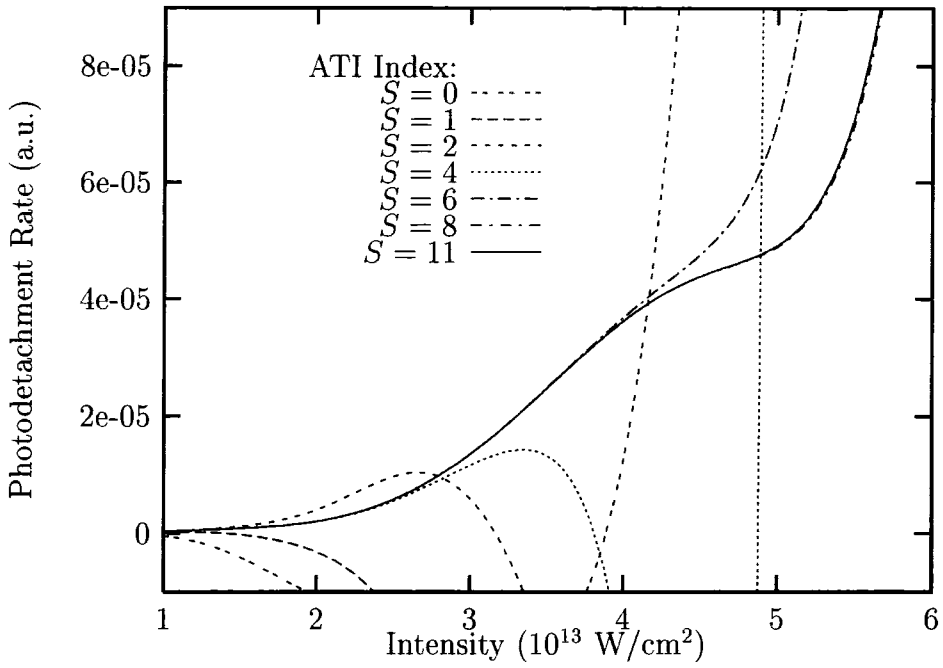

Figure 3.1: Resonant photodetachment from the 1D square-well using analytic momenta.

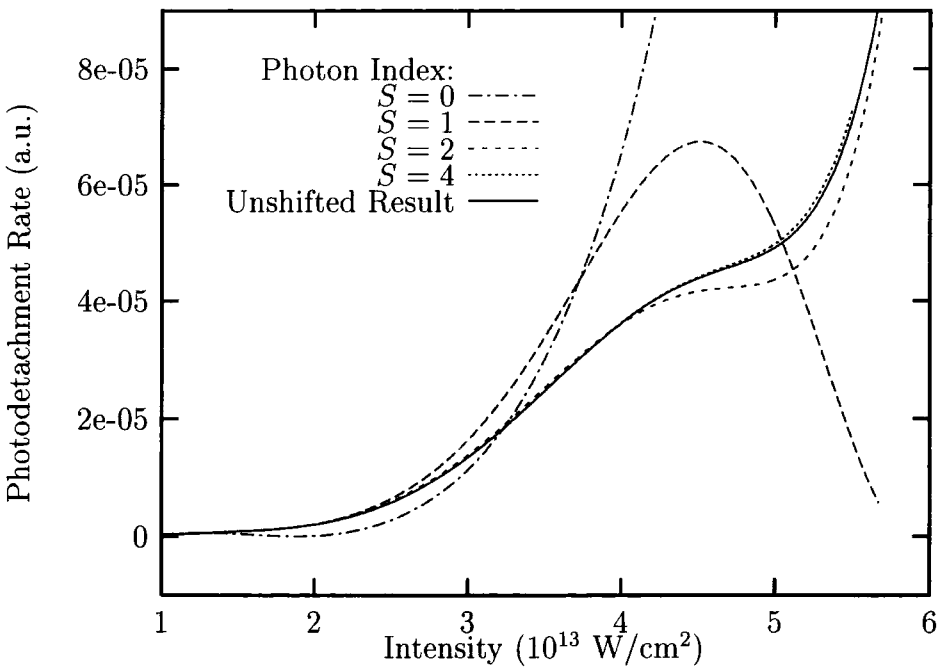

Figure 3.2: Resonant photodetachment from the 1D square-well using shifted momenta.

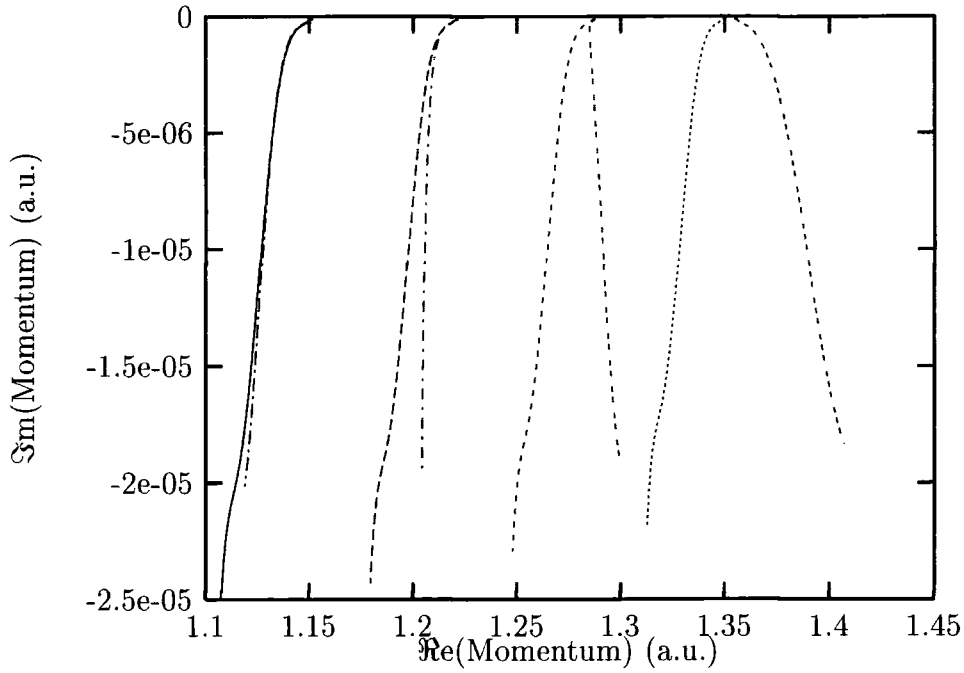

Figure 3.3: Selected channel momenta from the internal region for converged quasi-energies. Unshifted momentum indices (N) are: (————) +7; (- - - - -) +8; (- - - - -) +9; (·····) +10. Shifted momentum indices are: (— - — - —) +7; (- - - - - -) +8; (- - - - - -) +9; (- - - - - -) +10.

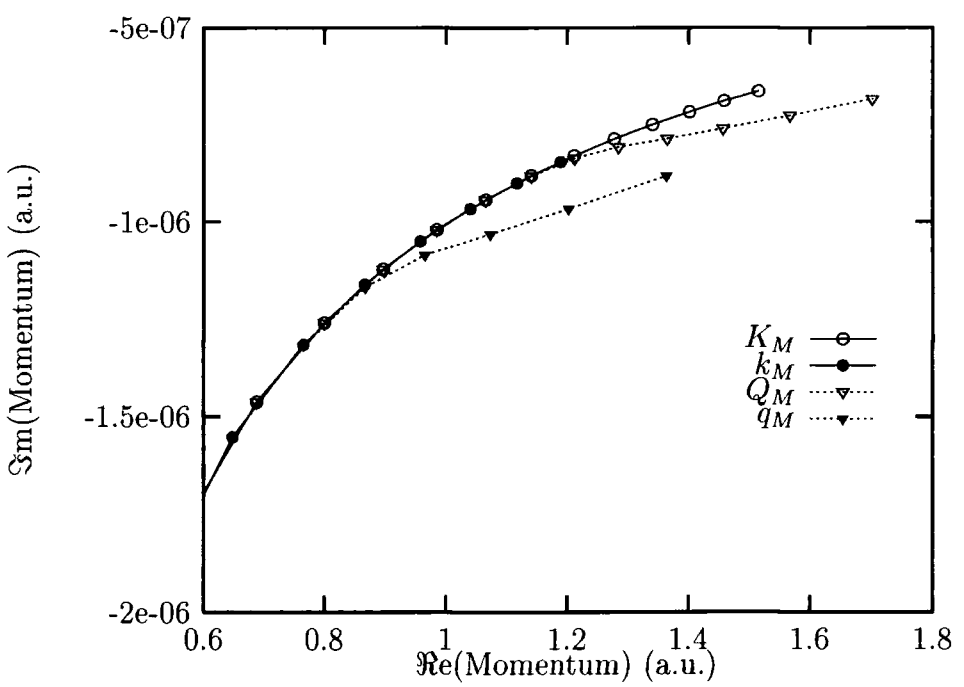

Figure 3.4: Momenta in the open channels at $I = 2 \times 10^{13}$ W/cm^2 and with a converged quasi-energy.

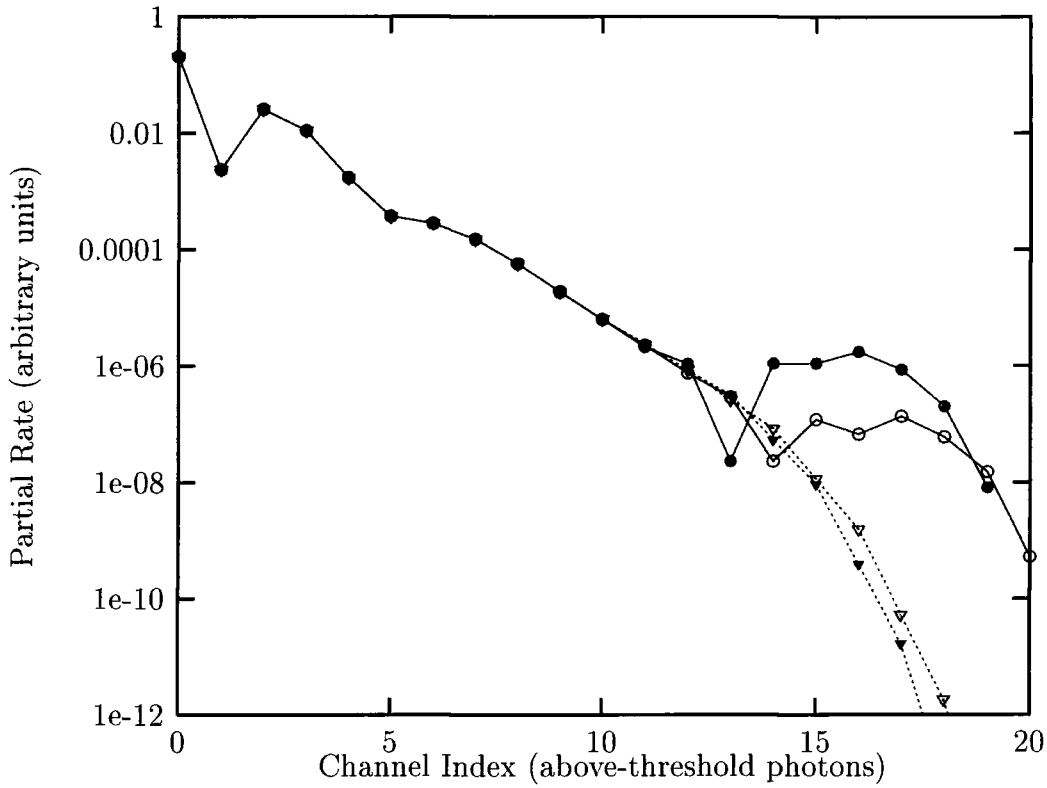

Figure 3.5: Partial rates of photodetachment at an intensity $I = 4 \times 10^{13}$ W/cm^2. Parameters are: (—●—) analytic momenta with 49 Floquet blocks; (—⊖—) analytic momenta with 51 Floquet blocks; (···▼···) shifted momenta with 49 Floquet blocks; (···▽···) shifted momenta with 51 Floquet blocks.

Chapter 4

Validity of the Single-Diabatic-Floquet-State Approximation

4.1 Theory of the Two-State Model

A laser pulse has initial and final intensities of zero, in between which there will be an intensity profile or envelope which may be rapidly varying (e.g. the $exp(-t^2/\tau^2)$ function) or slowly varying (e.g. the $sech^2(t/\tau)$ function), where the constant τ is a measure of the length of the pulse. For certain values of the intensity - each of which will be met on both the upward and downward sides of the pulse - the real parts of the quasi-energy trajectories (i.e. the energy levels of the atom dressed by the field) of a pair of dressed states may undergo either real or avoided crossings. Physically these correspond to multiphoton resonances, and as one passes through an avoided crossing while remaining in the same adiabatic state the character (including the composition in terms of partial waves) of that state will swap with that of its partner. At a true crossing there is no such distinction between diabatic and adiabatic states. In the limit of zero intensity each dressed state corresponds to a field-free atomic state and in the Floquet picture it is assumed that as one increases the intensity the dressed state evolves sufficiently slowly that the electron perceives a piecewise-constant intensity and at all times adiabatically follows this initial eigenvalue curve. However if the intensity varies sufficiently rapidly in the vicinity of the crossing there is a finite probability for the

electron to jump from one quasi-energy curve to the other. Assuming that the population was initially in the ground state the upper states may become significantly populated in this manner.

In order to study the dynamics of the atom-laser system in the neighbourhood of a curve crossing we can solve the time-dependent Schrödinger equation for a coupled two-state model. The wavefunction of the electron may be expressed as a superposition

$$\Psi(\boldsymbol{r},t) = \sum_{j=0}^{1} a_j(t)\exp[-iS_j(t)]\psi_j(\boldsymbol{r},t) \tag{4.1}$$

where $a_j(t)$ are coefficients and $S_j(t)$ are phase factors

$$S_j(t) = \int_0^t dt' E_j(t') \tag{4.2}$$

with quasi-energy eigenvalues $E_j(t')$ corresponding to the dressed-state eigenfunctions ψ_j. The two states are labelled by $j = 0, 1$. The coefficients must satisfy the initial condition $a_j(0) = \delta_{j,0}$. We substitute the total electron wavefunction into the time-dependent Schrödinger equation

$$\left[i\frac{d}{dt} - H(t)\right]\Psi(t) = 0 \tag{4.3}$$

where $H(t)$ is the full Hamiltonian of the atom-plus-field system

$$H(t) = H_A + H_I(t) \tag{4.4}$$

where H_A is the atomic Hamiltonian and $H_I(t)$ represents the interaction with the field. Before doing this we note two identities:

$$\frac{d}{dt} = \frac{\partial}{\partial t} + \frac{dI}{dt}\frac{\partial}{\partial I} \tag{4.5}$$

and

$$i\frac{d}{dt}\mathrm{e}^{-iS_j(t)} = E_j\mathrm{e}^{-iS_j(t)} \tag{4.6}$$

Thus the Schrödinger equation becomes

$$\sum_j \left[\left(i\frac{\partial}{\partial t} + i\frac{dI}{dt}\frac{\partial}{\partial I} - H(t)\right)a_j(t)\mathrm{e}^{-iS_j(t)}\psi_j(\boldsymbol{r},t)\right] = 0 \tag{4.7}$$

and after expanding the Floquet vector in a Fourier series

$$\psi_j(\boldsymbol{r},t) = \sum_n \mathrm{e}^{-in\omega t} F_{j,n}(\boldsymbol{r}) \tag{4.8}$$

we obtain

$$\sum_j \left[\left(i\frac{\partial a_j}{\partial t}\mathrm{e}^{-iS_j(t)} + i\frac{dI}{dt}a_j\mathrm{e}^{-iS_j(t)}\frac{\partial}{\partial I} \right)\psi_j(\boldsymbol{r},t) + \right.$$
$$\left. a_j\mathrm{e}^{-iS_j(t)} \sum_n \left(E_j - H_A - H_I(t) + i\frac{\partial}{\partial t} \right) \mathrm{e}^{-in\omega t} F_{j,n}(\boldsymbol{r}) \right] = 0 \tag{4.9}$$

Recall that the interaction with the field can be written as

$$H_I(t) = V_+\mathrm{e}^{-i\omega t} + V_-\mathrm{e}^{+i\omega t} \tag{4.10}$$

then we can multiply out the second term in equation (4.9)

$$\sum_n \left(E_j - H_A - H_I(t) + i\frac{\partial}{\partial t} \right) \mathrm{e}^{-in\omega t} F_{j,n}(\boldsymbol{r}) =$$
$$\sum_n \mathrm{e}^{-in\omega t} \left[(E_j - H_A + n\omega) F_{j,n}(\boldsymbol{r}) - V_+ F_{j,n-1}(\boldsymbol{r}) - V_- F_{j,n+1}(\boldsymbol{r}) \right] \tag{4.11}$$

But the expression in square brackets is identically zero (see equation (2.24)), leaving only

$$\sum_j \mathrm{e}^{-iS_j(t)} \left(\frac{\partial a_j}{\partial t} + \frac{dI}{dt}a_j\frac{\partial}{\partial I} \right) \mid \psi_j \rangle = 0 \tag{4.12}$$

Let us now pre-multiply by $\mathrm{e}^{-iS_0(t)}\langle\psi_0^* \mid$ and integrate over one cycle of $\tau \equiv \omega t$, *viz.*

$$\sum_j \int d\tau \mathrm{e}^{iS_{0j}(t)} \left\langle \psi_0^*(\tau) \left| \left(\frac{\partial a_j}{\partial t} + \frac{dI}{dt}a_j\frac{\partial}{\partial I} \right) \right| \psi_j(\tau) \right\rangle = 0 \tag{4.13}$$

where we have defined $S_{ij}(t) \equiv S_i(t) - S_j(t)$. Note the double conjugation in the bra, i.e. the products are effectively taken without any conjugation. Further, we can treat $S_{ij}(t)$, $a_j(t)$ and the time-derivatives of $a_j(t)$ and $I(t)$ as being approximately constant over the cycle time $2\pi/\omega$, giving

$$\sum_j \mathrm{e}^{iS_{0j}(t)} \left[\frac{\partial a_j}{\partial t} \int d\tau \langle \psi_0^*(\tau) \mid \psi_j(\tau) \rangle + \frac{dI}{dt}a_j \int d\tau \left\langle \psi_0^*(\tau) \left| \frac{\partial}{\partial I} \right| \psi_j(\tau) \right\rangle \right] = 0 \tag{4.14}$$

But the Floquet wavevectors are orthonormal

$$\int d\tau \langle \psi_i^*(\tau) \mid \psi_j(\tau) \rangle = \sum_n \langle F_{i,n}^* \mid F_{j,n} \rangle = \delta_{ij} \tag{4.15}$$

and so we can write

$$\frac{\partial a_0}{\partial t} = -\sum_j \mathrm{e}^{iS_{0j}(t)} \frac{dI}{dt} a_j U_{0j}(I) \tag{4.16}$$

where

$$U_{ij}(I) = \frac{1}{2\pi} \int_0^{2\pi} d\tau \left\langle \psi_i^*(\tau) \left| \frac{\partial}{\partial I} \right| \psi_j(\tau) \right\rangle \tag{4.17}$$

However it is readily seen that

$$U_{ij}(I) + U_{ji}(I) = \frac{1}{2\pi} \int_0^{2\pi} d\tau \frac{\partial}{\partial I} \langle \psi_i^*(\tau) \mid \psi_j(\tau) \rangle = \frac{\partial}{\partial I}(\delta_{ij}) = 0 \tag{4.18}$$

and thus $U_{ii}(I) = 0$. Hence the evolution equation for state $j = 0$ is

$$\frac{\partial a_0}{\partial t} = -\frac{dI}{dt} \mathrm{e}^{iS_{01}(t)} U_{01}(I) a_1(t) \tag{4.19}$$

and similarly for state $j = 1$ we obtain

$$\frac{\partial a_1}{\partial t} = -\frac{dI}{dt} \mathrm{e}^{iS_{10}(t)} U_{10}(I) a_0(t) \tag{4.20}$$

Note that $S_{ij}(t) = -S_{ji}(t)$ and $U_{ij}(I) = -U_{ji}(I)$.

There is one further problem which we have not yet discussed, namely, that the imaginary parts of the quasi-energies (and therefore of the function $S_{ij}(t)$) give rise to a non-oscillatory exponential function which may explode with time. But we may eliminate this term by a transformation of the time-dependent coefficients $a_j(t)$,

$$a_j(t) = a'_j(t) \exp\left[i \int^t dt' i\, \Im\mathrm{m}(E_j(t')) \right] \tag{4.21}$$

giving

$$\frac{\partial a_j}{\partial t} = \left(\frac{\partial a'_j}{\partial t} + \frac{\Gamma_j}{2} a'_j \right) \exp\left[i \int^t dt' i\, \Im\mathrm{m}(E_j(t')) \right] \tag{4.22}$$

Thus the evolution equation for the state labelled by j becomes

$$\frac{\partial a_i}{\partial t} = -\frac{\Gamma_i}{2} a_i(t) - \frac{dI}{dt} \mathrm{e}^{i\tilde{S}_{ij}(t)} U_{ij}(I) a_j(t) \tag{4.23}$$

where we now have

$$\tilde{S}_{ij}(t) = \int_0^t dt' \, \Re\mathrm{e}[E_i(t') - E_j(t')] \tag{4.24}$$

and where I have, for convenience, dropped the primes on the coefficients $a_i(t)$ and $a_j(t)$, $(j \neq i)$. The coupled equations of the two-state problem of non-adiabatic transitions have been studied previously by other authors [79], [80] in the context of atomic or molecular collisions and the associated S-matrices.

4.1.1 Ionisation from the Two-Level Atom

Let us compare equation (4.23) with the general evolution equation for a coupled two-state system

$$i\frac{\partial a_i}{\partial t} = -i\frac{\Gamma_i}{2}a_i(t) + \Omega_{ij}(t)a_j(t) \tag{4.25}$$

then by inspection we identify the coupling as

$$\Omega_{ij}(t) = -i\frac{dI}{dt}\mathrm{e}^{i\tilde{S}_{ij}(t)}U_{ij}(I) \tag{4.26}$$

and the system of two coupled equations takes the form

$$i\begin{pmatrix}\dot{a}_0\\ \dot{a}_1\end{pmatrix} = \begin{pmatrix}-i\Gamma_0/2 & \Omega_{01}\\ \Omega_{10} & -i\Gamma_1/2 - \Delta_d\end{pmatrix}\begin{pmatrix}a_0\\ a_1\end{pmatrix} \tag{4.27}$$

with a detuning Δ_d given by

$$\Delta_d = \Re\mathrm{e}(E_1 - E_0) - m\omega \tag{4.28}$$

Here m is the order of the m-photon resonance [146]. Premultiplying by $(a_0^*, 0)$ gives

$$ia_0^*\dot{a}_0 = -i\frac{\Gamma_0}{2} \mid a_0 \mid^2 + \Omega_{01}a_0^*a_1 \tag{4.29}$$

and by conjugation

$$-ia_0\dot{a}_0^* = i\frac{\Gamma_0}{2} \mid a_0 \mid^2 + \Omega_{01}^*a_0a_1^* \tag{4.30}$$

Subtracting these equations we obtain the result

$$-\frac{d}{dt} \mid a_0 \mid^2 = \Gamma_0 \mid a_0 \mid^2 + i(\Omega_{01} a_0^* a_1 - \Omega_{01}^* a_0 a_1^*) \tag{4.31}$$

and similarly for the upper state

$$-\frac{d}{dt} \mid a_1 \mid^2 = \Gamma_1 \mid a_1 \mid^2 - i(\Delta_d - \Delta_d^*) \mid a_1 \mid^2 + i(\Omega_{10} a_1^* a_0 - \Omega_{10}^* a_1 a_0^*) \tag{4.32}$$

Let us define the loss from the system between times t_a and t_b as

$$\Delta_{t_a,t_b} \left(\mid a_0 \mid^2 + \mid a_1 \mid^2 \right) = \sum_j \left(\mid a_j(t_a) \mid^2 - \mid a_j(t_b) \mid^2 \right) \tag{4.33}$$

then by integrating equations (4.31) and (4.32) with respect to time we can write the loss as

$$\Delta_{t_a,t_b} \left(\mid a_0 \mid^2 + \mid a_1 \mid^2 \right) = \int_{t_a}^{t_b} dt \, \left(\Gamma_0 \mid a_0 \mid^2 + \Gamma_1 \mid a_1 \mid^2 \right) + I_c(t_a, t_b) \tag{4.34}$$

where the coupling term is

$$I_c(t_a, t_b) = i \int_{t_a}^{t_b} dt \, [a_0 a_1^* (\Omega_{10} - \Omega_{01}^*) + a_0^* a_1 (\Omega_{01} - \Omega_{10}^*) + a_2 a_2^* (\Delta_d^* - \Delta_d)] \tag{4.35}$$

But from the definition of the detuning in equation (4.28) we know that Δ_d is real, making the coupling term

$$I_c(t_a, t_b) = i \int_{t_a}^{t_b} dt \, [a_0^* a_1 \Delta_\Omega - a_0 a_1^* \Delta_\Omega^*] \tag{4.36}$$

where $\Delta_\Omega(t) = \Omega_{01}(t) - \Omega_{10}^*(t)$. Using the definition of $\Omega_{ij}(t)$ from equation (4.26) we find that $\Delta_\Omega(t)$ is given by

$$\Delta_\Omega(t) = -2i \frac{dI}{dt} \Im\mathrm{m}[U_{01}(I)] \mathrm{e}^{i\tilde{S}_{01}(t)} \tag{4.37}$$

and inserting this into (4.34) we obtain the result

$$I_c(t_a, t_b) = 2 \int_{t_a}^{t_b} dt \left[\frac{dI}{dt} \Im\mathrm{m}[U_{01}(I)] \left(a_0^* a_1 \mathrm{e}^{i\tilde{S}_{01}(t)} + a_0 a_1^* \mathrm{e}^{-i\tilde{S}_{01}(t)} \right) \right] \tag{4.38}$$

So at a given time t we see that the strength of the cross-term $I_c(t, t + \delta t)$ is directly proportional to the imaginary part of the matrix element $U_{01}(I)$

of d/dI between the two states $j = 0, 1$. Except when close to resonance we expect this overlap to be approximately zero and hence equation (4.31) to reduce to

$$\sum_j \int_{t_a}^{t_b} dt\, \Gamma_j(t') \mid a_j(t') \mid^2 = \sum_j \left(\mid a_j(t_a) \mid^2 - \mid a_j(t_b) \mid^2 \right) \tag{4.39}$$

and this can be verified analytically by inserting the ansatz

$$a_j(t) = a_j(t_a) \exp\left[- \int_{t_a}^{t} dt' \frac{1}{2} \Gamma_j(t') \right] \tag{4.40}$$

into equation (4.39). Physically this is nothing other than an exponential decline in the populations of both states, governed by the decay rates Γ_j from the quasi-energies E_j. Inserting our ansatz into the left-hand side of (4.36) gives

$$- \sum_j \mid a_j(t_a) \mid^2 \int_{t_a}^{t_b} dt \left(\frac{d}{dt} \exp\left[- \int_{t_a}^{t_b} dt'\, \Gamma_j(t') \right] \right) = \sum_j \left(\mid a_j(t_a) \mid^2 - \mid a_j(t_b) \mid^2 \right) \tag{4.41}$$

which can be rewritten as

$$\sum_j \mid a_j(t_a) \mid^2 \left(1 - \exp\left[- \int_{t_a}^{t_b} dt'\, \Gamma_j(t') \right] \right) = \sum_j \left(\mid a_j(t_a) \mid^2 - \mid a_j(t_b) \mid^2 \right) \tag{4.42}$$

which is of course satisfied by assumption.

4.1.2 Unitarity of the Hamiltonian

We now come to the important issue of unitarity in our pair of coupled equations. The coupling $\Omega_{ij}(t)$ between the states is a complex function and the non-Hermiticity of the matrix element $U_{ij}(I)$ in equation (4.26) causes this coupling, and therefore also the Hamiltonian, to be non-Hermitian. This allows the possibility of a unitarity being violated at various times during the laser pulse and calls into question our interpretation of the time-dependent coefficients $a_0(t)$ and $a_1(t)$ as populations of the levels $j = 0, 1$ respectively. We can shed some light on this question of normalisation by considering the evolution of the time-reversed coefficients $a_0^\dagger(t)$ and $a_1^\dagger(t)$. Let us first

rewrite the equations for the un-reversed coefficients by applying the unitary transformation

$$a_j(t) \longrightarrow \exp\left[i\int^t dt' \,\Re\mathrm{e}(E_j)\right] \tag{4.43}$$

to obtain (c.f. equation (4.23))

$$\dot{a}_i(t) = -iE_i a_i(t) - \frac{\partial I}{\partial t}\left\langle \psi_i^* \left| \frac{\partial}{\partial I} \right| \psi_j \right\rangle a_j(t) \tag{4.44}$$

with $i \neq j$. Applying time-reversal we have

$$\dot{a}_i^\dagger(t) = -iE_i^* a_i^\dagger(t) - \frac{\partial I}{\partial t}\left\langle \psi_i \left| \frac{\partial}{\partial I} \right| \psi_j^* \right\rangle a_j^\dagger(t) \tag{4.45}$$

Therefore we can obtain an expression for the time-evolution of the product $a_i^{\dagger *}(t)a_i(t)$

$$\frac{d}{dt}a_i^{\dagger *}a_i = \dot{a}_i^{\dagger *}a_i + a_i^{\dagger *}\dot{a}_i = -\frac{\partial I}{\partial t}\left\langle \psi_i^* \left| \frac{\partial}{\partial I} \right| \psi_j \right\rangle (a_j^{\dagger *}a_i + a_i^{\dagger *}a_j) \tag{4.46}$$

Summing for the two states we find that

$$\frac{d}{dt}(a_0^{\dagger *}a_0 + a_1^{\dagger *}a_1) = - \frac{\partial I}{\partial t}\left[\left\langle \psi_0^* \left| \frac{\partial}{\partial I} \right| \psi_1 \right\rangle + \left\langle \psi_1^* \left| \frac{\partial}{\partial I} \right| \psi_0 \right\rangle\right](a_0^{\dagger *}a_1 + a_1^{\dagger *}a_2) = 0 \tag{4.47}$$

where the final step follows from equation (4.18). Hence the combination $(a_0^{\dagger *}a_0 + a_1^{\dagger *}a_1)$ will remain constant (and equal to unity) at all times. However, we must note that individually both $a_0^{\dagger *}a_0$ and $a_1^{\dagger *}a_1$ are complex and so do not have any clear physical interpretation. The fact that they sum to unity is a very useful check on the accuracy of our computations (see the discussion at the end of this chapter).

4.2 The Limit of Rapidly Varying Intensity

4.2.1 Introduction

As yet we have considered only an arbitrary laser pulse and we have not specified whether the crossing between the (real) energies of the two states

is a true crossing or an avoided crossing. However, this distinction is crucial in obtaining a physical understanding of the dynamics of the two-level atom during a laser pulse. In fact, the evolution of the atom in the field is clearer when the crossing is avoided, and there are a number of approaches which one might take to investigate this. We would like to consider a sharply peaked intensity profile together with a high peak intensity, both of which should result in a more rapid variation in intensity and therefore exert more pressure on the SDFS approximation. Intuitively one would expect that for an intensity which varies sufficiently rapidly the Floquet picture must break down and there should be significant population transfer during resonance. We will attempt to answer this question both numerically and analytically.

Recall equations (4.19) and (4.20) for the evolution of the coefficients $a_i(t)$ with time:

$$\frac{\partial a_i}{\partial t} = -\frac{dI}{dt} e^{iS_{ij}(t)} U_{ij}(I) a_j(t) \tag{4.48}$$

where $i \neq j$. Now if the intensity varies very rapidly the coefficients $a_i(t)$ will change significantly only during the very short time interval when the two states are exactly in resonance. In this case we may regard the phase $S_{ij}(t)$ as being approximately constant, say $S_{ij}(t) \equiv s_c$, and the equations (4.48) reduce to

$$\frac{d}{dI} a_0(t) = U_{01}(I) e^{is_c} a_1(t) \tag{4.49}$$

and

$$\frac{d}{dI} a_1(t) = -U_{01}(I) e^{-is_c} a_0(t) \tag{4.50}$$

which have the solutions [116]

$$a_0(t) = \cos\left[\int^I dI'\, U_{01}(I')\right] \tag{4.51}$$

and

$$e^{is_c} a_1(t) = -\sin\left[\int^I dI'\, U_{01}(I')\right] \tag{4.52}$$

so the population of the upper state at the mid-point of the pulse (i.e. at $I(t) = I_0$ having passed the crossing once) is

$$| a_1(0) |^2 = \left| \sin\left(\int^I dI' \, U_{01}(I') \right) \right|^2 \tag{4.53}$$

In section 4.2.4 we will discuss calculations using this formula for the case of an intensity varying as $I(t) = I_0 \exp(-t^2/t_p^2)$ with large values of I_0.

4.2.2 Landau-Zener Theory

The nature of the analytic problem differs depending on whether the crossing in energies is a true crossing (e.g. the 7-photon resonance discussed in section 4.3) or an avoided crossing (e.g. the 2-photon resonance described in section 4.2.4). At a crossing of the energies in a two-state model the problem of population transfer between these states is, under some circumstances, amenable to treatment by Landau-Zener theory [95]. The method involves a series of approximations which will be described below. Other authors have applied this Landau-Zener method to multiphoton resonances with Rydberg states in Xenon [157] and Potassium [148]. Recall equation (4.48) which we can rewrite as

$$\frac{da_i}{dt} = -iV_{ij}(t) \exp\left[i \int^t dt'(E_i - E_j) \right] a_j(t) \tag{4.54}$$

where

$$V_{ij}(t) = -i \frac{dI}{dt} U_{ij}(I) \tag{4.55}$$

In the neighbourhood of the resonance ($I(t) = I_{\text{res}}$) let us approximate $(E_j - E_i) = \chi t$ where

$$\chi = \frac{d}{dt}(E_j - E_i)\bigg|_{\text{res}} = \text{constant} \tag{4.56}$$

Thus

$$\int^t dt'(E_j - E_i)dt' = \chi \int^t dt' t' = \frac{1}{2}\chi t^2 \tag{4.57}$$

giving

$$\frac{d^2a_j}{dt^2} = -i\frac{d}{dt}\left[V_{ji}(t)a_i(t)\mathrm{e}^{i\chi t^2/2}\right] \tag{4.58}$$

Let us examine equation (4.55) in more detail. In the vicinity of the resonance the function dI/dt is a slowly varying function of time compared to the coupling $U_{ji}(I)$. But $U_{ji}(I)$ has a maximum at $I(t) = I_{\mathrm{res}}$ so we can make a second approximation, that $\partial V_{ji}/\partial t = 0$ for $I(t) \approx I_{\mathrm{res}}$. (As an example of this see figure 4.2 which plots both dI/dt and $U_{ji}(I)$ as functions of intensity in the neighbourhood of the resonance. This is for the case $\lambda = 204$ nm, to be described fully in section 4.2.4.)

Hence equation (4.58) becomes

$$\ddot{a}_j = -iV_{ji}(t)\mathrm{e}^{i\chi t^2/2}(\dot{a}_i + i\chi t a_i) \tag{4.59}$$

But we know that

$$\dot{a}_i = -iV_{ij}(t)a_i(t)\mathrm{e}^{-i\chi t^2/2} \tag{4.60}$$

so substituting back into (4.59) we get

$$\ddot{a}_j - i\chi t\left[-iV_{ji}(t)\mathrm{e}^{i\chi t^2/2}a_i\right] + \mid V_{ij}(t) \mid^2 a_j(t) = 0 \tag{4.61}$$

i.e.

$$\ddot{a}_j - i\chi t\dot{a}_j + \beta^2 a_j = 0 \tag{4.62}$$

where $\beta^2 \equiv \mid V_{ij}(t_{\mathrm{res}}) \mid^2$. Before solving this equation we must first manipulate it into a more convenient form by making three changes of variables. Firstly let $a_j(t) = w(t)\exp[i\chi t^2/4]$, giving

$$\ddot{w} + \left[\frac{i\chi}{2} + \left(\frac{\chi t}{2}\right)^2 + \beta^2\right] w(t) = 0 \tag{4.63}$$

then $z = \sqrt{\chi}\exp[i\pi/4]t$ giving

$$\frac{d^2w}{dz^2} + \left[\frac{1}{2} - \frac{z^2}{4} + \frac{\beta^2}{i\chi}\right] w(z) = 0 \tag{4.64}$$

and finally $n \equiv \beta^2/i\chi$ yielding

$$\frac{d^2w}{dz^2} + \left[n + \frac{1}{2} - \frac{z^2}{4}\right] w(z) = 0 \tag{4.65}$$

which is known as Weber's equation. We require a solution $a_1(t \gg t_{\rm res})$ given that at some initial time t_0 we have $a_i(t_0) = \delta_{i0}$ and

$$\left(\frac{\partial a_1}{\partial t}\right) \sim -iV_{10}(t_{\rm res})\mathrm{e}^{i\chi t^2/2} \tag{4.66}$$

The general solution has the form

$$w(z) = AD_n(z) + BD_n(-z) \tag{4.67}$$

where, for $\mid \arg z \mid < 3\pi/4$,

$$D_n(z) \sim \mathrm{e}^{-\frac{1}{4}z^2} z^n \left[1 - \frac{n(n-1)}{2z^2} + \cdots\right] \tag{4.68}$$

and, for $\pi/4 < \arg z < 5\pi/4$,

$$\begin{aligned} D_n(z) \sim\ & \mathrm{e}^{-\frac{1}{4}z^2} z^n \left[1 - \frac{n(n-1)}{2z^2} + \cdots\right] \\ & - \frac{(2\pi)^{\frac{1}{2}}}{\Gamma(-n)} \mathrm{e}^{n\pi i + \frac{1}{4}z^2} z^{-n-1} \left[1 + \frac{(n+1)(n+2)}{2z^2} + \cdots\right] \end{aligned} \tag{4.69}$$

Combining the above we obtain

$$\mid a_1(t = 0 \gg t_{\rm res}) \mid^2 = 1 - \exp(-2\gamma) \tag{4.70}$$

where

$$\gamma = \pi \mid V_{10}(t_{\rm res}) \mid^2 \left(\left| \frac{\partial}{\partial t}(E_1 - E_0) \right|_{t=t_{\rm res}} \right)^{-1} \tag{4.71}$$

Using equation (4.55) we can rewrite this as

$$\mid a_1(t = 0) \mid^2 = 1 - \exp\left(-\delta^2 \left| \frac{dI}{dt} \right|^2_{t=t_{\rm res}}\right) \tag{4.72}$$

where

$$\delta^2 = \frac{2\pi}{\mid \chi \mid} \mid U_{10}(I_{\rm res}) \mid^2 \tag{4.73}$$

is a real constant. Let us assume, say, an exponential profile for the intensity, *viz.*

$$I(t) = I_0 \exp\left(-\frac{t^2}{t_p^2}\right) \tag{4.74}$$

with a resonance located at

$$I_{\text{res}} = \frac{I_0}{x}, \qquad t_{\text{res}} = \left[-t_p^2 \ln\left(\frac{1}{x}\right)\right]^{\frac{1}{2}}, \qquad x > 1 \tag{4.75}$$

Now

$$\frac{dI}{dt} = -\frac{2t}{t_p^2} I_0 \exp\left(-\frac{t^2}{t_p^2}\right) = -\frac{2t}{t_p^2} I(t) \tag{4.76}$$

giving

$$\left.\frac{dI}{dt}\right|_{t=t_{\text{res}}} = -\frac{2I_{\text{res}}}{t_p}\left[-\ln\left(\frac{1}{x}\right)\right]^{\frac{1}{2}} \tag{4.77}$$

In order to consider a rapid variation in intensity across the crossing-region we want to let the peak intensity I_0 become arbitrarily large. But the resonant intensity I_{res} is a physical constant and so we see from equation (4.75) that x must also increase indefinitely. Thus

$$\lim_{I_0 \to \infty} \left.\frac{dI}{dt}\right|_{t=t_{\text{res}}} = -\frac{2I_{\text{res}}}{t_p}\left[-\lim_{x\to\infty} \ln\left(\frac{1}{x}\right)\right]^{\frac{1}{2}} \longrightarrow -\infty \tag{4.78}$$

and so

$$\lim_{I_0 \to \infty} \mid a_1(t=0) \mid^2 \longrightarrow 1 - \exp(-\delta^2 \,.\, \infty) = 1 \tag{4.79}$$

i.e. total transfer of population from the state $j = 0$ to the state $j = 1$. This result concurs with our prediction and will be shown to be in stark contrast with the regime investigated in sections 4.3 and 4.4 We will verify this result numerically in section 4.2.4.

4.2.3 Analytic Structure of the Quasi-Energy

Let us now consider in complete generality the probability of the electron making a diabatic jump between states at an avoided crossing in their energies. This can be achieved by allowing the field-strength $\mathcal{E}(t)$ to take on complex values, a technique which has been thoroughly investigated by Pont and Shakeshaft [112]. It is believed that $E(\mathcal{E})$ is, in general, non-singular everywhere in the (finite) complex $\mathcal{E}$-plane except for branch-point singularities

of the square-root type at which two branches join. One can picture $\mathcal{E}$ scanning the real axis and as one passes each branch point one of two phenomena will manifest: if the two branches meet in the complex E-plane at a real value of the energy E then passing the corresponding branch point in the $\mathcal{E}$-plane represents a multiphoton ionisation threshold; if, however, the two branches meet in the E-plane at a complex value of E then this instead corresponds to an intermediate multiphoton resonance. It is this latter case which is of interest to us here. Both of the branches which meet at a branch-point of this character are physically accessible and in general will correspond, in the limit of zero field-strength, to real bound states of the atom.

It is well known that (in the absence of a resonance) the probability that the atom remains in a particular state j, developing adiabatically as the field-strength varies, is given by

$$P_j = \left|\exp\left(-i\int_{-\infty}^{t} dt' E_j[\mathcal{E}(t')]\right)\right|^2 \tag{4.80}$$

i.e. exponential decay

$$P_j = \exp\left(2\Im\mathrm{m}\int_{-\infty}^{t} dt' E_j[\mathcal{E}(t')]\right) = \exp\left(-\int_{-\infty}^{t} dt' \Gamma_j[\mathcal{E}(t')]\right) \tag{4.81}$$

Let us instead suppose that there is a resonance in which state $j = 0$ swaps character with state $j = 1$ as $\mathcal{E}(t)$ increases. At this point we must generalise to a complex field-strength and in the complex $\mathcal{E}$-plane we see that the resonant field-strength ($\mathcal{E}_{\mathrm{res}}$) is located above the real axis in the right-hand half plane and that the branch cut is a straight line between this and its reflection in the real axis ($\mathcal{E}^*_{\mathrm{res}}$). An illustration of the set-up is given in figure 4.1.

Now a swapping in the characters of the states is associated with crossing the branch cut (i.e. integrating along the real axis from one side of the cut to the other) but if we wish to calculate the probability of remaining in the state with the same physical character (in effect jumping between the two states as they exchange character) then we can accomplish this by integrating along a contour in the $\mathcal{E}$-plane which goes around the branch cut and encircles the two branch points. So, having started out in a state $j = 0$ we can express

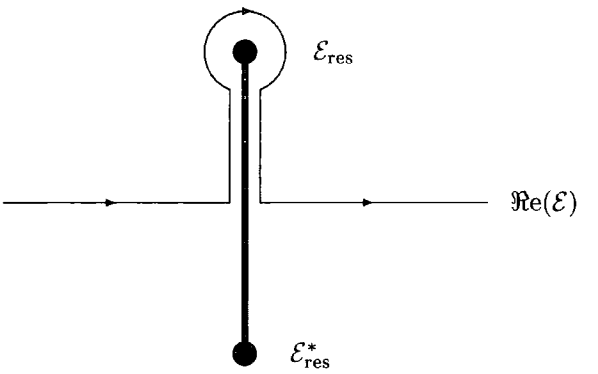

Figure 4.1: A schematic diagram showing the locations in the complex $\mathcal{E}$-plane of the two branch points associated with a single multiphoton resonance.

the probability of being, at some field-strength $\mathcal{E}(t) \gg \mathcal{E}_{\rm res}$, in the resonantly coupled state $j = 1$ as

$$P_1 = \exp\left(2\Im{\rm m}\int_{C'} dt\, E[\mathcal{E}(t)]\right) \tag{4.82}$$

where C' is the contour in the t-plane corresponding to the contour C traced out in the complex $\mathcal{E}$-plane [112]. In the neighbourhood of $\mathcal{E}_{\rm res}$ and $\mathcal{E}^*_{\rm res}$ we know that the quasi-energy behaves like a product of $\sqrt{(\mathcal{E}-\mathcal{E}_{\rm res})}$ and $\sqrt{(\mathcal{E}-\mathcal{E}^*_{\rm res})}$, i.e.

$$E^{\pm}(\mathcal{E}) \approx E_{\rm res}(\mathcal{E}) \pm C_{\rm res}(\mathcal{E})[(\mathcal{E}-\mathcal{E}_{\rm res})(\mathcal{E}-\mathcal{E}^*_{\rm res})]^{\frac{1}{2}} \tag{4.83}$$

where $C_{\rm res}(\mathcal{E})$ is a smoothly varying, non-singular function of $\mathcal{E}$. Let us define the difference between the two quasi-energies to be

$$\delta E(\mathcal{E}) = E^{+}(\mathcal{E}) - E^{-}(\mathcal{E}) = 2C_{\rm res}(\mathcal{E})[(\mathcal{E}-\mathcal{E}_{\rm res})(\mathcal{E}-\mathcal{E}^*_{\rm res})]^{\frac{1}{2}} \tag{4.84}$$

Making the further approximation that

$$C_{\rm res}(\mathcal{E}) \approx C_R = \text{constant} \tag{4.85}$$

within this region, and multiplying out the expression in square brackets we have

$$\delta E(\mathcal{E}) = 2C_R[(\mathcal{E} - \Re\mathrm{e}\,\mathcal{E}_{\mathrm{res}})^2 + (\Im\mathrm{m}\,\mathcal{E}_{\mathrm{res}})^2]^{\frac{1}{2}} \tag{4.86}$$

which clearly reaches its minimum value at the point $\mathcal{E} = \Re\mathrm{e}\,\mathcal{E}_{\mathrm{res}} \equiv \mathcal{E}_R$. At this minimum the gap between the real parts of the quasi-energies is given by

$$|\ \Re\mathrm{e}\,\delta E(\mathcal{E}_R)\ | = 2\ |\ (\Re\mathrm{e}C_R)(\Im\mathrm{m}\mathcal{E}_{\mathrm{res}})\ | \tag{4.87}$$

and it can be shown that this energy gap is equal to the Rabi flopping frequency Ω_0 between the levels $j = 0$ and $j = 1$ [112].

We continue to follow the method of Pont and Shakeshaft in order to obtain an expression for the probability of transition between the two energy levels. In the neighbourhood of the crossing we can write that

$$\dot{\mathcal{E}}_R \equiv \left.\frac{d\mathcal{E}}{dt}\right|_{t_R} = \frac{\mathcal{E}(t) - \mathcal{E}(t_R)}{t - t_R} \tag{4.88}$$

where t_R is the (real) time at which the crossing occurs, and we can rearrange this as

$$\mathcal{E}(t) = \mathcal{E}_R + (t - t_R)\dot{\mathcal{E}}_R \tag{4.89}$$

Therefore our probability for jumping between adiabatic curves is given by

$$P_1 = \exp\left(-\frac{2}{\dot{\mathcal{E}}_R}\Im\mathrm{m}\int_{\mathcal{E}_R}^{\mathcal{E}_{\mathrm{res}}} d\mathcal{E}\ \delta E(\mathcal{E})\right) \tag{4.90}$$

Making a convenient change of variables $\mathcal{E} = \mathcal{E}_R + ix$ we obtain

$$P_1 = \exp\left(-\frac{4}{\dot{\mathcal{E}}_R}\Re\mathrm{e}\int_0^{\Im\mathrm{m}\,\mathcal{E}_{\mathrm{res}}} dx\ C_R\sqrt{(\Im\mathrm{m}\ \mathcal{E}_{\mathrm{res}})^2 - x^2}\right) \tag{4.91}$$

But by trivial manipulations this becomes

$$P_1 = \exp\left(-2\Omega_0\frac{\Im\mathrm{m}\mathcal{E}_{\mathrm{res}}}{\dot{\mathcal{E}}_R}\int_0^1 dy\ (1 - y^2)^{\frac{1}{2}}\right) \tag{4.92}$$

(where Ω_0 is given by equation (4.87)) and by evaluating the definite integral our result is

$$P_1 = \mathrm{e}^{-\Omega_0\delta t} \tag{4.93}$$

where

$$\delta t \equiv \frac{\pi}{2}\left|\frac{\Im\mathrm{m}\mathcal{E}_{\mathrm{res}}}{\dot{\mathcal{E}}_R}\right| \tag{4.94}$$

Summarising the expression we have obtained so far, the probability for transition is

$$P_1 = \exp\left(-\pi \mid \Re\mathrm{e}C_R \mid\mid \Im\mathrm{m}\mathcal{E}_{\mathrm{res}} \mid^2 \frac{1}{\mid \dot{\mathcal{E}}_R \mid}\right) \tag{4.95}$$

where both C_R and $\mathcal{E}_{\mathrm{res}}$ are constants. But $\mathcal{E}(t) \propto \sqrt{I(t)}$ and if $I(t) \to \infty$ within a finite time interval (i.e. the rise-time of the pulse) then obviously we would expect that

$$\dot{\mathcal{E}}_R \equiv \left.\frac{d\mathcal{E}}{dt}\right|_{t_R} \longrightarrow \infty \tag{4.96}$$

similarly to earlier in this section, c.f. equation (4.78). Let us see this explicitly in the case of the laser pulse whose intensity envelope is given by equation (4.74). Here the temporal envelope for the field-strength is

$$\mathcal{E}(t) = \left[\frac{8\pi I(t)}{c}\right]^{\frac{1}{2}} = \left[\frac{8\pi I_0}{c}\right]^{\frac{1}{2}} \exp\left(-\frac{t^2}{2t_p^2}\right) \tag{4.97}$$

and assuming as before that the resonance occurs at the (real) intensity $I_{\mathrm{res}} = I_0/x$ we obtain

$$\left.\frac{d\mathcal{E}}{dt}\right|_{t_R} = -\left[-\frac{8\pi I_0}{ct_p^2}\ln\left(\frac{1}{x}\right)\right]^{\frac{1}{2}} \exp\left[\frac{1}{2}\ln\left(\frac{1}{x}\right)\right] \tag{4.98}$$

which readily reduces to

$$\left.\frac{d\mathcal{E}}{dt}\right|_{t_R} = -\left[-\frac{8\pi I_{\mathrm{res}}}{ct_p^2}\ln\left(\frac{1}{x}\right)\right]^{\frac{1}{2}} \tag{4.99}$$

and so once again we obtain

$$\lim_{I_0\to\infty} \dot{\mathcal{E}}_R = \lim_{x\to\infty} -\left[-\frac{8\pi I_{\mathrm{res}}}{ct_p^2}\ln\left(\frac{1}{x}\right)\right]^{\frac{1}{2}} \longrightarrow -\infty \tag{4.100}$$

Thus, from equation (4.95),

$$\lim_{I_0\to\infty} P_1 \longrightarrow \exp\left(-\frac{1}{\mid \infty \mid}\right) = \mathrm{e}^0 = 1 \tag{4.101}$$

i.e. a certainty of making the diabatic switch from level $j = 0$ to level $j = 1$. This is more satisfactory than the Landau-Zener approach because fewer approximations are made en route. The result is, of course, identical. Physically we understand this result as showing that if the field varies sufficiently rapidly then the resonance is passed so quickly that the atom has no time in which to undergo Rabi flopping. Thus, in this limit of rapidly varying intensity, the avoided crossing is passed in a time δt such that $1/\delta t$ is much greater than the energy gap Ω_0.

4.2.4 Numerical Results

Earlier in this section we have twice referred to a sample laser-pulse with an exponentially attenuated intensity-envelope, i.e. equation (4.74). We have performed calculations using such a pulse at the wavelength $\lambda = 204$ nm for which the ground state of Hydrogen undergoes an avoided crossing (two-photon resonance) with the $3s$ state at an intensity $I_{\text{res}} = 1.4 \times 10^{13}$ W/cm^2. The total rate of ionisation from the ground state is shown, for intensities up to 5.0×10^{13} W/cm^2, in figure 4.3 and the multiphoton resonance results only in a barely discernible shoulder in the rate. Note that no other resonances are present either at this wavelength. Figure 4.4 illustrates the avoided crossing in the real parts of the quasi-energies of the $1s$ and $3s$ states and from this one can see that the energy-gap is approximately 10^{-3} a.u. in magnitude. Recall that the probability of the electron jumping to the upper state is given (in the limit of rapidly varying intensity) by equation (4.53) and that from the discussions in sections 4.2.2 and 4.2.3 we expect this formula to yield the answer 'unity' in the limit of large I_0. The parameters we use here are a scaled pulse length of $t_p = 0.2$ ps and peak intensities of up to $I_0 = 10^{15}$ W/cm^2. The pulse is deemed to start at the time at which the intensity reaches one hundredth of its peak value and this yields a total duration of 35500 a.u. (compared to $t_p = 8270$ a.u.) with the peak centred on time $t = 0$.

Our complete results are displayed in figure 4.5. These are calculated using the simplified coupled-states formalism of equation (4.53) and the quasi-

energy data (which is required as input) was calculated using the Sturmian-Floquet code developed by Potvliege and Shakeshaft [121] [116] [119] (see also chapter five of this thesis.) We find that for all intensities $I_0 > 6 \times 10^{13}$ W/cm^2 the probability of making the diabatic transition (by time $t = 0$) is greater than 99%. Indeed, at $I_0 = 5.0 \times 10^{13}$ W/cm^2 our calculation predicts a 98.9% chance of the electron finishing in the $3s$ state, which is significantly higher than the value previously predicted by Potvliege and Shakeshaft [116]. The latter calculation also used the Sturmian-Floquet code but neglected the coupling with the continuum, resulting in wholly real quasi-energies. For intensities above $I_0 = 1 \times 10^{14}$ W/cm^2 we obtain a slow monotonic increase in the probability of transition, culminating in a probability of unity (exact to at least seven decimal places) at $I_0 = 8.7 \times 10^{14}$ W/cm^2. At still higher intensities our results indicate a slight falling off in the population of the upper state but we do not ascribe any physical meaning to this. Rather, at these intensities we are entering a new dynamical regime (the tunnelling regime) in which the Sturmian-Floquet approach - which provides the input data for our calculations - becomes invalid. The high-frequency parameter Ξ of Dörr *et al* [38] (see section 2.4.3), delineating the regime in which a multiphoton picture is appropriate, takes the values $\Xi(I_0 = 8 \times 10^{14}) = 0.99$ and $\Xi(I_0 = 2 \times 10^{15}) = 0.63$ where the intensities are expressed in units of W/cm^2. This confirms that at intensities $I \geq 10^{15}$ W/cm^2 the Floquet quasi-energies may not correspond exactly to the true physical energies. Further, at very high intensities relativistic processes will have some dynamical effects. Thus the numerical results vindicate the heuristic arguments and approximations made in sections 4.2.2 and 4.2.3 and confirm that in the limit of rapidly varying intensity the electron will always make the diabatic switch to the upper state at an avoided crossing in the energies of the two levels.

4.3 Dynamics at True Energy Crossings

4.3.1 Interplay between Dressed Quasi-Energy States

The behaviour of a two-level atom at a true crossing of the (real) energies is qualitatively different from that at an avoided crossing. Indeed, we are not aware of any simple analytical approaches (i.e. comparable to those of described in section 4.2) that are capable of providing us with physical insights into this situation. Instead we will pursue a rigorous numerical study of the evolution of this system in a time-dependent laser pulse and we will attempt to relate our results to those from actual experiments [36] [135] and to other theoretical results [108]. It will be shown that under some circumstances, contrary to our conclusions for avoided crossings, the excited state of the two-level atom tends to be most efficiently populated at a true crossing by a laser pulse whose temporal envelope varies slowly and smoothly with time.

By varying the wavelength and intensity of the incident radiation the number of multiphoton resonances suitable for study in atomic Hydrogen is bewilderingly large. See, for example, figure 4.6 showing the many resonances in evidence at $\lambda = 608$ nm [135]. (Without exception this chapter is concerned only with linearly polarised electric fields.) In choosing a few resonances to study we have two principal selection criteria: firstly that the resonance should be experimentally accessible and secondly that for simplicity the two energy levels coming into resonance should do so well away from interference from any other states. This is not the case, for example, for the case of $\lambda = 285$ nm and $I \approx 3.4 \times 10^{13}$ W/cm^2 where we have a 'triple crossing' between the $1s$, $4p$ and $4f$ states [102] [26]. In fact there is a true crossing between the $1s$ and $4p$ levels and an avoided crossing between the $1s$ and $4f$ levels at virtually the same intensity, and the dressed $1s$ state evolves adiabatically into a state with predominantly f-character. This interplay between three states is clearly not suited to description by a two-state model. In order to compare our results with experiments already performed we choose initially the case of $\lambda = 608$ nm and $I \approx 4.3 \times 10^{13}$ W/cm^2 at which there is

a true crossing between the $1s$ and $4f$ states. This crossing is illustrated in figure 4.7, in which the $4f$ energy level has been shifted downwards by $m\omega$ where $m = 7$ is the order of the multiphoton resonance.

4.3.2 Simulation of the Bielefeld Experiment

An experiment was performed in Bielefeld in 1992 using a wavelength of 608 nm and the results of this experiment have been widely reported and discussed [36], [98], [125], [135]. The most thorough numerical simulation to date is a Monte Carlo calculation using the results of Sturmian Floquet calculations (see the appendix to chapter five) and assuming that each state evolves as a separate diabatic Floquet state. A host of small details were taken into account in this calculation including: the temporal and spatial variation of the intensity; ionisation into the different ATI channels; depletion of the target and laser shot-to-shot fluctuations; detector binning and an angular dependence in the ionisation rate; and ponderomotive scattering of the photoelectrons. The result of all this is that the small-scale structure of the experimental results was very well reproduced but with one significant discrepancy, namely that the branching ratios between the zeroth and first ATI peaks are very different. Experimentally the first peak is considerably lower than the zeroth but in the calculation the reverse is true. However, the representation of the electron wavefunction in the neighbourhood of a resonance by a single Floquet state rather than by a linear combination of two Floquet states may lead to errors in the branching ratios (i.e. relative heights of the ATI peaks) while still providing accurate positions and widths for the resonances. A two state simulation of the populations of the $1s$ and $4f$ states during the laser pulse will not allow us to re-calculate the branching ratios but it will reveal whether the assumption of a single diabatic Floquet state is valid in the region of the resonance and therefore whether this *may* be the principal source of error in the Monte Carlo calculation.

Our plan has been to use equation (4.23)

$$\frac{\partial a_i}{\partial t} = -\frac{\Gamma_i}{2}a_i(t) - \frac{dI}{dt}e^{i\tilde{S}_{ij}(t)}U_{ij}(I)a_j(t)$$

to calculate the populations of the two levels $i = 0$ $(1s)$ and $i = 1$ $(4f)$ at all times during the pulse. We interpret the value of $\mid a_i(t) \mid^2$ as being the population of state i despite the conceptual problem of the normalisation of the Floquet wavefunction discussed in section 4.1.2. The temporal variation of intensity is given by

$$I(t) = I_0 \mathrm{sech}^2 \left(\frac{t}{t_p} \right) \tag{4.102}$$

where the peak intensity is $I_0 = 8 \times 10^{13}$ W/cm^2 and the scaled pulse length is

$$t_p = \frac{\Delta t_{FWHM}}{2 \cosh^{-1} \sqrt{2}} = 11726.41 \text{a.u.} \tag{4.103}$$

corresponding to a full-width-half-maximum time interval of $\Delta t_{FWHM} = 0.5$ ps. We now need to evaluate the terms on the right-hand side of equation (4.23), starting with

$$\frac{dI}{dt} = -\frac{2}{t_p} I_0(t) \, \mathrm{sech}^2 \left(\frac{t}{t_p} \right) \tanh \left(\frac{t}{t_p} \right) \tag{4.104}$$

The other terms, namely the total rates $\Gamma_i(t)$, the matrix elements $U_{ij}(I)$ and the phases $\exp[i\tilde{S}_{ij}(t)]$ may all be obtained from the Sturmian-Floquet calculation of the quasi-energies (as described in chapter five). The quasi-energies of the $1s$ and $4f$ states must be calculated at many distinct intensities in the range $I \in [0, I_0]$ and this data can then be used to interpolate for other intensity-values within the same range. The function $\tilde{S}_{ij}(t)$ (see equation (4.24) is evaluated by trapezoidal integration using interpolated quasi-energies. We can use equation (4.15) to express the complex function $U_{ij}(I)$ as

$$U_{01}(I) = \sum_{n=-\infty}^{\infty} \left\langle F^*_{0,n} \left| \frac{d}{dI} \right| F_{1,n} \right\rangle \tag{4.105}$$

and this scalar product is readily performed by the Sturmian-Floquet code. (Note the usual double conjugation in the bra.) This function has been plotted both as a function of intensity (see figure 4.8) and simply in the complex plane (see figure 4.9). We see from these that as expected, at both low and

high intensities $U_{ij}(I)$ is virtually zero but as one crosses the resonant intensity both the real and imaginary parts achieve large amplitudes. The time-integration is performed by one of a number of subroutines from the NAG library, utilising either the Adams or the Runge-Kutta algorithms. These are variable-step methods of solving a system of (real) first-order differential equations and so our two coupled complex equations must be represented by a set of four real equations. An accuracy of (tol $= 10^{-6}$) is found to be more than adequate. The sizes of the data-sets used in this calculation are: 228 quasi-energies for the ground state, 74 quasi-energies for the $4f$ state and 883 values of the matrix element $U_{ij}(I)$ of d/dI all of which were evaluated using the Sturmian-Floquet code.

4.3.3 Numerical Results

The $sech^2$ function is positive-definite (and symmetric about $t = 0$) and so we must arbitrarily choose a start time at which the value of $I(t)$ is negligibly small. We take this to be the time at which $I(t) = 10^{-2} \times I_0$ and this corresponds to a start time of approximately $t_0 = -36000$ a.u., making the total pulse duration 1.74 ps. Figure 4.10 shows the variation with time of the population in the dressed $1s$ state. We see from this that the resonance with the $4f$ state (located at times $t = \pm 9820$ a.u.) has little impact on the $1s$ population, with most of the depletion occurring at the highest intensities where the ionisation rate is also highest (see figure 4.6). Figure 4.11 shows the population of the dressed $4f$ state and from this we see that the resonant transfer of population from the dressed $1s$ results in peaks at both crossings of the resonance with amplitudes of approximately ten orders of magnitude greater than that at the peak intensity ($t = 0$). In between these two peaks the $4f$ population is depleted very rapidly by the high rate of ionisation from this state. However the crucial feature is that the peak population transferred is only 0.04%. Now from figure 4.6 we can define the resonance with the $4f$ as occupying the time interval $(-t_1, -t_2) \equiv (-10315, -8819)$ a.u. and integrating the total ionisation rate for the $1s$ state over this interval we find

that the total ionisation yield is 1.04% of the population. We can assume any population which is transferred to the dressed $4f$ state to be ionised effectively instantly but an addition of 0.04% to the directly ionised 1.04% is evidently negligible.

At non-zero intensities the non-Hermiticity of the Hamiltonian may in fact lead to a loss of unitarity, making a physical interpretation of $\mid a_1(t) \mid^2$ quite problematic. Thus, we would like to estimate the population transfer in a complementary way and we achieve this by making use of the symmetry of the dressed $3p$ population about the centre of the pulse (see fig. 4.11). This shows that any population transfer during the rise of the pulse is almost exactly mirrored by the reverse transfer during the decline of the pulse. So, we can obtain an estimate for the population transferred to the $4f$ state during the first passing of the resonance by looking instead at the population that is lost from this state during the second crossing of the resonance (i.e. while the intensity decreases). We *start* the calculation at the beginning of this second crossing with initial conditions $\mid a_0(t_2) \mid^2 = 0$ and $\mid a_1(t_2) \mid^2 = 1$ and we measure the transfer into the ground state by the end of the pulse, $t = t_0$. At the end of the resonance ($t = t_1$) we find that the instantaneous populations are $\mid a_0(t_1) \mid^2 = 1.125 \times 10^{-4}$ and $\mid a_1(t_1) \mid^2 = 1.471 \times 10^{-4}$ which, by the end of the pulse, have evolved to $\mid a_0(t_0) \mid^2 = 1.108 \times 10^{-4}$ and $\mid a_1(t_0) \mid^2 \approx 1 \times 10^{-17}$. This confirms that there is almost no transfer of population between these two states except during the resonance $t = (t_2, t_1)$ and that at intensities below the resonant intensity the ionisation rate of the ground state is negligibly small whereas that from the $4f$ state is still huge. Most importantly, we can conclude that the transfer in population during the time interval (t_2, t_0) is of the order of 0.01%. As stated above we expect this to be a fair approximation to the population transfer from the $1s$ to the $4f$ state during the rise of the pulse. Given the symmetry in the evolution equations (4.23) we would expect the height of the second resonant peak in figure 4.11 to be lower than that of the first by a factor which is the ratio of the populations of the dressed $1s$ state at those two times. We find that this rule is not satisfied exactly but that there is a discrepancy of approximately

30% which we consider to be acceptable given the small absolute value of the dressed $4f$ population.

Let us compare also the loss from the system during the pulse when there is no coupling between the states with that obtained in the coupled-states calculation described above. Given that all of the population is initially in the ground state ($j = 0$) there will never be any population in the dressed $4f$ state and we can neglect that entirely. Therefore the population in the ground state evolves with time as (c.f. equation (4.39))

$$P_0(t) = 1 - \int_0^t dt' \, \Gamma_0(t') P_0(t') \tag{4.106}$$

where $\Gamma_0(t)$ is the total rate of ionisation of state $j = 0$ at time t as given by the Sturmian-Floquet quasi-energies. (This total ionisation rate is displayed in figure 4.6.) For the same field parameters as listed above we find that the final (field-free) $1s$ population is 44.9% without coupling compared to 45.2% with coupling. Further, the population remaining in the $4f$ state (in the coupled calculation) at the end of the pulse is only 10^{-16}%. This reflects the fact that single-photon ionisation is an open channel for the $4f$ state, making the cycle-averaged ionisation rate very high indeed, even at moderate field-strengths.

Thus it would appear that the inclusion of a resonant coupling between the $1s$ and $4f$ dressed states does not significantly alter the population of the former, although one should note that the lack of population in the latter does *not* necessarily imply insignificant transfer between the two, because any population excited into the $4f$ state will be lost to the continuum almost instantaneously. From the figures mentioned above we see that the total loss from the system (at the end of the pulse) is 55.1% without coupling and only 54.8% with the resonant coupling. This is a highly counter-intuitive result and shows that our physical understanding of the dynamics is far from complete. In the next section we will attempt to improve our insight by looking not just at the dressed state populations but also at the projections of these onto the unperturbed atomic states.

4.3.4 Preservation of Unitarity

A potential problem with our calculations is the non-Hermitian nature of the coupling $U_{ij}(I)$. This means that at each crossing of the resonance it is entirely possible for the coefficients $a_0(t)$ and $a_1(t)$ to exceed unity. This does not happen in the case already studied (see figure 4.10) because the 7-photon coupling is relatively weak but, as will be demonstrated in section 4.4, it becomes more of a problem when the order m of the multiphoton resonance is lower. We would like to check that our computations are accurate by evaluating, instead of $(a_0^* a_0 + a_1^* a_1)$, the combination $(a_0^{\dagger *} a_0 + a_1^{\dagger *} a_1) = P_T(t)$ which is constrained to equal unity at all times (see equation (4.47)). The evolution with time of the coefficients $a_0^\dagger(t)$ and $a_1^\dagger(t)$ is given by equation (4.45). For good accuracy this must be solved simultaneously with equation (4.23) for the non-time-reversed coefficients and this is performed, as before, by a (variable step) Adams algorithm from the NAG library. Splitting the equations into their real and imaginary parts we now have a system of eight coupled first order differential equations to solve. The upshot is that the function $P_T(t)$ (as defined above) is found numerically to equal unity (in both its real and imaginary parts) to an accuracy of better than 10^{-7} at all times during the pulse. This discrepancy represents the absolute accuracy of the calculation and it is crucial that the populations in both the upper and lower states have magnitudes greater than this for our results to have any meaning. Performing the same calculation for other pulse durations yields results at least as good, satisfying us that our computations are not marred by numerical inaccuracies.

4.4 Calculations at 300 nm

4.4.1 Theoretical Considerations

We now present a very detailed study of the coupling at resonance of two Floquet states and analyse these results with the aid of data from a fully

numerical integration of the time-dependent Schrödinger equation [108]. The case we have chosen to study is the three-photon resonance at $I \approx 3 \times 10^{13}$ W/cm^2 between the $1s$ and $3p$ states. The relevant wavelength is $\lambda = 300$ nm (i.e. $\omega = 0.15205$ a.u. and (i.e. $\omega = 0.15205$ $\tau \equiv 2\pi/\omega = 41.32$ a.u.). The temporal profile of the laser pulse is chosen to be a sin^2 envelope for the vector potential $\boldsymbol{A}(t)$, yielding a sin^4 envelope for the intensity. Explicitly we write the time-dependent intensity as

$$I(t) = I_0 \sin^4\left(\frac{\pi t}{2t_p}\right) \tag{4.107}$$

such that the peak intensity occurs at time t_p and the total duration of the pulse is $2t_p$. Note that in contrast to the more slowly varying envelopes discussed in sections 4.2 and 4.3 this form gives precise turn-on and turn-off times for the laser-field and that the 'half maximum' duration of the pulse is only $0.728t_p$, i.e. briefer than the length of time t_p which one would obtain with a sinusoidal envelope.

To calculate the time-dependent populations of both states when coupled we use equation (4.23) derived in section 4.1,

$$\frac{\partial a_i}{\partial t} = -\frac{\Gamma_i}{2}a_i(t) - \frac{dI}{dt}e^{i\tilde{S}_{ij}(t)}U_{ij}(I)a_j(t)$$

and take $P_i(t) = \mid a_i(t) \mid^2$. We note (see figure 4.13) that the (true) crossing in the real parts of the quasi-energies occurs at the intensity $I_0 = 2.98 \times 10^{13}$ W/cm^2. The dressed state populations calculated in this way do not tell the whole story because we can also examine what happens during the laser pulse (in the cases of both coupled and uncoupled states) to the populations in the atomic states of the atom. Indeed, there is much advantage in doing so because we are then able to compare these time-dependent populations with the results of very detailed *ab initio* numerical calculations. The distinction between the *atomic* states of the unperturbed atom and the *dressed* states of the atom in the field is important and it is only at exactly zero field-strength that the two coincide. The qualitative change between zero-field and an arbitrarily small but finite field-strength is abrupt and discontinuous: in the absence of any external field the Coulomb potential supports infinitely

many bound states; however with an arbitrarily weak but non-vanishing field there can be no truly bound states [53]. (In the latter case only resonances exist but when these resonances have long lifetimes - when measured on the time-scale of the optical period τ - one can call them *quasi-bound* states and describe both their position and lifetime by means of a quasi-energy.) Of course in the context of the fully numerical calculation the notion of 'dressed states' is superfluous: one can calculate only the overlap of the time-evolved wavefunction with the wavefunctions of the field-free atomic states. Therefore our first task is to extract from our dressed-state populations the comparable populations of the atomic $1s$ and $3p$ states. We note that although in the case of non-coupled states the initial conditions (trivially) lead to the dressed $3p$ state remaining empty throughout, there may be a significant contribution from the dressed $1s$ state to the atomic $3p$ state.

Let us recall from equations (4.1) and (4.2) our complete time-dependent wavefunction

$$\Psi(\boldsymbol{r},t) = \sum_{j=0}^{1} a_j(t) \exp[-iS_j(t)]\psi_j(\boldsymbol{r},t)$$

which contains contributions from the two Floquet states $j = 0, 1$. To determine the component of Ψ lying in a given atomic state we can take the scalar product of this wavefunction with the wavefunction of a field-free atomic state $\phi_\alpha(\boldsymbol{r})$ (where we use α to label the atomic states to distinguish them from the dressed states which are denoted j as above). The total population in an atomic state α is therefore given by

$$P_\alpha(t) = \mid \langle \phi_\alpha^* \mid \Psi \rangle \mid^2 \tag{4.108}$$

Combining this expression with equation (4.8) we obtain

$$P_\alpha(t) = \left| \sum_{j=0,1} a_j(t) \mathrm{e}^{-iS_j(t)} \sum_{n'} \mathrm{e}^{-in\omega t} \langle \phi_\alpha^* \mid F_{j,n} \rangle \right|^2 \tag{4.109}$$

where the summation index n' runs over either the odd or the even values of n, according to the parity of the wavefunctions. For a harmonic component $F_{j,0}$ of even parity, n' runs over the even values of n when α labels an atomic

eigenfunction of even parity and n' runs over the odd values of n when α labels an atomic eigenfunction of odd parity. The converse applies when $F_{i,0}$ has odd parity. Thus

$$P_\alpha(t) = \left| \sum_{j=0,1} a_j(t) \mathrm{e}^{-iS_j(t)} \sigma_{j,\alpha}(t) \right|^2 \tag{4.110}$$

where

$$\sigma_{j,\alpha}(t) = \sum_{n'} \mathrm{e}^{-in\omega t} c_n^{(j,\alpha)}, \qquad c_n^{(j,\alpha)} = \langle \phi_\alpha^* \mid F_{j,n} \rangle \tag{4.111}$$

Note that the coefficients $c_n^{(j,\alpha)}$ vary slowly with time due to changes in the harmonic component $F_{j,n}(I)$ and that $\sigma_{j,\alpha}(t)$ varies much more rapidly due to the oscillating exponential factor.

From equation (4.111) we have seen that the coefficients $c_n^{(j,\alpha)}$ will vary slowly with intensity and that each of these coefficients is premultiplied by a very rapidly oscillating term of frequency $n\omega$. Now in practice, the coefficient with harmonic index $n = 0$ or $n = 1$ will dominate while those with indices $\mid n \mid \gg 0$ will be virtually zero and it is therefore instructive to write equation (4.111) as

$$\sigma_{j,\alpha}(t) = c_0^{(j,\alpha)} + \mathrm{e}^{-2i\omega t} c_2^{(j,\alpha)} + \mathrm{e}^{+2i\omega t} c_{-2}^{(j,\alpha)} + \cdots \tag{4.112}$$

for α of even parity, and

$$\sigma_{j,\alpha}(t) = c_1^{(j,\alpha)} + \mathrm{e}^{-2i\omega t} c_3^{(j,\alpha)} + \mathrm{e}^{+2i\omega t} c_{-1}^{(j,\alpha)} + \mathrm{e}^{-4i\omega t} c_5^{(j,\alpha)} + \mathrm{e}^{+4i\omega t} c_{-3}^{(j,\alpha)} + \cdots \tag{4.113}$$

for α of odd parity. So in either case we have a dominant term (subject to no oscillations) plus weaker terms whose leading order oscillates at a frequency of 2ω. Physically we interpret these as the dynamical oscillations of the electron driven by the field and passing the atomic nucleus twice in each cycle of the field. Note that equations (4.112) and (4.113) allow for interference and cancellation between the different oscillating terms and, moreover, that equation (4.110) permits interference between the contributions from differing dressed states. Recall that the optical period is $\tau = 41.32$ a.u. then we

would expect to find oscillations of time period $\tau' = 20.66$ a.u. in the populations of both the upper and lower states of our coupled two-level system for the duration of the laser pulse. This is very rapid indeed when compared to the full duration of the pulse which is typically several thousand atomic units..

4.4.2 Dressed States

Let us start by considering the loss from the system during the pulse when there is no coupling between the states. Given that all of the population is initially in the ground state ($j = 0$) there will never be any population in the dressed $3p$ state and we can neglect that entirely. As in section 4.3.3 the evolution of the population in the ground state is given by equation 4.106,

$$P_0(t) = 1 - \int_0^t dt' \, \Gamma_0(t') P_0(t')$$

where $\Gamma_0(t)$ is the total rate of ionisation of state $j = 0$ at time t, as obtained from the Sturmian-Floquet quasi-energies. (See a description of the Sturmian-Floquet method in chapter five.) This total ionisation rate is displayed in figure 4.12. Taking a moderate peak intensity of $I = 8 \times 10^{13}$ W/cm^2 we calculate the dressed $1s$ population for a laser pulse of duration $2t_p = 200\tau$ and find that the final (field-free) population is 57.33%. We note that due to the simple form of equation (4.106) this dressed-state population is monotonically decreasing and, in particular, never exceeds unity.

We can immediately contrast these numbers with the results obtained by coupling the two (dressed) states using equation 4.23. We will examine these in some detail, taking the same pulse duration and peak intensity as above. The variations with time of the dressed populations are shown in figures 4.14 (for the $1s$) and 4.15 (for the $3p$). In the case of the dressed $1s$ we observe a steady loss of population due to direct ionisation while the field intensity is high and also - when the states are coupled - small 'features' at each crossing of the resonance including a loss of unitarity on the first occasion (c.f. figure 4.10). Notice how little difference is made by introducing the resonant

coupling; the final discrepancy is only 0.02%! It is interesting to remark that the sin^4 profile for the laser intensity varies much more rapidly with time than the $sech^2$ envelope described in section 4.3. Indeed, if the conclusions from our study of atomic dynamics at an avoided crossing (see section 4.2) were applicable here, we might expect to see more of the dressed $1s$ population 'shaken' into the dressed 3p state when the two are coupled, but instead we have a very good agreement between the coupled and uncoupled results. We see that the dressed $3p$ population has two very sharp maxima (one at each resonance) when there is an influx of population from the ground state whilst between these (i.e. at very high intensities) the population plunges downwards due to the high rate of ionisation from the dressed $3p$ state at these intensities. This descent is punctuated by a series of irregularly spaced shoulders which we will comment upon later.

The overall peak in the dressed $3p$ population is 2.81%, occurring at the first crossing as one would expect. Let us also compare the relative heights of the two resonant peaks, weighted by dressed $1s$ populations at the respective times. We find a ratio ($3p$ population relative to $1s$ population) of 0.0274 at the first crossing and of 0.0279 at the second crossing, i.e. a difference of less than 2% which is what we would expect since it is exactly the same mechanism exciting electrons from the $1s$ to the $3p$ state in both cases, (c.f. the 30% in the case of the $1s-4f$ resonance at 608 nm.) After the laser-pulse has finished the coupled state calculations predict that for the 200-cycle pulse the $1s$ population is 57.35% and the $3p$ population is 0.43%. Thus, both from these numbers and from figure 4.14, the consequence of having included the coupling would appear to be of the order of a fraction of one percent, but on the other hand the violation of unitarity at resonance in the coupled-state calculation indicates that at finite field-strengths the actual populations may be noticably different, leading to different ionisation yields.

Let us also compare the total loss from the system, with and without coupling. Simply integrating the dressed $1s$ rate over time we observe that when the field is switched off we have lost 42.67% of the initial population, compared to 42.22% when the two states are coupled. Thus, as was the case with

the calculation described in section 4.3, the inclusion of a resonant coupling between the ground state and a more easily ionisible state actually decreases the total loss from the system! This is such a counter-intuitive result that one might suspect that our coupled states calculation is failing to take proper account of all the necessary factors. However, as will be seen in the following section, our results agree very well with those of fully numerical *ab initio* calculations [108]. Returning to figure 4.15, the temporal asymmetry in the $3p$ population arises from the term $\exp[i\tilde{S}_{ij}(t)]$ in equation (4.23) which is in all other respects symmetric in time about the mid-point of the pulse. Our data was obtained using the Sturmian-Floquet code and we used 113 quasi-energies for each of the dressed states and 498 values of the complex matrix element $U_{ij}(I)$ of d/dI. Long time-steps of, say, 10 a.u. were more than sufficient.

4.4.3 Atomic States

A Laser Pulse of Duration 200 fs

Of greater interest than the dressed state populations is the partitioning of the dressed $1s$ population between the $1s$ and $3p$ atomic states. Our time-dependent populations in the field-free atomic states were calculated using equation (4.110) where, for completeness, all Floquet numbers of the correct parity were included in the summation (rather than only the dominant and next-to-dominant terms). We took 50 values of the complex coefficient $c_n^{(j,\alpha)}$ (i.e. at different intensities) for each combination of the indices n, j and α. These are concentrated in the neighbourhood of the resonant intensity where their variation is most pronounced. The atomic state populations are evaluated on a time-scale of 0.5 a.u. or shorter in order to fully capture all the expected oscillations. In order to draw any quantitative conclusions from our atomic-state populations we must clearly perform some kind of averaging to damp out the leading-order oscillations. We choose to average over a sliding group of data-points whose length is to be optimised for the resulting clarity, but as one would expect, the smoothest results are obtained by averaging

over groups of data-points of length $\tau' = \tau/2 \approx 21$ a.u. (or some integer multiple therof) where τ is the optical period.

Comparative calculations have been performed by B Piraux (at the University of Louvain-la-Neuve). These consist of a fully numerical integration of the time-dependent Schrödinger equation on a grid with $\Delta t \ll 1$ a.u. and with all the same parameters (e.g. peak intensity, pulse profile and length, etc.) as in our calculation at 300 nm. The method involves expanding the wavefunction on a basis of complex Sturmian functions and spherical harmonics, *viz.*

$$\Psi(\boldsymbol{r}, t) = \sum_{n,l,m} C_{nlm}(t) S_{nl}^{(\kappa)}(r) Y_{lm}(\theta, \phi) \tag{4.114}$$

where the Sturmian functions are

$$S_{nl}^{(\kappa)}(r) = N_{nl}^{\kappa} r^{l+1} \mathrm{e}^{i\kappa r} L_{n-l-1}^{2l+1}(2i\kappa r) \tag{4.115}$$

and the associated Laguerre polynomials are given by

$$L_{n-l-1}^{2l+1}(x) = \frac{d^{2l+1}}{dx^{2l+1}} \sum_{k=0}^{n+l} (-1)^k \frac{(n+l)!}{(k!)^2 (n+l-k)!} x^k \tag{4.116}$$

In these calculations the total number of Sturmian basis functions employed per angular momentum is 120, the Sturmian parameter κ is given the value 0.2 and the angle of complex rotation is chosen to be 0.1 radians. This method will be explained in greater detail in chapter five of this thesis. The results he obtains exhibit the same rapid fluctuations as do our coupled-state calculations and moreover these oscillations have the same period, $\tau' = 21$ a.u.. Once again, in order to make any meaningful comparison with our own results, Piraux's data must be time-averaged in order to damp out the wild oscillations. (These typically have an amplitude of up to 30% of their averaged value, but this amplitude falls away to zero at either end of the pulse.) By common sense we again achieve optimal clarity by averaging over a sliding group of data-points whose length is τ' and for Piraux's results this implies averaging over groups of approximately 300 data-points.

Let us return to our laser pulse whose duration is $2t_p = 200\tau$. Figures 4.16 and 4.17 compare the (time-averaged) results of our calculations, both with

and without coupling the dressed states, to the (time-averaged) fully numerical results of Piraux [108]. In figure 4.16 we present the populations corresponding to the atomic $1s$ state. From this figure we see that the coupled and uncoupled $1s$ populations are virtually identical at all times, the only differences occurring at the two crossings of the resonance. At the first of these we observe a violation of unitarity in the results of the coupled calculation, arising from the non-Hermitian character of the complex coupling matrix whose elements are $U_{ij}(I)$. The $1s$ population from the uncoupled calculation also exhibits a strong 'feature' at the resonant intensity: a (local) minimum followed by a maximum during the rise of the pulse; and vice-versa during the fall of the pulse. There is however no breach of unitarity at any point. The occurrence of local minima and maxima in this atomic $1s$ population must clearly be attributed to cancellations between the overlap coefficients $c_n^{(j,\alpha)}(I)$ given by equation (4.111) because the *dressed* $1s$ population is, by definition, a monotonically decreasing function of time (see figure 4.14), and there is no other state with which interference could occur. Piraux's fully time-dependent results do not exhibit any sudden feature at either of the resonant times. It is expected that this difference reflects the way in which our equations are formulated (i.e. the non-Hermitian Hamiltonian) and is not a physical feature. Instead the $1s$ population decreases very smoothly, remaining at all (non-resonant) times very close to that predicted by our own results, and reaching a final value of 57.60%. Recall that the final value from the coupled states calculations was 57.35%. This excellent agreement indicates that the only dressed states to have any physical importance are the two which are included in our two-state model.

Figure 4.17 displays the populations corresponding to the atomic $3p$ state. When the levels are uncoupled the atomic $3p$ population comes purely from its overlap with the dressed $1s$ but when we include the coupling there is in addition a contribution from the dressed $3p$. The total dressed $3p$ population is mostly very small (see figure 4.15) but its overlap with the atomic $3p$ state is always very close to unity so this contribution can be significant. The results are clearly dramatic: the overlap between the dressed $1s$ state

and the atomic $3p$ state grows quite large but at resonance there is a sudden destructive interference with the contribution from the dressed $3p$ state, causing the (time-averaged) total atomic $3p$ population to reach a peak value of (approximately) only one third of that attained when the dressed states are not coupled. (There is no such effect in the $1s$ results because although there is a contribution from the dressed $3p$ to the atomic $1s$ the overlap between these states is of the order of one percent and when multiplied by the actual dressed $3p$ population this becomes completely negligible.) After the resonance (while the intensity is still rising) we observe slow oscillations in the total atomic $3p$ population and, as will be explained later on, this can be attributed to Rabi flopping between the two atomic states. It is important to note the role of the *phase* of the complex coefficients $a_j(t)$ in this cancellation process; see equation (4.110). The only point at which the 'uncoupled states' result matches that of the full calculation is during the mid-section of the pulse when the intensity is greatest. At this time the rate of ionisation from the dressed $3p$ state is so huge that there is essentially nothing left to interfere with the contribution from the dressed $1s$ state. Towards the end of the pulse we see that, in the coupled calculation, approximately half of a percent of population remains 'trapped' in the dressed $3p$ state due to the laser intensity being too low for significant ionisation too occur (even from this excited state). Contrastingly, in the uncoupled calculation, the dressed $1s$ state approaches the pure atomic $1s$ in character as the intensity dwindles to zero, leaving the atomic $3p$ state completely empty.

Also in figure 4.17, we can see the results of Piraux's fully time-dependent calculation. There are some small differences between our (coupled) results and his over the duration of the pulse but these may be due to the averaging mechanism but, in any case, when the field is turned off there is no net effect. A precise comparison of populations at the end of the pulse yields the following result: both we and Piraux obtain a fractional population of 0.43% in the atomic $3p$ state. At the first crossing of the resonance we reach a peak population of 1.84% compared to Piraux's 1.64%. The general conclusion of this figure is that our coupled-states calculation models very

accurately the full time-dependent calculation of Piraux. It is particularly interesting that the peaks in atomic $3p$ population do not coincide with the maximal dressed $3p$ populations (see figure 4.15). Whilst, for the dressed $3p$ state, the peak values occur at exactly the times at which the (real) energies are separated by 3ω, the atomic $3p$ population reaches its peak values at later times, the shift being approximately $400 - 500$ a.u.. We can offer the following physical explanation for this suppression mechanism. An electron in the dressed $3p$ state has a bound-state energy of around -0.054 a.u. at resonance, and this corresponds to a characteristic orbit time $t_e = 117$ a.u.. Thus the time-lag between the peak population in our calculation and that in Piraux's calculation may be expressed as $\Delta t \approx 3.5 t_e$. It may therefore be the case that in reality (i.e. the exact calculation) the electron is unable to react instantaneously to the rapidly changing conditions, as a result of which the transfer of population to the excited state is delayed, and moreover, the total transfer during resonance is smaller than would be obtained via an 'ideal' instantaneous response.

A complementary explanation follows naturally from the slow oscillations which follow the resonance. (We note that these oscillations diminish with time both in amplitude and in wavelength.) The time-periods of the oscillations are of the order of a few hundred atomic units and it is probable that the actual resonance coincides with a minimum in this pattern, thereby suppressing the apparent maximum in the population until a later time. Let us therefore understand the physical origin of these oscillations. Firstly, we recall that in figure 4.15 we observed a series of shoulders in the dressed $3p$ population during the section of the laser pulse immediately following the first passing of the resonance. It is not unreasonable to speculate that these may be related to the slow oscillations that are apparent in the atomic-state populations. In order to compare the two we first compensate for the exponential decay in our coupled dressed states results. We assume that our dressed $3p$ population is, during this section of the pulse, varying principally in response to direct ionisation at a rate given by $\Gamma_1(t)$. Hence, for times falling in the interval $[t_a, t_b]$ we can define a decay-compensated population

via

$$P_1'(t) = \exp\left[\int_{t_a}^{t} dt'\, \Gamma_1(t')\right] P_1(t) \tag{4.117}$$

where $P_1(t)$ is the actual population in the dressed $3p$ state.

This expression is compared to the relevant section of (Piraux's) atomic-state results in figure 4.18. We find that our decay-compensated result exhibits strong oscillations of increasing frequency, comparable to those illustrated in figure 4.17, but that the positions of the maxima and minima differ and that the time-periods do not match exactly either. We can summarise this by saying that the wiggles are qualitatively similar to those which are evident in the (time-averaged) atomic-state results. These common qualitative features lead us to speculate that the slow oscillations in our dressed $3p$ population share a common origin with those in the atomic $3p$ population. (These oscillations are unnoticable in the ground state population because their amplitude is relatively small.) Specifically, the frequency of the oscillations rises with intensity (up to the peak intensity which occurs at $t = t_p \approx 4130$ a.u.) and that over this same interval of time the energy gap between the dressed states is gradually widening. Let us define this gap to be $\Delta E(I) = \Re\mathrm{e}(E_{3p} - E_{1s}) - 3\omega$. From our quasi-energy data we find that $\Delta E(I = 5 \times 10^{13}) = 0.0082$ a.u. and $\Delta E(I = 7 \times 10^{13}) = 0.0164$ a.u. where the intensities are, as always, expressed in units of W/cm^2. The corresponding time intervals may be defined as $\Delta T = 2\pi/\Delta E = 770$ a.u. and 380 a.u. respectively. Comparing these characteristic time-scales with the curves plotted in figures 4.17 and 4.18 reveals that the oscillations occurring in both sets of results may consistently be interpreted as Rabi flops between two intensity-dependent states.

We can dissect our coupled-states results to reveal the contributions to the total atomic $3p$ population from each of the two dressed states separately. The result of this is displayed in figure 4.19. We find that at early times the total atomic $3p$ population is indistinguishable from its dressed $1s$ component and then at resonance the dressed $3p$ contribution surges upwards to augment the resonant population (but is always smaller in magnitude than the dressed $1s$ contribution). While the field-intensity is high the contribution from the

dressed $3p$ is negligible once more and the total atomic $3p$ population merges with the contribution from the dressed $1s$ state. At the second resonance the dressed $3p$ state again plays a role and as the field dies away we are left with the atomic $3p$ population coming purely from the dressed $3p$ state, in complete contrast to the roles taken by the two dressed states during the turn-on of the pulse. Since, in the limit of zero field-strength, the dressed state wavefunctions approach their atomic counterparts this behaviour is nothing other than what we would expect. The situation at the beginning of the pulse simply reflects the initial condition that the dressed $3p$ state be completely empty.

Laser Pulses of Different Duration

In this section we describe calculations at 300 nm but with durations of between $2t_p = 50\tau$ and $2t_p = 400\tau$. (It may be helpful to note that at this wavelength one can quite accurately approximate $\tau = 1$ fs.) At the shorter end of this scale we draw further comparisons with the exact results of Piraux (obtained by direct integration of the time-dependent Schrödinger equation) [108] and at the longer end we are able to compare our results with those of Pen and Jiang [102] who solve the time-dependent Schrödinger equation in momentum space. The three additional calculations that we have performed are: $2t_p = 50\tau$ with $I_0 = 8 \times 10^{13}$ W/cm^2; $2t_p = 80\tau$ with $I_0 = 6 \times 10^{13}$ W/cm^2; and $2t_p = 400\tau$ with $I_0 = 10^{14}$ W/cm^2. In each case the envelope for the field intensity has the form of a sin^4 function. In the first of these we couple the dressed $1s$ and $3p$ states in our two-state model to obtain final atomic-state populations of 87.21% in the $1s$ and 0.43% in the $3p$. By comparison, the results of Piraux's fully time-dependent calculation are 87.28% and 0.42% respectively, so once again the methods are in very good agreement. Turning to the populations during the laser pulse we find a broadly similar picture to that already seen for the longer pulse of 200τ. The peak population transfer (i.e. at the first crossing) to the dressed $3p$ state is 3.9% which is rather more than in the pulse of 200τ but is still very small compared to the $1s$ population. During the middle of the pulse we find that

approximately 1% of the dressed $1s$ population lies in the atomic $3p$ state, whilst at the end of the pulse the remaining $3p$ population dwindles to only the 0.43% mentioned above. As was the case for the laser pulse of 200τ, we find that at early times the atomic $3p$ population comes mainly from the dressed $1s$ state whereas towards the end of the pulse the residual atomic $3p$ population comes solely from the dressed $3p$ state. Note that because this much shorter pulse has the same peak intensity as that lasting 200τ, the rate of change of intensity during resonance will be greater. However, this more rapid variation in intensity manifestly does not lead to a corresponding increase in the final population of the $3p$ state.

We now comment briefly on a similar calculation carried out with a peak intensity $I_0 = 6 \times 10^{13}$ W/cm^2 and a total duration $t_p = 80\tau$. This particular combination of parameters was chosen (empirically) to maximise the final value of the $3p$ population. Our results show, however, that this final population is still only 0.77%. In the coupled states calculation the maximal atomic $3p$ population (at resonance) is only 1.4%, in contrast to the peak dressed $3p$ population of 3.3%. This difference is due to strong interference between the two coherently summed contributions to the atomic $3p$ population, as described for the laser pulse of 200τ. But there is also a severe breach of unitarity at this time $t_{\rm res}$ and so the values of our time-dependent coefficients are probably not altogether meaningful. Rather, we should look at the final populations which - for the $1s$ state - are: 88.24% when coupling the states; 88.34% when not coupling the states; and 88.46% when performing the exact numerical calculation. (Once again, this comparative calculation was performed by B Piraux [108].) As in all of our previous calculations, the final $3p$ populations are less than 1%. Thus, despite some differences over time between the coefficients $a_0(t)$ and $a_1(t)$ when coupling the $1s$ and $3p$ dressed states compared to when the dressed $1s$ state is allowed to decay in isolation, the effect of this coupling is to leave the final ground state population practically unchanged from the value which is obtained by simple exponential decay. Our results are consistent with the view that the resonant coupling between the $1s$ and $3p$ energy levels at a wavelength of 300 nm is

insignificant with regard to the distribution of the initial population across the various dressed states. In other words, we have no reason to doubt the applicability of the single diabatic Floquet state approximation, but neither can we rule out the transfer of a significant proportion of population into the dressed $3p$ state from which it would be effectively instantly ionised (this is a single-photon process), leaving little residual transfer when the field is turned off.

A series of three-dimensional fully-numerical calculations have been performed by Pen and Jiang [102], making use of the momentum-space representation of the Schrödinger equation. (A clear description of this method is given, for the case of a Hydrogenic atom, by Bransden and Joachain [11].) Pen and Jiang expand their momentum-space wavefunction on a basis of spherical harmonics,

$$\psi(\boldsymbol{p}) = \sum_{j,l,m} \nu_j^{lm}(t)\phi_j(p)Y_{lm}(\theta,\phi) \tag{4.118}$$

where $\nu_j^{lm}(t)$ are coefficients (to be determined) carrying the dependence on the radial momentum coordinate p, and $\phi_j(p)$ are orthonormalised piecewise-constant functions

$$\phi_j(p) = \begin{cases} \frac{1}{\sqrt{p_{j+1}-p_j}} & p_j < p < p_{j+1} \\ 0 & \text{otherwise} \end{cases} \tag{4.119}$$

Calculations are performed at 285 nm and at 300 nm with a range of peak intensities varying from 6.5×10^{13} W/cm^2 up to 10^{14} W/cm^2. In each case the amplitude of the electric field vector is assumed to follow a sin^2 envelope (or a sin^4 function for the intensity, as in all the other calculations described in this section) and the full-width half-maximum time is 400 fs. At 300nm this corresponds to a total duration of approximately $2t_p = 800\tau$, i.e. much longer than any laser pulse that we have so far considered. With a peak intensity of 10^{14} W/cm^2 Pen and Jiang calculate that the final $1s$ population is 40.6% and that the final $3p$ population is 17.5%. We have performed a comparative calculation using this same set of parameters and we find that the final ground state population is only 1.9% and that the remaining $3p$ population amounts to only 0.0012%. In other words, we predict that at least 98% of the initial

population will be lost from the system. This is surely what one would expect in a case in which the laser intensity is very high over such a long duration. We are confident that our own results are not in error because, in all of our previous calculations, our results have matched closely the exact numerical results of B Piraux [108]. Pen and Jiang use 250 momentum elements for each of 15 partial waves and it may well be that this basis set is insufficient to accurately represent the momentum-space wavefunction.

4.5 Conclusions

In this chapter we present the results of calculations using a two-state model of the Hydrogen atom in an intense laser field. We consider resonant couplings between the two states and examine separately the cases in which the two energy leves undergo avoided crossings and true crossings. In the case of avoided crossings, a heuristic analytical approach is adopted in which we show that, in the limit of rapidly varying intensity, the probability of the atom making a transition to the state with the same adiabatic character approaches unity. This unsurprising result is confirmed by numerical calculations (for the $1s - 3s$ resonance at 204 nm) which show that (for a scaled pulse-length of 0.2 ps) the probability of transition exceeds 99% for all peak intensities greater than 6×10^{13} W/cm^2. In the case of a true crossing the dynamics are less readily amenable to physical interpretation. Recent calculations (made within the rotating wave approximation) suggest that in this case a rapidly varying intensity leads to a smaller transfer of population than would be obtained from a slow, smoothly varying intensity profile. This is because the excited state population tends to be very sensitive to the gradient of the energy difference between the two states, and a steep gradient gives rise to oscillations in the excited state population which 'shakes' this population up into the continuum [28].

We have performed a series of coupled-state calculations at a wavelength of 300 nm and have compared our results with those of other authors [108] [102] and with a simple formula in which the ground state population varies due

to direct (i.e. non-resonant) ionisation alone. Surprisingly, we find that the addition of a three-photon resonant coupling to a state from which single-photon ionisation is possible does not increase the total loss from the ground state and that in some cases this loss is even fractionally reduced! Thus, although our results agree very well with the exact numerical results of Piraux [108], there remain some conceptual challenges in acquiring a physical understanding of these results. We detect Rabi oscillations in the off-resonant population of the excited state, although the very high ionisation rate from this state means that these oscillations are only apparent as 'shoulders' in the exponentially decaying dressed-state population. The Rabi-flopping is much clearer in the atomic-state results of Piraux [108] and is reproduced almost exactly when our dressed state populations are projected onto the field-free atomic states. This is due to destructive interference between the contributions from the two dressed states to the atomic $3p$ population.

Finally, we use the coupled-states formalism to simulate a calculation performed by Pen and Jiang [102] in which we calculate the final populations of the field-free states following an intense laser pulse whose duration is approximately 0.8 ps. We find that their three-dimensional momentum-space calculation vastly overestimates the fraction of the initial population that will remain bound after the field is turned off.

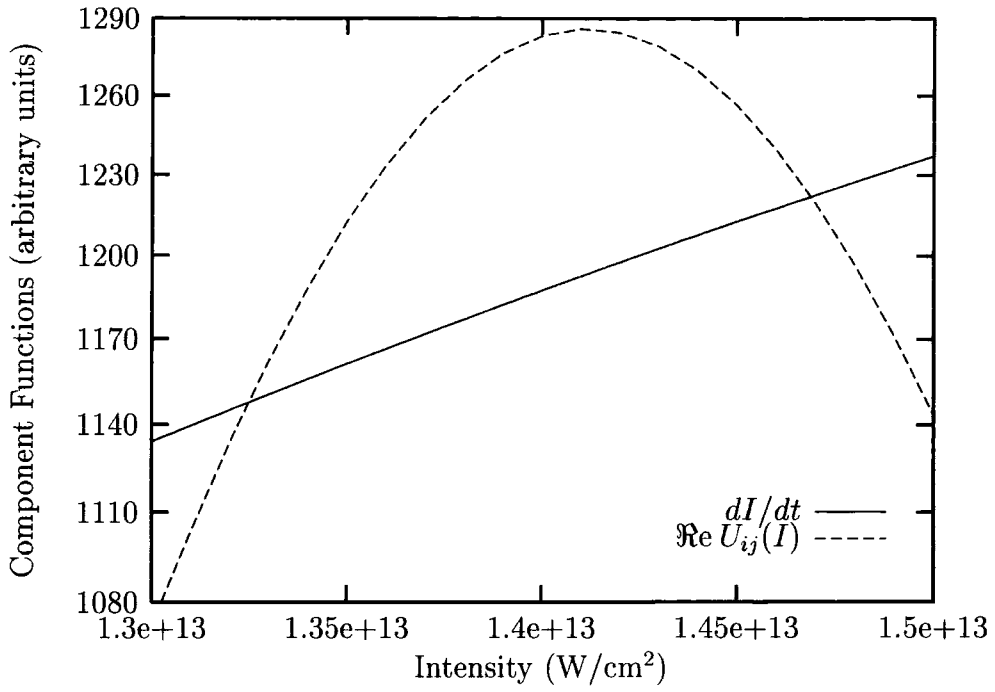

Figure 4.2: Components of the function $V_{ij}(t)$ in the region of the two-photon resonance at 204 nm.

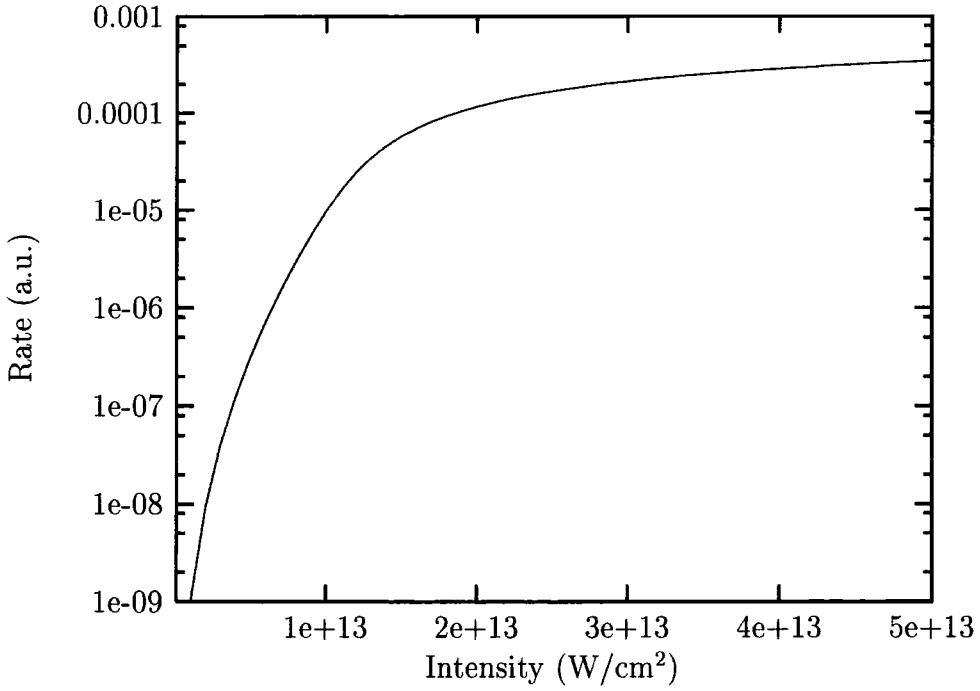

Figure 4.3: Total rate of ionisation of H($1s$) by linearly polarised radiation at 204 nm. These results are calculated using the Sturmian-Floquet code.

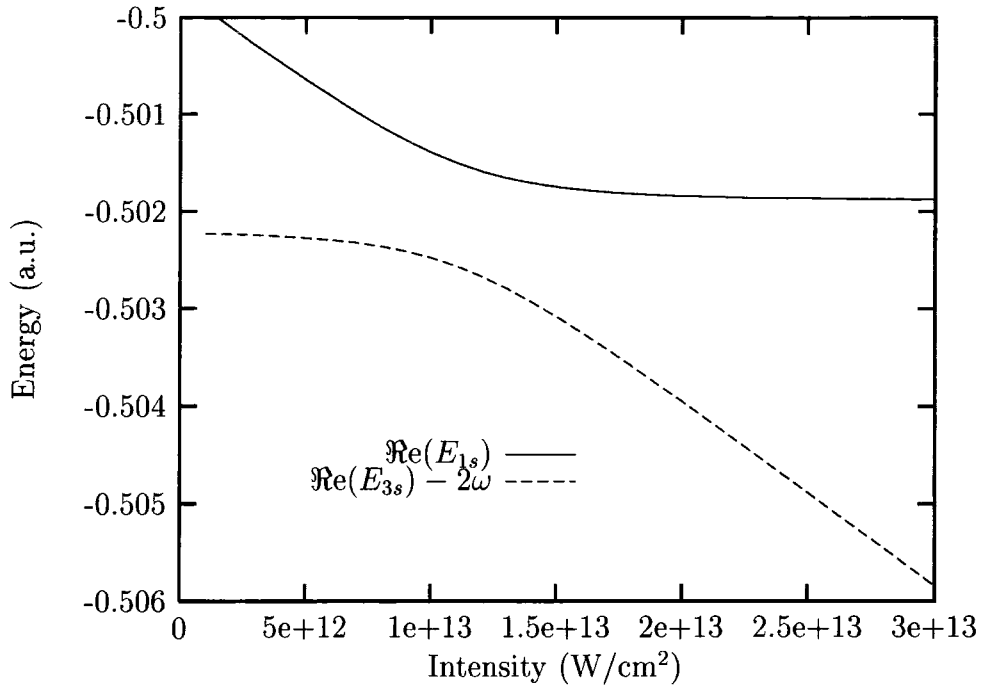

Figure 4.4: Avoided crossing between the (real) energies of H($1s$) and H($3s$) at 204 nm.

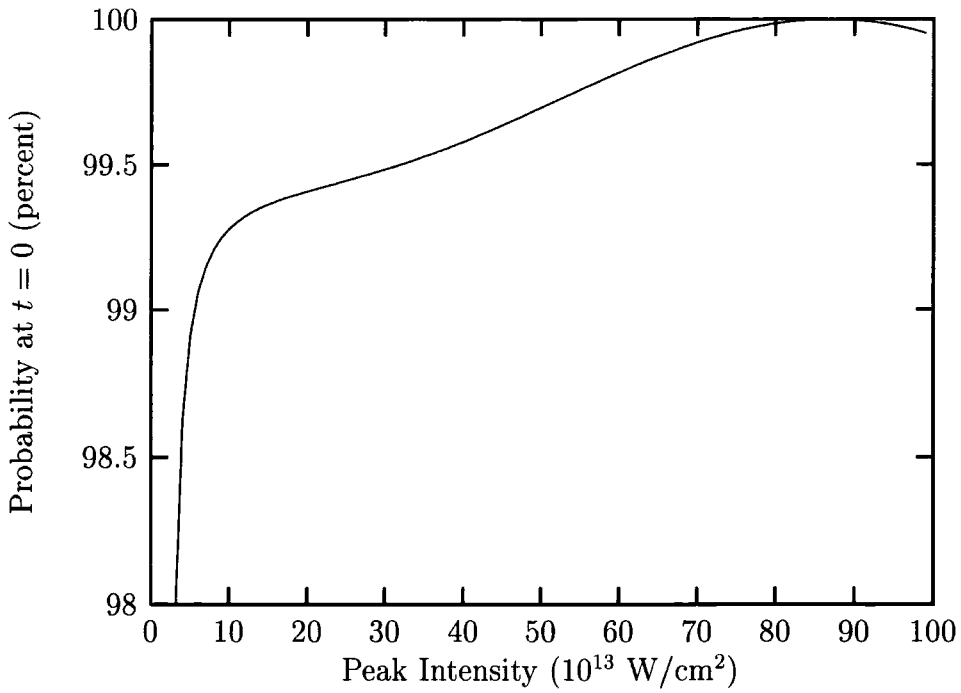

Figure 4.5: Probability of making a diabatic transition H($1s$) $\longrightarrow$ H($3s$) during a laser pulse of rapidly varying intensity at 204 nm.

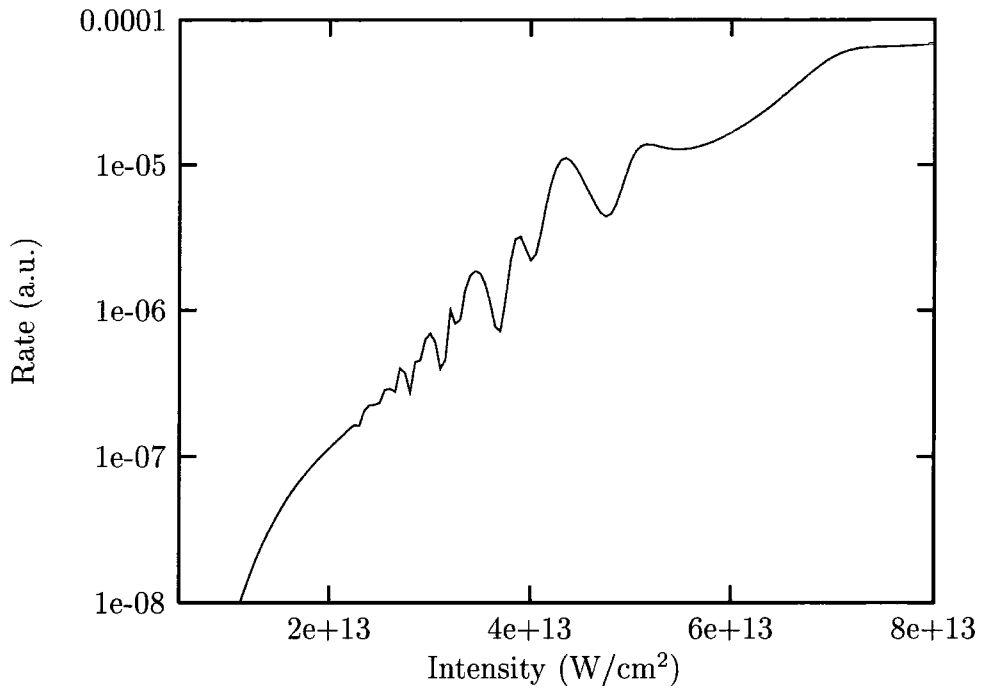

Figure 4.6: Total rate of ionisation of H($1s$) by linearly polarised radiation at 608 nm. These results are calculated using the Sturmian-Floquet code.

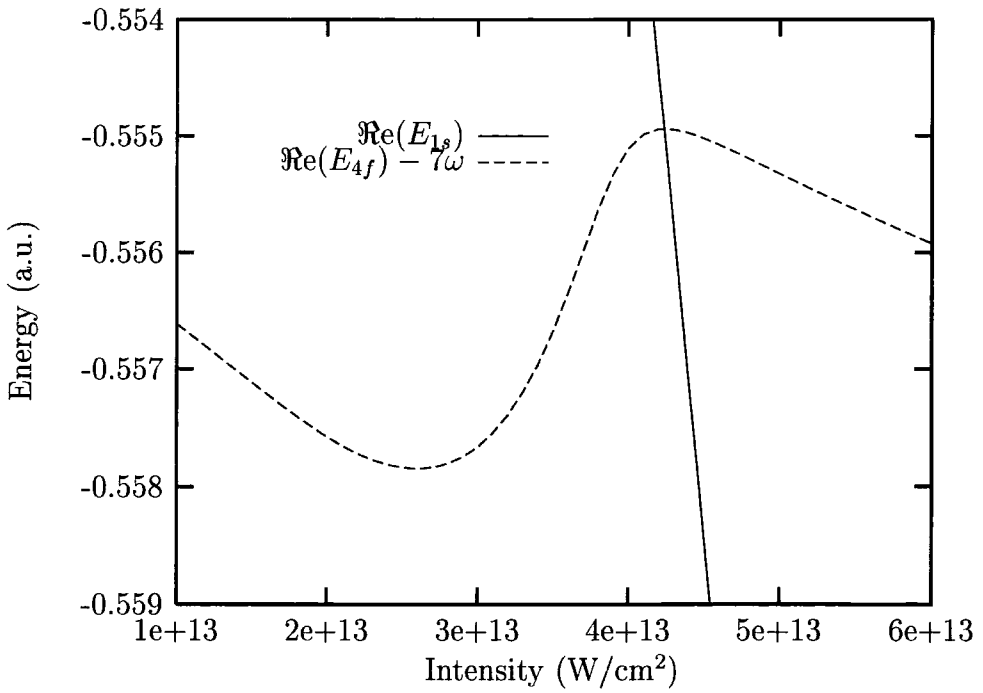

Figure 4.7: True crossing between the (real) energies of H($1s$) and H($4f$) at 608 nm.

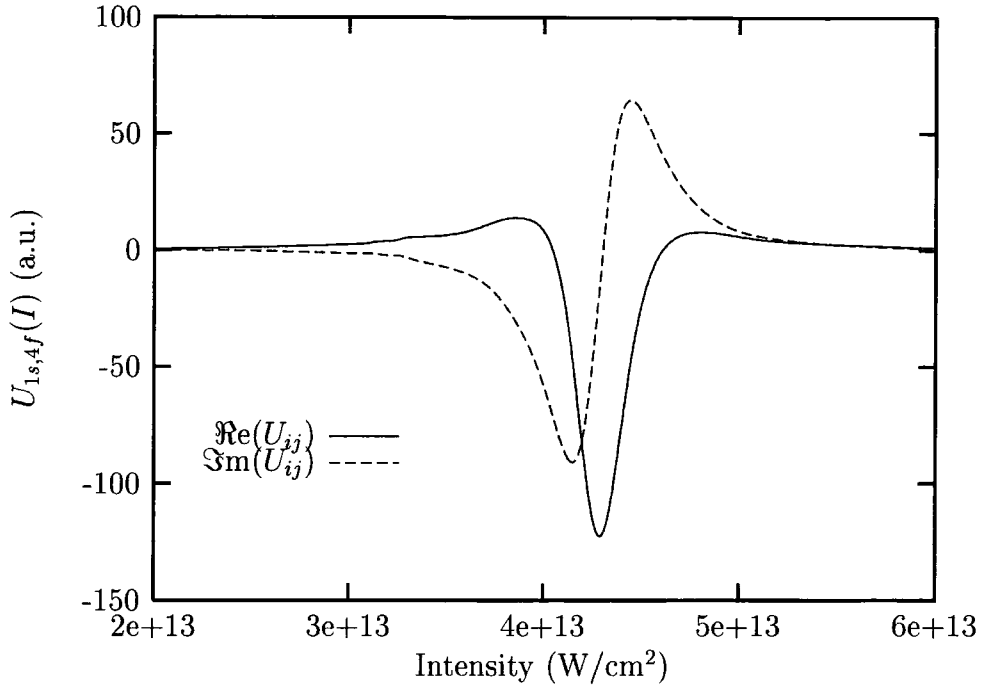

Figure 4.8: Matrix element of d/dI between the $1s$ and $4f$ states of Hydrogen at 608 nm.

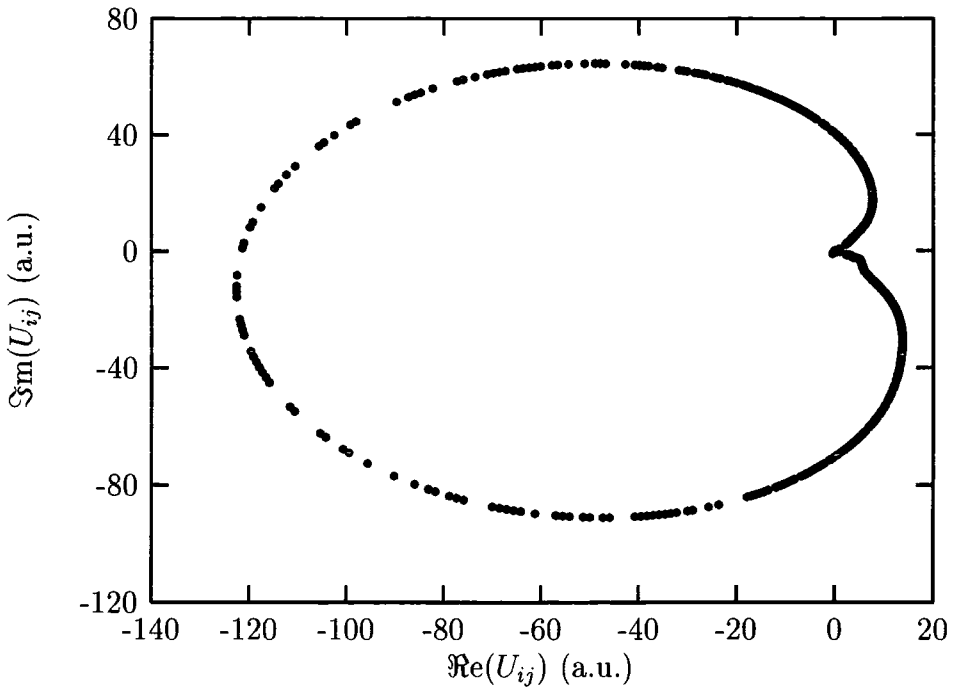

Figure 4.9: Matrix element of d/dI between the $1s$ and $4f$ states of Hydrogen at 608 nm.

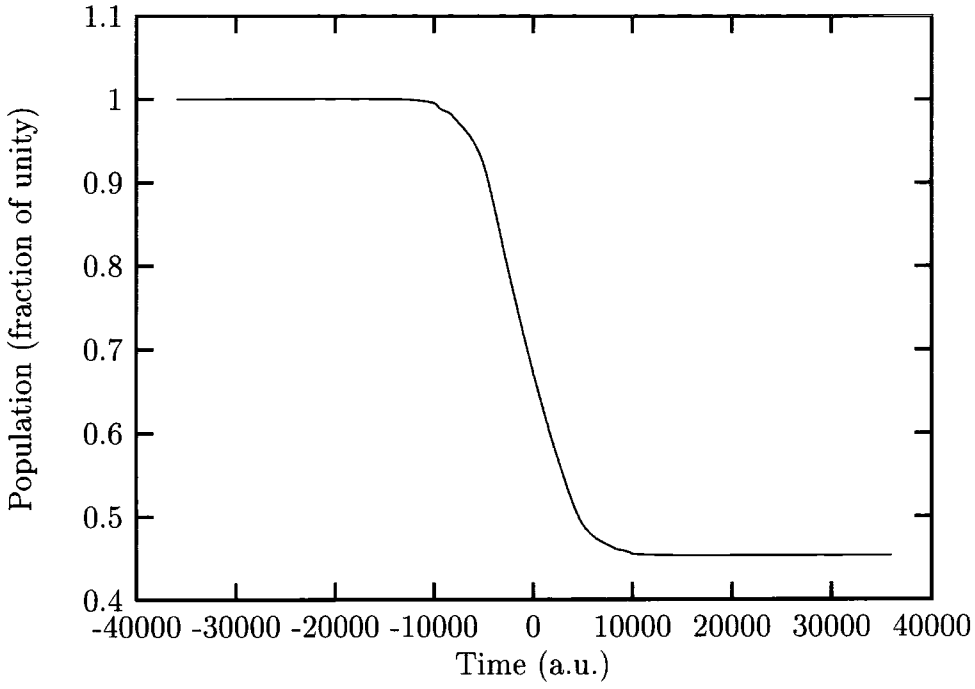

Figure 4.10: Population in the H($1s$) dressed state during a pulse of 1.74 ps at 608 nm. The $1s$ and $4f$ dressed states are coupled by a 7-photon resonance in a two-state model.

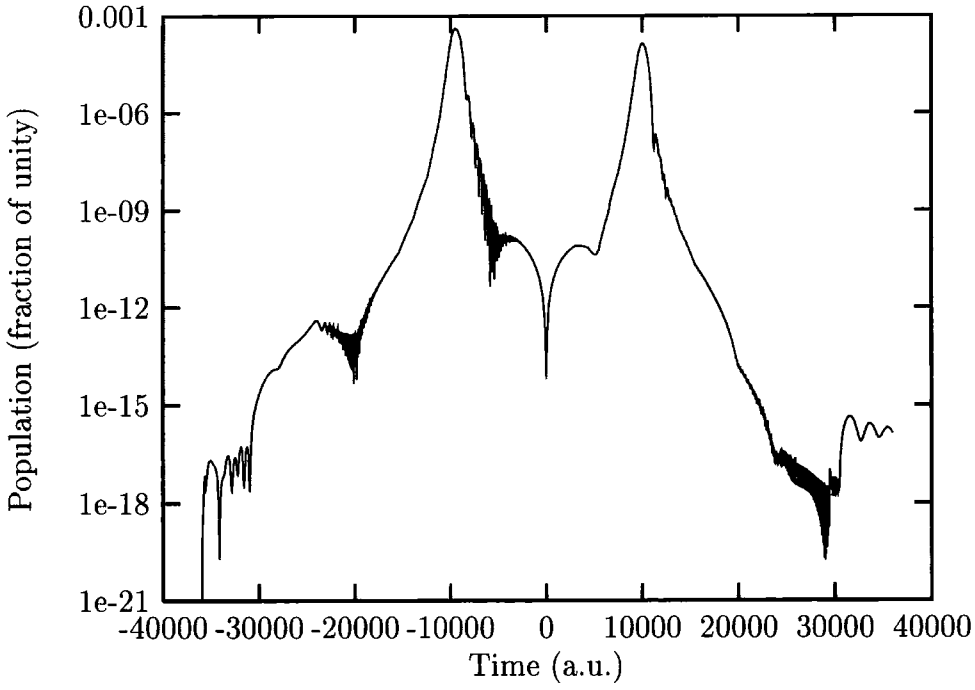

Figure 4.11: Population in the H($4f$) dressed state during a pulse of 1.74 ps at 608 nm. The $1s$ and $4f$ dressed states are coupled by a 7-photon resonance in a two-state model.

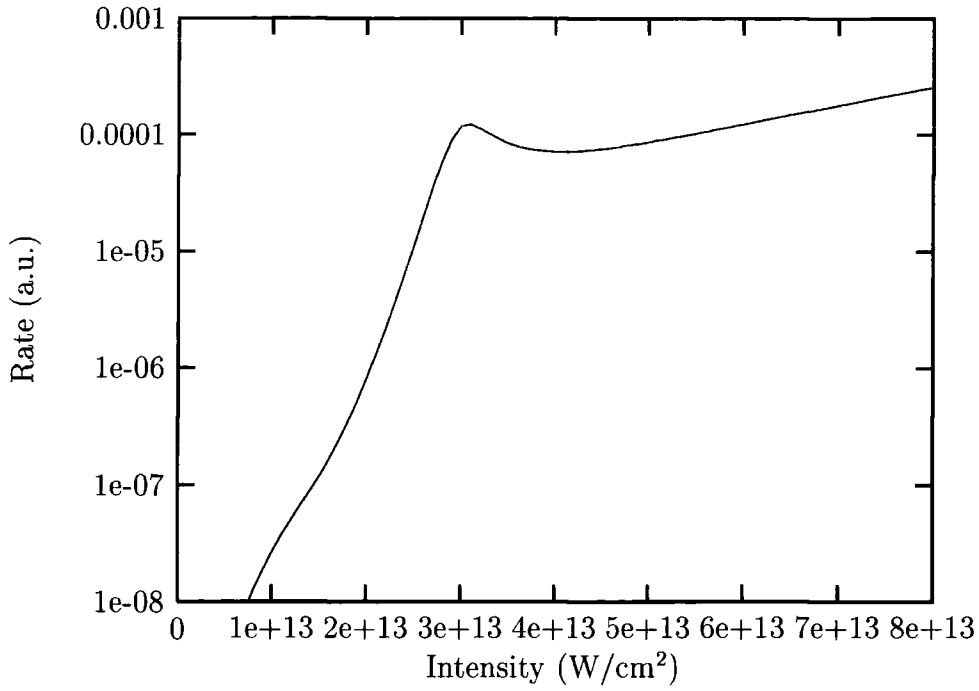

Figure 4.12: Total rate of ionisation of H($1s$) by linearly polarised radiation at 300 nm. These results are calculated using the Sturmian-Floquet code.

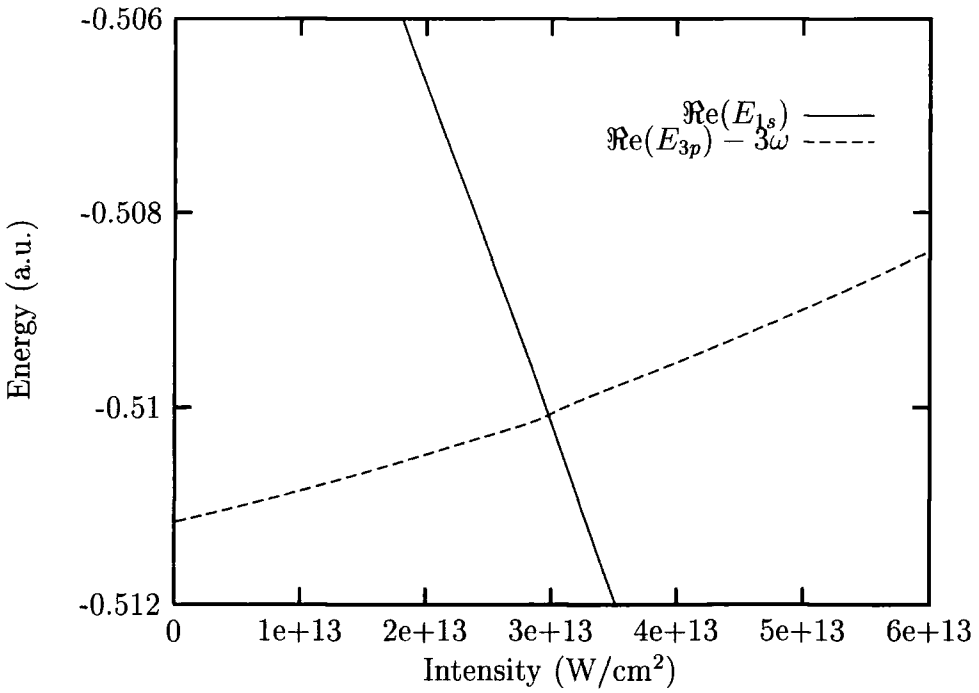

Figure 4.13: True crossing in the (real) energies of H($1s$) and H($3p$) at 300 nm.

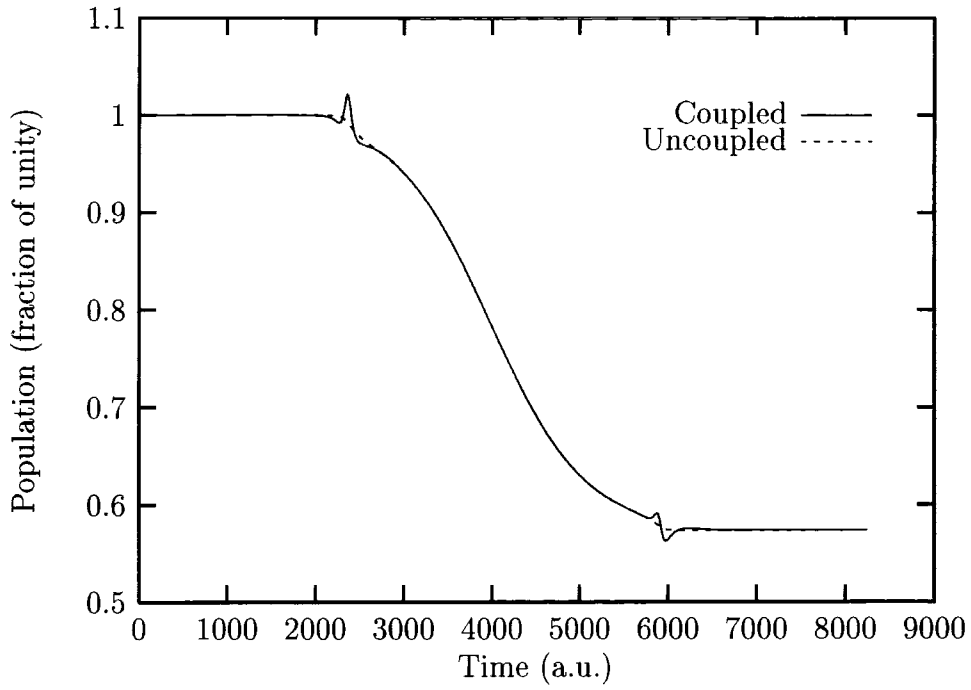

Figure 4.14: Population in the H($1s$) dressed state during a laser pulse of 200 cycles at 300 nm. The $1s$ and $3p$ dressed states are coupled by a 3-photon resonance in a two-state model.

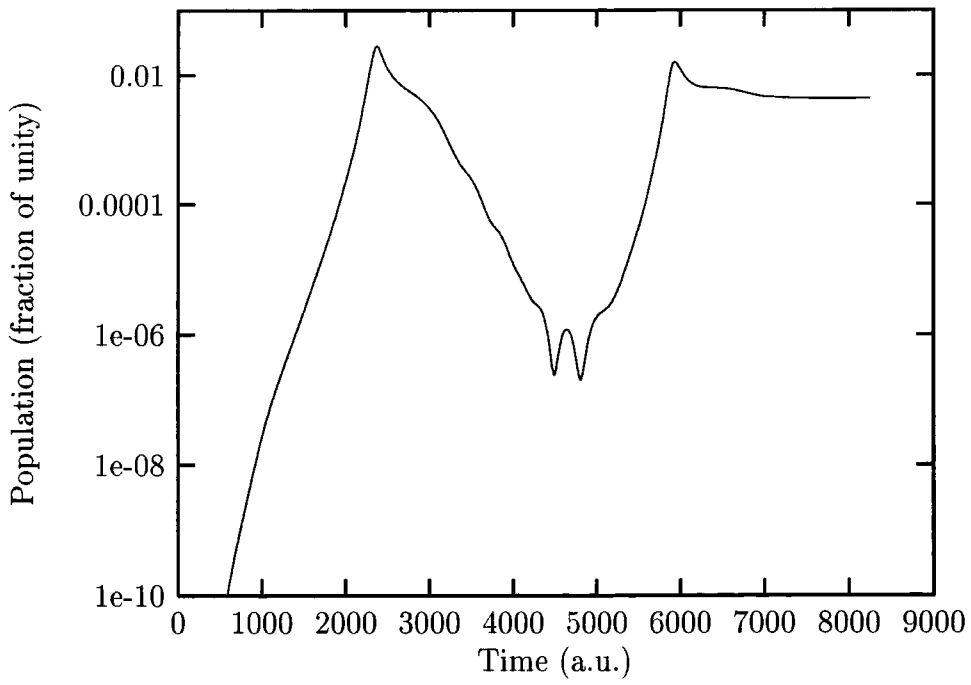

Figure 4.15: Population in the H($3p$) dressed state during a laser pulse of 200 cycles at 300 nm. The $1s$ and $3p$ dressed states are coupled by a 3-photon resonance in a two-state model.

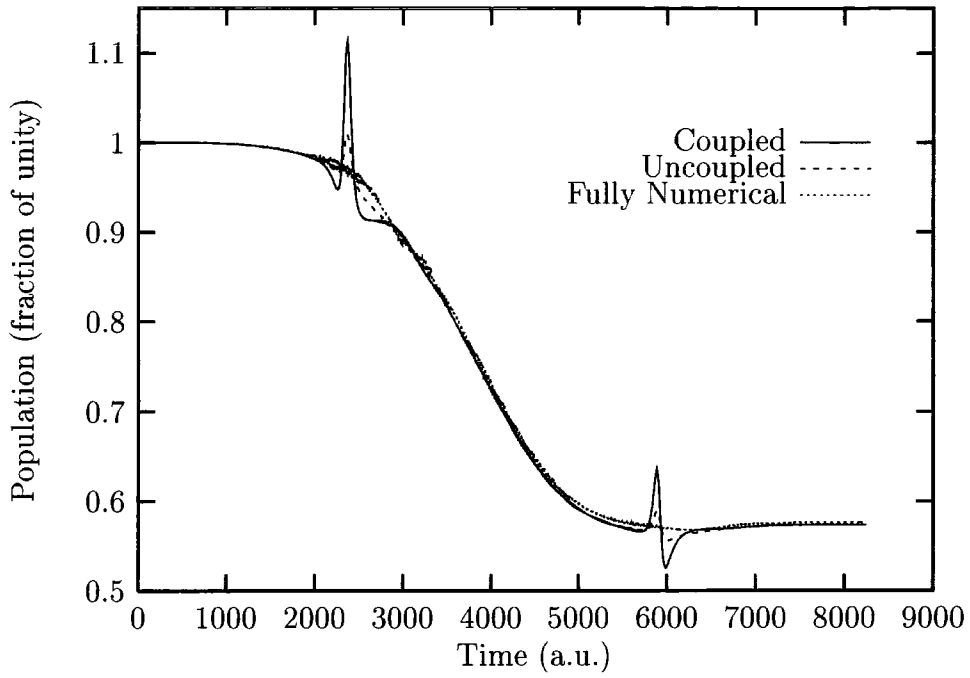

Figure 4.16: Population in the H($1s$) atomic state during a laser pulse of 200 cycles at 300 nm. The populations displayed in this figure have been time-averaged over half the optical period.

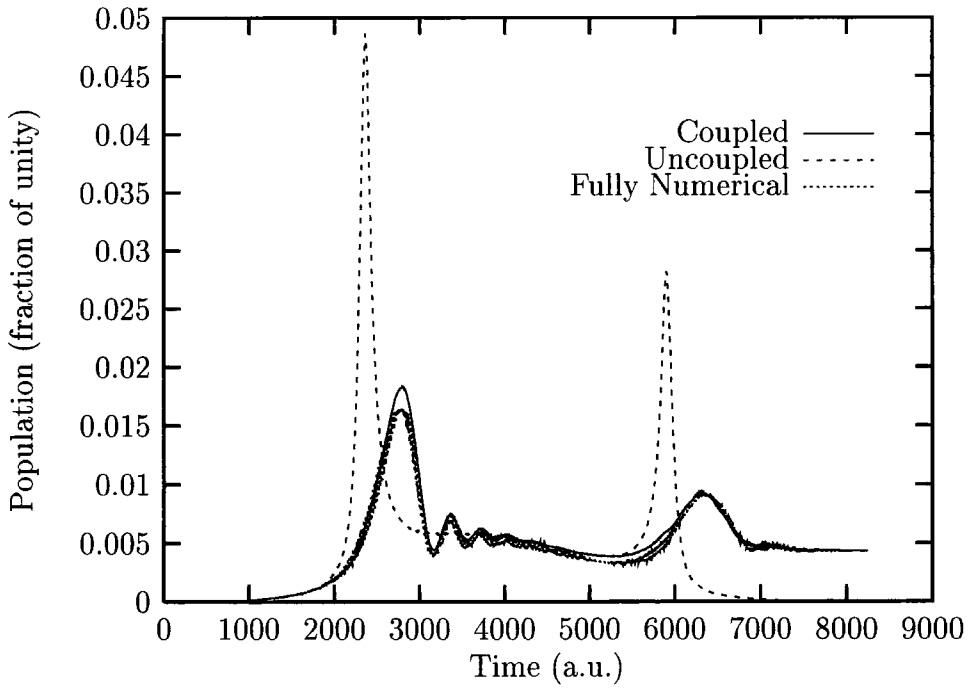

Figure 4.17: Population in the H($3p$) atomic state during a laser pulse of 200 cycles at 300 nm. The populations displayed in this figure have been time-averaged over half the optical period.

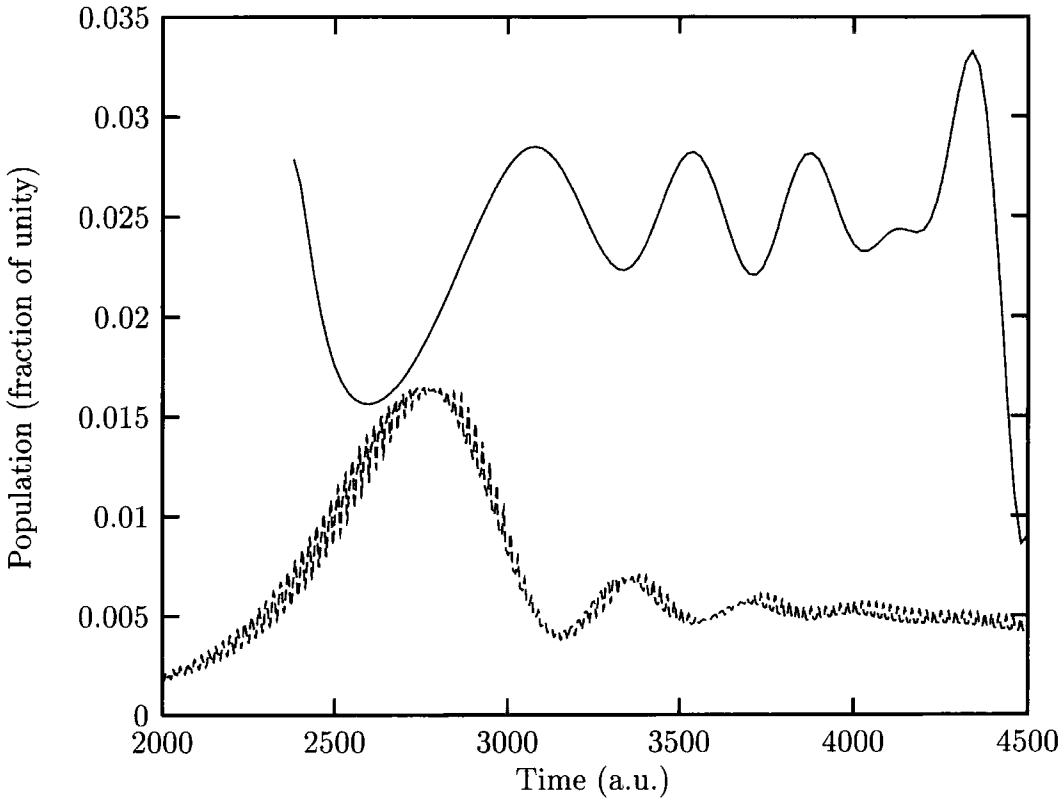

Figure 4.18: Oscillations in the dressed H($3p$) population after compensation for exponential decay. Curves are: (———) decay-compensated dressed $3p$ population from the coupled-states caclulation; (– – – –) cycle-averaged atomic $3p$ population from the time-dependent calculation.

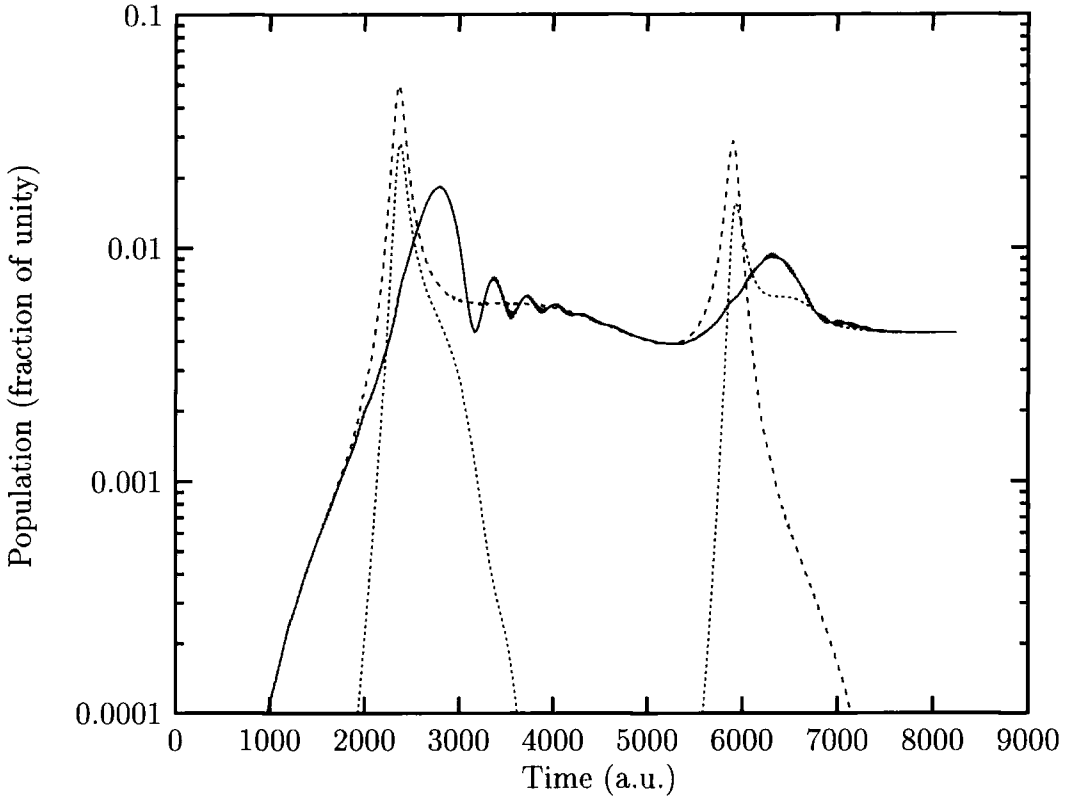

Figure 4.19: Contributions from the dressed states to the cycle-averaged atomic $3p$ population. Curves are: (———) total atomic 3p population; (– – – –) contribution from the dressed $1s$ state; (- - - - - -) contribution from the dressed $3p$ state.

Chapter 5

Sturmian-Floquet Calculations for Atomic Hydrogen

5.1 Introduction

Throughout this century the Hydrogen atom has very often proved to be the ideal testing ground for pioneering conceptual work within all branches of theoretical physics. In saying this we include the early development of quantum theory in the 1920s, continual analytical work taking advantage of the fact that the H-atom is only a two-body system, group-theoretical work of relevance to particle-physics [75] [43] [70], and laser-atom interactions in the context of (theoretical) atomic physics [21]. In particular, exact analytical expressions for the unperturbed Coulomb wave-functions are known for atomic Hydrogen. This allows us to write explicitly the multiphoton matrix elements since single-photon dipole matrix elements are expressed via a combination of two hypergeometric functions. While the same is not true of multi-electron atoms, the Hydrogen atom is a blue-print for more complex atoms and in many applications the conclusions drawn from Hydrogen may reasonably be extrapolated to these multi-electron atoms. Of course there are additional physical phenomena (e.g. electron-electron correlations and autoionising states) associated specifically with multi-electron atoms which cannot be deduced from the study of Hydrogenic systems. Accurate *ab initio* calculations are now possible for complex atoms in the absence of an external

field [16] and in the presence of one or more laser fields [17] [18] [19] [36] [84] but the necessity of taking into account all of the electron-electron interactions makes these calculations hugely demanding in terms of computer time. Of course, Hydrogen has never been an ideal subject for experiments and the most difficult aspect of measuring cross-sections for the Hydrogen atom is in producing a sufficiently intense source of the monatomic atoms. (Usually, microwave discharge is used to make H atoms from H_2 gas.) Experiments have instead been performed either with one of the noble gases (e.g. Helium [83], Neon [8] [9], Argon [139] or Xenon [3] [14] [25]) or with one of the Alkali elements (e.g. Sodium [54] or Cesium [40]) or with an Alkali-Earth (e.g. Magnesium [41]). These frequently involve preparing the atoms in a circular Rydberg state in order that the lifetime of the atom (due to selection rules) is relatively long.

We are interested here in the partial rates of ionisation and the angular distributions of those partial rates. By partial rates we mean the rates of ionisation Γ_N into each of the above-threshold ionisation channels corresponding to the absorption of $N \geq N_0$ photons where N_0 is the minimum number of photons required to ionise the atom. (See the discussion in section 2.4.3.) The partial rates, summed over all such channels, must equal the total (cycle-averaged) rate of ionisation, *viz.*

$$\sum_{N=N_0}^{\infty} \Gamma_N = \Gamma \tag{5.1}$$

and the partial rates themselves can be angle-resolved to give an angular distribution $d\Gamma_N/d\Omega$ (where $\Omega \equiv \sin\theta d\theta d\phi$) for the photo-electrons ejected with a given energy. For a linearly polarised beam the quantisation axis is usually taken along the electric field vector, i.e. perpendicular to the direction of propagation. However, within the dipole approximation the field is effectively homogeneous on the length-scale of the atom and so the propagation direction does not appear the equations describing the system. Instead one expects the distribution of photo-electrons to by cylindrically symmetric about the polarisation axis, allowing us to study these distributions as functions of θ only. If the radiation is circularly polarised then it is normal

to choose the quantisation axis to lie along the (positive) beam axis and the polarisation plane will of course be perpendicular to this. But once again there exists only one 'special' direction (the propagation-quantisation axis) and so the photo-electron distributions will be cylindrically symmetric about this axis. This simplification is not possible when the laser field is elliptically polarised and so for an arbitrarily polarised field one must study the angular distributions as functions of both θ and ϕ. In general, since the instantaneous (oscillating) electric field acts in the forward and backwards directions for equal portions of each optical period the distribution of photo-electrons is also symmetric in the forward and backward directions and we need only consider values of theta in the range $[0, \frac{\pi}{2}]$. An exception to this would be a beam comprising a superposition of odd and even harmonics and in this case one would have to examine the distribution over the range $\theta \in [0, \pi]$ in order to obtain a complete picture of the ionisation yield.

This picture of distinct ATI channels separated in energy by the photon energy ω is only valid in the multiphoton regime, i.e. for intensities at which the ionisation process can be described by the simultaneous absorption of many photons from the field. At very high intensities, but for long wavelengths ($\omega \ll E_I$), we enter the tunneling regime in which the dominant ionisation process is for the electrons to tunnel out directly through the barrier. This will only occur (assuming linearly polarised light) during narrow time-intervals (twice per optical cycle) during which the Coulomb barrier is strongly suppressed by the field *and* the time required by the electron to tunnel out [90] is sufficiently short (i.e. much shorter than the time during which this process is at all probable). In the tunneling regime the electrons may tunnel through the barrier with a range of energies, making the above-threshold photo-electron spectrum continuous rather than discrete. The electrons emitted in this manner will be ejected in the instantaneous direction of the oscillating field, i.e. strongly aligned with the polarisation vector, whereas photo-electrons due to multiphoton processes are expected to possess more structured angular distributions (see, e.g. the results presented in chapter two).

5.1.1 Theoretical Approaches

During the last decade or so great strides have been made both experimentally and theoretically in producing and understanding above-threshold ionisation spectra [57] [21] [150]. Theoretical efforts have concentrated on the Hydrogen atom but the conclusions drawn from this work have successfully been applied to recent and novel experimental data obtained using the noble gases [9] [100] [163]. In modelling theoretically these various experiments it is always instructive to perform both time-dependent and time-independent calculations because these methodologies are often complementary and may highlight different physical aspects. One of the most successful time-independent approaches, especially during the last decade, has been the Sturmian-Floquet theory in which the Floquet ansatz is made and the resulting Floquet Hamiltonian representing the set of time-independent, coupled, linear equations is projected onto a basis of complex Sturmian functions. (See Potvliege and Shakeshaft in [57].) The first detailed reports of such calculations were presented by Chu and Reinhardt [22] and by Maquet *et al* [92] although it should be stressed that their method is not identical to that currently employed. Specifically, Maquet *et al* perform a complex scale transformation on the position variables and solve the resulting eigenvalue problem on a basis of *real* L^2 functions whereas we retain the complex, non-Hermitian, *physical* Hamiltonian and solve on a basis of complex Sturmian functions. Further, these authors choose to represent the atom-field interaction in the length gauge whereas we prefer to work in the velocity gauge. Nonetheless, the development of the theory by Maquet *et al* contributed directly to the conception of the current Sturmian-Floquet theory.

An extensive theoretical description of Sturmian-Floquet theory was developed by Potvliege and Shakeshaft [116] [117] [118] [119] and applications of the theory have been presented in many subsequent papers by these authors. Partial rates of ionisation and the angular distributions of the photo-electrons were first calculated (using this method) by Potvliege and Shakeshaft [120]. However, at that time it was possible to consider only a monochromatic field

and a relatively small basis set of Sturmian functions, limiting the range of computations which could be performed. The theory was then generalised to include multi-coloured radiation but initially only for incommensurable frequencies (see chapter seven). The results of these calculations were presented by M Dörr *et al* [33]. Most recently, the Sturmian-Floquet code has been further developed by R M Potvliege and a brief summary of recent work by this author appears in [98]. Meanwhile, other approaches to the study of ATI spectra have also been taken, most notably the R-Matrix-Floquet theory, based on the early R-Matrix theory by Burke *et al* [5] [16] and developed over recent years by Burke, Franken and Joachain [17] [18] and by M Dörr *et al* [34] [36] [19] to model all aspects of the interactions between radiation fields and (in general) complex atoms or ions. In particular, the R-Matrix code presently in use is capable of performing two-colour calculations for both commensurable [10] and incommensurable frequencies [68]. Currently a time-dependent R-Matrix theory is also being developed [20] and will certainly provide fascinating comparisons with the time-independent Floquet version of the theory. Finally, while describing theories based on the Floquet formalism there is the *adiabatic theory* of Telnov and Chu [149] [150] which is a time-independent theory appropriate to very low-frequency fields (i.e. an approximate Floquet theory). Within this framework (valid for $\omega \ll E_I$) these authors have calculated photo-electron spectra and also the corresponding angle-resolved spectra. However their results reported so far encompass only monochromatic light fields.

Leaving Floquet methods behind entirely one comes to the fully time-dependent theories in which one integrates (numerically) the time-dependent Schrödinger equation. Many such calculations continue to yield important results but we would like to draw attention to the calculations of Véniard *et al* who have proceeded with numerical solutions of the (three-dimensional) time-dependent Schrödinger equation and have produced results covering many aspects of multiphoton processes in atomic Hydrogen [93] [151] [152]. They are concerned primarily with two-colour or multi-coloured photo-ionisation of H($1s$) where the additional colours are all high harmonics of the fundamental field

(i.e. commensurable frequencies). In particular the phase dependence of the ionisation rate and of the photo-electron spectrum is investigated and control of this phase (under some circumstances) facilitates a reversal of the ATI peak heights. A sophisticated manipulation of the specific ATI peaks becomes possible when several higher harmonics (referred to as a 'Dirac comb') are used together. What Véniard *et al* do not study, even in the two-colour case, is the angular distribution of the photo-electrons. Another theoretical treatment of two-colour ionisation in which one frequency is much higher than the other has been devised by A Cionga [23] [98]. This involves the so-called *radiative dressing approach* which is an improvement on the well-known Coulomb-Volkov method. In the latter method the initial state is taken to be an 'undressed' ground state and one represents the final state as a Coulomb-Volkov wave, *viz.*

$$\Psi(\boldsymbol{r},t) = \exp[i\boldsymbol{k}\cdot\boldsymbol{\alpha}(t)]\Psi_{\boldsymbol{k}}(\boldsymbol{r},t) \tag{5.2}$$

where $\boldsymbol{\alpha}(t)$ represents the quiver motion of a classical electron in the field and $\Psi_{\boldsymbol{k}}(\boldsymbol{r},t)$ is a Coulomb wave with incoming behaviour. In the method used by Cionga one applies radiative dressing to both the initial and final states of the atom in the field where this dressing is performed within first order perturbation theory. The method is therefore invalid for fields whose intensity exceeds a few 10^{12} W/cm^2 but is quite sufficient at most of the intensities currently being employed in two-colour calculations, (see Véniard *et al* [151] and chapter seven of this thesis). The advantage of this scheme is that the relevant S-matrix may be calculated analytically and this simplicity affords the possibility of some qualitative physical insights. Cionga's method enables the computation of angular distributions in addition to the partial rates of ionisation and in this respect is, as far as we are aware, the only published work on the angular dependence of the photo-ionisation spectrum for two-colour processes.

The present chapter is intended as an extended theoretical and technical overview of the various elements which are essential to an understanding of the results presented in both of the two succeeding chapters. In particular, sections 5.2 and 5.3 deal with theoretical considerations while section 5.4

describes and explains the values that we have taken for the various computational parameters which arise in the Sturmian-Floquet code. In chapters six and seven respectively we present our own results for the multiphoton ionisation of H($1s$) by a monochromatic circularly polarised field and by a bichromatic linearly polarised field. In both cases we examine in detail the quasi-energies, total (cycle-averaged) rates of ionisation, partial rates of ionisation and angular distributions of the photo-electron spectra. We do this over a range of intensities encompassing different dynamical regimes and, in the case of the two-colour calculation we also vary the relative phase of the two beams.

5.2 Sturmian-Floquet Theory

The Sturmian-Floquet method has been developed over the last decade and is most readily applicable to the problem of a Hydrogen atom (or another one-electron ion) in a laser field. The method can comfortably deal with polychromatic incident radiation but in applications become intractable when more than one of the beams has a high intensity. In describing the method we will, for simplicity, assume a monochromatic field but in chapter seven this will be generalised to the case of a two-colour field. Further, we assume that the laser field is homogeneous over atomic dimensions (i.e. the dipole approximation) and we work in the velocity gauge. In this gauge the interaction of the atom with the field is contained in the time-dependent potential

$$H_I(t) = -\frac{1}{c}\boldsymbol{A}(t)\cdot\boldsymbol{p} \tag{5.3}$$

where $\boldsymbol{p}$ is the canonical momentum of the electron in the atomic centre-of-mass frame. Note that this potential does not include the term in $\boldsymbol{A}^2$ which, within the dipole approximation, can be removed by a simple gauge transformation. As described in earlier chapters we write the time-dependent potential as the sum of two parts

$$H_I(t) = V_+ \mathrm{e}^{-i\omega t} + V_- \mathrm{e}^{i\omega t} \tag{5.4}$$

where

$$V_+ = -\frac{1}{2c}\boldsymbol{A_0}\cdot\boldsymbol{p} \tag{5.5}$$

and $V_- = V_+^\dagger$. We make the standard Floquet ansatz

$$\Psi(\boldsymbol{r},t) = \mathrm{e}^{-iEt}\sum_{N=-\infty}^{\infty}\mathrm{e}^{-iN\omega t}\,\psi_N(\boldsymbol{r}) \tag{5.6}$$

and substituting this into the time-dependent Schrödinger equation we obtain the coupled Floquet equations

$$(E+N\omega-H_A)\psi_N(\boldsymbol{r}) = V_+\psi_{N-1}(\boldsymbol{r}) + V_-\psi_{N+1}(\boldsymbol{r}) \tag{5.7}$$

Physically we must also impose the relevant boundary conditions, namely that the harmonic components $\psi_N(\boldsymbol{r})$ should be regular at the origin and should behave as a superposition of outgoing waves at $r\sim\infty$:

$$\psi_N(\boldsymbol{r}) \sim \sum_M f_{NM}(\hat{\boldsymbol{r}},E)r^{i\nu_M}\frac{\mathrm{e}^{ik_M r}}{r} \tag{5.8}$$

where the factor $r^{i\nu_M}$ takes account of the logarithmic distortion due to the tail of the (long-ranged) Coulomb function. Here, as previously, we interpret the atom as having absorbed N photons of which M are real photons and $N-M$ are virtual photons.

In the Sturmian-Floquet approach we now expand the harmonic components on a basis of complex Sturmian functions (for the radial component) and of the standard spherical harmonics

$$\psi_N(\boldsymbol{r}) = \sum_{lmn} F^{(N)}_{lmn}Y_{lm}(\hat{\boldsymbol{r}})\frac{1}{r}S^{(\kappa)}_{nl}(r) \tag{5.9}$$

where the radial Sturmian functions are given in terms of the associated Laguerre polynomials by

$$S^{(\kappa)}_{nl}(r) = N^{\kappa}_{nl}r^{l+1}\mathrm{e}^{i\kappa r}L^{2l+1}_{n-l-1}(2i\kappa r) \tag{5.10}$$

(where the N^{κ}_{nl} are normalisation constants) or in terms of the equivalent hypergeometric functions by

$$S^{(\kappa)}_{nl}(r) = \frac{1}{(2l+1)!}\sqrt{\frac{(n+l)!}{(n-l-1)!}}(-2i\kappa r)^{l+1}\mathrm{e}^{i\kappa r}\,{}_1F_1(l+1-n;2l+2;-2i\kappa r) \tag{5.11}$$

where the associated Laguerre polynomials are given by (4.116) and the (confluent) hypergeometric functions are defined by

$$ {}_1F_1(a;b;z) = \frac{\Gamma(b)}{\Gamma(a)} \sum_{j=0}^{\infty} \frac{\Gamma(a+j)}{\Gamma(b+j)\Gamma(1+j)} z^i, \qquad |\, z \,| < \infty \tag{5.12} $$

Expanding on a basis of complex Sturmians is equivalent to transforming the equations by complex scaling and expanding the wavefunctions on a real basis. In practice the number of non-zero terms in expansion (5.9) is significantly reduced by parity restrictions. Namely, if $\delta \equiv \pm 1$ is the parity of the initially unperturbed bound state then we have $F^{(N)}_{lmn} = 0$ unless $(-1)^N\delta = (-1)^l$ and there may be further restrictions due to azimuthal symmetries. For example, if the light is linearly polarised along the angular momentum quantisation axis and if the atom is initially in a state characterised by a well-defined magnetic quantum number m_0 then we have that $F^{(N)}_{lmn} = \delta_{mm_0} F^{(N)}_{lm_0n}$.

The wave-number κ is, in general, complex, while the radial variable r is real but appears only in the combination κr. For $r \approx \infty$ we have $S^{(\kappa)}_{nl}(r) \approx c_{nl} r^n \mathrm{e}^{i\kappa r}$ where c_{nl} is a constant, in accordance with (5.8). The orthonormality property

$$ \int_0^{\infty} dr S^{(\kappa)}_{n'l}(r) \frac{1}{r} S^{(\kappa)}_{nl}(r) = \delta_{n'n} \tag{5.13} $$

can be analytically continued throughout the complex κ-plane. In fact, any well behaved function $f(r)$ that vanishes as r^{l+1} for $r \approx 0$ and behaves as an outgoing wave $r^v \mathrm{e}^{i\kappa r}$ for $r \approx \infty$ can be expanded as

$$ f(r) = \sum_n f_n S^{(\kappa)}_{nl}(r) \tag{5.14} $$

with coefficients f_n that vanish for $n \approx \infty$ provided that [142] [115]

$$ |\, \arg(\kappa) - \arg(k) \,| < \frac{\pi}{2} \tag{5.15} $$

Recall from chapter two that $k_M(E)$ is a double-valued function of the complex quasi-energy E but that in order for the wavefunction to satisfy physical boundary conditions there is only one correct sign for k_M. If M-photon absorption is an open channel then the vector k_M lies almost parallel to, but

just below, the positive real axis (of the complex k-plane), making an angle of less than θ_o with this axis, where

$$\tan(\theta_o) = \frac{\Gamma}{2[E_0 + N_0(I)\omega]} \tag{5.16}$$

with quasi-energy $E = (E_0 + \Delta - i\Gamma/2)$ and where $N_0(I)$-photon ionisation is the lowest open channel at the intensity I. If on the other hand M-photon ionisation is a closed channel then $k_M(E)$ points almost parallel to the positive imaginary axis (in the k-plane) but slightly to the left of it by an angle smaller than θ_c where

$$\tan(\theta_c) = -\frac{\Gamma}{2[E_0 + (N_0 - 1)\omega]} \tag{5.17}$$

Thus the boundary conditions (see equation 5.8) are implicitly satisfied by the choice of κ which must lie in the upper-right-hand quadrant of the complex k-plane such that

$$\theta_c < \arg(\kappa) < \frac{\pi}{2} - \theta_o \tag{5.18}$$

This choice ensures that the basis functions oscillate and decrease exponentially at large distance. (Note that this scenario is quite different from that for the Sturmian expansion of the Coulomb Green's function [29] in which one takes either $\arg(\kappa) = 0$ or $\arg(\kappa) = \pm\pi/2$ depending on the energy.) Ideally one would take various values of κ within a single basis set but due to computational considerations we find it more convenient to restrict ourselves to just a single value. Taking just one value of κ is then equivalent to performing a complex dilatation $r \to r\exp(i\theta)$ in the Floquet equations and then solving the resulting eigenvalue problem on a basis of real L^2 functions, however we prefer to retain the real Hamiltonian with the complex basis.

Let us introduce the matrix operator H_{NM} where

$$H_{NM} = (H_A - N\omega)\delta_{N,M} + V_+\delta_{N,M+1} + V_-\delta_{N,M-1} \tag{5.19}$$

and we can now rewrite equation (5.7) as

$$\sum_M H_{NM} \mid \psi_M\rangle = E \mid \psi_N\rangle \tag{5.20}$$

Further we project equation (5.19) onto the basis of Sturmian functions and thereby obtain a set of coupled linear equations for the expansion coefficients $F_{lmn}^{(N)}$ of the harmonic components ψ_N,

$$\bar{\boldsymbol{H}}\boldsymbol{y} = E\boldsymbol{N}\boldsymbol{y} \tag{5.21}$$

where $\boldsymbol{y}$ is a column vector comprising all of the expansion coefficients, $\bar{\boldsymbol{H}}$ is the square matrix that is the basis-set representation of the operator matrix whose elements are H_{NM} and $\boldsymbol{N}$ is the block-diagonal matrix whose diagonal blocks are submatrices that are just basis-set representations of the identity operator. One should note here that $\bar{\boldsymbol{H}}$ is a block tri-diagonal matrix in which each block is a square submatrix representing the operator H_{NM}. If one were instead to have retained the $\boldsymbol{A}^2$ term in the interaction potential (5.3) then $\bar{\boldsymbol{H}}$ would be block quintidiagonal and, although still sparse, this would amount to a very significant increase in the size of the computation.

The matrix $\bar{\boldsymbol{H}}$ consists typically of many thousands of rows and columns, making the method of choice for solving equation (5.21) for a (single) eigenvalue and corresponding eigenvector that of inverse iteration [129]. A brief description is as follows (but see also section 2.3 of this thesis and Potvliege and Shakeshaft in [57]). One obtains the true eigenvector $\boldsymbol{y}$ by iterating the matrix equation

$$(\bar{\boldsymbol{H}} - E'\boldsymbol{N})\boldsymbol{y}^{(j+1)} = \boldsymbol{N}\boldsymbol{y}^{(j)} \tag{5.22}$$

where E' is an initial guess for the (complex) quasi-energy E. After j iterations, each component of eigenvector $\boldsymbol{y}^{(j)}$ converges, up to some overall normalisation towards the corresponding component of the true eigenvector $\boldsymbol{y}$, although some components will converge faster than others. With a good guess for E' convergence will typically have been achieved in all components while j is still in single figures and if j reaches fifty with some channels remaining unconverged it is unlikely that further iterations will improve matters. There are two conditions that must be fulfilled for convergence to take place: E' must be closer to E than to any other eigenvalue of $\bar{\boldsymbol{H}}$; and the initial trial-vector $\boldsymbol{y}^{(0)}$ must not be orthogonal to $\boldsymbol{y}$. Convergence is defined

by some pre-set tolerance, ϵ, in the ratios between corresponding components of the normalised eigenvector, $\tilde{\boldsymbol{y}}^{(j)}$, from successive iterations

$$\frac{\tilde{y}_i^{(j+1)}}{\tilde{y}_i^{(j)}} = 1 + \epsilon \tag{5.23}$$

where $\tilde{y}_i^{(j)}$ is the i^{th} component of the vector $\tilde{\boldsymbol{y}}^{(j)}$. This condition must be satisfied in *every* channel i and for good convergence one may specify a relative error, say, ($\epsilon < 10^{-4}$) with which one need not subsequently have to improve the eigenvalue by a variational method. After convergence the eigenvalue itself is given by

$$\boldsymbol{y}^{(j+1)} = \frac{1}{(E - E')}\boldsymbol{y}^{(j)} \tag{5.24}$$

Note that, once convergence has been reached, this eigenvalue E is given by the ratio of *any* component (labelled by i) to itself between consecutive iterations j and $j + 1$.

5.3 Derivation of Matrix Elements for N-Photon Ionisation

Let us now derive an expression for the partial rates of multiphoton ionisation and for the angular distributions of the photo-electrons into each of the above-threshold channels. In fact, we calculate first (for each channel $N \geq N_0$) the ionisation rate into each solid angle $d\Omega$ and then integrate over angles to obtain the partial rates Γ_N. At large times $t = T \sim \infty$ we can write the N-photon ionisation rate into a solid angle $d\Omega$ as

$$\frac{d\Gamma_N}{d\Omega} = \rho(E_f) dE \frac{d}{dT} \mid A_{fi}(\Omega, T) \mid^2 \tag{5.25}$$

where $\rho(E_f)$ is the density of 'final' states f in the (real) energy interval $(E_f, E_f + dE)$ and $A_{fi}(\Omega, T)$ is the ionisation amplitude from an initial state i to the final state f. This ionisation amplitude may be expressed as [116]

$$A_{fi}(\Omega, T) = -i \int_0^T dt \mathrm{e}^{i(E_f - E_i - \Delta_i)t} \sum_n M_n \mathrm{e}^{-in\omega t} \tag{5.26}$$

where E_i and E_f are then the unperturbed energies of the initial and final states respectively, Δ_i is the Stark shift of state i and M_n is an ionisation matrix element. Let us write

$$\beta \equiv E_f - E_i - \Delta_i - n\omega \tag{5.27}$$

then

$$A_{fi}(\Omega, T) = -i \sum_n M_n \int_0^T dt e^{i\beta t} \tag{5.28}$$

but we know that

$$\int_0^\infty dt e^{i\beta t} = i\mathcal{P}\left(\frac{1}{\beta}\right) + \pi\delta(\beta) \tag{5.29}$$

where $\mathcal{P}(1/\beta)$ is the (finite) principal part of the integral. For a group of states within a narrow energy bandwidth this part of the solution does not contribute to the ionisation rate, so we obtain

$$A_{fi}(\Omega, T) = -i\pi \sum_n M_n \delta(E_f - E_i - \Delta_i - n\omega) \tag{5.30}$$

For simplicity we set $E_{in} = E_i + \Delta_i + n\omega$ and then the ionisation amplitude becomes

$$A_{fi}(\Omega, T) = -i\pi \sum_n M_n \delta(E_f - E_{in}) \tag{5.31}$$

Returning to equation (5.26) we obtain for the time-derivative of the ionisation amplitude

$$\frac{d}{dT} A_{fi}(\Omega, T) = -i \sum_n M_n e^{i(E_f - E_{in})T} \tag{5.32}$$

and noting that

$$\frac{d}{dT} \mid z \mid^2 = \frac{d}{dT}(zz^*) = z\frac{dz^*}{dT} + \frac{dz}{dT}z^* \tag{5.33}$$

we find that

$$\frac{d}{dT} \mid A_{fi}(\Omega, T) \mid^2 = 2\pi \sum_{nm} M_n M_m^* e^{-i(E_{in} - E_{im})T} \tag{5.34}$$

Further, we take the cycle-average of this expression,

$$\frac{\omega}{2\pi} \int_0^{2\pi/\omega} dT \frac{d}{dT} \mid A_{fi}(\Omega, T) \mid^2 = \omega \sum_{nm} M_n M_m^* \int_0^{2\pi/\omega} dT e^{-i(E_{in} - E_{im})T} \tag{5.35}$$

Clearly, this expression is only non-zero for $n = m$, and so we are left with

$$\frac{\omega}{2\pi}\int_0^{2\pi/\omega} dT \frac{d}{dT} \mid A_{fi}(\Omega, T) \mid^2 = 2\pi \mid M_N \mid^2 \tag{5.36}$$

where $N \equiv n = m$. Now, in equation (5.25) the density of states factor $\rho(E_f)$ is determined by the normalisation convention used for the final-state wavefunction $\mid \Psi_f\rangle$ for the electron in the absence of the field. We take this normalisation condition to be

$$\langle \Psi_f(\boldsymbol{k}) \mid \Psi_f(\boldsymbol{k'})\rangle \ = \delta^3(\boldsymbol{k} - \boldsymbol{k'}) \tag{5.37}$$

where $\boldsymbol{k}$ is the momentum vector of the outgoing electron. Thus $\rho(E_f) = 1/(16\pi^2)$ and we obtain our angular N-photon rate

$$\frac{d\Gamma_N}{d\Omega} = 2\pi \frac{1}{16\pi^2} \mid M_N \mid^2 \tag{5.38}$$

Another important theoretical consideration is the manner in which one chooses to normalise the Floquet wavefunction. Note that, since all states of an atom in an electric field, however weak, are decaying, the expression $\langle \Psi \mid \Psi\rangle$ is divergent. Instead we take the cycle-average of a scalar product of the time-reversal operator $\mathcal{T}^\dagger$ taken over the spatial variables

$$\frac{\omega}{2\pi}\int_0^{2\pi/\omega} dt \left\langle \tilde{\Psi}\left(-t + \frac{\pi}{\omega}\right) \middle| \mathcal{T}^\dagger \middle| \Psi(t)\right\rangle = 1 \tag{5.39}$$

where $\mid \tilde{\Psi}(t)\rangle$ differs from $\mid \Psi(t)\rangle$ in that the angular momentum of the electron is reversed and the direction of propagation and sense of polarisation of the light are also reversed. The physical reason for the inclusion of the time-reversal operator is that without it the norm of the wavefunction decays with time as $\mathrm{e}^{-\Gamma t}$ where Γ is the cycle-averaged decay rate for a specific atomic state, whereas if - when taking the norm - one applies time-reversal to one of the wavefunctions then the flux which is lost through the decay of the unreversed function is balanced by the incoming flux from the time-reversed wavefunction. In the special case that the atom is initially in the $1s$ state and that the laser field is linearly polarised the normalisation condition (5.39) reduces to [114]

$$\sum_N (\psi_N \mid \psi_N) = 1 \tag{5.40}$$

where the scalar product $(x \mid y)$ is taken *without* complex conjugation [119], *viz.*

$$(x \mid y) \equiv \int d^3\boldsymbol{r}\, x(\boldsymbol{r}) y(\boldsymbol{r}) \tag{5.41}$$

When the field is not linearly polarised the corresponding recipe is to complex conjugate the angular terms (i.e. the spherical harmonics) but not the radial term [127].

Further, we can integrate equation (5.38) over angles to obtain the N-photon rate

$$\Gamma_N = \int d\Omega \left(\frac{d\Gamma_N}{d\Omega} \right) \tag{5.42}$$

and then sum over the ATI channels to write the total rate of ionisation as

$$\Gamma = \sum_{N \geq N_0} \Gamma_N \tag{5.43}$$

In fact, this method of calculating Γ is independent of the value obtained from the quasi-energy, $\Gamma = -2\Im\mathrm{m}(E)$, and the equivalence of these two expressions constitutes an important check on the overall accuracy of the calculation. Next, we require an expression for the N-photon matrix element M_N appearing in equation (5.38). This is a coherent sum of the amplitudes $f_{NM}(\hat{\boldsymbol{r}}, E)$ defined in equation (5.8). Note that in the velocity gauge the harmonic components $\mid \psi_N \rangle$ include contributions from the absorption and emission of virtual as well as real photons. This index N labels the number of real photons, M is the total number of photons absorbed, and so $M - N$ is the number of virtual absorptions. Let us define the real quantities R and χ by

$$R\mathrm{e}^{i\chi} = -\frac{1}{\omega c} \boldsymbol{k_f} \cdot \boldsymbol{A_0} \tag{5.44}$$

where $\boldsymbol{k_f}$ is the momentum vector of the ejected electron, as described above. Two equivalent expressions for M_N are derived in the appendix to reference [117]. These are

$$M_N = \sum_M \mathrm{e}^{i(N-M)\chi} J_{M-N}(R) \, \langle \Psi_f \mid (H_A^\dagger - H_A) \mid \psi_M \rangle \tag{5.45}$$

and

$$M_N = \frac{1}{J_0(R)} \left[\langle \Psi_f \mid V_+ \mid \psi_{N-1} \rangle + \langle \Psi_f \mid V_- \mid \psi_{N+1} \rangle \right] \tag{5.46}$$

where $J_M(z)$ is the regular Bessel function. In the first of these expressions we see that for every harmonic component $\mid \psi_M \rangle$ there exists a term (corresponding to the term in $f_{NM}(\hat{\boldsymbol{r}}, E)$ is equation (5.8)) which contributes to the amplitude for the absorption of N real photons. In equation (5.46) only two of the harmonic components appear explicitly but contribution from the others are (in part) implicitly included through the Bessel function $J_0(R)$. The equivalence of equations (5.45) and (5.46) provides a second check on the accuracy of our numerical methods.

5.4 The Sturmian-Floquet Code

The code used to perform the calculations described in this chapter has been developed over a number of years, principally by R M Potvliege, but with contributions in the early stages also by R Shakeshaft and M Dörr. The capabilities of the code are, for a one-electron atom in an AC or DC electric field (or fields) of arbitrary frequency, intensity and polarisation, to calculate: the Stark shift and cycle-averaged decay rate of the atom; the partial rates of ionisation into the above-threshold channels; the angular distribution of the photo-electrons into each of those channels; and the rate of harmonic generation. The laser field may be monochromatic or polychromatic (subject to the size of the resulting matrices) with either commensurable or incommensurable frequencies, the beams may be either co-linear or alternatively subtend some angle at the atom, and a phase difference at time $t = 0$ between the two beams may be specified. Further, the electronic mass may be either 1.0 a.u. or the appropriate reduced mass and the calculation may be performed either perturbatively or non-perturbatively. Most importantly, in a calculation performed on a basis of complex Sturmian functions, the parameters of the Sturmian basis are to be specified and should be tailored to suit a given combination of atom plus field.

Recall from the expansion of the harmonic components on the basis of Sturmians and spherical harmonics, (5.9),

$$\psi_N(\boldsymbol{r}) = \sum_{lmn} F^{(N)}_{lmn} Y_{lm}(\hat{\boldsymbol{r}}) \frac{1}{r} S^{(\kappa)}_{nl}(r)$$

that we need to specify the ranges of the photon number N, the angular momentum l, the number of Sturmian functions $n_{bf} \equiv \max.(n)$ to be used per $\{l, m\}$-channel, and the Sturmian parameter κ. This last item, κ, is a complex number and is in fact specified by two real parameters, θ_r and $\mathcal{E}_{\rm st}$:

$$\theta_r = 90^\circ - \arg(\kappa), \qquad \mathcal{E}_{\rm st} = -\frac{1}{2} \mid \kappa \mid^2 \qquad \text{a.u.} \qquad (5.47)$$

In practice, one chooses $5^\circ \leq \theta_r \leq 30^\circ$ and $-0.3 \leq \mathcal{E}_{\rm st} \leq -0.05$ a.u.. For calculations involving many channels the inverse iteration will typically only converge to the quasi-energy within a narrow window for each of θ_r and $\mathcal{E}_{\rm st}$. The Sturmian-Floquet code was first used to calculate the partial rates of ionisation and their angular distributions in 1990 [120] and at that time it proved impossible to obtain any converged results for ionisation of H($1s$) by linearly polarised light of 1064 nm at intensities beyond the perturbative regime. The source of this difficulty was the high threshold number of photons ($N_0 = 12$) required for photo-ionisation to occur at this wavelength. Instead, the authors chose the wavelength 532 nm at which only six photons are required to ionise the atom and, at intensities of around 2×10^{13} W/cm^2, a typical basis set was: $-8 \leq N \leq 21$, $0 \leq l \leq 11$, $n_{bf} = 80$, $\theta_r = 15^\circ$ and $\mathcal{E}_{\rm st} = -0.075$ a.u.. Then, in the Monte Carlo simulation of the Bielefeld experiment in 1993 [125] [135], the partial rates were calculated for the ionisation of H($1s$) by a linearly polarised beam of $\lambda \approx 600$ nm at intensities up to 8×10^{13} W/cm^2. The basis set required for this was: $-12 \leq N \leq 31$, $0 \leq l \leq 9$, $n_{bf} = 71$, $\theta_r = 15^\circ$ and $\mathcal{E}_{\rm st} = -0.075$ a.u..

In the present calculations (1997) for the ionisation of H($1s$) by circularly polarised monochromatic radiation of 608 nm at intensities of up to 8×10^{14} W/cm^2 (see chapter six) we take (typically), $-8 \leq N \leq 41$, $0 \leq l \leq 45$, $n_{bf} = 110$, $\theta_r = 10^\circ$, $\mathcal{E}_{\rm st} = -0.25$ a.u. and $n_{lm} = 8$. This last parameter n_{lm} is the number of channels (running over l and m) which are to be taken

into account for each value of N. When the beam is linearly polarised then there is no variation in m and this parameter is determined simply from the maximum value of l by including only the channels allowed by parity: for max.(l) odd we have $n_{lm} = (l_{\max} + 1)/2$ whereas for max.(l) even we have $n_{lm} = (l_{\max} + 2)/2$. When the beam is circularly polarised we need, for a given N, only to consider the channels with $l \geq N$ and here n_{lm} is the number of such channels to be included, again allowing for parity. Note that in this case we must have $l_{\max} \geq N_{\max}$ but that for a given N only a subset n_{lm} from the large range of l are included. When the beam is elliptically polarised the corresponding expression for n_{lm} yields greater values than are listed above for linear polarisation and the size of n_{lm} is the primary difficulty in performing calculations with elliptically polarised radiation. In our calculations for the ionisation of H$(1s)$ by a linearly polarised beam at 1064 nm in combination with its 15^{th} harmonic (see chapter seven) we (typically) took the basis set: $-8 \leq N \leq 37$, $0 \leq l \leq 15$, $n_{bf} = 110$, $\theta_r = 7°$ and $\mathcal{E}_{\text{st}} = -0.20$ a.u.. At the highest intensities and when using a big basis set these calculations only converged for values of θ_r, $5° \leq \theta_r \leq 9°$.

As described in section 5.2, the matrix $\bar{\boldsymbol{H}}$ representing the system of coupled equations can be block-LU decomposed such that the largest inhomogeneous system of linear equations to be solved has only the dimension of the largest submatrix of $\bar{\boldsymbol{H}}$. This dimension is in fact the product of just two numbers: the number of radial basis functions n_{bf} per $\{l, m\}$; and the largest number of angular momentum components to be considered for a given block, i.e. n_{lm} itself. Thus, from the figures given above, we see that typically we are dealing with matrices of dimension $n_{bf} \times n_{lm} \approx 900$. In a large-scale application the CPU time required is roughly proportional to the number of harmonic components and to the cube of the dimension of the submatrices. The Sturmian-Floquet basis-set possesses several other properties conducive to rapid computations (when one takes only a single value of κ). One may readily obtain simple analytical expressions for the matrix elements of the kinetic energy operator, the Coulomb potential and of the absorption or emission dipole operators $V_{\pm}$ (in either the length or the velocity gauge). The

matrices representing these quantities are all very sparse, and the recurrence relations for the Sturmian functions simplify matters still further. It is hoped that the Sturmian-Floquet code, together with a full user-manual, will be published in the near future.

5.5 Appendix: Calculation of Photo-Electron Spectra

In theory the ATI spectrum comprises simply a series of discrete energy peaks separated by the photon energy ω. These peaks are located at energies given by the sum of the initial energy $\Re\mathrm{e}(E)$ of the electron in a dressed state of the atom in the laser field and the energy $N\omega$ of the quanta absorbed from the field (where $N \geq N_0$). But in practice these peaks acquire a finite width which depends on the length of the pulse and on other factors. See, for example, the experimental results reported by Kupersztych *et al* [83] and Agostini *et al* [4]. The discrete peaks predicted by Floquet calculations correspond to the photo-electron spectrum one would expect from an infinitely long pulse at constant intensity. However we can perform a convolution of the partial rates (as calculated by the Floquet method) with the temporal envelope of the electric field to generate a realistic photo-electron spectrum which can be compared with experiment.

Following the work of Véniard *et al* [152] we choose a trapezoidal envelope for the electric field strength. In other words, the laser pulse consists of a linear ramp, $\mathcal{E}_0 = 0 \rightarrow \mathcal{E}_0^{(M)}$, followed by a plateau at fixed field strength $\mathcal{E}_0^{(M)}$ and finally another linear ramp down to zero field. We introduce the notation t_r for the ramp time and t_p for the plateau time, thus the total duration of the pulse is $T = 2t_r + t_p$. For simplicity we express these times in units of the laser period τ (or, in the case of there being two laser fields, the period τ_L of

the fundamental beam). Explicitly we write the field strength as

$$\mathcal{E}_0(t) = \begin{cases} t\mathcal{E}_0^{(M)} & 0 \leq t < t_r \\ \mathcal{E}_0^{(M)} & t_r \leq t \leq t_r + t_p \\ (T-t)\mathcal{E}_0^{(M)} & t_r + t_p < t \leq T \\ 0 & \text{otherwise} \end{cases} \tag{5.48}$$

Let E' denote the independent energy variable and let $E_N = \Re\mathrm{e}(E) + N\omega$ denote the energies of the discrete ATI peaks. Then we can define the difference between these two energies to be

$$\Omega_N(E') = \frac{1}{\omega}(E' - E_N) \tag{5.49}$$

where Ω_N is expressed in units of the photon energy ω (or, in the case of there being two fields, the fundamental frequency ω_L).

For a square pulse (i.e. a field-strength which is constant over a finite time-interval (t_0, t_1) and zero elsewhere) it is evident that the energy spectrum due to the N^{th} ATI peak is given by the square modulus of the Fourier Transform of the frequency Ω_N, *viz.*

$$S_N(E') = \left| \int_{t_0}^{t_1} dt\, \mathrm{e}^{i2\pi\Omega_N t} \right|^2 \tag{5.50}$$

The complete energy spectrum is therefore a sum over the open channels,

$$S(E') = \sum_{N \geq N_0} S_N(E') \tag{5.51}$$

and we can modify expression (5.50) and (5.51) to take account of a more general envelope for the field-strength by including this temporal envelope in the Fourier transform. Thus, our Fourier transform is given by

$$\mathcal{F}(\Omega_N) = \int_0^T dt\, \mathcal{E}_0(t) \exp(2\pi i \Omega_N t) \tag{5.52}$$

and by performing the integration one readily obtains

$$\mathcal{F}(\Omega_N) = \frac{\mathcal{E}_0^{(M)}}{\Delta^2}[-1 + \mathrm{e}^{it_r\Delta} + \mathrm{e}^{i(t_r+t_p)\Delta} - \mathrm{e}^{iT\Delta}] \tag{5.53}$$

where $\Delta \equiv 2\pi\Omega_N$. Hence the photo-electron spectrum for a finite pulse duration is

$$S(E') = \sum_{n=0}^{n_t} W(n) \sum_{N \geq N_0} \Gamma_N(\mathcal{E}_0^{(n)}) \mid \mathcal{F}(\Omega_N) \mid^2 \tag{5.54}$$

where $\mathcal{E}_0^{(n)} = (n/n_t)\mathcal{E}_0^{(M)}$ and the relative weighting of the ramp and plateau sections is given by

$$W(n) = \begin{cases} 2 & n < n_t \\ n_t t_p & n = n_t \end{cases} \tag{5.55}$$

In practice it is found that the contribution to the total spectrum $S(E')$ from the ramp-on and ramp-off regions is virtually zero [126] and so one may reasonably make the approximation $\Gamma_N(\mathcal{E}_0^{(n)}) = 0$ whenever $n < n_t$. In general the quasi-energies E (appearing in Ω_N) and the partial rates of ionisation Γ_N should be evaluated at n_t distinct field strengths $\mathcal{E}_0^{(n)}$.

Véniard *et al* [152] obtain the photo-electron spectrum for a Hydrogen atom in a two-colour laser field consisting of the fundamental beam and its thirteenth harmonic. They take a total pulse duration $T = 8\tau_L$ comprising two ramps of length $t_r\tau_L$ together with a plateau of length $t_p = 6\tau_L$. At the Ti:Sapphire frequency for which they perform their calculations this corresponds to a relatively short pulse whose duration is approximately 28 fs. In our own calculations with a two-colour field we adopt (see chapter seven), for purposes of comparison, the same proportions for our trapezium. Because this pulse is also well-suited to experimental comparisons, we retain these parameters also for our monochromatic calculations (see chapter six).

Chapter 6

Differential Rates for Hydrogen in a Circularly Polarised Laser Field

6.1 Overview of the Calculations

In this chapter we present the results of calculations performed using a monochromatic beam at 608 nm, corresponding to $\omega = 0.075$ a.u., which is circularly polarised in a left-handed sense. Ionisation due to circularly polarised beams is known (analytically) to be independent of the sense of polarisation provided that the initial state is spherically symmetric. In the context of H($1s$) this is a 'long' wavelength in the sense that the photon energy ω is much smaller than the ionisation potential of the atom $E_I = 0.5$ a.u.. We choose this wavelength for two reasons: firstly because, being a long wavelength, we expect to be able to reach the tunneling regime in the limit of high intensity; and secondly because the wavelength is not so long that the absorption of many above-threshold photons becomes highly unlikely (and therefore impossible to calculate). In fact, at low intensities, a minimum of seven photons are required at this wavelength. We choose five representative intensities I of the incident radiation, as displayed in table 6.1. When the radiation is circularly polarised one observes no resonances in the intensity-dependent ionisation rate from H($1s$). This is because the absorption of several circularly polarised photons populates only the Rydberg states with

Table 6.1: Properties of H($1s$) with circularly polarised light at selected intensities and at 608 nm.

I (10^{13} W/cm^2)	N_0	γ_K	$\Gamma(1s)$ (a.u.)	$P_{1s}(t=\tau)$
0	7	∞	0.000	1.000
2	8	4.444	$1.374\ 10^{-9}$	1.000
4	8	3.143	$1.154\ 10^{-7}$	1.000
15	10	1.623	$1.321\ 10^{-4}$	0.989
32	13	1.111	$2.319\ 10^{-3}$	0.823
62	18	0.798	$1.300\ 10^{-2}$	0.337

$l \geq m = N$ which have almost no overlap with the ground state due to the angular momentum barrier, and so intermediate transitions are highly improbable. Of course, the upshot is that the total rates of ionisation are much lower than they would be with linearly polarised light of the same intensity and the absence of resonances also considerably facilitates the computation of quasi-energies, etc.. At the lowest intensity to be considered, $I = 2 \times 10^{13}$ W/cm^2, we have already crossed the one-photon threshold but we are close to the boundary region in which perturbation theory yields to the multiphoton regime. At our next two intensities, 4×10^{13} and 1.5×10^{14}, we are placed firmly in the multiphoton picture as indicated by the Keldysh parameter γ_K [74] which is greater than unity. (See section 3.3.2 for a description of the Keldysh parameter.)

Column five in table 6.1 gives the probability $P_{1s}(t = \tau)$ that the Hydrogen atom will remain in the ground state after one cycle of the laser field. (Note from the frequency ω that the optical period is $\tau \equiv 2\pi/\omega = 83.75$ a.u..) With $I = 3.2 \times 10^{14}$ W/cm^2 we see that the Keldysh parameter is only fractionally greater than unity and that an appreciable fraction (18%) of the atoms are ionised within one cycle of the field. Therefore we may expect the dynamics to contain elements of both multiphoton and tunneling processes. At the highest intensity, 6.2×10^{14}, one requires a minimum of $N_0 = 18$ photons to be absorbed for ionisation to occur at all (c.f. $N_0 = 7$ in the zero-field limit) and additionally less than half of the atomic population remains after one cycle of the field. Floquet theory relies on the concept of a cycle-averaged

rate Γ and if nearly all the atoms are ionised within one optical cycle then this approach becomes invalid. Thus, at 6.2×10^{14} W/cm^2, we have clearly reached the limit of the intensity-regime in which Floquet theory provides us with physically meaningful results (at this wavelength).

6.2 Quasi-Energies and the Partial Rates of Ionisation

We calculate the Floquet quasi-energy eigenvalues $E = (E_R, -i\Gamma/2)$ by solving the coupled Floquet equations using the method of inverse iteration, as described in section 5.2 [129]. The total rate of ionisation from H($1s$) for intensities ranging from zero up to 8×10^{13} W/cm^2 is displayed in figure 6.1. Note the absence of resonant enhancements over this entire range. For the calculation of the quasi-energies we used the basis set: $-10 \leq N \leq 33$, $0 \leq l \leq 37$, $n_{bf} = 60$, $\theta_r = 8°$, $\mathcal{E}_{\rm st} = -0.20$ a.u. and $n_{lm} = 7$. See section 5.4 for an explanation of these parameters. In figure 6.2 we examine more closely the high-intensity section of the total rate of ionisation and highlight the rates at three of the intensities chosen in table 6.1. The optical cycle-time is $\tau = 83.75$ a.u. ≈ 2 fs so in a typical laser-pulse of, say, 100 fs we see from the values of $P_{1s}(t = \tau)$ in table 6.1 that for $I > 3 \times 10^{13}$ W/cm^2 there will be essentially no atoms remaining by the end of the pulse. (This is of course neglecting the variation of intensity with time.) In table 6.2 we show the quasi-energies of H($1s$) at the five intensities chosen in table 6.1 together with the branching ratio between the first two ATI channels $S = 0, 1$ where $S \equiv N - N_0$ is the ATI photon index.

Figure 6.3 shows the partial rates of ionisation Γ_N as a function of the photon number N at all five intensities. Note that due to channel closings as the Stark shift increases in magnitude the curves start at different values of N. The curve for $I = 2 \times 10^{13}$ W/cm^2 has been normalised such that $\Gamma_N(S = 0) = 1$ and all the others have been normalised such that $\Gamma_N(I, S = 0) = \Gamma_N(I = 2 \times 10^{13})$. We see that when the intensity is 2×10^{13} W/cm^2

Table 6.2: Quasi-energies and branching ratios of H($1s$) with circularly polarised light at selected intensities and at 608 nm.

I (10^{13} W/cm^2)	E (a.u.)	$\Gamma_N(S=0):\Gamma_N(S=1)$
2	$(-0.52578054, -6.867707\ 10^{-10})$	1.57
4	$(-0.55184562, -5.767676\ 10^{-8})$	0.371
15	$(-0.69550768, -6.605126\ 10^{-5})$	$5.71\ 10^{-2}$
32	$(-0.91840293, -1.159637\ 10^{-3})$	$6.75\ 10^{-3}$
62	$(-1.31123562, -6.500636\ 10^{-3})$	$1.17\ 10^{-5}$

the rate is greatest into the lowest ATI channel $S = 0$. In contrast, at 4×10^{13} W/cm^2 8-photon ionisation is still an open channel but the relative heights of the first two peaks have reversed and the N-photon rate is now strongest into channel $S = 1$. From table 6.2 we see this pattern extended, with the branching ratio between the first two (open) ATI channels being a monotonically decreasing function of intensity. In fact, the curves in figure 6.3 are well converged only for limited ranges of N. Specifically: for all N at 2×10^{13} W/cm^2; for $N \leq 13$ at 4×10^{13} W/cm^2; for $N \leq 13$ at 1.5×10^{14} W/cm^2; for $N \leq 15$ at 3.2×10^{14} W/cm^2; and for $N \leq 21$ at 6.2×10^{14} W/cm^2. However, when varying the parameters of the basis set, we find that even in cases where the results have not achieved convergence with respect to all of the parameters the general trend is still quite accurate. At the highest intensity we used the basis set: $-8 \leq N \leq 41$, $0 \leq l \leq 45$, $n_{bf} = 100$, $\theta_r = 10°$, $\mathcal{E}_{\rm st} = -0.25$ a.u. and $n_{lm} = 8$. At lower intensities fewer harmonic components are sufficient (for example $-8 \leq N \leq 33$) but the other parameters must still be large. Convergence to an accuracy of, say, $\pm 2\%$ is deemed to be acceptable.

In figure 6.4 we examine the partial rates as a function of S rather than N and we take the lower intensities only in order to have as many converged channels as possible. The curve at 1.5×10^{14} W/cm^2 has been normalised to unity in channel $S = 0$ and the other two curves have been normalised to 20 at $S = 0$ in order to fit comfortably on the same scale. It has been known

for many years that the peak heights of the ATI spectrum should, for long wavelengths, follow an envelope whose form is polarisation dependent and which can be analytically derived using adiabatic theory [99] [103] [29]. For linearly polarised light this envelope takes the form of a decaying exponential with a maximum at $N = N_0$, *viz.*

$$\Gamma_N = \Gamma\left(\frac{2\gamma_P^3}{3\pi}\right)\frac{1}{\sqrt{(N-N_0)}}\exp\left[-\frac{2\gamma_P^3}{3}(N-N_0)\right] \tag{6.1}$$

although this formula is invalid for channels near the threshold $N - N_0 \approx 1$. Following Perelomov *et al* [103] [104] [105] we define an *adiabaticity* parameter γ_P (which is related to but not identical to the Keldysh parameter γ_K) by

$$\gamma_P = \frac{\omega}{\omega_t} = \frac{\omega}{E_I}\frac{\mathcal{E}_0}{2\mathcal{E}} = \frac{2}{3}\gamma_K \tag{6.2}$$

where ω_t is the tunneling frequency and where we further define the field-strength $\mathcal{E}_0$ to be $\mathcal{E}_0 = (2/3)(2E_I)^{3/2}$. The condition $\gamma_P \ll 1$ is necessary for the validity of equation (6.1).

When the field is circularly polarised we have the analogous distribution of ATI peak-heights,

$$\Gamma_N = \Gamma\left(\frac{\gamma_P}{\pi N_S}\right)^{1/2}\exp\left[-\frac{\gamma_P}{N_S}(N-N_S)^2\right] \tag{6.3}$$

which has a maximum at the saddle point N_S given by

$$N_S = 2N_0\left[1 - \frac{1}{3}\gamma_P^2 + \cdots\right] \approx 2N_0 \tag{6.4}$$

Once again, the adiabaticity parameter γ_P must be small and so we have a Gaussian distribution, symmetric about a maximum at $N = N_S$. The marked difference between the distributions (6.1) and (6.4) may be attributed to the differing angular momenta imparted by the photons from linearly and circularly polarised beams. In linearly polarised light, the photons do not have a definite angular momentum projection onto the quantisation axis but with circularly polarised light each photon has a projection equal to ± 1, depending on whether the sense of polarisation is left-handed (+) or right-handed (-).

6.2.1 Keldysh Theory

Both types of distribution have been verified in detailed calculations by M Dörr *at al* [31] for the rates of multiphoton detachment from the H^- ion at the CO_2 laser wavelength (i.e. around $\lambda = 10$ μm). In fact these calculations use either Keldysh theory or Faisal-Reiss Theory rather than the Floquet method. Both of these are approximate methods in which the initial wavefunction of the atom in the electric field is assumed to be the unperturbed atomic wavefunction. Clearly the validity of this approximation will depend partly on the actual Stark shift of the atom in the field. In Keldysh theory this approximation is made in the length gauge (in which the interaction Hamiltonian is given by $H_I(t) = -\boldsymbol{r} \cdot \boldsymbol{\mathcal{E}}(t)$) and so one would expect good accuracy for ground states (i.e. when distances are small) and correspondingly poor results for Rydberg states. The Faisal-Reiss version makes the same approximation but in the velocity gauge, leading to different results when the laser intensity is very strong [31]. At this extremely long wavelength and at low intensity (but with $\gamma_K = 0.43$) it was possible to perform Keldysh calculations with photon numbers $N \geq 60$, compared to $N_0 = 23$. Both the exponential decline for linear polarisation and the Gaussian distribution for circular polarisation were well reproduced. In particular the saddle point was found to occur at $N_S = 42 = 1.83N_0$ which is close to but slightly below the value predicted by equation (6.4).

The paper by M Dörr *et al* [31] presents partial rates of ionisation from a Yukawa potential whose parameters are chosen so as to model the properties of the H^- ion. In particular, calculations are performed for a circularly polarised beam at the CO_2 frequency, $\omega = 0.00440$ a.u., at intensities varying from zero up to 2×10^{11} W/cm^2. Reference [31] does not present any of the corresponding angular distributions for the photo-electrons but these have instead been calculated recently (using both the Keldysh and Faisal-Reiss approximations) by R M Potvliege [128]. This affords us the possibility of reproducing these results using the Sturmian-Floquet code and comparing the angular distributions to see whether or not these approximate theories can

Table 6.3: Partial rates of ionisation of the H^- ion by circularly polarised radiation at $I = 2.5 \times 10^{10}$ W/cm^2 and $\omega = 0.00440$ a.u.. All rates are given in atomic units. The Faisel-Reiss rates marked with asterisks are numerically unreliable.

Channel (N)	Keldysh Theory	Faisal-Reiss	Sturmian-Floquet
9	1.319×10^{-12}	1.262×10^{-12}	1.222×10^{-12}
10	2.236×10^{-10}	2.128×10^{-10}	2.166×10^{-10}
11	1.068×10^{-9}	1.004×10^{-9}	1.046×10^{-9}
12	1.686×10^{-9}	1.577×10^{-9}	1.659×10^{-9}
13	1.554×10^{-9}	1.491×10^{-9}	1.534×10^{-9}
15	5.592×10^{-10}	$*5.146 \times 10^{-10}$	5.542×10^{-10}
20	3.955×10^{-12}	$*1.374 \times 10^{-12}$	3.942×10^{-12}
30	1.757×10^{-18}	$*5.252 \times 10^{-21}$	1.751×10^{-18}

capture the more accurate distributions predicted by the Sturmian-Floquet method. We choose to make this comparison for the Yukawa potential (H^- ion) rather than the Hydrogen atom because the Keldysh and Faisal-Reiss methods are known to be much less reliable for Hydrogen than they are for H^-. The field-free binding energy of H^- is -0.0275654 a.u. and at the CO_2 frequency one therefore requires a minimum of $N_0 = 7$ photons for ionisation to occur. We choose to compare the various methods at the moderate intensity of $I = 2.5 \times 10^{10}$ W/cm^2 for which the Keldysh parameter takes the value $\gamma_K = 12.0$. At this intensity the lowest order ionisation process involves $N_0 = 9$ photons. The parameters of the Sturmian basis set used in this computation are: $-12 \leq N \leq 35$, $0 \leq l \leq 39$, $n_{bf} = 60$, $\theta_r = 20°$, $\mathcal{E}_{\rm st} = -0.08$ a.u. and $n_{lm} = 6$. See section 5.4 for an explanation of these parameters. The partial rates into the first thirty ATI channels have been obtained by the three different methods and data for selected channels are presented in table 6.3.

The partial rates from both the Sturmian-Floquet and the Keldysh methods are well converged over at least the first twenty ATI channels (i.e. including all those shown in table 6.3). However the results calculated using the Faisal-Reiss method suffer from numerical inaccuracies in the channels $N \geq 15$ (or $S \geq 6$). To compare the different sets of results let us consider only the ATI

peak corresponding to a (global) maximum in the ATI spectrum, namely, channel $N = 12$. Here we find that the Keldysh rate is 1.6% greater than the Sturmian-Floquet rate and that the Sturmian-Floquet rate is in turn 5.2% greater than the Faisal-Reiss rate. Thus the Keldysh rate is much closer to the Floquet result than is the Faisal-Reiss rate and this pattern is repeated over the less important channels. Even in channel $N = 30$ we see from table 6.3 that the discrepancy between the Keldysh and the Sturmian-Floquet results is only approximately 0.4%. We will return to discuss the angular distributions obtained by these methods in section 6.3.

M Dörr *et al* show that, following the arguments in [99] [103], the electron is most likely to leave the atom carrying a drift momentum approximately equal to the instantaneous quiver momentum $k_q(t) = \mathcal{E}(t)/\omega$ which it possessed immediately prior to escape. Note the connection with the quiver energy $E_P = \mathcal{E}_0^2/(4\omega^2)$: The root-mean-square value of k_q is

$$k_q^{(\mathrm{rms})} = \frac{\mathcal{E}_0(t)}{\sqrt{2}\omega} = \sqrt{2E_P} \tag{6.5}$$

The instantaneous value of k_q depends crucially on the polarisation of the electric field. For a linearly polarised beam the magnitude of the electric field vector $\mid \mathcal{E}_0 \cos(\omega t) \mid$ oscillates between zero and $\mathcal{E}_0$ and since ionisation is most likely to occur when the field reaches its maximum amplitude the electron will be ejected with a drift momentum of near zero. Hence the global peak in the photo-electron rate occurs for energy values close to the threshold. In contrast, for circular polarisation the electric field vector is of constant magnitude, giving $k_q(t) = \sqrt{2E_P}$ at all times, and so one expects a drift energy $\sim E_P$. Hence the energy distribution for the photo-electrons should reach a maximum at around $N = N_0 + E_P/\omega$.

6.2.2 The High-Intensity Regime and Tunneling Theory

Returning to the present (Hydrogenic) calculations, we only have $\gamma_P \ll 1$ for the highest intensity, $I = 6.2 \times 10^{14}$ W/cm^2, for which $N_0 = 18$. But, as

described above, the partial rates which we have calculated for this case are accurate only up to channel $N = 21 \ll 2N_0$ and so we cannot hope to observe the Gaussian distribution of peak heights. In figure 6.4 we see, qualitatively, at 4×10^{13} W/cm^2 the onset of this pattern, with the highest ATI peak having shifted from $S = 0$ to $S = 1$. At 1.5×10^{14} W/cm^2 unfortunately our results (for the partial rates though not the total rate) are not well converged beyond the maximum at $S = 3$ and so while we can tentatively say that we begin to observe the characteristic bell-shaped structure of ATI peaks (when plotted on a linear scale) the most we can accurately conclude is that our results are consistent with that pattern. Figure 6.5 shown the photo-electron yield at the two lowest intensities, this time with a model (trapezoidal) laser pulse. This has been performed in order to demonstrate the effect of the Stark shifting and to facilitate qualitative comparisons with experiment by providing a finite energy-width for the peaks. See, for example, Kupersztych *et al* [83] and Agostini *et al* [4]. To this end we take a short pulse of duration $8\tau \approx 16$ fs which is made up of a plateau at the peak intensity lasting for 6τ enclosed by linear ramps of duration τ. The yield has been generated by performing a convolution of the Γ_N-spectrum with the Fourier transform of the laser pulse. This method is described in more detail in the appendix to chapter five. Note that the horizontal (Stark) shifting of the peaks is large despite the relatively low intensities involved.

Finally in this section we present a discussion of the tunneling regime. As has been discussed above, and may be seen from the values of the Keldysh parameter in table 6.1, a tunneling picture is appropriate (at 608 nm) for intensities $I > 4 \times 10^{14}$ W/cm^2, i.e. $\gamma_K < 1$. But, at still higher intensities we reach the so-called over-the-barrier (OTB) regime in which the Coulomb potential is suppressed by the field to such an extent that the electrons can simply flow out over the top rather than tunneling through a classically forbidden region. We denote the critical intensity above which OTB ionisation can occur $I_{\rm cr}$. Beyond this one has the characteristic atomic intensity $I_{\rm au} = 6.43641 \times 10^{15}$ W/cm$^2 \equiv 1$ a.u.. Thus in order for there to exist a tunneling regime to exist at a given frequency $\omega < E_I$ the critical frequency must satisfy the inequal-

ity $4 \times 10^{14} < I_{\rm cr} < 6.44 \times 10^{15}$ W/cm^2. R Shakeshaft *et al* [143] provide a general expression for the critical intensity of a complex atom (initially in its ground state) in the limit of a static field, namely

$$I_{\rm cr} = \sec^2(\zeta/2)\frac{cZ^6}{128\pi} \mid E_{dc} \mid^4 \tag{6.6}$$

where the polarisation of the radiation is $\zeta = 0$ for linear polarisation or $\zeta = \pi/2$ for circular polarisation, E_{dc} is the (real) energy of the atom in a DC field, and Z is the number of the atomic species. However, equation (6.6) is not applicable to Hydrogen because, in a static electric field, this atom has an exceptional symmetry arising from the fact that the Schrödinger equation is separable in the parabolic co-ordinates $\xi = r + z$ and $\eta = r - z$. Instead one can solve numerically a transcendental equation [143] to obtain $I_{\rm cr}\cos^2(\zeta/2) \approx 8 \times 10^{14}$ W/cm^2. Since we are interested here in circularly polarised light this is actually $I_{\rm cr} \approx 2 \times 10^{15}$ W/cm^2. Hence the onset of OTB ionisation does not impose any further restriction on the intensity-window within which we may expect to observe tunneling behaviour because $I_{\rm cr}$ is much greater than the intensity at which the atoms become totally ionised within one optical cycle and the Floquet approach breaks down. In summary, our calculation at $I = 6.2 \times 10^{14}$ W/cm^2 is expected to exhibit tunneling behaviour.

Figure 6.6 shows the total rate of ionisation of H($1s$) due to a circularly polarised beam at 608 nm in comparison with the rate due to a DC field. We see that at $I = 10^{14}$ W/cm^2 the AC rate exceeds the DC rate by approximately one order of magnitude but also that for $I > 6 \times 10^{14}$ W/cm^2 there is virtually no difference between these rates. Indeed, it is known that in general, as the wavelength increases, the AC rate approaches the DC rate from above [143]. The convergence of the AC and DC rates may be taken as a further qualitative indication that ionisation will proceed predominantly by tunneling. An analytic expression for the ionisation rate of H($1s$) in a DC field due to tunneling is [29]

$$\Gamma_{dc} = \frac{4}{\mathcal{E}_0}\exp\left(-\frac{2}{3\mathcal{E}_0}\right) \tag{6.7}$$

but this formula is only approximate. In fact, equation (6.7) is exact in the limit $I/I_{\rm cr} \to 0$ rather than $I \to I_{\rm cr}$. Recently, a new adiabatic approach has been developed [149] [150] which, within the time-independent Floquet framework, makes a further approximation by writing an adiabatic ansatz for the harmonic components. This assumes that the laser frequency is small compared with the ionisation potential of the atom but the external field is treated fully non-perturbatively. As yet, this approach has been applied mainly to multiphoton detachment from the H^- ion by radiation of 10.6 μm and both photo-electron yields and their angular distributions have been obtained. Comparisons with full Floquet calculations show the method to provide good agreement with previous calculations [149].

6.3 Angular Distributions of the Photo-Electrons

6.3.1 General Features

At low laser-intensities the typical patterns of angular distributions for both linearly and circularly polarised light have been known for many years [29]. In the perturbative limit the result for circularly polarised light was derived in 1972 by Lambropoulos [86] and was later recovered by Faisal [46] from an approximate expression valid at arbitrary field-strengths. In this eponymous approximation Faisal writes the N-photon rate (or squared amplitude) in the perturbative limit as

$$\mid T^{(N)} \mid^2 = (E_i - E_j)^2 \mid \tilde{\phi}_i(\boldsymbol{k}) \mid^2 E_P^N \left(\frac{k^N}{c^N N!} \right)^2 \sin^{2N} \theta_k \qquad (6.8)$$

where E_i and E_j are the (real) energies of the initial and final states states respectively, $\boldsymbol{k} \equiv (k, \theta_k, \phi_k)$ is the momentum vector and E_P is the ponderomotive energy of the electron in the field. The function $\tilde{\phi}_i(\boldsymbol{k})$ is the Fourier transform of an unperturbed Floquet wavefunction $\phi_i(\boldsymbol{r})$, *viz.*

$$\Phi_i(\boldsymbol{r}, t) = \exp(-iE_i t)\phi_i(\boldsymbol{r}) \qquad (6.9)$$

and

$$\phi_i(\boldsymbol{r}) = \frac{1}{(2\pi)^{3/2}} \int d\boldsymbol{s} \tilde{\phi}_i(\boldsymbol{s}) \exp(-i\boldsymbol{s}.\boldsymbol{r}) \tag{6.10}$$

where $\Phi_i(\boldsymbol{r}, t)$ is the total unperturbed wavefunction for the atom in state i. We see from equation (6.8) that the angular dependence in the differential rate is $(d\Gamma_N/d\Omega) \sim \sin^{2N}\theta_k$. Physically this means that there will be no electrons ejected at small angles (near parallel with the beam axis) and that most photo-electrons will emerge into the polarisation plane, i.e. perpendicular to the beam axis.

This behaviour may be readily understood as follows. To lowest non-vanishing order, the N-photon rate comes simply from the absorption of N quanta from the field, each of which carries one unit of angular momentum and (for left-handed polarisation) one magnetic unit also. Now the spherical harmonics of arbitrary order are given by [11]

$$Y_{lm}(\theta, \phi) = (-1)^m \left[\frac{(2l+1)}{4\pi} \frac{(l-m)!}{(l+m)!}\right]^{1/2} \sin^m\theta \frac{d^m}{d(\cos\theta)^m} P_l(\cos\theta) e^{im\phi} \tag{6.11}$$

and we note that the Legendre polynomials $P_l(\cos\theta)$ are of order l. Thus, in the term Y_{NN}, the differentiation leaves only the numerical coefficient of the leading term in the Legendre polynomial and the only θ-dependence left in equation (6.11) is the $\sin^N\theta$. Taking the square modulus we find that

$$|\, Y_{NN}(\theta)\,|^2 = \frac{(2N+1)}{4\pi(2N)!} \sin^{2N}\theta \tag{6.12}$$

At arbitrary field-strengths one may express the angular-dependent N-photon amplitude $M_N(\theta)$ (c.f. equation (5.45)) as

$$M_N(\theta) = \sum_M J_{M-N}(R) \sum_{l=M}^{\infty} c_{Ml} Y_{lM}(\theta) \tag{6.13}$$

where the parity of the wavefunctions requires that $l = M, M+2, M+4...$ Note that the azimuthal quantum number can only take the value $m = M$ due to the absorption of M circularly polarised quanta. More simply, we can write

$$M_N(\theta) = \sum_M J_{M-N}(R) M_{NM}(\theta), \qquad M_{NM}(\theta) = \sum_{l=M}^{\infty} c_{Ml} Y_{lM}(\theta) \tag{6.14}$$

Therefore the squared amplitude for the absorption of M real and virtual photons (of which N are real) may be written as

$$\mid M_{NM}(\theta) \mid^2 = \mid c_{MM} Y_{MM}(\theta) \mid^2 \left[1 + \frac{c_{M,M+2}}{c_{MM}} \frac{Y_{M+2,M}(\theta)}{Y_{MM}(\theta)} + \cdots \right]^2 \tag{6.15}$$

Thus, in the perturbative limit we would have $\mid c_{MM} \mid \gg \mid c_{M,M+2} \mid$ but at higher intensities there may be strong contributions from the next-to-leading and higher order terms.

6.3.2 Results of our Calculations

Figure 6.7 shows the angular distribution of photo-electrons into the first thirteen above-threshold channels with an incident intensity of $I = 2 \times 10^{13}$ W/cm^2. We see that, at least qualitatively, the distributions follow the pattern predicted above with the maximum rate being at right-angles to the beam axis and the rate falling off like $\sin\theta$ as θ decreases. (A quantitative comparison with perturbation theory will be made later on.) Further, we see that the distribution is broadest in the $S = 0$ channel (corresponding to $N = 8$) and becomes increasingly strongly squashed into the polarisation plane as S increases. This behaviour is also consistent with the $\sin^{2N}\theta$ formula described above. Figures 6.8 and 6.9 show the corresponding distributions at the higher intensities $I = 1.5 \times 10^{14}$ W/cm^2 and $I = 6.2 \times 10^{14}$ W/cm^2 respectively. In these we plot only the distributions into the first five ATI channels because our results for the higher order channels are not fully converged with respect to the various parameters in the Sturmian basis set, (see section 5.4). At 1.5×10^{14} W/cm^2 we observe no deviation from the behaviour demonstrated at 2×10^{13} W/cm^2 and in fact the same is true at 4×10^{13} W/cm^2 and 3.2×10^{14} W/cm^2, namely, that the distribution is broadest into channel $S = 0$ and that it becomes increasingly peaked about $\theta = 90°$ as S increases. At 6.2×10^{14} W/cm^2 the curves still possess very much the same sinusoidal form (although more strongly peaked because here $N_0 = 18$) but the lowest ATI channel no longer has the broadest distribution. In fact, the results for $S = 3, 4$ are not well converged and any differences in

channels $S = 0 \rightarrow 2$ from the pattern observed at lower intensities may also be due to numerical inaccuracies. The main point is that these distributions are featureless, possessing no local maxima, and are qualitatively similar to what one might expect from perturbation theory.

We now look at each ATI channel $N \geq N_0$ in turn and compare the angular distributions at different intensities with each other and with perturbation theory. Figure 6.10 shows the results for channel $N = 8$ which, at both the intensities displayed, is the lowest open channel. Here we find perfect agreement with the perturbative prediction of $\mid f_{N=8}(\theta) \mid^2 \sim \sin^{16}\theta$. For $N = 13$ (see figure 6.11) we are able to compare the results at 2×10^{13} W/cm^2 ($S = 5$), 1.5×10^{14} W/cm^2 ($S = 3$) and 3.2×10^{14} W/cm^2 ($S = 0$). We find, unsurprisingly, that the curve for $I = 2 \times 10^{13}$ W/cm^2 lies almost on top of the perturbative curve but we also find that the curves at the higher intensities (lying far into the multiphoton regime) are still very close to the perturbative result, although marginally broader. This effect is seen most clearly in figure 6.12 which presents the results for channel $N = 15$. Here we find the low intensity result still in perfect agreement with perturbation theory and the very high intensity result being similar but up to about 5% greater (on the normalised scale) for values of θ around $70° \rightarrow 80°$. Figure 6.13 compares the results at 2×10^{13} W/cm^2 ($S = 10$) and 6.2×10^{14} W/cm^2 ($S = 0$) with perturbation theory. Rather than finding a greater discrepancy between the curves here than at $I = 3.2 \times 10^{14}$ W/cm^2 we find that the agreement has become better, with the high-intensity (tunneling) distribution displaying no side-lobes or other distinctive features and still lying remarkably close to the perturbative result. Our results for this channel and this intensity are very accurately converged with respect to all of the parameters in the Sturmian basis set. Finally we look at channel $N = 20$ (see figure 6.14) and find perfect agreement between angular distributions calculated at 2×10^{13} W/cm^2 ($S = 12$) and 6.2×10^{14} W/cm^2 ($S = 2$) and with perturbation theory.

6.3.3 Analysis of Matrix Elements

These results leave us with two principal questions: why do the angular distributions in the multiphoton regime (i.e. $I \sim 10^{14}$ W/cm^2) not differ from those predicted by perturbation theory; and why, in the tunneling regime (i.e. $I > 4 \times 10^{14}$ W/cm^2), does one not see still more differences? Remembering equation (6.15) there can only be two numerical explanations for this behaviour: either we still have $\mid c_{M,l=M} \mid \gg \mid c_{M,l=M+2} \mid$ as at very low intensities; or the coefficients $c_{M,l}$, $l > M$, are of the same order of magnitude as the leading coefficient c_{MM} but they somehow conspire to reproduce the same net effect. In figure 6.15 we examine these coefficients at the very low intensity of $I = 10^{11}$ W/cm^2 in the arbitrarily chosen case of ATI channel $N = 13$ and electron ejection angle $\theta = 75°$. We find that the only leading term c_{MM} contributing to the N-photon rate is that with $M = N = 13$. This can be attributed to the Bessel function $J_{N-M}(R)$ is equation (6.14) which for small arguments is virtually zero except when the index $N - M = 0$. Also the absolute magnitude of the ratio $c_{M,M+2}/c_{MM}$ is less than 10^{-3}. Thus, at low intensity we find that the coefficients c_{Ml} select the term in $l = M$ and that in combination with the Bessel function we are left with only the spherical harmonic whose indices are $l = m = N$.

In figure 6.16 we plot the same quantities but this time at the intensity $I = 3.2 \times 10^{14}$ W/cm^2 for which $N = 13$ is the lowest open channel (c.f. figure 6.11). Here we see that the leading coefficient $c_{M,l=M}$ is of roughly equal magnitude for $M = 10, 11, 13, 15$ *and* 16 and that all the other coefficients with $l = M$ are much smaller. Also it is clear that for all five of these constants the next-to-leading and higher order terms are at least a factor of 10 smaller and so are negligible. The answer to our question then is that unlike at low intensities there are several spherical harmonics with roughly equal coefficients (only one of which $\sim \sin^{2N}\theta$) and yet somehow these act together to produce only a $\sin^{2N}\theta$ dependence. We can see the mechanism behind this from equation (6.14) with the help of equation (5.44). The Bessel

function $J_{N-M}(R)$ acts, for small arguments R, like [2]

$$J_{N-M}(R) \sim \frac{1}{\Gamma(N-M+1)} \left(\frac{R}{2}\right)^{N-M} \sim R^{N-M} \tag{6.16}$$

But from equation (5.44) we see that R contains an angular dependence, *viz.*

$$R = \left(\frac{kA_0}{\omega c}\right) \cos\beta, \qquad \cos\beta = \frac{\boldsymbol{k}.\boldsymbol{A_0}}{kA_0} \tag{6.17}$$

To obtain β we note that the vector $\boldsymbol{A_0}$ lies (by definition) wholly in the polarisation plane and therefore has zero component along the polar axis. Let (θ, ϕ) be the angular co-ordinates of the vector $\boldsymbol{k}$ and $(\pi/2, \tilde{\phi})$ be the co-ordinates of $\boldsymbol{A_0}$ with respect to the same axes, then one immediately sees that $\cos\beta = \sin\theta\cos(\phi - \tilde{\phi})$, giving $R \propto \sin\theta$. Thus, taking only the leading angular momentum terms $l = M$, equation (6.13) becomes

$$M_N = \sum_M c_{MM} J_{N-M}(R) Y_{MM}(\theta) = \sum_M \tilde{c}_{MM} \sin^N(\theta) \tag{6.18}$$

where the coefficient $\tilde{c}_{MM}$ has absorbed the other constants. This means that whenever $kA_0 \gg \omega c$ the angular distribution into channel N will always have the form $\sin^{2N}\theta$ irrespective of which harmonic components are the principal contributors.

Having given a numerical discussion of the angular distributions we would also like to describe these effects in terms of physical ideas. Let us introduce the concept of a 'propensity rule' - the idea that a transition or class of transitions is much more likely than alternative but possible transitions. This is different from a selection rule in that none of the transitions are 'forbidden' due to symmetries of the system; they are simply less likely, due to dynamical factors. Fano describes how a propensity rule may emerge from an analysis of the structure of a relevant matrix element [47]. See the appendix to this chapter for a brief description of this method. The conclusion is that for the absorption of photons by atoms the transitions satisfying $l \to l+1$ is strongly favoured over those with $l \to l-1$. Similarly, when emitting a photon, the transition $l \to l-1$ is favoured over $l \to l+1$. Physically this amounts to detecting a consistent relationship between the overlap of the (N, l)-wavefunction with the $(N, l+1)$-wavefunction on the one hand

and the overlap of the (N, l)-wavefunction with the $(N, l-1)$-wavefunction on the other. Thus for each photon absorbed from the field the most likely outcome is $l \rightarrow l+1$ which has the effect of increasing the relative importance of spherical harmonic $Y_{NN}(\theta)$. The same is of course true of linearly polarised beams but in that case one also has to deal with resonant enhancements in the ionisation rate and their magnitude far outweighs the preferential selection of $Y_{NN}(\theta)$ by propensity.

At $I = 6.2 \times 10^{14}$ W/cm^2 the dominant ionisation mechanism is tunneling and a multiphoton picture is less appropriate. We are not aware of any analytic expressions having been obtained within tunneling or adiabatic theory for the angular distribution of photo-electrons in this regime. Delone and Krainov [29] comment that the fraction of electrons distributed out of the polarisation plane should be very small but an exact expression is not given. Physically, we can picture the electrons tunneling through the Coulomb barrier with equal probability at all times. This is because, in contrast to linearly polarised light in which the field-strength reaches a maximum twice per optical cycle, the electric field vector is of constant magnitude in a circularly polarised beam. Therefore the barrier is equally suppressed at all times and we would expect the electron to be emitted in the instantaneous direction of the field, i.e. wholly within the polarisation plane. However, our results show that the angular distribution of photo-electron from H($1s$) in this regime is not skewed towards the polarisation plane ($\theta = 90°$) at very high intensities. We cannot offer a satisfactory physical explanation for this distribution.

6.3.4 Differential Rates from Keldysh Theory

Finally in this section we can return to discuss the predictions of Keldysh theory and Faisal-Reiss theory for the angular distributions of photo-electrons, following the partial rates that were obtained by these methods in section 6.2. Unlike the partial rates which had previously been reported in [31] the corresponding angular distributions have only recently been calculated [128]. We have carried out a series of Sturmian-Floquet calculations (as described

in the previous section) at the same frequency and intensity in order to see whether these angular distributions generated by these simpler methods might shed some light on the results we have already calculated for atomic Hydrogen. The fixed intensity of the laser field is $I = 2.5 \times 10^{10}$ W/cm^2 and we give it the CO^2 frequency of $\omega = 0.00440$ a.u.. In addition to comparing the three methods mentioned so far with each other we can also compare the results to those of perturbation theory which predicts simple $\sin^{2N}\theta$ distributions as described earlier in this section. Having obtained results over many ATI channels we present in figure 6.17 only the distributions into channels $S = 0$ and $S = 19$. For $S = 0$ we find that all three of the calculated results agree very closely (i.e. to better than 1%) with the $\sin^{18}\theta$ curve predicted by perturbation theory.

In table 6.3 we saw that while the partial rates of the Keldysh calculation are in close agreement with those calculated by the Sturmian-Floquet code over many channels, the partial rates obtained by the Faisal-Reiss method diverged when $S \geq 6$. The angular distributions contrast strongly with this picture, showing an absolute difference of less than 3% between any pair of calculated results. In particular the Faisal-Reiss result and the Sturmian-Floquet result are almost indistinguishable in figure 6.17 and this leads us to conclude that the angular dependence in the Floquet rates should be explicable in terms of the simpler physics of the Faisal-Reiss model. In Faisal's method [44] the N-photon transition matrix (T-matrix) element for a circularly polarised field is found to depend on a Bessel function whose argument is proportional to $\sin\theta$. Thus, when the constant of proportionality is small (which holds at low intensities), the square modulus of the transition matrix element acquires a $\sin^{2N}\theta$ dependence as is described in equation (6.8). Our Sturmian-Floquet calculations reveal that while the partial rates of ionisation exhibit highly non-perturbative characteristics at high intensities the angular distribution of the photo-electrons always remains close to perturbative predictions. Further, for the case of H^-, the same perturbative results are also obtained by the Keldysh and the Faisal-Reiss methods.

6.4 Conclusions

In this chapter we present results for the ionisation of H($1s$) by a monochromatic circularly polarised field of $\lambda = 608$ nm at intensities varying from zero up to 10^{15} W/cm^2. The total rates (given by $\Gamma = -2 \times \Im\mathrm{m}(E)$) of MPI are well converged (with respect to the basis-parameters) up to this intensity but the highest intensity at which we have obtained accurate *partial* rates and differential rates is $I = 6.2 \times 10^{14}$ W/cm^2. In fact, this is also the highest intensity at which the Floquet approach is applicable (in the context of the ground state of Hydrogen) because at higher intensities the atom is ionised so rapidly that the concept of a cycle-averaged rate is not meaningful. In order to study the differing photo-electron yields as one moves from the perturbative regime through an MPI region into a tunneling regime we select five representative intensities of the incident field. The lowest of these is $I = 2 \times 10^{13}$ W/cm^2 and the highest is $I = 6.2 \times 10^{14}$ W/cm^2, as mentioned above. The Keldysh parameter indicates that a tunneling picture is appropriate for intensities $I > 4 \times 10^{14}$ W/cm^2. The results we have obtained for the partial rates of MPI are consistent with the analytical formulae derived by Nikishov and Ritus [99] and by Perelomov *et al* [103] [104] [105] however at our wavelength of 608 nm we are unable to compute ATI peak-heights over sufficiently many channels to locate the saddle-point predicted by these authors. A Gaussian distribution of ATI peak-heights with a saddle-point at the expected photon number N_S has been obtained by M Dörr *et al* for H^- at the much longer wavelength of 10.6 μm [31].

In each channel $N \geq N_0$ we present the angular distributions of the photo-electrons at various intensities and compare these with each other and also with the predictions of perturbation theory [86] [44]. At 608 nm the number of photons required to ionise the atom is $N_0 = 7$ at zero field, rising to $N_0 = 18$ at $I = 6.2 \times 10^{14}$ W/cm^2. In all ATI channels and at all intensities the angular dependence that we obtain is very close to the $\sin^{2N}\theta$ behaviour predicted by perturbation theory. There is almost no departure from this even as one enters the tunneling regime. We explain why this should be so

by analysing the structure of the relevant N-photon transition amplitude M_N (in which the angular dependence is contained both in a linear superposition of the spherical harmonics and in an ordinary Bessel function of argument $R \propto \sin\theta$) and find that provided the inequality $kA_0 \gg \omega c$ holds there will be no departure from the characteristic angular distribution $\mid M_N \mid^2 \propto \sin^{2N}\theta$. This inequality indicates that there should exist an intensity beyond which this pattern of behaviour breaks down but at 608 nm this will only occur in the ultra-intense regime. We also offer a more physical interpretation of these angular distributions in terms of the well-known propensity rule for atomic transitions. Following the example of Fano [47] we derive the propensity rules for photo-absorption and photo-emission in the context of radial wavefunctions of the WKB type. We believe that arguments of this type should be widely applicable to other models such as our Coulomb potential.

6.5 Appendix: Heuristic Derivation of the Propensity Rule for Atomic Transitions

Here we describe briefly the way in which one may obtain the well-known propensity rule that in atomic photo-absorption processes the transitions with $l \rightarrow l+1$ are much preferred to those with $l \rightarrow l-1$. This argument has been previously reported by Fano [47] and we apply the same reasoning to deduce the corresponding rule that in atomic photo-emission processes the transitions with $l \rightarrow l-1$ have a much greater propensity those with $l \rightarrow l+1$. The physical origin of propensity lies in the differing scalar products of the initial state (with angular momentum quantum number l) with each of the two classes of final states whose angular momenta are $l' = l+1$ or $l' = l-1$. Following Fano [47] we illustrate this by considering the relevant matrix elements of the radial transition operator $T(r)$. For simplicity we assume radial wavefunctions of the Wentzel-Kramers-Brillouin (WKB) type [7] and conjecture that a similar analysis can be applied under more general

circumstances. Thus the wavefunctions are given by

$$\psi_{i,f}(r) \propto \sin\left[\int_0^r k_{i,f}(r')dr'\right] \tag{6.19}$$

and the radial matrix elements T_{fi} are simply

$$T_{fi} = \int_0^\infty dr\psi_f(r)T(r)\psi_i(r) \tag{6.20}$$

where i and f denote the initial and final states respectively. But from (6.19) and using the identity $2\sin\theta\sin\theta' = \cos(\theta-\theta') - \cos(\theta+\theta')$ one can readily see that

$$\psi_f(r)\psi_i(r) \propto \cos\left(\int_0^r [k_f(r') - k_i(r')]dr'\right) - \cos\left(\int_0^r [k_f(r') + k_i(r')]dr'\right) \tag{6.21}$$

The essential point is that the value of T_{fi} as given by equation (6.20) can be maximised by manipulating the integrand such that it varies slowly rather than undergoing rapid oscillations which lead mainly to cancellation. From equation (6.21) we see that the second term will typically exhibit fast oscillations and so can be neglected while in the first term we can substitute

$$k_{i,f} = [2(E_{i,f} - V_{i,f}(r))]^{1/2} \tag{6.22}$$

and proceed to consider the l-dependence of the atomic potential $V_j(r)$ for an atom in the state j. This radial potential takes the form

$$V_j(r) = -\frac{1}{r} + \frac{l(l+1)}{r^2} \tag{6.23}$$

which implies that $V_j(r; l+1) > V_j(r; l)$ for all values of l. Let us examine the function

$$G_{fi}(r; l, l') = \sqrt{E_f - V_f(r; l')} - \sqrt{E_i - V_i(r; l)} \tag{6.24}$$

which appears in the integrand of equation (6.21). To minimise oscillations in the integrand of (6.20) we require $G_{fi}(r; l) \approx 0$ and therefore

$$E_f - E_i \approx V_f(r; l') - V_i(r; l) \tag{6.25}$$

We should now consider separately the cases of photo-absorption and photo-emission. In the former case we know that $E_f - E_i > 0$ and so equation

(6.25) requires that $V_f(l') - V_i(l) > 0$ which from (6.23) means that $l' > l$ or, to satisfy the well known selection rule $\Delta l = \pm 1$, $l \to l + 1$. Conversely for photo-emission we have $E_f - E_i < 0$ and the same argument leads us to conclude that $l' < l$ or in other words $l \to l - 1$. It should be stressed that this is only a heuristic argument and that, although we have no reason to believe so, the conclusions may not hold for states with small values of either l or n. (This is because the WKB method is essentially a semi-classical approximation and so in order to justify taking the classical limit we ought to be considering large values of the relevant quantum numbers.)

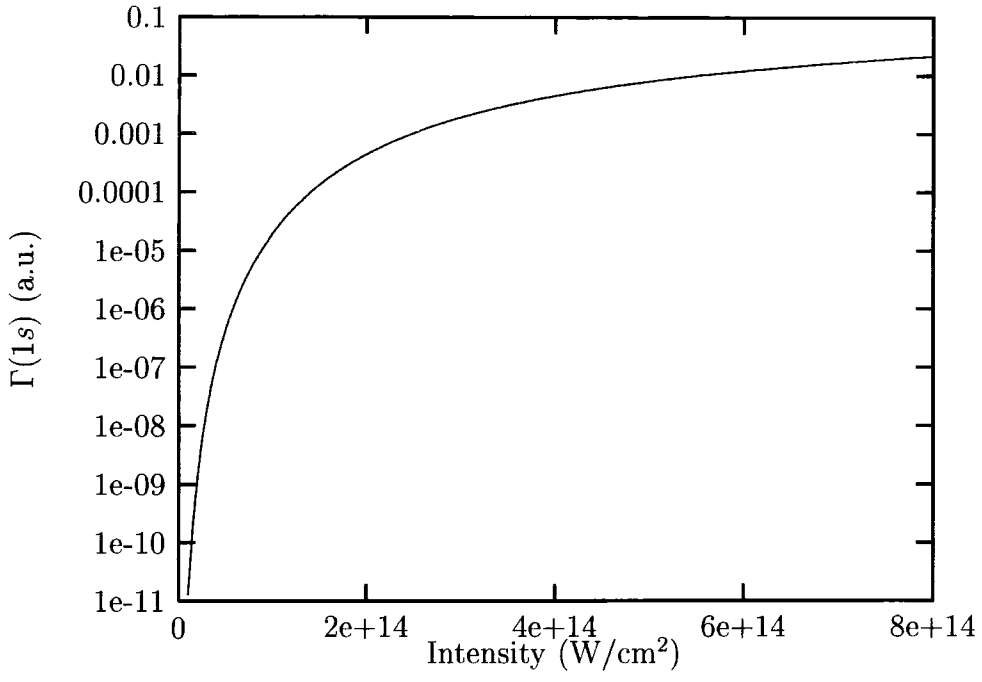

Figure 6.1: Total rate of ionisation of H($1s$) at 608 nm with circularly polarised light.

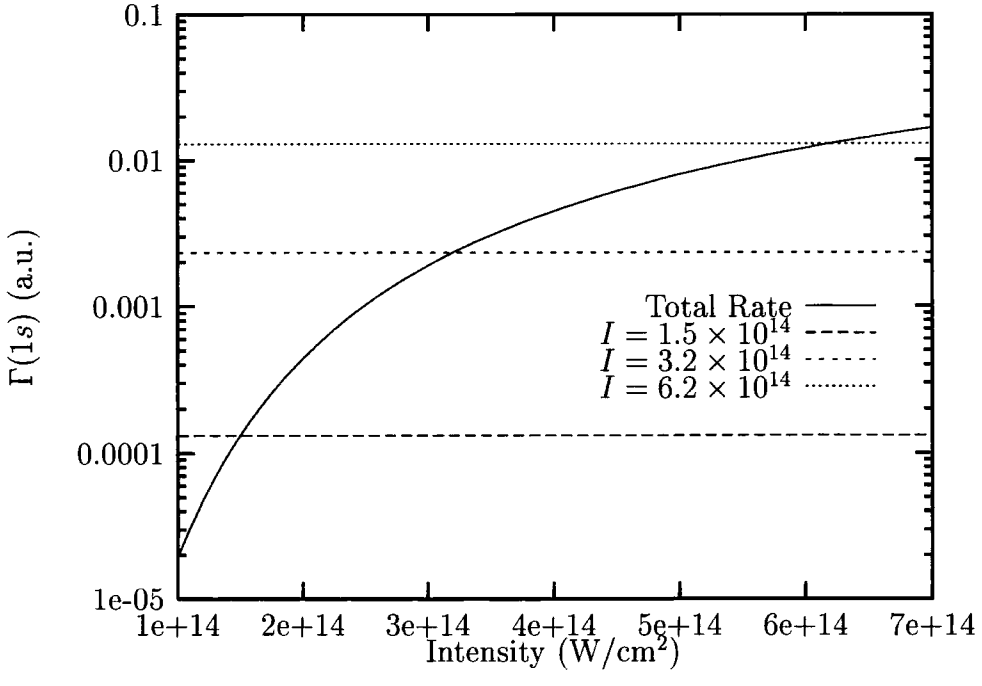

Figure 6.2: Total rate of ionisation of H($1s$) at 608 nm with circularly polarised light. Rates at three selected intensities relevant to our calculations have been singled out.

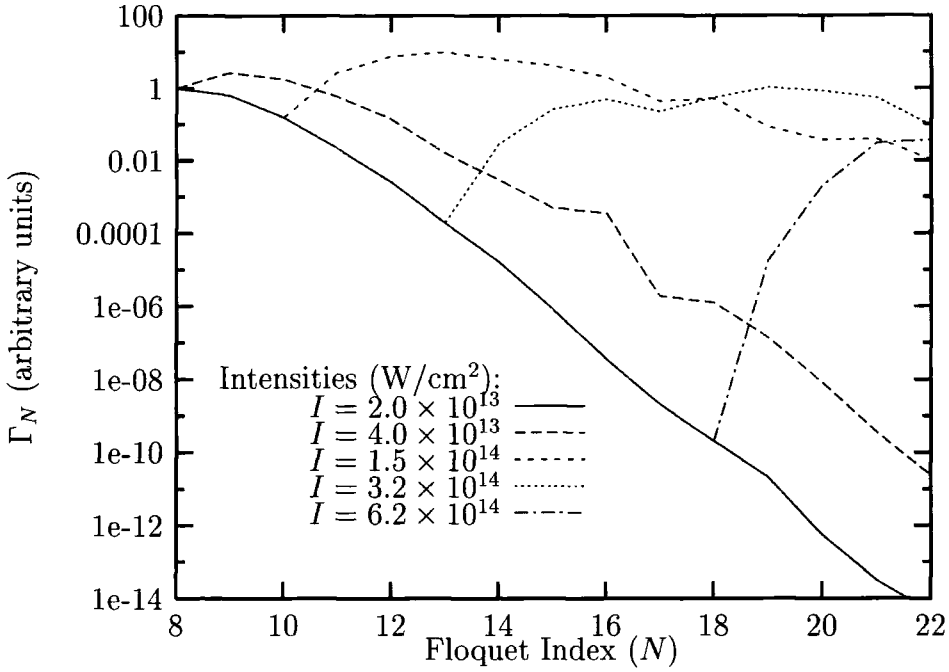

Figure 6.3: Partial rates of ionisation of H($1s$) at 608 nm with circularly polarised light and with a range of intensities. Results have been normalised such that $\Gamma_N(I, S = 0) = \Gamma_N(I = 2 \times 10^{13})$ and $\Gamma_N(I = 2 \times 10^{13}, S = 0) = 1$.

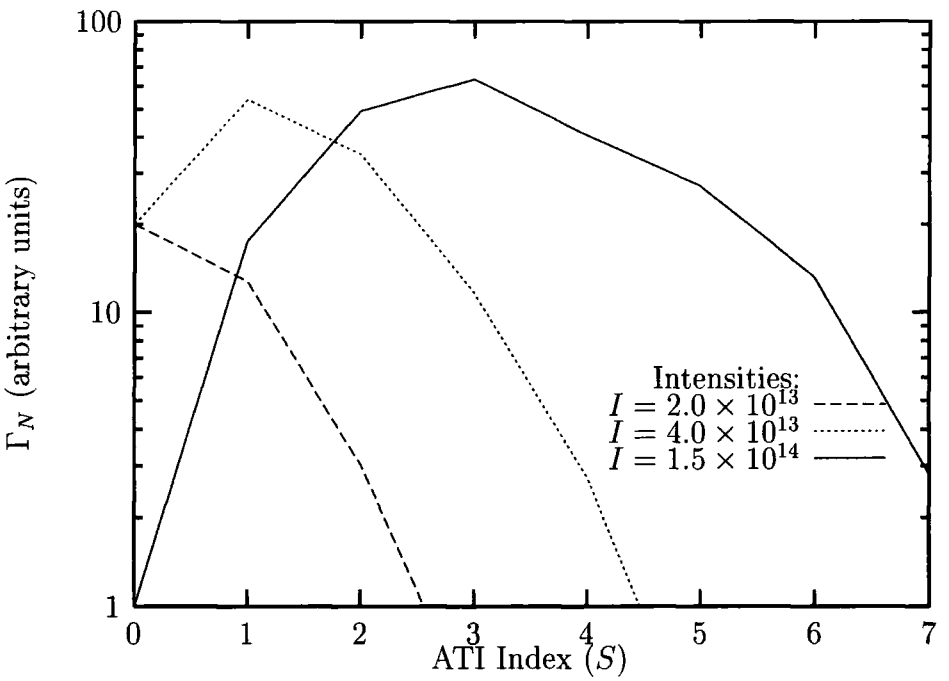

Figure 6.4: Partial rates of ionisation of H($1s$) at 608 nm with circularly polarised light. Relatively low intensities are considered and results are shown only for the lower ATI channels.

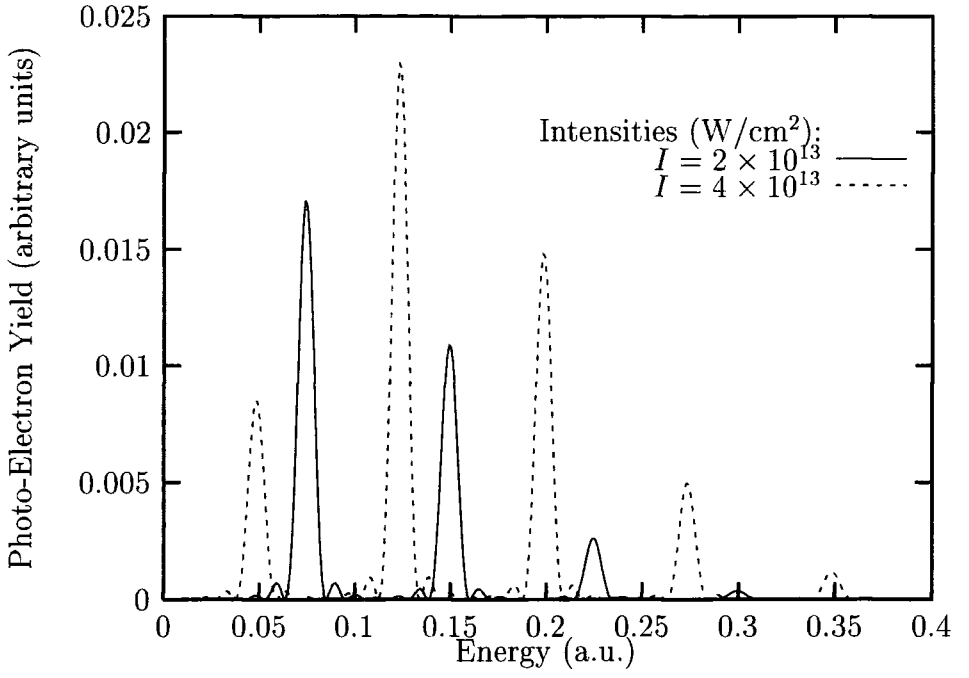

Figure 6.5: Photo-electron spectra for ionisation from H($1s$) at 608 nm with circularly polarised light. The lower-intensity curve has been scaled upwards by a factor of 50.

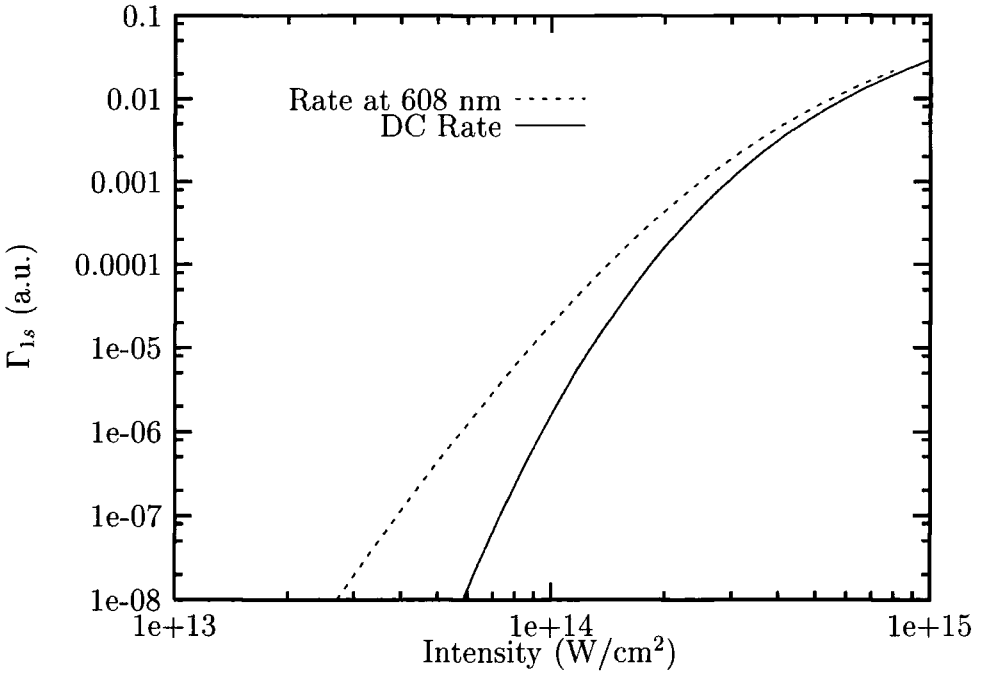

Figure 6.6: A comparison of the total rate of ionisation from H($1s$) due to a circularly polarised beam at 608 nm with the DC rate.

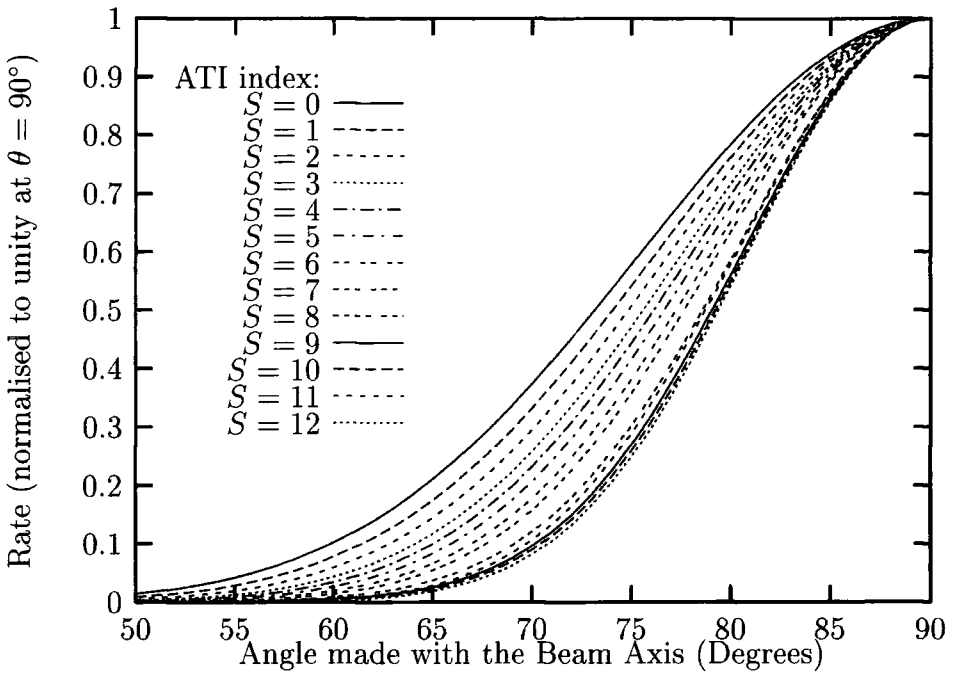

Figure 6.7: Angular distributions of photo-electrons from H($1s$) into the lower ATI channels for circularly polarised light at 608 nm and with $I = 2.0 \times 10^{13}$ W/cm^2.

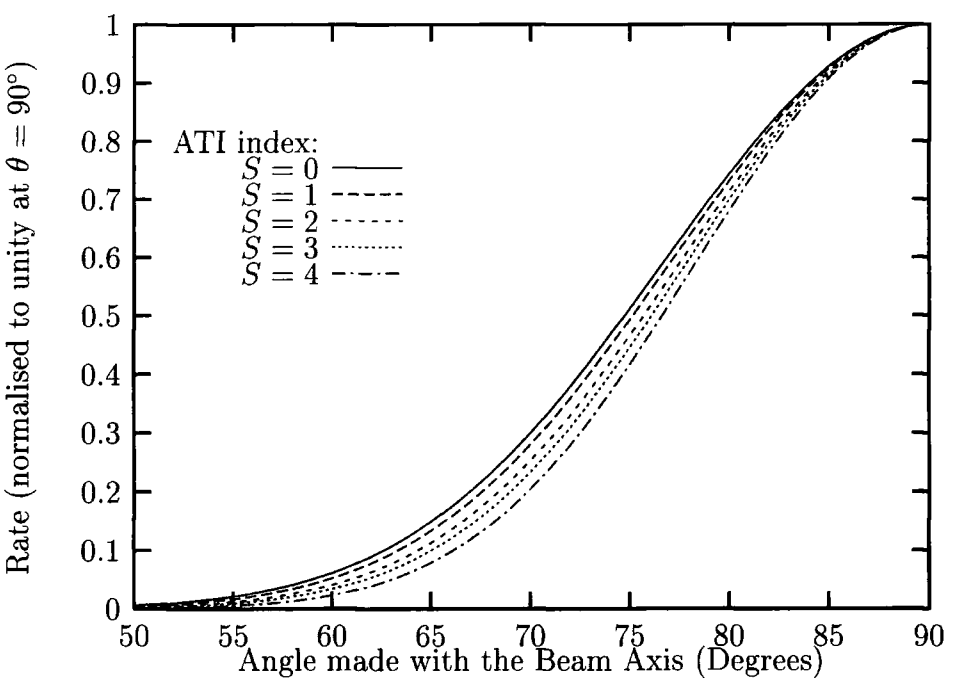

Figure 6.8: Angular distributions of photo-electrons from H($1s$) into the lower ATI channels for circularly polarised light at 608 nm and with $I = 1.5 \times 10^{14}$ W/cm^2.

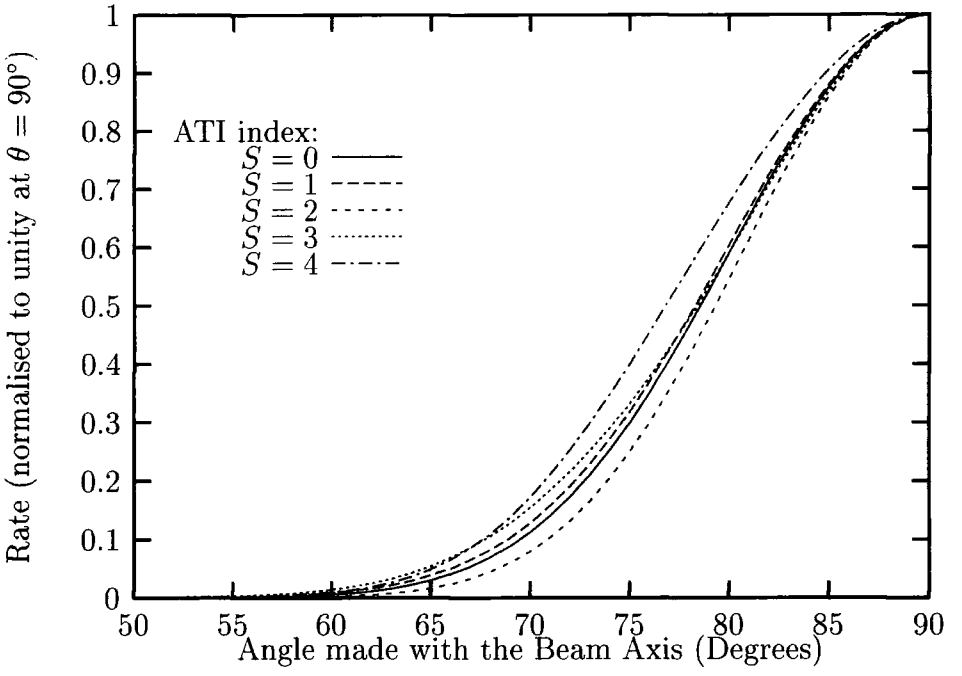

Figure 6.9: Angular distributions of photo-electrons from H($1s$) into the lower ATI channels for circularly polarised light at 608 nm and with $I = 6.2 \times 10^{14}$ W/cm^2.

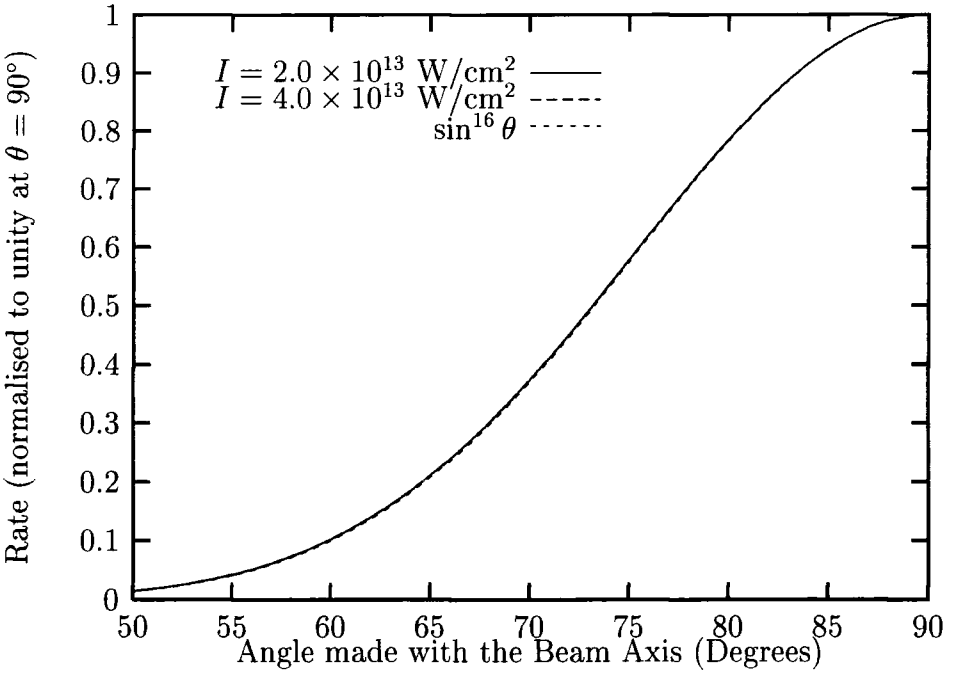

Figure 6.10: Angular distributions of photo-electrons from H($1s$) into the ATI channel $N = 8$ for circularly polarised light of various intensities at 608 nm. A comparison with the perturbative prediction is also shown.

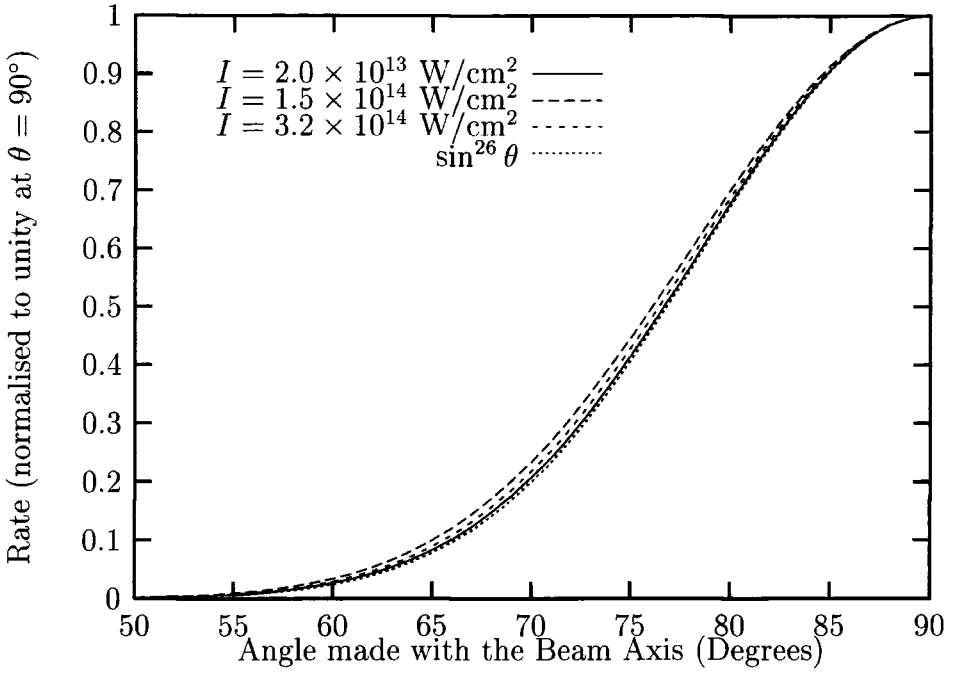

Figure 6.11: Angular distributions of photo-electrons from H($1s$) into the ATI channel $N = 13$ for circularly polarised light of various intensities at 608 nm. A comparison with the perturbative prediction is also shown.

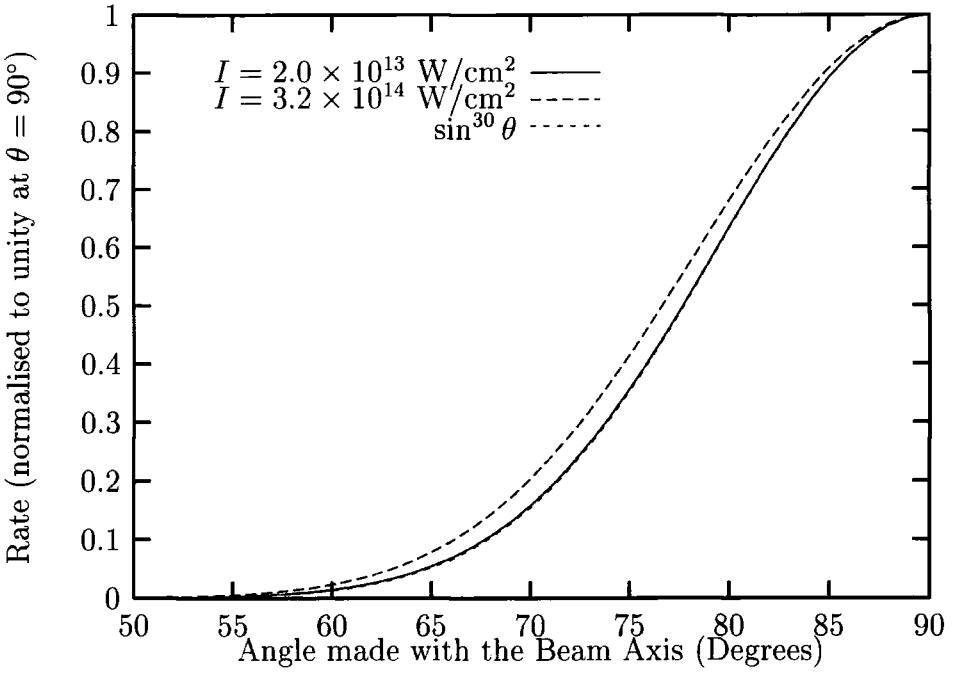

Figure 6.12: Angular distributions of photo-electrons from H($1s$) into the ATI channel $N = 15$ for circularly polarised light of various intensities at 608 nm. A comparison with the perturbative prediction is also shown.

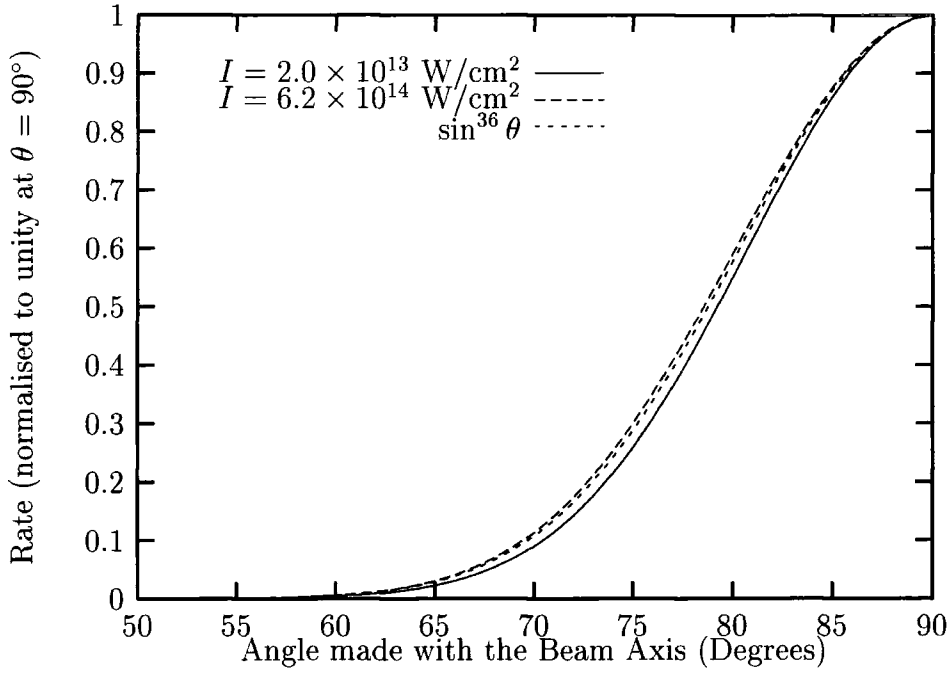

Figure 6.13: Angular distributions of photo-electrons from H($1s$) into the ATI channel $N = 18$ for circularly polarised light of various intensities at 608 nm. A comparison with the perturbative prediction is also shown.

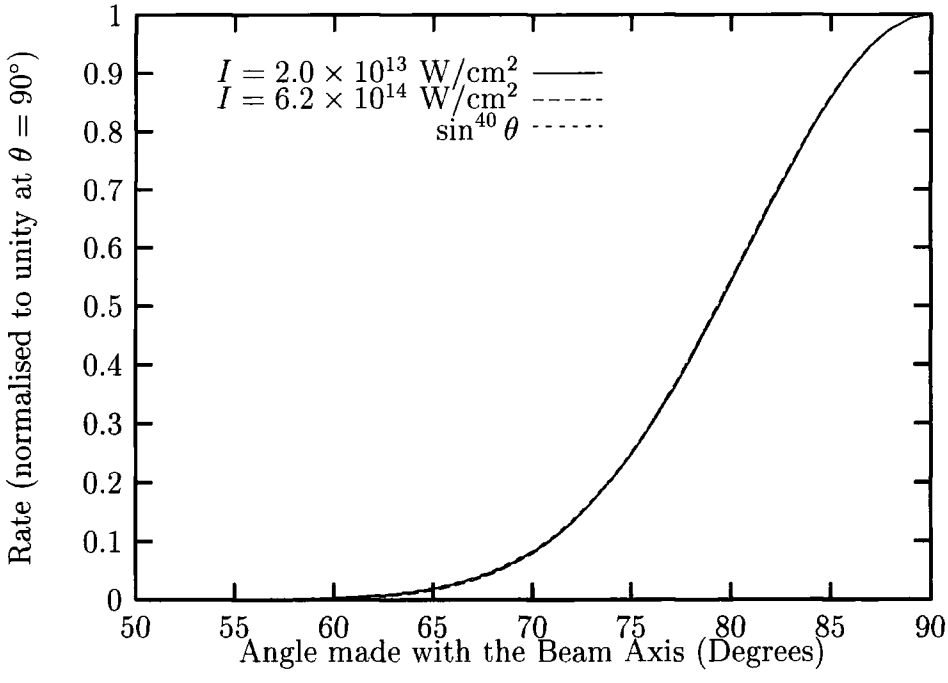

Figure 6.14: Angular distributions of photo-electrons from H($1s$) into the ATI channel $N = 20$ for circularly polarised light of various intensities at 608 nm. A comparison with the perturbative prediction is also shown.

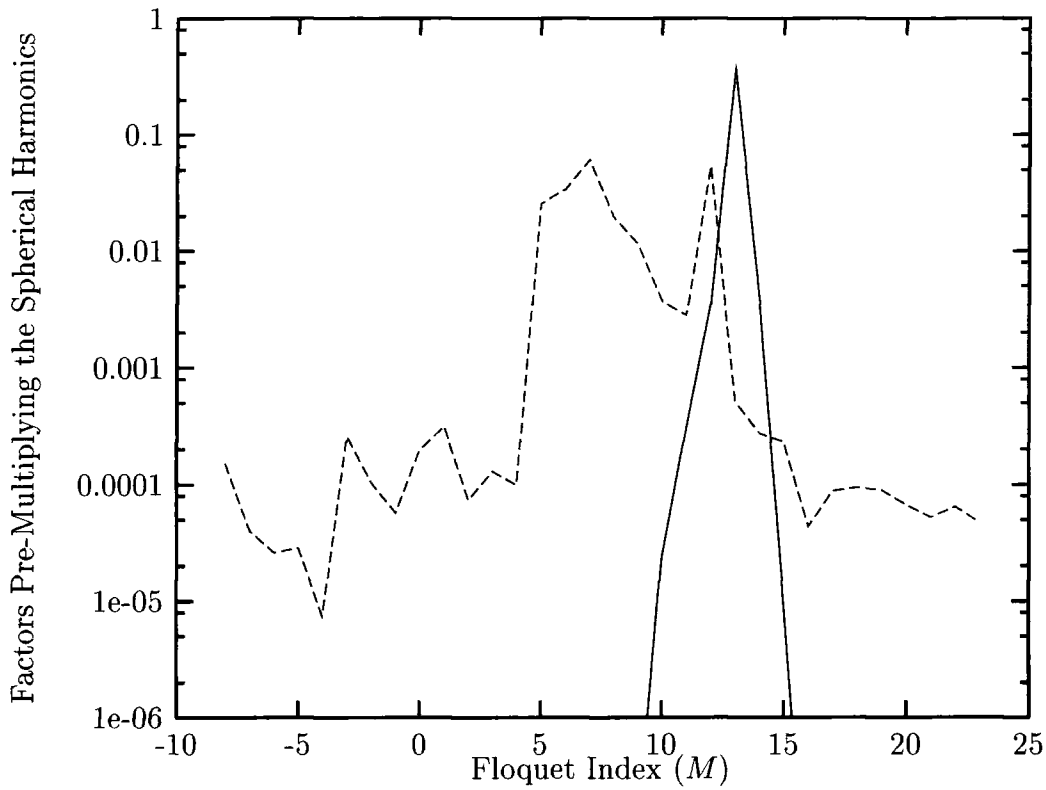

Figure 6.15: Numerical factors pre-multiplying the spherical harmonics $Y_{Ml}(\theta)$, $l \geq M$, in the calculation of the angular distribution of photoelectrons from H($1s$) due to a circularly polarised laser field. Other parameters are: $I = 1.0 \times 10^{11}$ W/cm^2, $\lambda = 608$ nm and $\theta = 75°$. The solid curve (———) represents the leading coefficient (i.e. that with $l = M$) multiplied by 10^{20} and the dashed curve (- - - -) represents the ratio of the next-to-leading term (i.e. that with $l = M + 2$) to this leading term. The ATI channel is $N = 13$.

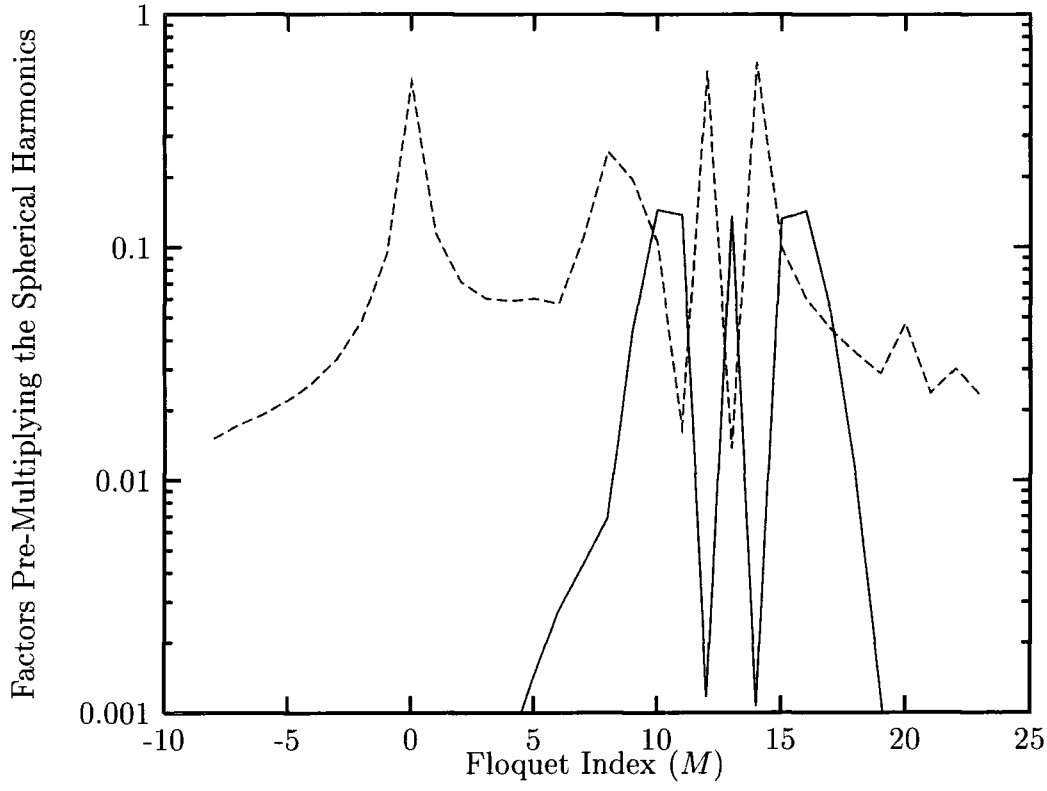

Figure 6.16: Numerical factors pre-multiplying the spherical harmonics $Y_{Ml}(\theta)$, $l \geq M$, in the calculation of the angular distribution of photoelectrons from H($1s$) due to a circularly polarised laser field. Other parameters are: $I = 3.2 \times 10^{14}$ W/cm^2, $\lambda = 608$ nm and $\theta = 75°$. The solid curve (———) represents the leading coefficient (i.e. that with $l = M$) multiplied by 10^3 and the dashed curve (- - - -) represents the ratio of the next-to-leading term (i.e. that with $l = M + 2$) to this leading term. The ATI channel is $N = 13$.

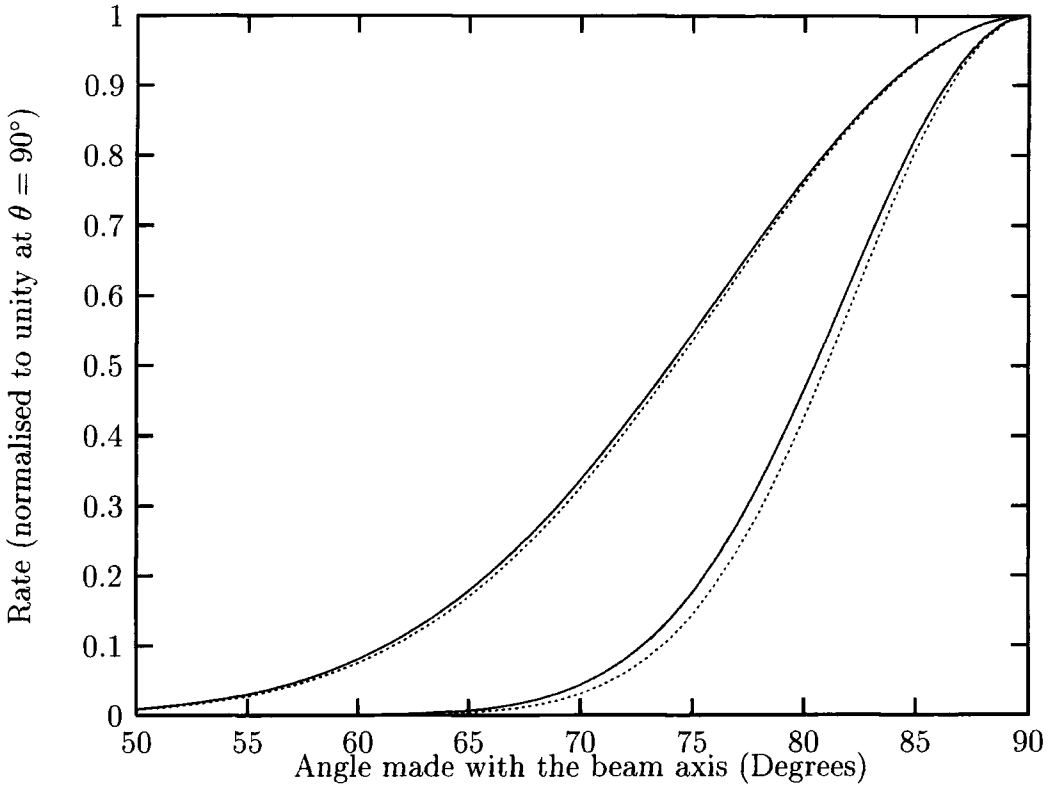

Figure 6.17: Angular distribution of photo-electrons from H^- due to a circularly polarised laser field of frequency 0.00440 a.u. and intensity 2.5×10^{10} W/cm^2. The upper group of curves corresponds to photo-electrons ejected into the $S = 0$ ATI channel whilst the lower group represents photo-electrons ejected into the $S = 19$ channel. The different curves within each grouping are: (———) Sturmian-Floquet calculation; (– – – –) Keldysh calculation by R M Potvliege [128]; (- - - - - -) Faisal-Reiss calculation by R M Potvliege [128]; (·····) results predicted by perturbation theory. In practice, the KFR results are almost indistinguishable from the Sturmian-Floquet results.

Chapter 7

Differential Rates for Hydrogen in a Two-Colour Laser Field

7.1 Two-Colour Floquet Theory

In chapter five we presented an overview of Sturmian-Floquet theory and for the sake of clarity that exposition was limited to the case of a monochromatic laser field. We now generalise the theory to the case of two (arbitrary) frequencies and then present the results of calculations in which the second colour is a high harmonic of the fundamental beam. Let us take first the general case of a bichromatic field whose two frequencies ω_L and ω_H are incommensurable (that is, they cannot be expressed as the ratio of two integers). Hereafter the subscript 'L' denotes quantities relating to the low-frequency field and 'H' denotes the corresponding quantities for the high-frequency field. Using the same notation as in previous sections we have the unperturbed atomic Hamiltonian

$$H_A = \frac{\boldsymbol{p}^2}{2} - \frac{1}{r} \tag{7.1}$$

and (working in the velocity gauge) the atom-field interaction

$$H_I(t) = -\frac{1}{c}\boldsymbol{A}(t)\cdot\boldsymbol{p} \tag{7.2}$$

where $\boldsymbol{p}$ is the canonical momentum of the electron (in the centre-of-mass frame) and $\boldsymbol{A}(t)$ is the classical vector potential of the field in the dipole

approximation. Writing the vector potential as

$$\boldsymbol{A}(t) = \Re\mathrm{e}(\boldsymbol{A_{0H}}\mathrm{e}^{-i\omega_H t}) + \Re\mathrm{e}(\boldsymbol{A_{0L}}\mathrm{e}^{-i\omega_L t}) \tag{7.3}$$

we can express the interaction potential as

$$H_I(t) = V_{H+}\mathrm{e}^{-i\omega_H t} + V_{H-}\mathrm{e}^{+i\omega_H t} + V_{L+}\mathrm{e}^{-i\omega_L t} + V_{L-}\mathrm{e}^{+i\omega_L t} \tag{7.4}$$

where

$$V_{H+} = -\frac{1}{2c}\boldsymbol{A_{0H}}\cdot\boldsymbol{p} \qquad \text{and} \qquad V_{L+} = -\frac{1}{2c}\boldsymbol{A_{0L}}\cdot\boldsymbol{p} \tag{7.5}$$

with $V_{H-} = V_{H+}^{\dagger}$ and $V_{L-} = V_{L+}^{\dagger}$ [33]. The time-dependent Schrödinger equation is

$$i\frac{d}{dt} \mid \Psi(t)\rangle = [H_A + H_I(t)] \mid \Psi(t)\rangle \tag{7.6}$$

and one looks for solutions of the form

$$\mid \Psi(t)\rangle = \mathrm{e}^{-iEt}\sum_{m,n}\mathrm{e}^{-i(m\omega_H + n\omega_L)t} \mid \psi_{m,n}\rangle \tag{7.7}$$

The harmonic component with indices (m,n) represents the absorption of m high-frequency and n low-frequency real or virtual photons. Substituting (7.7) into (7.6) one obtains the usual set of coupled, time-independent equations for the harmonic components $\mid \psi_{m,n}\rangle$

$$\begin{aligned}(E + m\omega_H + n\omega_L - H_A) \mid \psi_{m,n}\rangle = {} & V_{H+} \mid \psi_{m-1,n}\rangle + V_{H-} \mid \psi_{m+1,n}\rangle \\ & + V_{L+} \mid \psi_{m,n-1}\rangle + V_{L-} \mid \psi_{m,n+1}\rangle\end{aligned} \tag{7.8}$$

We must now impose the physical boundary conditions that the harmonic components should be regular at the origin $r \sim 0$ and should behave as a superposition of outgoing waves at $r \sim \infty$ (c.f. equation (5.8))

$$\langle \boldsymbol{r} \mid \psi_{m,n}\rangle = \sum_{m',n'} f_{m'n'mn}(\hat{\boldsymbol{r}}, E)\, r^{i\nu_{m'n'}}\frac{1}{r}\,\exp[ik_{m'n'}(E)\, r] \tag{7.9}$$

where the wave number k_{mn} of the $(m,n)^{\text{th}}$ channel is defined by

$$k_{mn}(E) = [2(E + m\omega_H + n\omega_L)]^{1/2} \tag{7.10}$$

The logarithmic distortion due to the Coulomb tail is taken into account by the inclusion of $\nu_{mn} = Z/k_{mn}$ where Z is the charge of the residual ion [119]. The coefficient $f_{m'n'mn}(\hat{\boldsymbol{r}}, E)$ is the amplitude for absorbing m' high-frequency and n' low-frequency *real* photons in the channel (m, n). Taken together, equations (7.8) and (7.9) form an eigenvalue problem for the (complex) quasi-energy E.

If instead the frequencies ω_L and ω_H are commensurable then we can write $\omega_H/N_H = \omega_L/N_L$ (for integers N_H and N_L) and define a *fundamental frequency* $\omega \equiv \omega_L/N_L$. Then our Floquet-Fourier ansatz is (c.f. equation (7.7))

$$| \Psi(t)\rangle = \mathrm{e}^{-iEt} \sum_n \mathrm{e}^{-in\omega t} \, | \psi_n\rangle \tag{7.11}$$

and substituting this into the time-dependent Schrödinger equation the harmonic components must satisfy the coupled equations [33]

$$\begin{aligned}(E + n\omega - H_A) \, | \psi_n\rangle = V_{H+} \, | \psi_{n-N_H}\rangle + V_{H-} \, | \psi_{n+N_H}\rangle \\ + V_{L+} \, | \psi_{n-N_L}\rangle + V_{L-} \, | \psi_{n+N_L}\rangle\end{aligned} \tag{7.12}$$

The eigenvalue E in this case depends not only on the frequencies and intensities of the two-colour field but also on the relative phase between the two beams. This is obvious if one considers the trivial case with $\omega_H = \omega_L$ and $I_H = I_L$ and arbitrary phase-difference (at $t = 0$) ϕ. Here, if $\phi = 0$ then the separate amplitudes of the two field-strengths augment each other, whereas if $\phi = \pi$ then they will cancel exactly at all times, leaving a constant total amplitude of zero. With incommensurable frequencies a simple phase transformation can remove this phase dependence but with commensurable frequencies one must always consider a specific phase.

With the exception of the trivial example above in which both fields are identical the addition of a phase-lag to the low-frequency field, i.e. $\cos(N_L\omega t) \to \cos(N_L\omega t + \phi_L)$, is not equivalent to the subtraction of the same phase from the high-frequency field. Rather, the equivalent phase change in the high-frequency field is $\cos(N_H\omega t) \to \cos(N_H\omega t + \phi_H)$ where $\phi_H = -(N_H/N_L)\phi_L$. Thus, one must be careful to specify to which field the phase is to be added. The eigenvalue E (and therefore also the decay rate Γ) is in fact periodic in

ϕ_L with period $\phi_P = 2\pi(N_L/N_H)$ [33]. We note that if ω_H is a high harmonic of ω_L then we have $N_L = 1$ and $N_H \gg 1$, giving $\phi_P \to 0$. If instead the phase is added to the high-frequency field then the periodicity in ϕ_H is given by $\phi_P = 2\pi(N_H/N_L) > 2\pi$. But there is also an independent 2π-periodicity and so one does not gain any further insight by discussing dynamics over a longer period. In our calculations we always add any phase difference into the high-frequency field and we drop the subscript 'H' and talk only in terms of a phase-lag $\phi \equiv \phi_H$.

For a field consisting of two commensurable frequencies the Floquet Hamiltonian may be written in block-matrix form (c.f. equation (5.19)

$$H_{nn'} = (H_A - n\omega)\delta_{nn'} + V_{H+}\delta_{n,n'+N_H} + V_{H-}\delta_{n,n'-N_H} + V_{L+}\delta_{n,n'+N_L} + V_{L-}\delta_{n,n'-N_L} \quad (7.13)$$

Results calculated using the Sturmian-Floquet formalism for ionisation by two-colour fields of commensurable frequencies have been previously reported by R M Potvliege in [98] and by Potvliege and Smith [121] [123] [124]. However this was for the case of a fundamental beam together with a low order harmonic (second, third, fifth or seventh), which is very different from the high-harmonic case which we present here. This work follows from the calculations on the ionisation of Hydrogen by two fields of incommensurable frequencies which was reported in some detail in [33]. Above threshold ionisation for atoms in a two-colour field has also been investigated both experimentally and theoretically by H G Muller *et al* [97] for the case with $\lambda_L = 1064$ nm and its second harmonic. The two beams had approximately equal intensities and the experiment involved a gas of Krypton atoms. It was found that the relative phase between the two beams plays an important role in determining both the ionisation rate and the relative heights and widths of the ATI peaks. Other experimental work on two-colour photo-ionisation processes has been performed by Schumacher *et al* [140] and Schins *et al* (both within Muller's group). Additional theoretical work has been carried out by A Cionga *et al* [23] [98] and is based on a radiative dressing approach. A brief description of this method and of other theoretical approaches is given

in section 5.1.

7.2 Overview of the Calculations

In this section we present the results of calculations for the ionisation of H($1s$) in a bichromatic laser field of commensurable frequencies. The important difference between this case and that of incommensurable frequencies (i.e. where the ratio of the two frequencies is not a rational number) is that the two fields act coherently and the relative phase between them may be expected to play a role. In particular it will be possible for the atom to arrive in a given final (continuum) state by a variety of different paths, i.e. one can always substitute N_H low-frequency photons for N_L high-frequency photons where the ratio of the frequencies is $\omega_H/\omega_L = N_H/N_L$ and the numbers N_L and N_H are integers. Thus, one expects to see interference between these competing ionisation processes. We take 1064 nm as the wavelength of the fundamental beam. This corresponds to a frequency $\omega_L = 0.04283$ a.u. which in the context of the ionisation potential $E_I = 0.5$ a.u. of H($1s$) is a very low frequency, requiring a minimum of 12-photon absorption for ionisation to occur in weak fields. Low frequency calculations are problematic in the Floquet approach because the large number of harmonic components needed for convergence results in very large matrices. However, 1064 nm is a realistic experimental wavelength and for that reason we take this as our fundamental. Calculations at this wavelength have also been performed by A Cionga; see her contribution in [98]. For the high-frequency field we take the fifteenth harmonic $\omega_H = 15\omega_L$ which corresponds roughly to a wavelength of 70.93 nm. In all our calculations this harmonic beam acts at a fixed intensity $I_H = 1\times10^9$ W/cm^2. Experimentally, harmonics such as this can be generated with efficiencies of up to about 10^{-5} at the present time, implying that in our case we would need to take $I_L > 10^{14}$ W/cm^2. This is somewhat higher than the actual intensities at which we can perform calculations at this wavelength but this is not a problem because experimentally an ultra-intense beam could always be attenuated to give the lower value of I_L that

Table 7.1: Properties of H($1s$) with bichromatic linearly polarised light at selected intensities I_L of the fundamental at 1064 nm and with $I_H = 10^9$ W/cm^2.

I_L (W/cm^2)	N_0	$\Re$e(E) (a.u.)	γ_K
5×10^{11}	12	-0.501687	11.35
2×10^{12}	12	-0.507566	5.673
12ω cut	–	-0.513872	–
13ω cut	–	-0.556695	–
2×10^{13}	14	-0.578119	1.794

we require. We choose both beams to be linearly polarised.

In table 7.1 we give the three intensities I_L of the fundamental which we have chosen to consider. We see that although the Stark shift at the two lowest intensities increases the ionisation potential of the atom by a noticeable amount, the 12-photon ionisation channel is still open. The 12-photon and 13-photon cuts are also given and the minimum number of (low-frequency) quanta required for multiphoton ionisation of the atom at $I_L = 2 \times 10^{13}$ W/cm^2 is fourteen. The real parts of the quasi-energies given in table 7.1 apply to both the fundamental beam acting alone and the two-colour calculation since the harmonic beam at such a low intensity does not contribute any Stark shift. Finally in this table we list the values of the Keldysh parameter γ_K [74] (described in section 3.3.2). These values indicate that even at the highest intensity considered there will not be any tunneling ionisation and we can describe the ionisation process simply in terms of the photons of both frequencies absorbed and emitted. Table 7.2 lists, for the same three intensities I_L as in table 7.1, the decay rates, firstly due to the fundamental beam acting alone (Γ_L), secondly due to the harmonic field acting alone (Γ_H), and lastly due to the bichromatic field ($\Gamma_{\rm bi}$). It can be seen that at both of the lower intensities the ionisation rate from H($1s$) due to the monochromatic beam acting alone is almost too small to calculate, in contrast to the real parts of the quasi-energies (see table 7.1) where the Stark shifts are quite significant. In the first row we also give the ionisation rate for the harmonic

Table 7.2: Ionisation rates of H($1s$) with bichromatic linearly polarised light at selected intensities I_L of the fundamental at 1064 nm and with $I_H = 10^9$ W/cm^2. There is no phase-lag between the two fields.

I_L (W/cm^2)	Γ_L (a.u.)	Γ_H (a.u.)	Γ_{bi} (a.u.)
0	–	$2.7673\ 10^{-8}$	–
5×10^{11}	~ 0	–	$2.7670\ 10^{-8}$
2×10^{12}	$\sim 10^{-18}$	–	$2.7671\ 10^{-8}$
2×10^{13}	$1.056\ 10^{-9}$	–	$2.5830\ 10^{-8}$

field acting alone and find that it is greater than the rate when the fundamental (at any of the given intensities) is acting. This effect is very minor at low intensities I_L but when $I_L = 2 \times 10^{13}$ W/cm^2 the total rate ionisation due to the bichromatic field drops by 6.66% compared to the rate from the bare harmonic field. This shows that, far from the rates of the two constituent beams summing to give the rate when both act together, we instead get an interference effect between the two resulting in this decrease in the total yield.

Our aim in this section is to present the results of calculations of the photo-electron yields and their angular distributions for the ionisation of H($1s$) by a two-colour field. At low intensities of the fundamental (i.e. $I_L = 5 \times 10^{11}$ W/cm^2) we expect single-photon ionisation (SPI) to be the dominant ionisation process. That is, the only significant contribution to the calculated ionisation rate comes from the absorption of one high-frequency photon plus zero low-frequency photons. At $I_L = 2 \times 10^{12}$ W/cm^2 the decay rate due to multiphoton ionisation (MPI) is still virtually zero and so we still expect the most probable path by which by which ionisation occurs to involve the absorption of a single high-frequency photon. At intensities such as this the photo-electron spectrum may however be 'dressed' by the absorption of $\pm 1, \pm 2 \ldots$ low-frequency photons and so the most likely energy of the emerging electrons may no longer be $E_{1s}(I) + \omega_H$. At very high intensities of the fundamental ($I_L \geq 2 \times 10^{13}$ W/cm^2) the MPI rate is nearly as great as that involving absorption of a high-frequency photon. Therefore one would expect

the two processes to compete and to observe evidence of this interference in the partial rates and angular distributions. Calculations along these lines have previously been performed by Véniard *et al* [151] [152] although at a lower wavelength of the fundamental and with a different harmonic order for the high-frequency beam. Their results [151] span a range of intensities of the fundamental and to a large extent agree with the scheme described above. Véniard's results have, in the case of figure 2(a) of their paper, been reproduced by calculations using the Sturmian-Floquet code [126]. This figure of Véniard's is reproduced here (and is labelled figure 7.1) for purposes of comparison.

7.3 Quasi-Energies and the Partial Rates of Ionisation

As was shown in table 7.2 the decay rates $\Gamma(I) = -2\Im\mathrm{m}(E)$ are virtually zero when $I \leq 2 \times 10^{12}$ W/cm^2 and so the quasi-energy at these intensities lies essentially on the negative real axis. The quasi-energies for H($1s$) with a linearly polarised monochromatic beam at 1064 nm have been calculated by R M Potvliege in [57] and a relevant subset of these are reproduced here in figure 7.2. We see that in the intensity range $I = (1.54, 2.55) \times 10^{13}$ W/cm^2 the dressed $1s$ state shifts steadily to deeper energies and the total rate of ionisation increases by a factor of approximately forty. A series of resonance peaks are clearly shown in the figure (corresponding to 12- or 13-photon transitions to intermediate states) but these occur at intensities well below 2×10^{13} W/cm^2 and therefore our own calculations are concerned with non-resonant ionisation. Figure 7.3 compares the total rates of ionisation of H($1s$) at 1064 nm both with and without the harmonic field acting. Only 65 quasi-energies have been calculated in the case of the bichromatic field and so the fact that the fine structure of very narrow resonance between 2.5 10^{13} W/cm^2 and 3.0 10^{13} W/cm^2 is not well reproduced does not indicate that these resonances have been suppressed. Rather, figure 7.3 gives a general impression of the extent to which multiphoton ionisation contributes to the

overall decay rate in the two-colour field at intensities $I \geq 10^{13}$ W/cm^2. The basis set used in obtaining these quasi-energies is: $-8 \leq N \leq 33$, $0 \leq l \leq 11$, $n_{bf} = 90$, $\theta_r = 7°$ and $\mathcal{E}_{\rm st} = -0.20$ a.u.. For an explanation of these parameters see section 5.4. It has been established that the results obtained are well converged with respect to these various parameters.

Figure 7.4 shows the photo-electron yield from H($1s$) for a simple model pulse with $I_L = 5 \times 10^{11}$ W/cm^2. The temporal dependence of the intensity is chosen to have a trapezoidal shape with the same parameters as were discussed for figure 6.5 in section 6.2. This is the same pulse envelope which was taken by Véniard *et al* [151] in their calculations and we choose the same to facilitate a more direct qualitative comparison with their results. The method by which we calculate the spectrum corresponding to a given set of partial rates Γ_N is described in the appendix to chapter five. This short pulse ($8\tau \approx 28$ fs) gives rise to reasonably broad ATI peaks, each of which possesses a small family of fringes whose magnitude is no more than about 5% of the height of the principal peak. It has been shown that the variation of intensity during the ramp-on and ramp-off periods contributes almost nothing to the final photo-electron yield [126]. However D A Telnov and S-I Chu [150] have found, taking a low-frequency, adiabatic approach that the intensity-profile of the pulse does play in important role in determining the photo-electron spectrum and the relevant angular distributions. The single prominent peak located at the energy value of 0.14 a.u. corresponds to the absorption just one high-frequency photon and no low-frequency photons. The principal sub-peaks to either side represent the less probable processes of absorbing $(1\omega_H \pm 1\omega_L)$ photons and at an energy ≈ 0.27 a.u. the bump corresponding to $(1\omega_H + 3\omega_L)$ is just visible. A very similar result to this is obtained by Véniard *et al* [151] at 800 nm with $\omega_H = 13\omega_L$, $I_L = 5 \times 10^{11}$ W/cm^2 and $I_H = 3 \times 10^8$ W/cm^2. The sub-peaks in their photo-electron spectrum are smaller in proportion to the main peak than ours our, despite the ratio I_L/I_H being bigger in their case, and we attribute this difference to the shorter wavelength in their calculation making low-frequency photon absorptions and emissions a little less probable than in our case. The two-

colour photo-electron spectrum for linearly polarised beams at 800 nm (i.e. the Ti:S wavelength) plus a high (odd-numbered) harmonic has also been investigated by Cionga [98] in the radiative dressing approach. Results have been calculated for the 13^{th} harmonic and are found to agree well with those of Véniard *et al.*

Figure 7.5 shows the absolute partial rates Γ_N obtained with $I_L = 5 \times 10^{11}$ W/cm^2. Additionally we vary the relative phase of the two beams at time $t = 0$ and find that this makes no difference whatsoever to the calculated results. This is not surprising given the extremely minor role played by the fundamental at this intensity. (Recall the disparity in decay rates shown in table 7.2.) Our result is consistent with the statement by R M Potvliege in [98] that phase dependence is insignificant when the order of the harmonic is such that interference between the different ionisation paths requires the exchange of a large number of photons. For these calculations our basis set was: $-8 \leq N \leq 37$, $0 \leq l \leq 11$, $n_{bf} = 110$, $\theta_r = 15°$ and $\mathcal{E}_{\text{st}} = -0.25$ a.u.. (The meaning of these parameters is explained in section 5.4.) This is more than sufficient for the results shown in figure 7.5 to be converged to an accuracy of better than 1% and in fact they remain well converged up to channel $N = 20$ beyond which there is some loss of convergence primarily with respect to the number of radial basis functions n_{bf} in the Sturmian expansion.

Figure 7.6 illustrates the photo-electron spectrum when $I_L = 2 \times 10^{12}$ W/cm^2. Here we find that the peak corresponding to the absorption of $(1\omega_H + 0\omega_L)$ photons is no longer the highest ATI peak and that it is approximately a factor of three smaller than that for the absorption of $(1\omega_H - 1\omega_L)$ photons. So the two main peaks correspond to the absorption processes $(1\omega_H \pm 1\omega_L)$ and the highest order process to manifest itself in this case is the $(1\omega_H + 5\omega_L)$ transition (giving rise to photo-electrons with an energy of approximately 0.35 a.u.). A similar pattern of ATI peaks was obtained by Véniard *et al* [151] at 800 nm with $\omega_H = 13\omega_L$, $I_L = 3 \times 10^{12}$ W/cm^2 and $I_H = 3 \times 10^8$ W/cm^2 but as in the previous comparison our spectrum spreads out to an above-threshold index one higher than theirs. When comparing (in our calculation) the sum

of the partial rates to the total rate obtained from the quasi-energy (recall equation (6.13)) we find that the two methods agree to within approximately 1%. This is a measure of the accuracy of our methods. Figure 7.7 shows the phase dependence of these partial rates at $I_L = 2 \times 10^{12}$ W/cm^2 and once again we find almost no differences between the various cases. The very slight discrepancies for the rates into channels $N = 17, 18$ are likely to be of numerical origin. The basis set which we took for these calculations was the same as that used at $I_L = 5 \times 10^{11}$ W/cm^2 and we find that the partial rates are converged to an accuracy of 1% or better in the channels $N \leq 17$. Beyond this there is a loss of convergence with respect to the number of radial basis functions n_{bf} amounting to, for example, a possible error of approximately 10% in channel $N = 18$.

In figure 7.8 we present the partial rates into the first three ATI channels with $I_L = 2 \times 10^{13}$ W/cm^2. In fact these results proved extremely difficult to converge (due to a sizeable MPI rate) and the partial rates are accurate only in the channels $S = 0, 1$. The basis set used in these calculations was: $-8 \leq N \leq 37$, $0 \leq l \leq 15$, $n_{bf} = 110$, $\theta_r = 7°$ and $\mathcal{E}_{\rm st} = -0.20$ a.u.. With respect to the number of harmonic components we performed trial calculations with max.$(N) = 25$, 31, 33, 35, 37 and 39 and found that with max.$(N) \geq 33$ we obtain convergence to a level better than 1% in the first two above-threshold channels but also that even with max.$(N) = 37$ the results in channel $S = 2$ remain very far from convergence. Moving on to the angular momenta we find that even in channel $S = 0$ one must choose max.$(l) \geq 15$ in order to have convergence to a level better than 1%. Max.$(l) = 15$ is sufficient in channels $S = 0, 1$ but not thereafter. The highest value for which we performed a trial computation is $0 \leq l \leq 17$. For the radial basis functions we have compared results with $n_{bf} = 100$, 110 and 120. These reveal that choosing $n_{bf} = 110$ is sufficient for convergence in channels $S = 0, 1$ to the level of 2% but these three cases diverge beyond that. At this high intensity we do now see considerable differences in the rates when different phases ϕ between the two beams are taken at $t = 0$. We find that the branching ratio $\Gamma_N(S = 0)/\Gamma_N(S = 1)$ is smallest when the

Table 7.3: Ionisation rates of H($1s$) with $I_L = 2 \times 10^{13}$ W/cm^2 and with varying phases ϕ at time $t = 0$.

Phase (deg.)	Total Rate Γ (a.u.)
0	$2.5830\ 10^{-8}$
45	$2.6052\ 10^{-8}$
90	$2.6587\ 10^{-8}$
120	$2.6965\ 10^{-8}$
180	$2.7344\ 10^{-8}$

two beams are initially in phase and that it is approximately 30% greater for the other phases which we consider. The sum of the partial rates differs here from the total rate (evaluated by $\Gamma = -2\Im\mathrm{m}(E)$) by as much as 10% but we also note that in all cases the partial rates sum to less than the total rate. Moreover the photo-electron spectrum has a plateau extending over many ATI peaks and has not fallen off to zero when the truncation value ($N = 37$) is reached. Therefore some significant contributions to the sum of the partial rates may have been omitted, leading to the apparent discrepancy with the total rate of ionisation. Thus we believe that our calculations at this intensity are much more accurate than the figure of 10% would indicate. Véniard *et al* [151] also obtain a phase dependent photo-electron spectrum at high intensities $I_L > 10^{13}$ W/cm^2 and in one case are able to reverse the relative heights of a pair of adjacent ATI peaks. The effect in our calculations is less dramatic than this.

We also observe a small phase dependence in the total rates of ionisation and these are given in table 7.3. We see from this that the total rate of ionisation increases steadily as the phase increases from zero to π and that the ratio $\Gamma(\phi = \pi)/\Gamma(\phi = 0)$ yields a total increase of around 6%. Recall from the discussion of table 7.2 that the ionisation rate when the bichromatic field is acting is (when $\phi = 0$) about 6.7% smaller that that from the harmonic field alone. We believe that the similarity in these figures is not a coincidence and that the choice of phase $\phi = \pi$ optimally minimises the interference effect between competing ionisation paths. Recall from section 7.1 that the phase

dependence in the ionisation should have period given by $\phi_P = 2\pi(N_H/N_L)$ where $\omega_H/N_H = \omega_L/N_L$ [33]. In our case this gives $\phi_P = 30\pi$ radians and is therefore of no importance. We see from table 7.3 that the quasi-energy eigenvalue E does vary with the phase but this variation will simply have a period of 2π. To conclude this section we can remark that our results do not support the assertion by R M Potvliege in [98] that when interference processes require the exchange of large numbers of photons the phase dependence in the ionisation rate is insignificant.

7.4 Angular Distributions of the Photo-Electrons

The angular distribution of photo-electrons from H($1s$) using linearly polarised monochromatic radiation is typically peaked about the polarisation axis (i.e. $\theta = 0$) and falls off to zero at $\theta \approx \pi/2$. This is because the distributions are proportional to the square of the Legendre Polynomial $P_l(\cos\theta)$ where l is the angular momentum quantum number of the final state and θ is the angle made by the direction of propagation of the outgoing electron with the polarisation axis [29]. For any l these polynomials have maxima at $\theta = 0$ and π, i.e. the distributions are symmetric in the forwards and backwards directions. In fact, since $P_l(\cos\theta)$ contains only the powers of theta whose parity is the same as the parity of l we can write the distribution as a sum over the even powers of $\cos\theta$,

$$\frac{d\Gamma_N}{d\Omega} = \sum_{n=0}^{l} a_N \cos^{2n}\theta \tag{7.14}$$

and so the higher the value of l, the more oscillatory the distribution is likely to be. As yet, very little has been published on the topic of the angular distribution of photo-electrons due to polychromatic radiation. The only example of which we are aware is the work by A Cionga in [98] using the radiative dressing method in which the Coulomb-Volkov wavefunctions are modified by the addition of perturbative corrections (as described in section 5.1). Cionga performs calculations principally at the the Ti:S frequency (or

equivalently, 800 nm) for the fundamental beam together with either its 13^{th} or 21^{st} harmonic. The intensity of the fundamental is chosen to lie in the range 10^{11} to 10^{12} W/cm^2 which is perhaps (at the upper end of this range) the limit at which one can expect accuracy within this pseudo-perturbative approach. Calculations have also been reported [98] at 1064 nm but where the high frequency is incommensurable with the fundamental frequency.

In figure 7.9 we plot the angular distributions into the first six ATI channels for bichromatic linearly polarised radiation The intensity of the fundamental is $I_L = 5 \times 10^{11}$ W/cm^2 and there is zero phase-lag between the two beams. We see that with the single exception of the curve corresponding to $S = 3$ all of them decrease smoothly from an initial maximum at $\theta = 0°$ to near zero at $\theta = 90°$ as predicted above. However, the lack of oscillations in these distributions is consistent with single-photon absorption (and in particular the absorption of one high-frequency photon). The curve marked $S = 3$ corresponds to the channel $N = 15$ and this differs from the other channels in being the only one not to include the additional absorption or emission of any low-frequency photons. Curiously, this curve ($N = N_H$ in figure 7.9) differs markedly from the $\cos^2\theta$ dependence that one would expect for an SPI process. It may be that this discrepancy arises from the absorption and emission of equal numbers of virtual low-frequency photons, simultaneously with the absorption of the one real high-frequency photon. MPI distributions with $N \geq 12$ will typically oscillate strongly and yet none of the distributions shown in figure 7.9 display any nodes. Whilst not necessarily inconsistent with high-order MPI (i.e. the linear combination of even powers of $\cos\theta$ may conspire such that all of the oscillations cancel each other out) this does tend to indicate that primary route to ionisation at this intensity does not involve the absorption of many photons of the fundamental field. Physically we can say that, having absorbed one high-frequency photon, the electron moves away from the nucleus so fast that it does not experience the oscillations of the low-frequency field until it has travelled a long distance. Cionga [23] [98] has performed similar calculations with $I_L = 5 \times 10^{11}$ W/cm^2 though at 800 nm and with the 21^{st} rather than the 15^{th} harmonic. She does not indicate

what value is taken for the other intensity, I_H. Despite these differences we see that figure 7.9 compares strikingly well with figure 3(b) of reference [98] (in the range $\theta = 0 \rightarrow \pi/2$). This figure of Cionga's is reproduced here (and is labelled figure 7.10) for purposes of comparison. In particular we observe that rates into the channels $N \neq N_H$ have a maximum at $\theta = 0°$ and fall off smoothly towards zero as θ approaches 90°. In contrast, the rate into channel $N = N_H$, although near-maximum at $\theta = 0°$ increases gradually to a maximum at $\theta \approx 30°$ before decaying towards zero in the same way as applies to the other channels. The fact that N_H has a very different value in Cionga's calculation than in ours (i.e. 21 rather than 15) and yet the angular distribution of the photo-electrons is so similar argues strongly that one should give a physical interpretation to the various features of these distributions.

In figure 7.11 we show the distributions for the same six channels but this time with an intensity of $I_L = 2 \times 10^{12}$ W/cm^2 for the low-frequency field. (Once again, the relative phase between the two fields is zero.) Here we see the same general pattern as at 5×10^{11} W/cm^2, i.e. rates which are strong at $\theta = 0°$ and which slope gently towards zero at $\theta = 90°$ without exhibiting any fluctuations in between. However, this simple picture holds only for channels $N = 12, 13$ and 17. The three ATI channels centred around the single-photon absorption channel $N = 15$ have very different angular distributions. This is consistent with the most probable ionisation paths being the absorption of $(1\omega_H \pm 1\omega_L)$ photons, as we saw in figure 7.6. The distribution into channel $N = 15$ has a global maximum at $\theta = 63°$ and that into channel $S = 14$ reaches its maximum value at $\theta = 32°$. Let us compare our results at this intensity with those of Cionga in [98]. She does not report calculations at this intensity of the fundamental but instead presents results at $I_L = 10^{12}$ W/cm^2. Once again there is a strong qualitative similarity between our results and hers. The latter are shown in figure 3(c) of reference [98]. In the channels $N \neq N_H$ she finds the same angular distributions as at lower intensities and we also obtain this straightforward slope from a maximum at $\theta = 0°$ to zero at $\theta = 90°$ with the exception of channel $N = N_H + 1$ as

described above. This difference is probably due to the higher intensity used in our calculation. In channel $N = N_H$ the agreement between our results and Cionga's is surprisingly great given the differences in the defining parameters of our calculations. (We should stress that she uses the harmonic $N_H = 21$ rather than $N_H = 15$.) In both cases the angular distribution starts with a moderate value at $\theta = 0°$, reaches a maximum at around $\theta = 60°$ whose magnitude is greater than twice that at $\theta = 0°$ and then falls off to zero in the direction perpendicular to the quantisation axis. In figure 7.12 we examine the phase dependence of the angular distributions with $I_L = 2 \times 10^{12}$ W/cm^2 and take as an example the channel $N = 15$. It is clear that, as with the partial rates in figure 7.7 there is no phase dependence at this intensity. We attribute this to the large number of low-frequency photons needed to reach the same photo-electron energy as can by attained by the absorption of a single high-frequency photon.

In figure 7.13 we have the interesting case of the angular distribution of photo-electrons into the ATI channel $S = 0$ (or $N = N_0 = 14$) when the fundamental beam has its highest intensity of $I_L = 2 \times 10^{13}$ W/cm^2. We take five different phases (added to the high-frequency field) in the range $\phi = 0° \rightarrow 180°$ and observe a continuous variation in the distribution as ϕ increases from zero to π. In all five cases the distributions are very similar in the range $\theta = 0° \rightarrow 30°$, exhibiting a maximum at $\theta = 0°$ and falling rapidly to zero at $\theta \approx 27°$, but thereafter they diverge. The distribution with $\phi = 0°$ reaches its greatest value at $\theta = 90°$ whereas with increasing ϕ the rate at $\theta = 90°$ moves progressively downwards and reaches a minimum with $\phi = 180°$. Specifically, with $\phi = 0°$ the (14-photon) rate at $\theta = 90°$ is 1.17 times that at $\theta = 0°$ while, with $\phi = 180°$, the corresponding ratio is only 0.38, reversing the dominant angle at which the photo-electrons are ejected. In order to study this case experimentally one would need to generate the 15^{th} harmonic with an efficiency of 5×10^{-5} and as far as we are aware this figure is very close to that which can be obtained from currently available sources, without needing to further attenuate the fundamental beam [62]. The calculations of Véniard *et al* [151] at the Ti:Sapphire frequency are already (in principle) accessible

to experiment although there are practical difficulties in the coherent control of the two beams. Referring back to table 7.2 we believe that at 1064 nm and with a harmonic intensity of 10^9 W/cm^2 the fundamental intensity of $I_L = 2\times10^{13}$ W/cm^2 is the lowest at which one might reasonably expect to observe the effects of phase-difference between the two fields. Of course, with a weaker harmonic beam such effects should be apparent at lower intensities of the fundamental. Finally, concerning figure 7.13 we would like to comment that the position of the side-lobes at $\theta = 40°$ and $\theta = 90°$ are unlikely to have any physical significance. Rather, they are symptomatic of interference between ionisation routes whose probabilities are of similar orders of magnitude, as shown in table 7.2.

We are now able to compare angular distributions into a given above-threshold channel ($N \geq N_0$) due to monochromatic and bichromatic fields of differing intensities. At each intensity the calculations for the bichromatic field use the same basis set as was used when computing the partial rates of ionisation. (Indeed, the code computes both quantities simultaneously.) These basis sets are described in section 7.3. However the convergence of the (normalised) angular distributions with respect to the various parameters of the basis need not occur at the same rate as was observed in the case of the partial rates. Therefore a systematic study is required in order to be assured of presenting well-converged results in the remainder of this section. At $I_L = 5 \times 10^{11}$ W/cm^2 there is a slight loss of convergence for the angular distributions into ATI channels $S \geq 6$ but (at least for $S < 9$) an upper bound for the magnitude of this error is 2%. At $I_L = 2 \times 10^{12}$ W/cm^2 there is excellent convergence (i.e. an error much smaller than 1%) of the distributions into channels $S = 0 \rightarrow 2$ with respect to all parameters. In channels $S = 3 \rightarrow 5$ the same is true with the exception of the number of radial basis functions n_{bf}, with respect to which we observe a loss of accuracy of up to 2%. In channel $S = 6$ there is an additional error amounting to up to 3% due to incomplete convergence with respect to the number of harmonic components. At $I_L = 2 \times 10^{13}$ W/cm^2 we consider only the lowest two open channels $N = 14, 15$. For the distribution into channel $N = 14$ we

find that our results are very well converged (better than 1%) except for θ in the range $70° \rightarrow 90°$ in which there is a potential error of up to 5% due to the number of basis functions included in the calculation. For $N = 15$ the convergence with respect to the number of basis functions is better but at the global maximum in this distribution (i.e. at $\theta \approx 70°$, see figure 7.16) there is a difference of 6% between the result computed with max.$(l) = 15$ and that with max.$(l) = 17$. The level of accuracy over all the rest of this distribution and with respect to the other basis parameters is much better than this. All of the figures above relate to the calculations for a bichromatic field. A similar analysis of results due to the fundamental beam only (but at the same intensities) reveals very good levels of convergence (better than 1% in all cases) with the single exception of the distribution into channel $S = 5$ at $I = 2 \times 10^{12}$ W/cm^2 for which there are sizeable errors of approximately 5% with respect to the number of basis functions and 15% with respect to the number of angular momenta (max.$(l) = 11$ versus max.$(l) = 9$). Having established that the level of convergence in our results is sufficient for a meaningful discussion we are now in a position to present those results.

Starting with the lowest open channel ($N = 12$) we display our results in figure 7.14. Here we have four curves representing the angular distributions of the 12-photon partial rate due to monochromatic radiation (at 1064 nm) at intensities 5×10^{11} W/cm^2 and 2×10^{12} W/cm^2, and bichromatic radiation consisting of the same fundamental plus the 15^{th} harmonic at the fixed intensity $I_H = 10^9$ W/cm^2. One immediately notes that both of the distributions resulting from the monochromatic fields display a more complicated structure than their two-colour counterparts. This is because in a monochromatic calculation this channel is accessible only by the absorption of twelve photons and as discussed earlier this naturally leads to oscillations in the distribution which can be expressed as a sum over even powers of $\cos\theta$. The general trend of the curves plotted in this figure is that the maximum rate coincides with the polarisation axis and that the rate is near-zero in the plane perpendicular to this axis. The same comments apply to the rates into the channel $N = 13$ and consequently we do not plot these rates here.

For channel $N = 14$ we plot the various angular distributions in figure 7.15. A relative phase of zero at time $t = 0$ is assumed. In this channel for which, in the two-colour calculation, only one low-frequency photon need be emitted we obtain very different results depending on whether the harmonic field is, or is not, included. At low intensities of the fundamental the harmonic field serves to significantly broaden the distribution so that although the maximum value still occurs at around $\theta = 0°$ the rate falls to approximately only half of this value at $\theta = 45°$. Comparing a few representative data values at $\theta = 45°$: at $I_L = 5 \times 10^{11}$ W/cm^2 we have a (normalised) rate of 0.38 with the harmonic field compared to 0.19 without the additional field; at $I_L = 2 \times 10^{12}$ W/cm^2 we have a (normalised) rate of 0.78 with the harmonic field compared to 0.17 without this second field. With $I_L = 2 \times 10^{13}$ W/cm^2 we obtain the curve that has already appeared in figure 7.13. This angular distribution is peaked in both the $\theta = 0°$ and $\theta = 90°$ directions and is close to zero (never more that 4% of its initial value) for angles θ between 25° and 60°. The difference in form between this result and that at lower intensities may be explained by interference effects between the absorption processes $(0\omega_H + 14\omega_L)$ and $(1\omega_H - 1\omega_L)$ the amplitudes for which are approximately equal in magnitude.

We display the relevant angular distributions into the ATI channel $N = 15$ in figure 7.16. Here, as for $N = 14$, we see that the distributions when the harmonic field is acting are very different from those for the monochromatic beam. Moreover we are able to compare the angular distribution of photo-electrons produced by the *harmonic beam acting alone* with those due to the bichromatic fields. We find that even at the lowest intensity of the fundamental (i.e. $I_L = 5 \times 10^{11}$ W/cm^2) the angular distribution is quantitatively different when the low-frequency field is acting in addition to the harmonic field. To be precise, the distribution from the bichromatic field at this intensity is much broader than that from the (monochromatic) harmonic field. Comparing (normalised) values at $\theta = 45°$: the rate from the harmonic field alone is 0.50 compared to 0.90 when the weak low-frequency field is also acting. Note that the value of 0.5000 is in accordance with equation (7.14)

which predicts that for one-photon absorption (and $l = 1$ for the final state) we have a angular distribution which is $\sim \cos^2\theta$. Here $\cos^2(\pi/4) = 0.5$. The fact that the addition of such a weak fundamental beam has such a dramatic effect on the angular distribution due to the harmonic beam is curious and may be due to the absorption and emission of equal numbers of virtual low-frequency photons during the ionisation process. It should be remembered that all photons carry just one unit of angular momentum irrespective of their energy.

Finally we come the angular distributions into the higher channels $N \geq 16$. Our numerical results are not well converged for the channels $N \geq 18$ (except in the lowest intensity case) so we will briefly discuss the results for ATI channel $N = 17$ as our last example. These distributions are shown in figure 7.17, and in this we observe none of the side-lobes which were evident in channels $N = 14$ and 15. Instead, both for the monochromatic low-frequency beam and the two-colour field the distributions are strongly peaked about the polarisation axis, fall to around half of their maximum value by $\theta = 30°$, and are approximately zero (on a linear scale) for $\theta \geq 60°$. There is in fact very close agreement between the monochromatic and bichromatic results at $I_L = 5\times10^{11}$ W/cm^2 and qualitative if not quantitative agreement at $I_L = 2 \times 10^{12}$ W/cm^2. Clearly one would not expect the absorption processes $(1\omega_H + 2\omega_L)$ and $17\omega_L$ to yield the same type of angular distibutions. In fact, we observe from figure 7.17 that at both intensities it is the distribution due to the monochromatic field that falls off the faster as θ increases and this is entirely in accordance with the common-sense view that when more photons are absorbed the resulting distribution will become more strongly peaked about the polarisation axis. (This is due to the propensity rule that when each photon is absorbed the likely outcome is that the angular momentum quantum number will rise by unity, rather than falling by the same amount [163]. The concept of propensity is discussed in the appendix to chapter six.) Thus we can speculate that (in the bichromatic case) when more low-frequency photons are absorbed than high-frequency photons, even when these low-frequency photons by themselves contribute almost nothing

to the ionisation rate, the angular distribution of the ejected electrons will be determined primarily by the angular momentum of the low-frequency photons. (To see this one should also refer to the single-harmonic-photon angular distribution in figure 7.16.)

7.5 Conclusions

It has already been shown that, at least in a simple low-intensity case, the two-colour Sturmian-Floquet code can quantitatively reproduce the results reported by Véniard *et al* [151] for the ionisation of Hydrogen by a low-frequency linearly polarised laser field together with one of its high harmonics [126]. In this chapter we present a systematic study of this process at the longer wavelength of 1064 nm. We fix the intensity of the high-frequency beam (15^{th} harmonic) at $I_H = 10^9$ W/cm^2 and vary the intensity of the fundamental over the range $I_L = 5 \times 10^{11} \rightarrow 2 \times 10^{13}$ W/cm^2. Thus we are able to draw conclusions concerning the generality of the results obtained by Véniard *et al* at 800 nm and we make predictions, for example, the phase-dependence of the total and partial rates of ionisation, that are experimentally verifiable at the wavelength we have chosen. Further, we examine the angular dependence of the photo-electrons and, at low intensities, draw qualitative comparisons with the results of Cionga [98]. We also demonstrate the phase-dependence of these angular distributions at high intensities of the fundamental beam. As far as we are aware there do not exist any comparable theoretical predictions for the differential rates of photo-ionisation in this high-intensity regime.

In order to study three distinct dynamical regimes we choose three representative intensities of the fundamental beam: $I_L = 5 \times 10^{11}$, 2×10^{12} and 2×10^{13} W/cm^2. All three of these cases (combined with the 15^{th} harmonic at constant intensity) are experimentally accessible using current technology by starting with a laser field of high intensity, say, $I = 2 \times 10^{14}$ W/cm^2 and then splitting this into two equal parts, one of which will be converted into the 15^{th} harmonic (with a conversion efficiency $\sim 10^{-5}$) and the other of

which will be attenuated by a factor sufficient to leave a beam of intensity I_L. These may then be recombined and a relative phase ϕ introduced into the harmonic field. We find that, except at the highest value of I_L, there is no phase dependence in any of the total rates, partial rates or differential rates of ionisation. This confirms predictions made by Potvliege in [98] that when fields of commensurable frequencies are combined the relative phase between the fields is important only when the harmonic field is of a low harmonic order (e.g. $N_H = 3$). However, our results demonstrate a variation with phase in the total rate of ionisation at $I_L = 2 \times 10^{13}$ W/cm^2 (with an amplitude of approximately 6%) and we propose that the choice of phase $\phi \approx 0°$ at time $t = 0$ optimally minimises the ionisation rate. A similar variation is observed in the partial rates of ionisation (which are calculated independently of the total rate). The angular distribution of photo-electrons is strongly phase-dependent for angles $\theta > 60°$ (measured from the polarisation axis) but roughly phase-independent at smaller angles.

At low intensity, $I_L = 5 \times 10^{11}$ W/cm^2, the total rate of ionisation due to the fundamental field alone is virtually zero and the most probable route to the continuum in the corresponding two-colour field is the absorption of a single high-frequency photon. However the angular distribution of photo-electrons in this instance is not the $\cos^2\theta$ function that on would expect for a single-photon absorption process and is instead much broader. The same type of distribution is calculated by Cionga [98] within the radiative dressing approach. At $I_L = 2 \times 10^{12}$ W/cm^2 the highest ATI peaks are those corresponding to the absorption of $(1\omega_H \pm 1\omega_L)$ photons, i.e. although the rate of ionisation due to the fundamental field alone is approximately ten orders of magnitude smaller than that due to the harmonic field the absorption (or emission) of one or two low-frequency photons is more probable than the absorption of none. The angular distribution of photo-electrons into the ATI channel $N = N_H$ exhibits a global maximum at $\theta = 63°$. This, again, is completely different from the $\cos^2\theta$ dependence that would result simply from the absorption of one high-frequency photon. Given that the MPI rate is negligibly small at this intensity the only explanation is that the

ionisation process is modulated by the absorption and emission of several virtual photons.

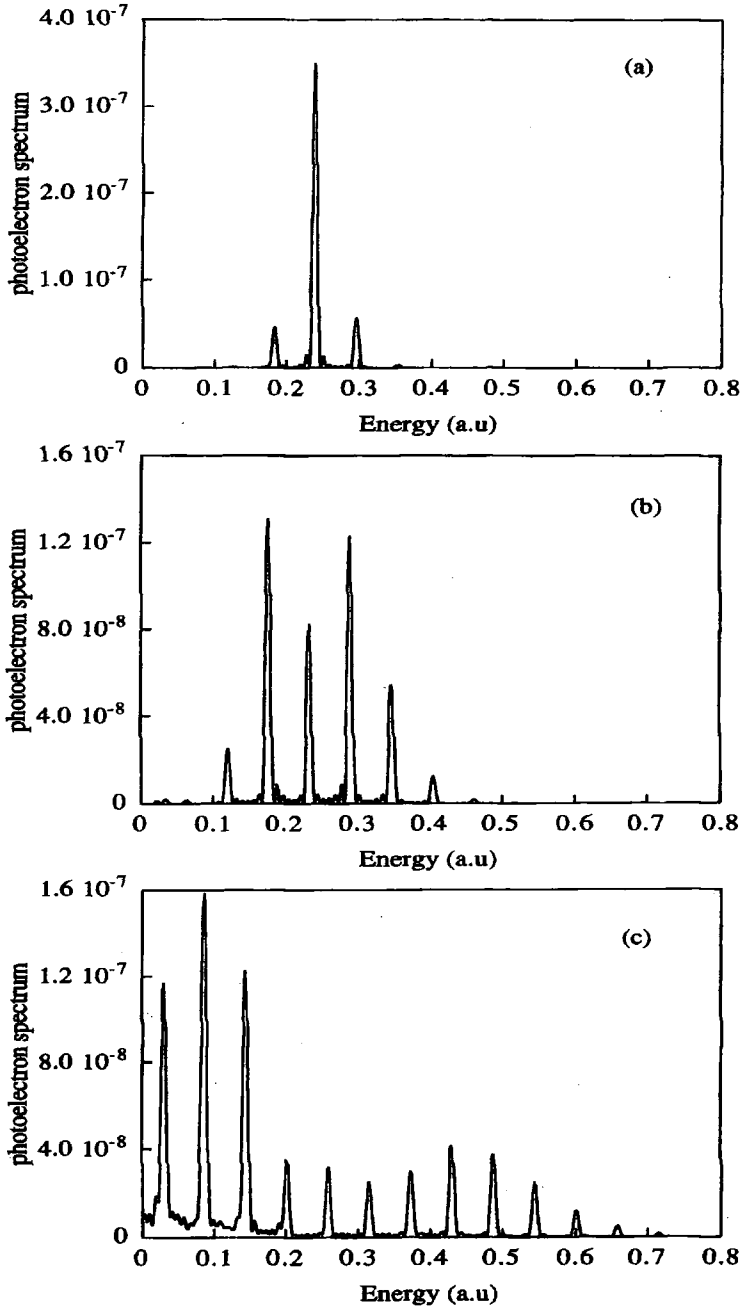

Figure 7.1: Effect of the laser intensity on two-colour photo-electron spectra for radiation pulses containing the fundamental frequency of a Ti:Sapphire laser ($\omega_L = 1.55$ eV) and its thirteenth harmonic with a fixed intensity $I_H = 3 \times 10^8$ W/cm^2. These figures present the results of Véniard *et al* [151]. The laser intensities are: (a) $I_L = 5 \times 10^{11}$ W/cm^2; (b) $I_L = 3 \times 10^{12}$ W/cm^2; (c) $I_L = 1.75 \times 10^{13}$ W/cm^2. Note the change of scales.

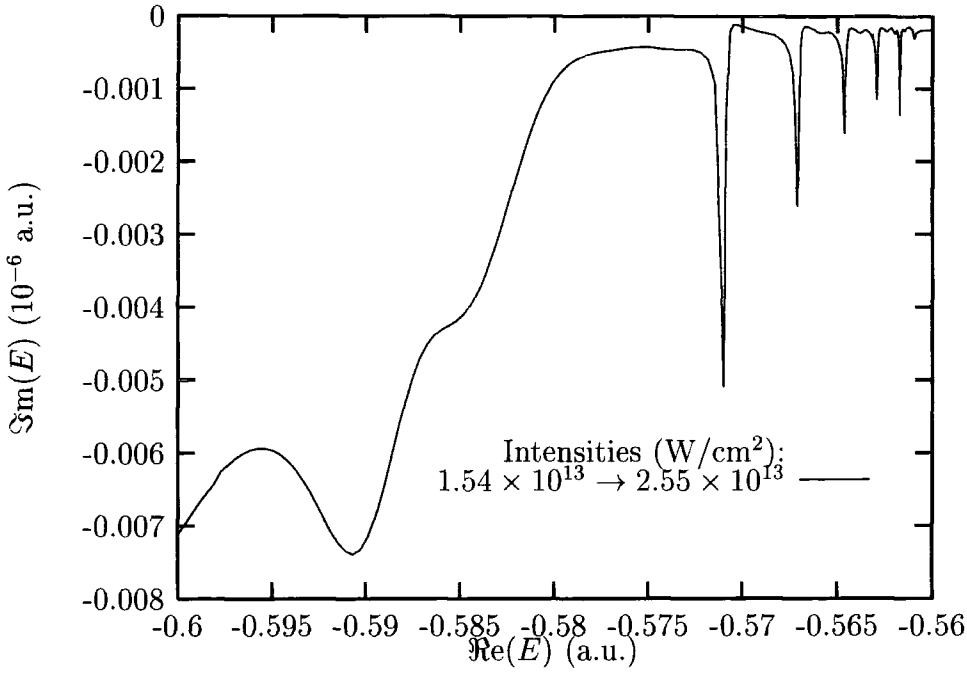

Figure 7.2: Quasi-energies of H($1s$) at 1064 nm with linearly polarised light at intermediate intensities. The results plotted here were calculated by R M Potvliege [57].

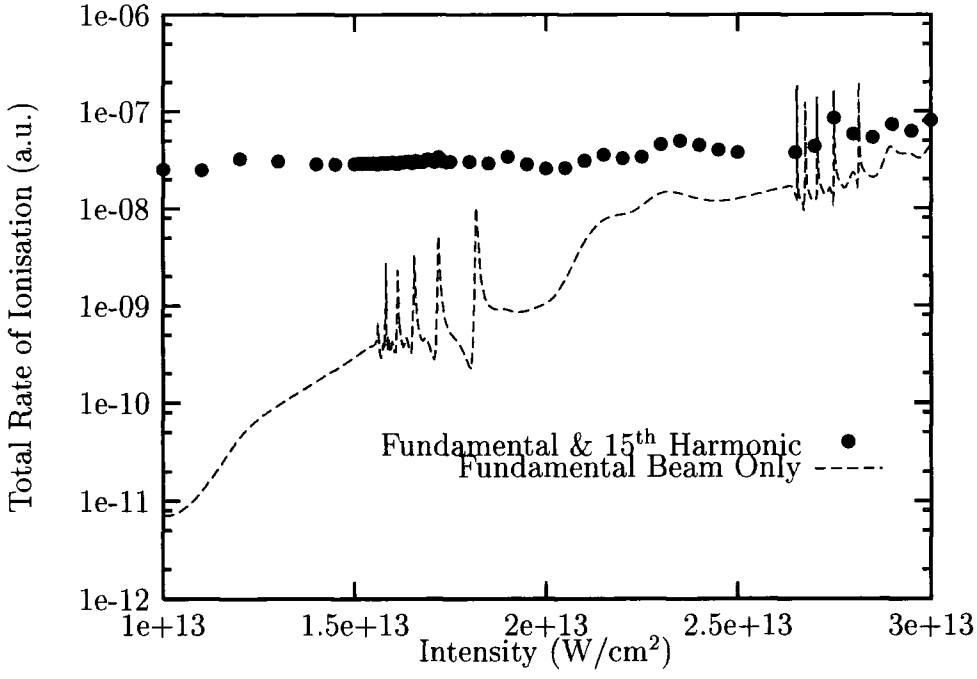

Figure 7.3: The total rate of ionisation of H($1s$) at 1064 nm both with and without an additional field of the 15th harmonic at a fixed intensity of 10^9 W/cm^2. Both beams are linearly polarised.

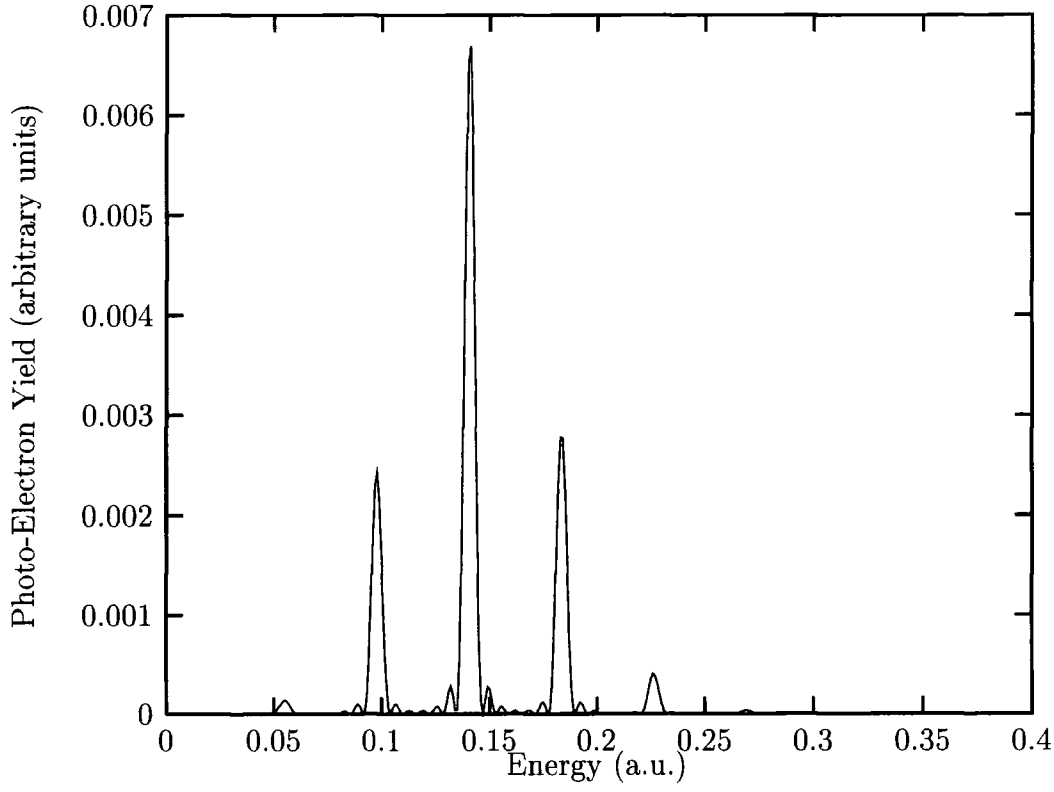

Figure 7.4: Photo-electron yield from H($1s$) due to two-colour multiphoton ionisation using $\lambda_L = 1064$ nm together with its 15^{th} harmonic ($\equiv \lambda_H$). Both beams are linearly polarised and, additionally, are in phase at time $t = 0$. Their intensities are $I_L = 5.0 \times 10^{11}$ W/cm^2 and $I_H = 1.0 \times 10^9$ W/cm^2.

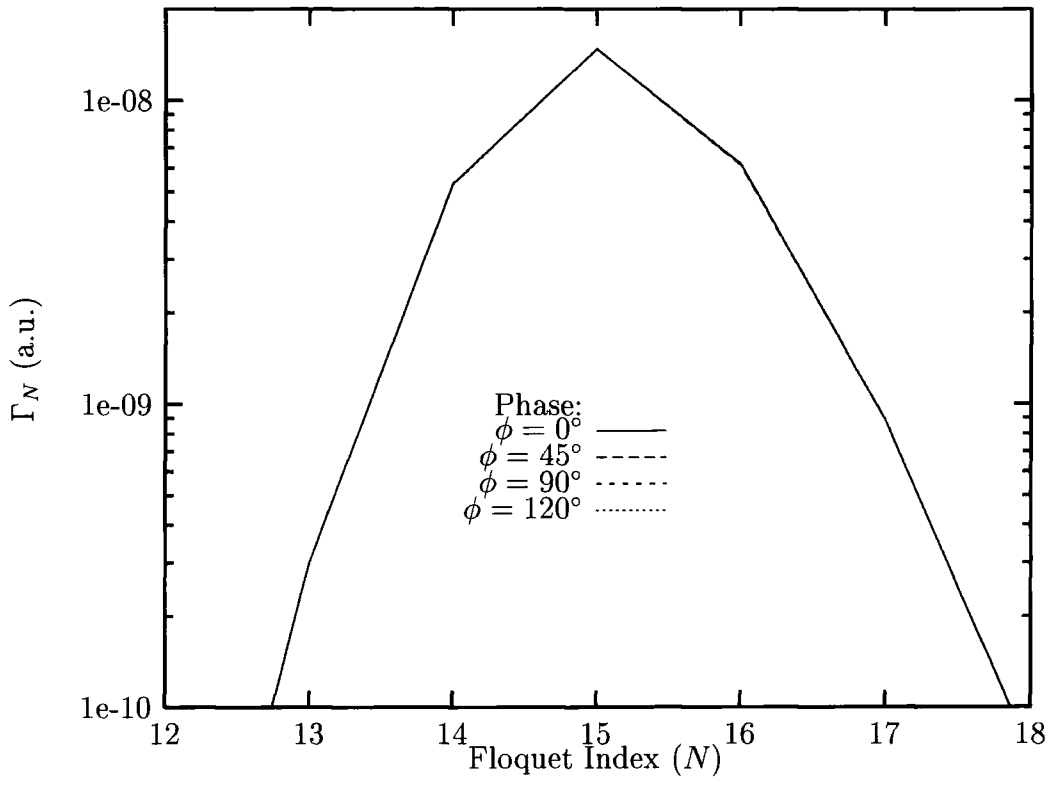

Figure 7.5: Partial rates of two-colour ionisation from H($1s$) into the lower ATI channels where the fundamental beam is at 1064 nm with an intensity of $I_L = 5.0 \times 10^{11}$ W/cm^2 and the high-frequency beam is its 15$^{\text{th}}$ harmonic at an intensity of $I_H = 1.0 \times 10^9$ W/cm^2. Differing phases ϕ at time $t = 0$ are considered.

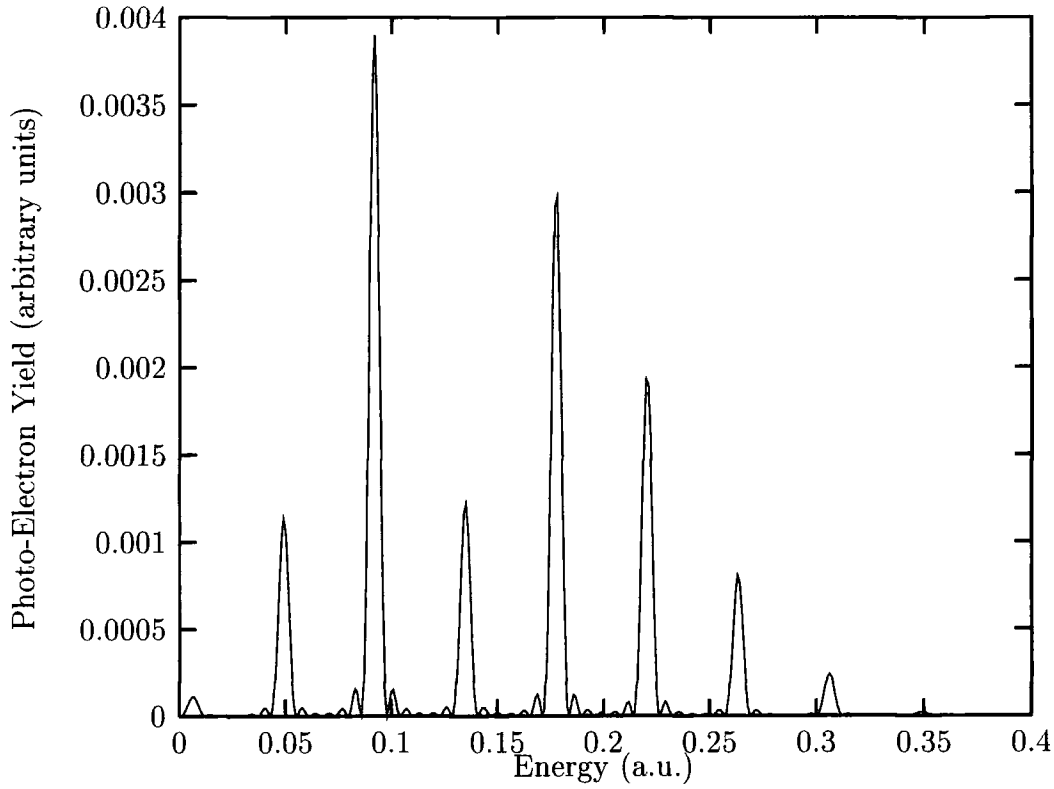

Figure 7.6: Photo-electron yield from H($1s$) due to two-colour multiphoton ionisation using $\lambda_L = 1064$ nm together with its 15^{th} harmonic ($\equiv \lambda_H$). Both beams are linearly polarised and, additionally, are in phase at time $t = 0$. Their intensities are $I_L = 2.0 \times 10^{12}$ W/cm^2 and $I_H = 1.0 \times 10^9$ W/cm^2.

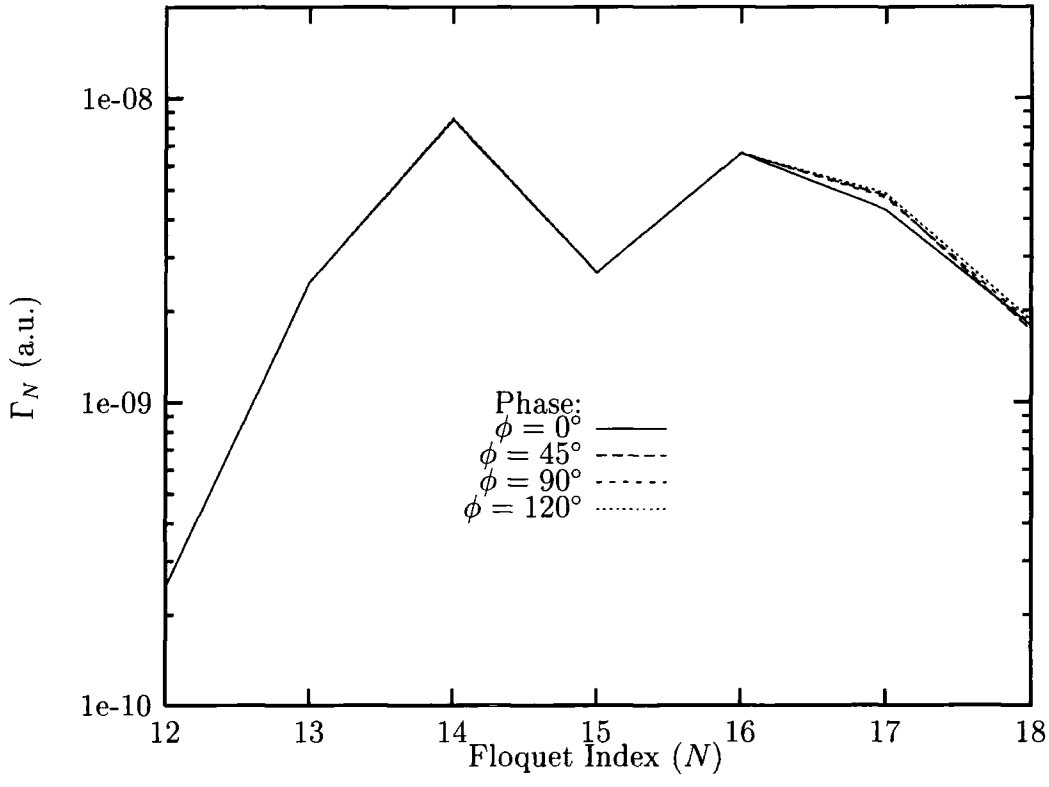

Figure 7.7: Partial rates of two-colour ionisation from H($1s$) into the lower ATI channels where the fundamental beam is at 1064 nm with an intensity of $I_L = 2.0 \times 10^{12}$ W/cm^2 and the high-frequency beam is its 15^{th} harmonic at an intensity of $I_H = 1.0 \times 10^9$ W/cm^2. Differing phases ϕ at time $t = 0$ are considered.

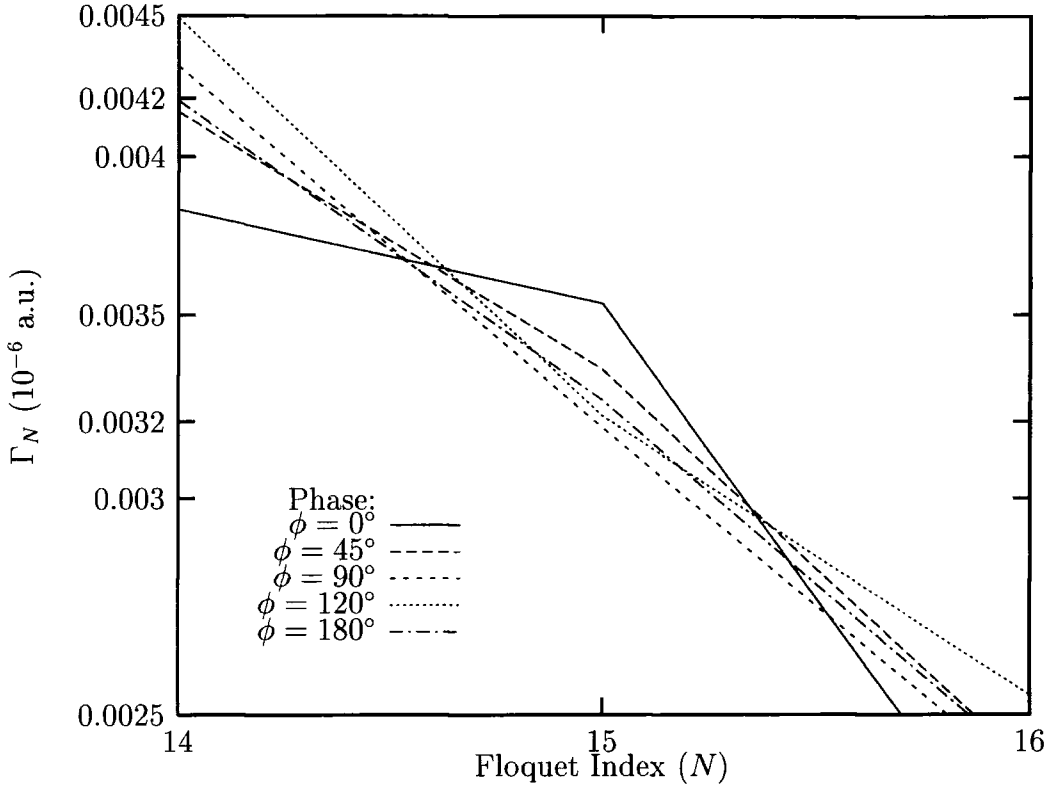

Figure 7.8: Partial rates of two-colour ionisation from H($1s$) into ATI channels $S = 0 \rightarrow 2$ only, where the fundamental beam is at 1064 nm with an intensity of $I_L = 2.0 \times 10^{13}$ W/cm^2 and the high-frequency beam is its 15^{th} harmonic at an intensity of $I_H = 1.0 \times 10^9$ W/cm^2. Differing phases ϕ at time $t = 0$ are considered.

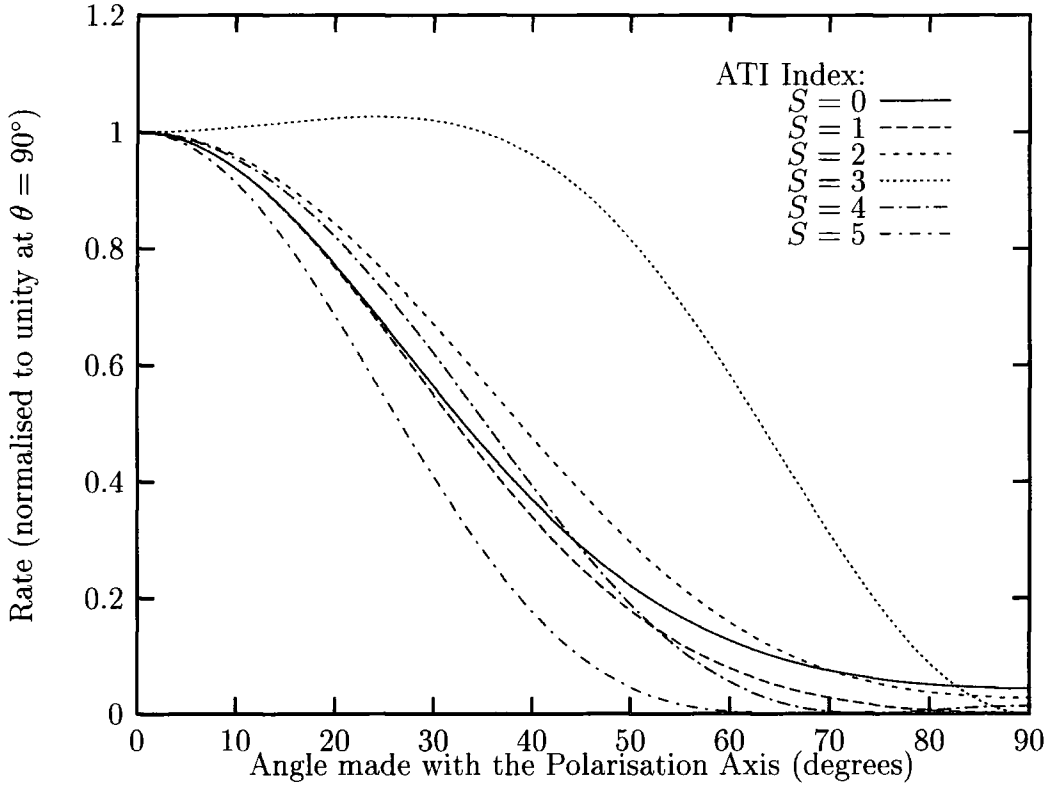

Figure 7.9: Angular distributions of photo-electrons from H($1s$) into the lower ATI channels due to two-colour ionisation where the fundamental beam is at 1064 nm with an intensity of $I_L = 5.0 \times 10^{11}$ W/cm^2 and the high-frequency beam is its 15^{th} harmonic at an intensity of $I_H = 1.0 \times 10^9$ W/cm^2.

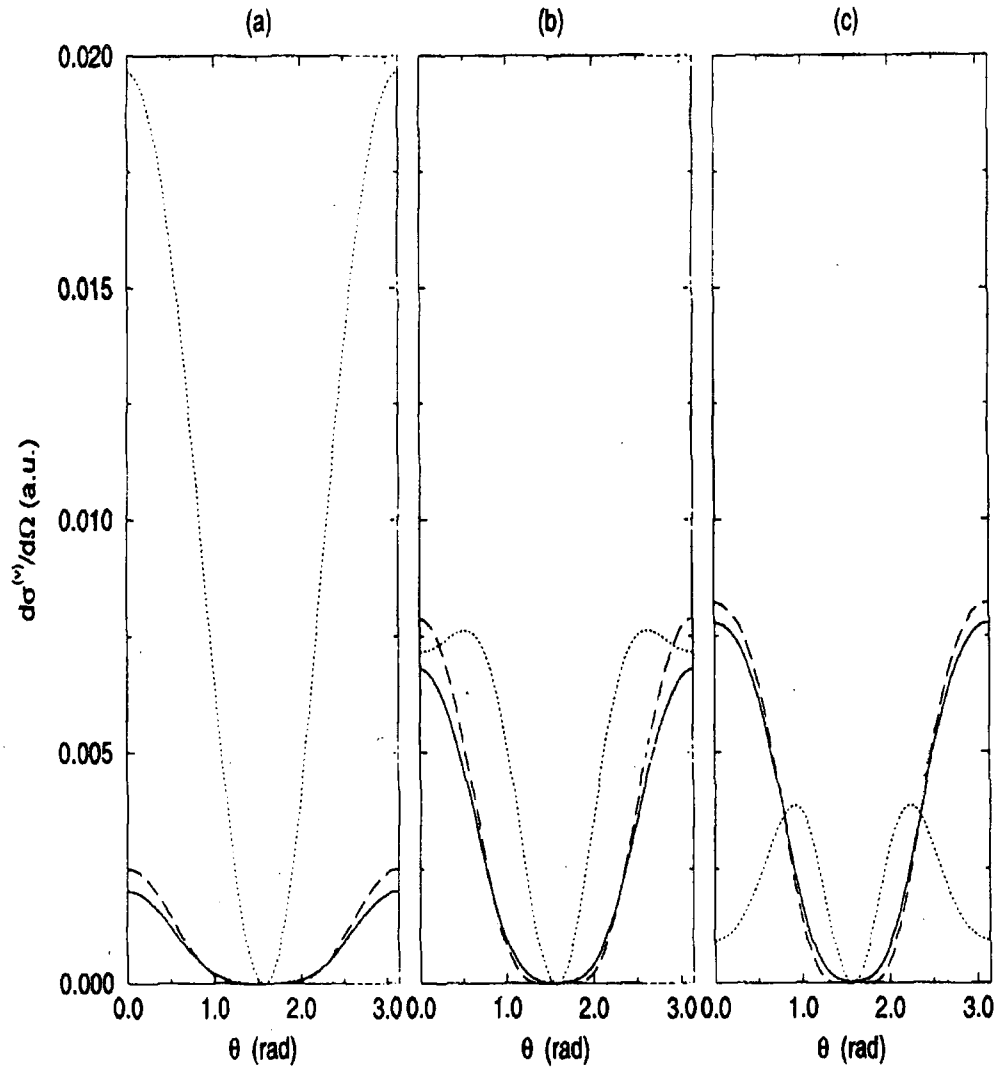

Figure 7.10: Differential cross-sections for atomic Hydrogen in a laser field at the Ti:Sapphire frequency and its 21^{st} harmonic. These figures present the results of Cionga [98]. In each figure the curves are: (- - - -) $N = N_H - 1$; ($\cdots\cdots\cdots$) $N = N_H$; (———) $N = N_H + 1$. The laser intensities are: (a) $I_L = 10^{11}$ W/cm^2; (b) $I_L = 5 \times 10^{11}$ W/cm^2; (c) $I_L = 10^{12}$ W/cm^2.

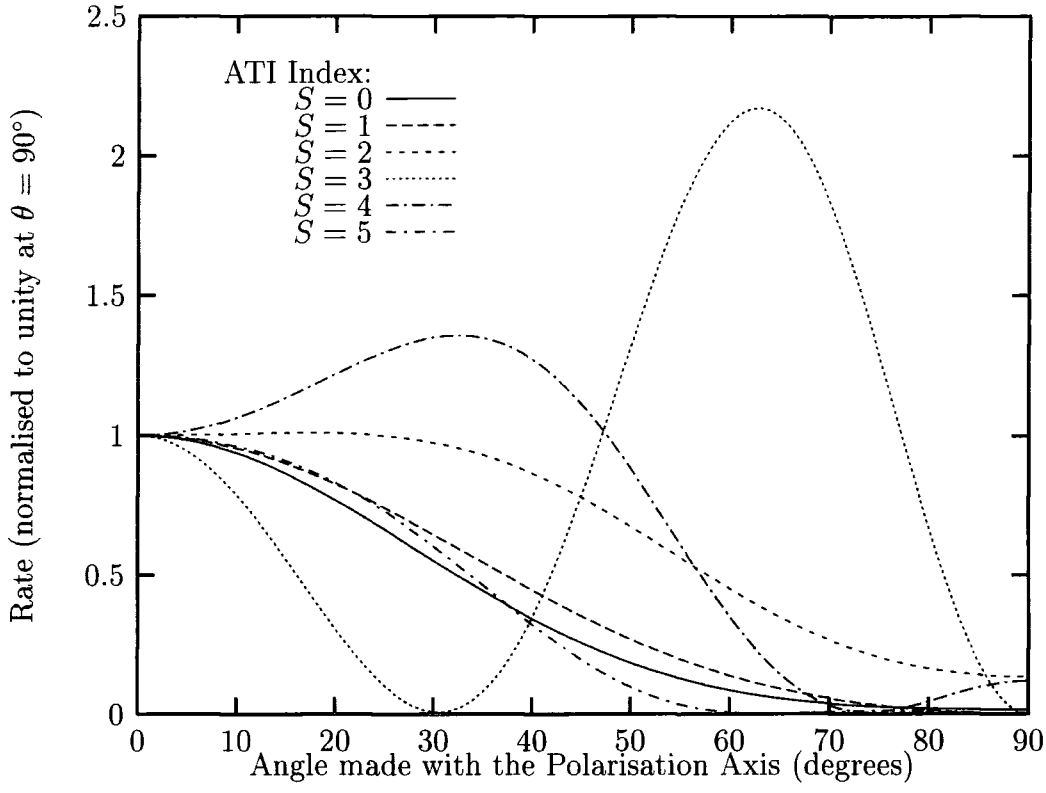

Figure 7.11: Angular distributions of photo-electrons from H($1s$) into the lower ATI channels due to two-colour ionisation where the fundamental beam is at 1064 nm with an intensity of $I_L = 2.0 \times 10^{12}$ W/cm^2 and the high-frequency beam is its 15^{th} harmonic at an intensity of $I_H = 1.0 \times 10^9$ W/cm^2.

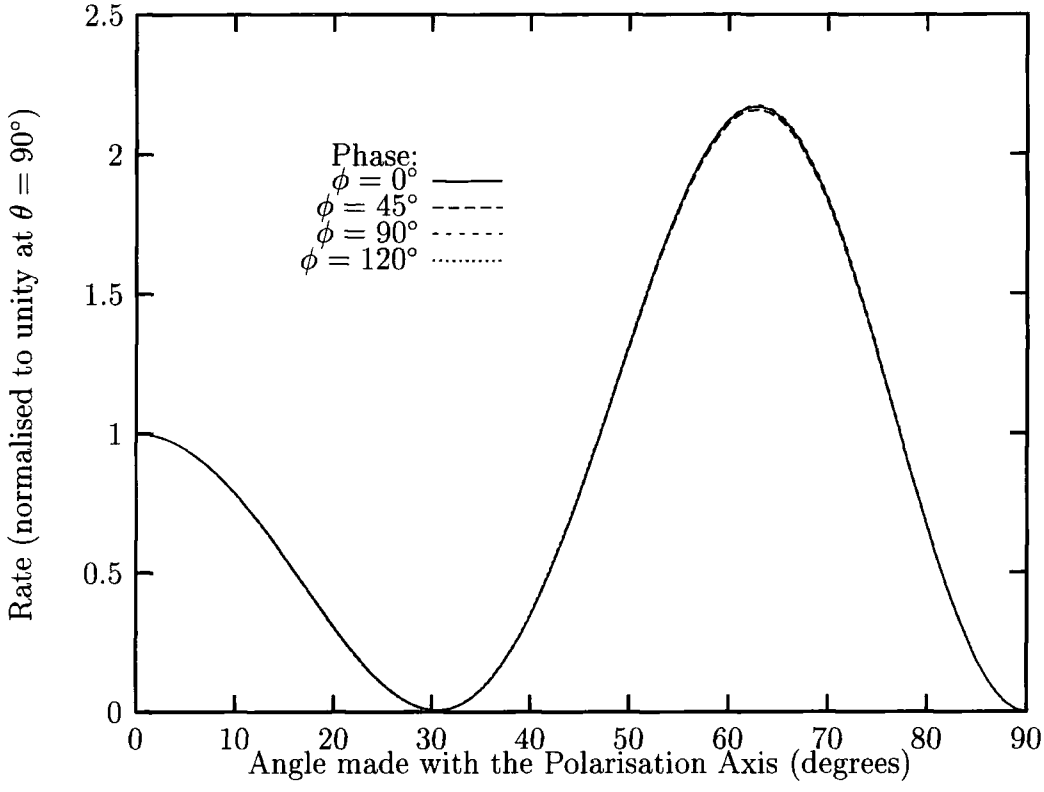

Figure 7.12: Angular distributions of photo-electrons from H($1s$) into the ATI channel $N = 15$ due to two-colour ionisation where the fundamental beam is at 1064 nm with an intensity of $I_L = 2.0 \times 10^{12}$ W/cm^2 and the high-frequency beam is its 15$^{\text{th}}$ harmonic at an intensity of $I_H = 1.0 \times 10^9$ W/cm^2. Differing phases ϕ between the two beams at time $t = 0$ are considered.

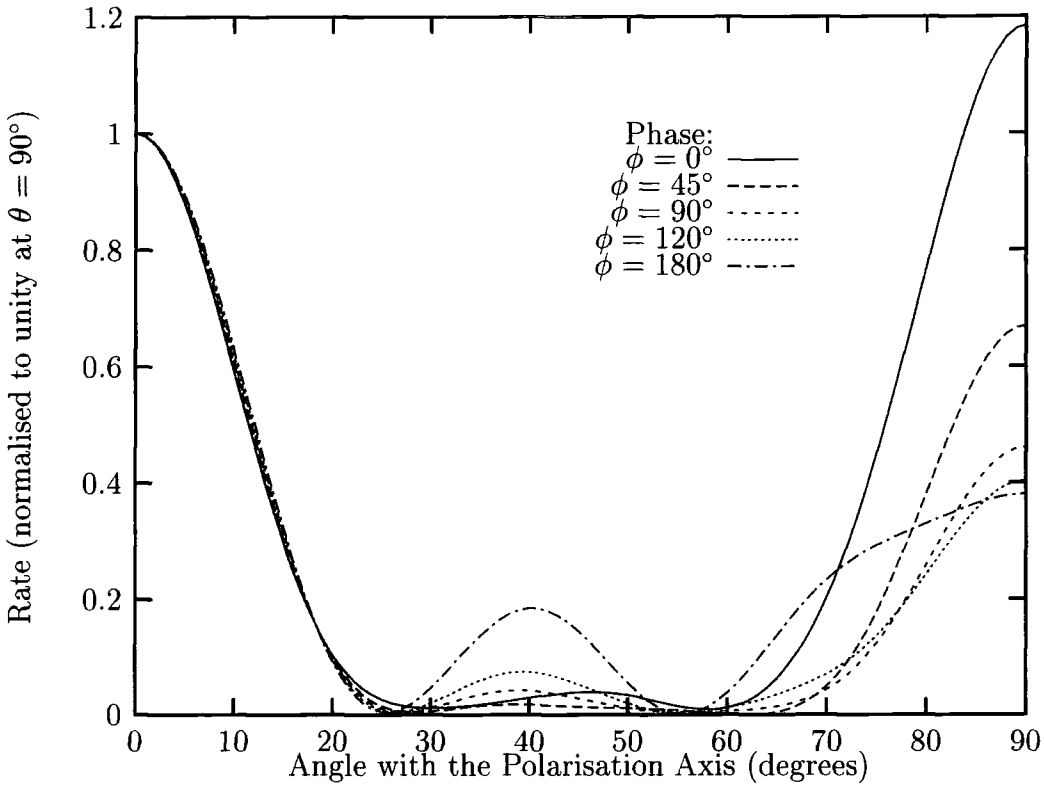

Figure 7.13: Angular distributions of photo-electrons from H($1s$) into the ATI channel $S = 0$ due to two-colour ionisation where the fundamental beam is at 1064 nm with an intensity of $I_L = 2.0 \times 10^{13}$ W/cm^2 and the high-frequency beam is its 15^{th} harmonic at an intensity of $I_H = 1.0 \times 10^9$ W/cm^2. Differing phases ϕ between the two beams at time $t = 0$ are considered.

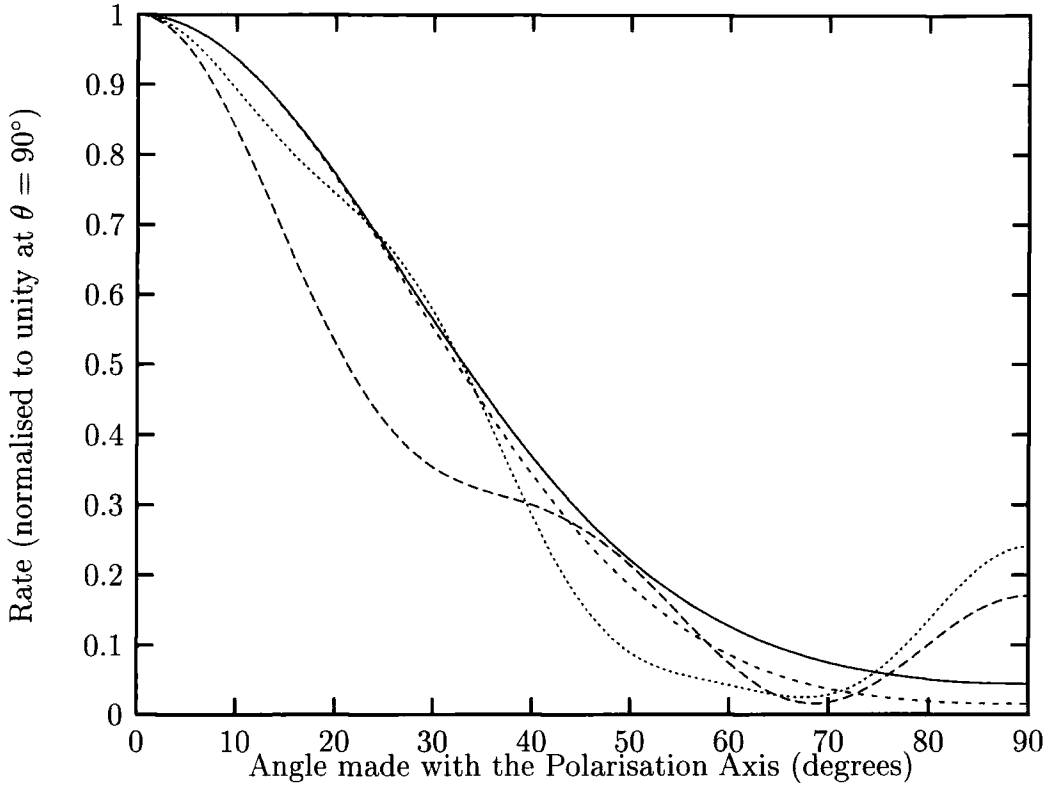

Figure 7.14: Angular distributions of photo-electrons from H($1s$) into the ATI channel $N = 12$ due to two-colour ionisation where the fundamental beam of 1064 nm varies in intensity and its 15^{th} harmonic is at the fixed intensity of $I_H = 1.0 \times 10^9$ W/cm^2. Both beams are in phase at time $t = 0$. Intensities are (in W/cm^2): (———) $I_L = 5.0 \times 10^{11}$, with the harmonic field; (– – – –) $I_L = 5.0 \times 10^{11}$, without the harmonic field; (- - - - - -) $I_L = 2.0 \times 10^{12}$, with the harmonic field; (·····) $I_L = 2.0 \times 10^{12}$, without the harmonic field.

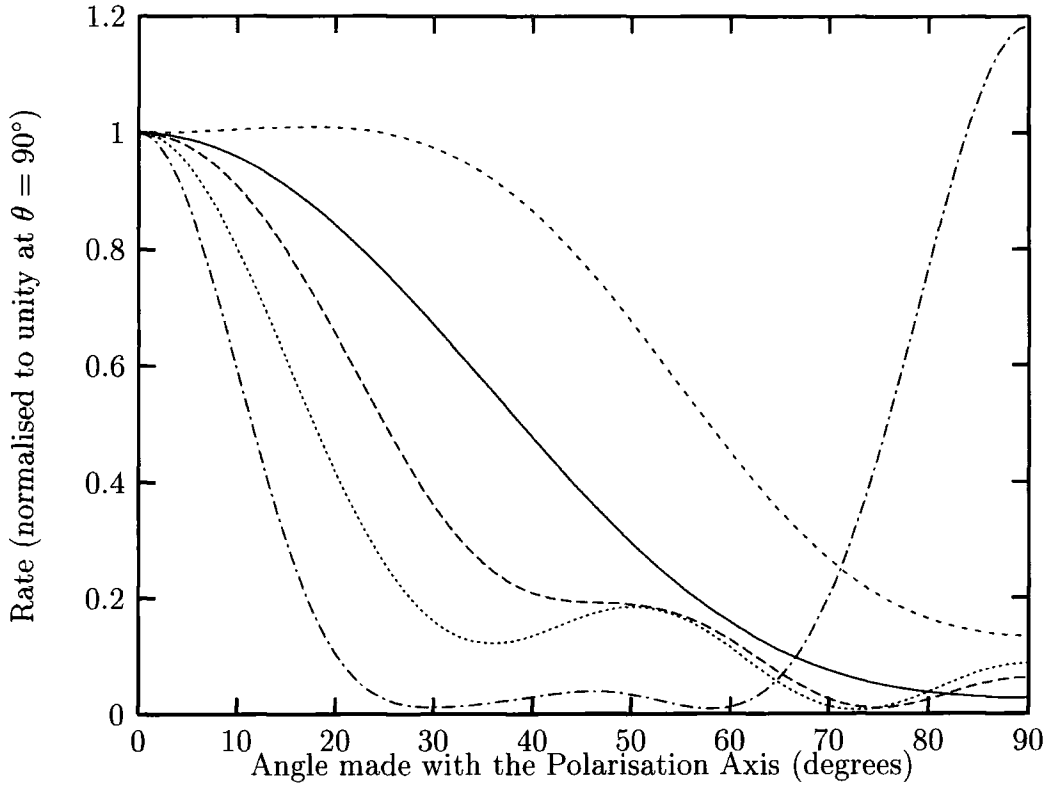

Figure 7.15: Angular distributions of photo-electrons from H($1s$) into the ATI channel $N = 14$ due to two-colour ionisation where the fundamental beam of 1064 nm varies in intensity and its 15^{th} harmonic is at the fixed intensity of $I_H = 1.0 \times 10^9$ W/cm^2. Both beams are in phase at time $t = 0$. Intensities are (in W/cm^2): (———) $I_L = 5.0 \times 10^{11}$, with the harmonic field; (- - - -) $I_L = 5.0 \times 10^{11}$, without the harmonic field; (- - - - - -) $I_L = 2.0 \times 10^{12}$, with the harmonic field; (·····) $I_L = 2.0 \times 10^{12}$, without the harmonic field; (- - - - - -) $I_L = 2.0 \times 10^{13}$, with the harmonic field.

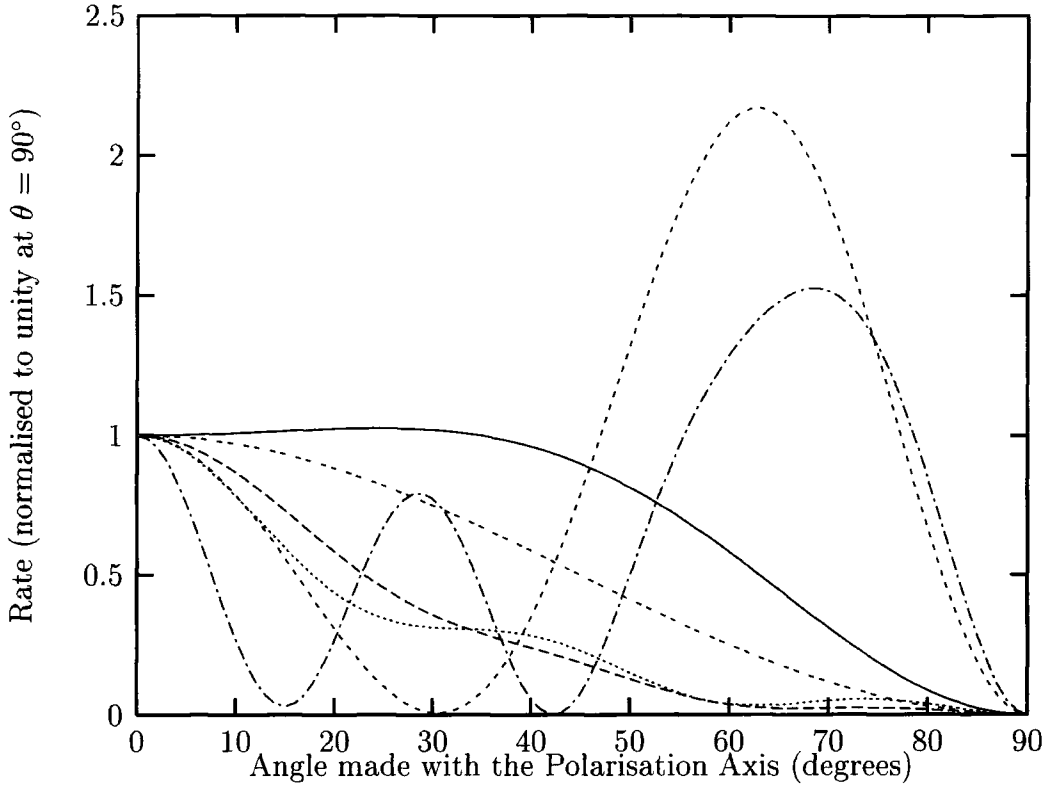

Figure 7.16: Angular distributions of photo-electrons from H($1s$) into the ATI channel $N = 15$ due to two-colour ionisation where the fundamental beam of 1064 nm varies in intensity and its 15^{th} harmonic is at the fixed intensity of $I_H = 1.0 \times 10^9$ W/cm^2. Both beams are in phase at time $t = 0$. Intensities are (in W/cm^2): (———) $I_L = 5.0 \times 10^{11}$, with the harmonic field; (– – – –) $I_L = 5.0 \times 10^{11}$, without the harmonic field; (- - - - - -) $I_L = 2.0 \times 10^{12}$, with the harmonic field; (· · · · · · · ·) $I_L = 2.0 \times 10^{12}$, without the harmonic field; (– – – – – –) $I_L = 2.0 \times 10^{13}$, with the harmonic field; (- - - - - - - -) harmonic beam acting alone.

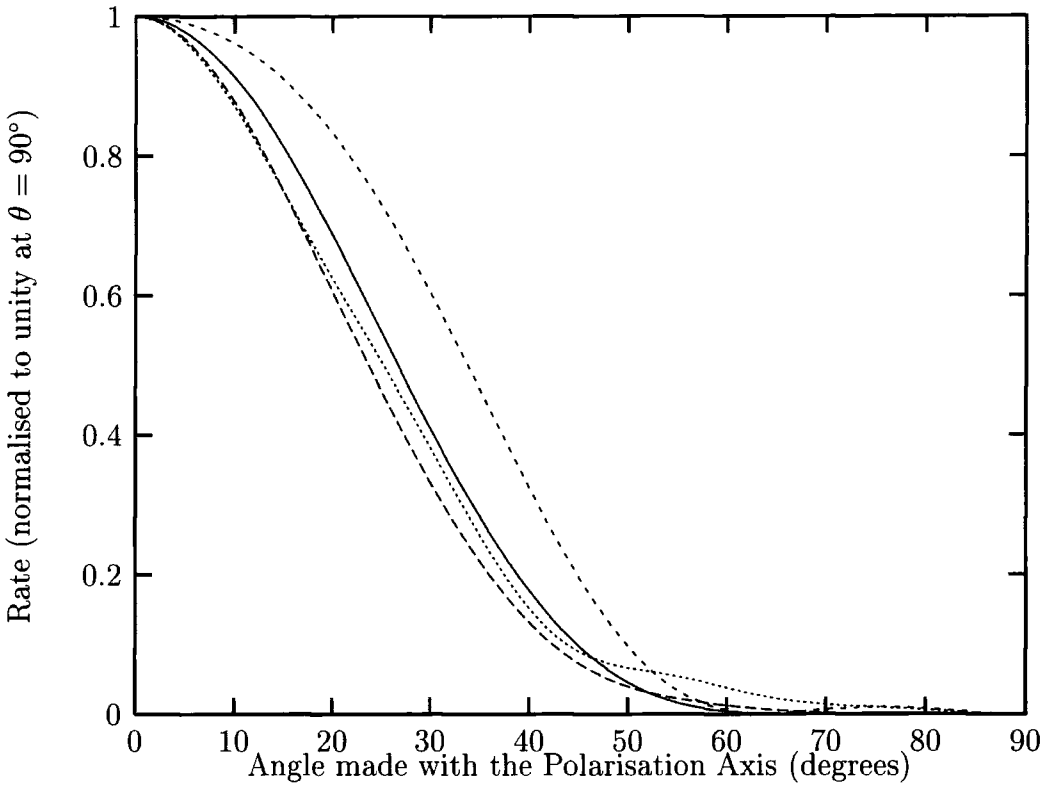

Figure 7.17: Angular distributions of photo-electrons from H($1s$) into the ATI channel $N = 17$ due to two-colour ionisation where the fundamental beam of 1064 nm varies in intensity and its 15^{th} harmonic is at the fixed intensity of $I_H = 1.0 \times 10^9$ W/cm^2. Both beams are in phase at time $t = 0$. Intensities are (in W/cm^2): (———) $I_L = 5.0 \times 10^{11}$, with the harmonic field; (- - - -) $I_L = 5.0 \times 10^{11}$, without the harmonic field; (- - - - - -) $I_L = 2.0 \times 10^{12}$, with the harmonic field; (·····) $I_L = 2.0 \times 10^{12}$, without the harmonic field.

Bibliography

[1] T Åberg, X Mu, J Ruscheinski and B Crasemann, *Physica Scripta* **50** 357 (1994).

[2] M Abramowitz and I A Stegun, *Handbook of Mathematical Functions* (Dover, 1965).

[3] P Agostini, F Fabre, G Mainfray, G Petite and N K Rahman, *Phys Rev Lett* **42** 1127 (1979).

[4] P Agostini, A Antonetti, P Breger, M Crance, A Migus, H G Muller, and G Petite, *J Phys B* **22** 1971 (1989).

[5] D R Bates and B Bederson (Eds.), *Advances in Atomic and Molecular Physics, vol 11*, (Academic Press, 1975). P G Burke and W D Robb (applicability of the R-Matrix method to atomic processes) 143-214.

[6] L Benassi and V Grecchi, *J Phys B* **13** 911 (1980).

[7] H A Bethe and E E Salpeter, *Quantum Mechanics of One- and Two-Electron Atoms* (Plenum, 1957). 4-20 (Hydrogen atom without external fields).

[8] M P de Boer, J H Hoogenraad, R B Vrijen, L D Noordam and H G Muller, *Phys Rev Lett* **71** 3263 (1993).

[9] M P de Boer, J H Hoogenraad, R B Vrijen, R C Constantinescu, L D Noordam and H G Muller, *Phys Rev A* **50** 4085 (1994).

[10] B Borca *et al*, *Unpublished* (1996).

[11] B H Bransden and C J Joachain, *Physics of Atoms and Molecules* (Longman, 1983). 86-88 (spherical harmonics), 136-145 (wavefunc-

tions for one-electron atoms), 621-628 (Hydrogenic wavefunctions in momentum-space).

[12] B H Bransden and C J Joachain, *Introduction to Quantum Mechanics* (Longman, 1989). 326-330 (three-dimensional square-well model).

[13] R Bruzzese, A Sasso and S Solimeno, *Riv Nuov Cim* **12** 1 (1989).

[14] P H Bucksbaum, M Bashkansky, R R Freeman, T J McIlrath and L F DiMauro, *Phys Rev Lett* **56** 2590 (1986).

[15] P H Bucksbaum, R R Freeman, M Bashkansky and T J McIlrath, *Phys Rev Lett* **58** 349 (1987).

[16] P G Burke and K T Taylor, *J Phys B* **8** 2620 (1975).

[17] P G Burke, P Francken and C J Joachain, *Europhys Lett* **13** 617 (1990).

[18] P G Burke, P Francken and C J Joachain, *J Phys B* **24** 761 (1991).

[19] P G Burke and C J Joachain (Eds.), *Photon and Electron Collisions with Atoms and Molecules* (to be published). M Dörr (*R*-Matrix-Floquet Theory of Multiphoton Processes); V Véniard, R Taïeb and A Maquet (multicolour photo-ionisation of atoms).

[20] P G Burke and V M Burke, *Unpublished* (1997).

[21] K Burnett, V C Reed and P L Knight, *J Phys B* **26** 561 (1993).

[22] S-I Chu and W P Reinhardt, *Phys Rev Lett* **39** 1195 (1977).

[23] A Cionga, V Florescu, A Maquet and R Taïeb, *Phys Rev A* **47** 1830 (1993).

[24] C Cohen-Tannoudji, B Diu and F Laloë, *Quantum Mechanics, Vol II* (Wiley, 1977). 1059-1071 (electric multipole moments).

[25] P B Corkum, N H Burnett and F Brunel, *Phys Rev Lett* **62** 1259 (1989).

[26] H C Day and R M Potvliege, *Unpublished* (1996).

[27] H C Day, A S Fearnside and R M Potvliege, *Submitted to Phys Rev A* (1997).

[28] H C Day and R M Potvliege, *Unpublished* (1997).

[29] N B Delone and V P Krainov, *Multiphoton Processes in Atoms* (Springer, 1994). 66-75 (tunneling theory); 83-98 (multiphoton ionisation of the Hydrogen atom).

[30] M Dörr, R M Potvliege and R Shakeshaft, *Phys Rev A* **41** 558 (1990).

[31] M Dörr, R M Potvliege, D Proulx and R Shakeshaft, *Phys Rev A* **42** 4138 (1990).

[32] M Dörr, R M Potvliege, D Proulx and R Shakeshaft, *Phys Rev A* **43** 3729 (1991).

[33] M Dörr, R M Potvliege, D Proulx and R Shakeshaft, *Phys Rev A* **44** 574 (1991).

[34] M Dörr, M Terao-Dunseath, J Purvis, C J Noble, P G Burke and C J Joachain, *J Phys B* **25** 2809 (1992).

[35] M Dörr, D Feldmann, R M Potvliege, H Rottke, R Shakeshaft, H K Welge and B Wolff-Rottke, *J Phys B* **25** L275 (1992).

[36] M Dörr, P G Burke, C J Joachain, C J Noble, J Purvis and M Terao-Dunseath, *J Phys B* **26** L275 (1993).

[37] M Dörr, J Purvis, M Terao-Dunseath, P G Burke, C J Joachain and C J Noble, *J Phys B* **28** 4481 (1995).

[38] M Dörr, O Latinne and C J Joachain, *submitted to Phys Rev A* (1997).

[39] M Dörr at a meeting of the *Network for Atoms in Super-Intense Laser Fields* in Daresbury, England (1997).

[40] N J van Druten, R Trainham and H G Muller, *Phys Rev A* **51** R898 (1995).

[41] N J van Druten and H G Muller, *J Phys B* **29** 15 (1996).

[42] E Van Duijn, M Gavrila and H G Muller, *Phys Rev Lett* **77** 3759 (1996).

[43] I H Duru and H Kleinert, *Fortschritte der Physik* **30** 401 (1982).

[44] F H M Faisal, *J Phys B* **6** L89 (1973).

[45] F H M Faisal, *Theory of Multiphoton Processes* (Plenum, 1987).

[46] F H M Faisal, L Dimou, H J Stiemke and M Nurhuda, *Journal of Nonlinear Optical Physics and Materials* **4** 701 (1995).

[47] U Fano, *Phys Rev A* **32** 617 (1985).

[48] A S Fearnside, R M Potvliege and R Shakeshaft, *Phys Rev A* **51** 1471 (1995).

[49] A S Fearnside, *PhD Thesis* (1996).

[50] M V Fedorov and A M Movsesian, *J Phys B* **21** L155 (1988).

[51] D R Flower, *Physics World* **9** 37 (October 1996).

[52] R R Freeman, P H Bucksbaum, H Milchberg, S Darack, D Schumacher and M E Geusic, *Phys Rev Lett* **59** 1092 (1987).

[53] H Friedrich, *Theoretical Atomic Physics* (Springer, 1990). 93-115 (electromagnetic interactions), 181-185 (atoms in an oscillating electric field), 249-258 (multiphoton processes).

[54] T F Gallagher, *Phys Rev Lett* **61** 2304 (1988).

[55] A Galindo and P Pascual, *Quantum Mechanics II* (Springer, 1991). 200-206 (gauge transformations).

[56] M Gavrila and J Z Kamiński, *Phys Rev Lett* **52** 614 (1984).

[57] M Gavrila (Ed.), *Advances in Atomic, Molecular and Optical Physics, Supplement 1: Atoms in Intense Laser Fields* (Academic Press, 1992). R M Potvliege and R Shakeshaft (Floquet calculations in atomic Hydrogen) 373; M Gavrila (atoms in high-frequency fields) 435.

[58] R Gebarowski, P G Burke, K T Taylor, M Dörr, M Bensaid and C J Joachain, *J Phys B* **30** 1837 (1997).

[59] S Geltman, *J Phys B* **27** 257 (1994).

[60] S Geltman, *Phys Rev A* **45** 5293 (1992).

[61] S Geltman, *Chem Phys Lett* **237** 286 (1995).

[62] T E Glover, R W Schoenlein, A H Chin and C V Shank, *Phys Rev Lett* **76** 2468 (1996).

[63] R Grobe and M V Fedorov, *Phys Rev Lett* **68** 2592 (1992).

[64] R Grobe and M V Fedorov, *J Phys B* **26** 1181 (1993).

[65] J Grochmalicki, M Lewenstein and K Rzażewski, *Phys Rv Lett* **66** 1038 (1991).

[66] J L Hall, E J Robinson and L M Branscomb, *Phys Rev Lett* **14** 1013 (1965).

[67] C S Han, *J Phys B* **27** 5707 (1994).

[68] H W van der Hart, *J Phys B* **29** 2217 (1996).

[69] W C Henneberger, *Phys Rev Lett* **21** 838 (1968).

[70] R Ho and A Inomata, *Phys Rev Lett* **48** 231 (1982).

[71] J Hoogenraad, R B Vrijen and L D Noordam, *Phys Rev A* **50** 4133 (1994).

[72] J Javanainen, J H Eberly and Qichang Su, *Phys Rev A* **38** 3430 (1988).

[73] J Javanainen and J H Eberly, *Phys Rev A* **39** 458 (1989).

[74] L V Keldysh, *Sov Phys JETP* **20** 1307 (1965).

[75] H Kleinert, *Foundations of Physics* **23** 769 (1993).

[76] V P Krainov and M A Preobrazhenskii, *Zh Eksp Teor Fiz* **103** 1143 (1993).

[77] H A Kramers, *Collected Scientific Papers* (Amsterdam: North-Holland, 1956) 866.

[78] J L Krause, K J Schafer and K C Kulander, *Phys Rev A* **45** 4998 (1992).

[79] P S Krstić and R K Janev, *Phys Rev A* **34** 157 (1986).

[80] P S Krstić and R K Janev, *Phys Rev A* **37** 4625 (1988).

[81] K C Kulander and B W Shore, *J Opt Soc AM B* **7** 502 (1990).

[82] K C Kulander, J Cooper and K J Schafer, *Phys Rev A* **51** 561 (1995).

[83] J Kupersztych, L A Lompré, G Mainfray and C Manus, *J Phys B* **21** L517 (1988).

[84] N J Kylstra, M Dörr, C J Joachain and P G Burke, *J Phys B* **28** L685 (1995).

[85] K J LaGattuta, *Phys Rev A* **41** 5110 (1990).

[86] P Lambropoulos, *Phys Rev Lett* **29** 453 (1972).

[87] P Lambropoulos and H Walther (Eds.), *Multiphoton Processes 1996* (Institute of Physics, 1997). C J Joachain (*R*-Matrix theory of multiphoton processes) 46; V P Krainov (ionisation rates and energy-angular distributions in the barrier-suppression regime) 98; B Sheehy, B Walker, R Lafon, M Widmer, A Gambhir, L F diMauro, P Agostini and K C Kulander (electron dynamics in the tunneling regime) 106.

[88] O Latinne, N J Kylstra, M Dörr, J Purvis, M Terao-Dunseath, C J Joachain, P G Burke and C J Noble, *Phys Rev Lett* **74** 46 (1995).

[89] L A Lompré, A L'Huillier, G Mainfray and C Manus, *J Opt Soc Am B* **2** 1906 (1985).

[90] S Lundquist, A Ranfagni, V Sa-yakanit and L S Schulman (Eds.) *Path Summation: Achievements and Goals* (World Scientific, 1988). A Ranfagni and D Mugnai (notes on the tunneling time and trajectory) 246.

[91] J J Macklin, J D Kmetec and C L Gordon *Phys Rev Lett* **70** 766 (1993).

[92] A Maquet, S-I Chu and W P Reinhardt, *Phys Rev A* **27** 2946 (1983).

[93] A Maquet, T Millack and V Véniard, *Acta Physica Polonica A* **86** 191 (1994).

[94] E Mese and R M Potvliege, *Unpublished* (1996).

[95] N F Mott and H S W Massey, *The Theory of Atomic Collisions* (Oxford University Press, 1933). 804-806 (Landau-Zener theory).

[96] H G Muller, A Tip and M J van der Wiel, *J Phys B* **16** L679 (1983).

[97] H G Muller, P H Bucksbaum, D W Schumacher and A Zavriyev *J Phys B* **23** 2761 (1990).

[98] H G Muller and M V Fedorov (Eds.), *Super Intense Laser Atom Physics IV* (Kluwer Academic, 1996). H G Muller (a classification of stabilisation mechanisms) 1; R M Potvliege (Sturmian-Floquet calculations in Hydrogen) 133; E van Duijn, M Gavrila and H G Muller (the concept of adiabatic separability) 233; A Cionga (two-colour photo-ionisation) 391.

[99] A I Nikishov and V I Ritus, *Sov Phys JETP* **23** 168 (1966).

[100] G G Paulus, W Nicklich, Huale Xu, P Lambropoulos and H Walther, *Phys Rev Lett* **72** 2851 (1994).

[101] G G Paulus, W Nicklich and H Walther, *Europhys Lett* **27** 267 (1994).

[102] Ue-Li Pen and Tsin-Fu Jiang, *Phys Rev A* **53** 623 (1996).

[103] A M Perelomov, V S Popov and M V Terent'ev, *Sov Phys JETP* **23** 924 (1966).

[104] A M Perelomov, V S Popov and M V Terent'ev, *Sov Phys JETP* **24** 207 (1967).

[105] A M Perelomov and V S Popov, *Sov Phys JETP* **25** 336 (1967).

[106] M S Pindzola and M Dörr, *Phys Rev A* **43** 439 (1991).

[107] B Piraux, A L'Huillier and K Rzazewski (Eds.), *Super Intense Laser Atom Physics III* (Plenum, 1993).

[108] B Piraux, *Private Communications* (1996-1997).

[109] M Pont, N R Walet, M Gavrila and C W McCurdy, *Phys Rev Lett* **61** 939 (1988).

[110] M Pont and M Gavrila, *Phys Rev Lett* **65** 2362 (1990).

[111] M Pont, R Shakeshaft and R M Potvliege, *Phys Rev A* **42** 6969 (1990).

[112] M Pont and R Shakeshaft, *Phys Rev A* **43** 3764 (1991).

[113] M Pont, R M Potvliege, R Shakeshaft and Zhong-jian Teng, *Phys Rev A* **45** 8235 (1992).

[114] M Pont, R M Potvliege, R Shakeshaft and P H G Smith, *Phys Rev A*, **46** 555 (1992).

[115] R M Potvliege and R Shakeshaft, *Phys Rev A* **38** 1098 (1988).

[116] R M Potvliege and R Shakeshaft, *Phys Rev A* **38** 4597 (1988).

[117] R M Potvliege and R Shakeshaft, *Phys Rev A* **38** 6190 (1988).

[118] R M Potvliege and R Shakeshaft, *Phys Rev A* **39** 1545 (1989).

[119] R M Potvliege and R Shakeshaft, *Phys Rev A* **40** 3061 (1989).

[120] R M Potvliege and R Shakeshaft, *Phys Rev A* **41** 1609 (1990).

[121] R M Potvliege and P H G Smith, *J Phys B* **24** L641 (1991).

[122] R M Potvliege and R Shakeshaft, *Physics of Electronic and Atomic Collisions* (Institute of Physics, 1992) 497.

[123] R M Potvliege and P H G Smith, *J Phys B* **25** 2501 (1992).

[124] R M Potvliege and P H G Smith, *Phys Rev A* **48** R46 (1993).

[125] R M Potvliege, *Unpublished* (1993).

[126] R M Potvliege, *Unpublished* (1996).

[127] R M Potvliege, *Private Communication* (1997).

[128] R M Potvliege, *Unpublished* (1997).

[129] W H Press, W T Vetterling, S A Teukolsky and B P Flannery, *Numerical Recipes in Fortran* (Cambridge University Press, 1986). The downhill simplex method in multidimensions 402; inverse iteration 487.

[130] J Purvis, M Dörr, M Terao-Dunseath, C J Joachain, P G Burke and C J Noble, *Phys Rev Lett* **71** 3943 (1993).

[131] Qichang Su, J H Eberly and J Javanainen, *Phys Rev Lett* **64** 862 (1990).

[132] J van de Ree, J Z Kaminski and M Gavrila, *Phys Rev A* **37** 4536 (1988).

[133] H R Reiss, *J Opt Soc Am B* **4** 726 (1987).

[134] H Rottke, B Wolff, X Brickwedde, D Feldmann and K H Welge, *Phys Rev Lett* **64** 404 (1990).

[135] H Rottke, B Wolff-Rottke, D Feldmann, K H Welge, M Dörr, R M Potvliege and R Shakeshaft, *Phys Rev A* **49** 4837 (1994).

[136] R A Sacks and A Szöke, *Phys Rev A* **40** 5614 (1989).

[137] K J Schafer and K C Kulander, *Phys Rev A* **45** 8062 (1992).

[138] K J Schafer, B Yang, L F DiMauro and K C Kulander, *Phys Rev Lett* **70** 1599 (1993).

[139] J M Schins, P Breger, P Agostini, R C Constantinescu, H G Muller, G Grillon, A Antonetti and A Mysyrowicz, *Phys Rev A* **52** 1272 (1995).

[140] D W Schumacher, F Weihe, H G Muller and P H Bucksbaum, *Phys Rev Lett* **73** 1344 (1994).

[141] F Schwabl, *Quantum Mechanics* (Springer, 1988). 289-300 (interaction of an atom with a radiation field).

[142] R Shakeshaft, *Phys Rev A* **34** 244 and 5119 (1986).

[143] R Shakeshaft, R M Potvliege, M Dörr and W E Cooke, *Phys Rev A* **42** 1656 (1990).

[144] J N Shirley, *Phys Rev B* **138** 979 (1965).

[145] J N Shirley and S Stenholm *J Phys A* **10** 613 (1977).

[146] B W Shore, *The Theory of Coherent Atomic Excitation, Volume 1: Simple Atoms and Fields* (Wiley, 1990). 216-239 (two-state models).

[147] S Solimeno, B Crosignani and P Di Porto, *Guiding, Diffraction and Confinement of Optical Radiation* (Academic Press, 1986).

[148] J G Story, D I Duncan and T F Gallagher, *Phys Rev Lett* **70** 3012 (1993).

[149] D A Telnov and S-I Chu, *Phys Rev A* **50** 4099 (1994).

[150] D A Telnov and S-I Chu, *J Phys B* **28** 2407 (1995).

[151] V Véniard, R Taïeb and A Maquet, *Phys Rev Lett* **74** 4161 (1995).

[152] V Véniard, R Taïeb and A Maquet, *Phys Rev A* **54** 721 (1996).

[153] R M A Vivirito and P L Knight, *J Phys B* **28** 4357 (1995).

[154] E A Volkova, A M Popov and O V Smirnova, *Zh Eksp Teor Fiz* **106** 1360 (1994).

[155] G S Voronov and N B Delone, *JETP Lett* **1** 66 (1965).

[156] G S Voronov and N B Delone, *Sov Phys JETP* **23** 54 (1966).

[157] R B Vrijen, J H Hoogenraad, H G Muller and L D Noordam, *Phys Rev Lett* **70** 3016 (1993).

[158] A Weingartshofer, J K Holmes, G Caudle, E M Clarke and H Krüger, *Phys Rev Lett* **39** 269 (1977).

[159] E T Whittaker and G N Watson, *A Course of Modern Analysis* (Cambridge University Press, 1902). 347 (Weber's equation).

[160] E P Wigner, *Phys Rev* **70** 15 (1946).

[161] Lian-Ao Wu, *Phys Rev A* **50** 5317 (1994).

[162] W Xiong, F Yergeau, S L Chin and P Lavigne, *J Phys B* **21** L159 (1988).

[163] Baorui Yang, K J Schafer, B Walker, K C Kulander, P Agostini and L F DiMauro, *Phys Rev Lett* **71** 3770 (1993).

[164] Y B Zel'dovich, *Sov Phys Usp* **16** 427 (1973).